AMAX-DOAS trace gas column observations from research aircraft over California

Final Report

Contract 09-317

Prepared for:

The California Air Resources Board

Principal Investigator:

Rainer M. Volkamer

Assistant Professor & CIRES Fellow
Department of Chemistry and Biochemistry
University of Colorado, Boulder

Final report submitted to ARB

February 21, 2014

Acknowledgements

We thank the NOAA Twin Otter research aircraft flight crew for their support during the campaign, T. Deutschmann (University of Heidelberg, Germany) for providing McArtim, C. Fayt and M. v. Roozendael (IASB-BIRA, Belgium) for WINDOAS software. We acknowledge J. Stutz (University of California, Los Angeles) for providing AERONET data from the Caltech site. We also thank our collaborators S.-W. Kim (NOAA, Boulder) and C. Cai (CARB) for providing atmospheric chemistry model results and the Atmospheric Remote Sensing Group at Earth Science Research Laboratory, NOAA Boulder for their support during the entire project.

Disclaimer

This report was prepared as one of the project deliverables associated with contract number 09-317 with the California Air Resources Board. The statements and conclusions in this report are those of the authors from the University of Colorado, Boulder, and not necessarily those of the California Air Resources Board. The mention of commercial products, their sources, or their use in connection with the material reported herein is not to be construed as actual or implied endorsement of such products.

Table of Contents

Executive Summary

Tropospheric ozone (O_3) and fine particulate matter (PM) adversely affect public health and are relevant to climate. In California's South Coast Air Basin (SCAB) and Central Valley the concentrations of fine particulate matter (PM 2.5) and O_3 frequently exceed health-based standards. Both O_3 and a major portion of PM 2.5 are secondary pollutants, i.e., formed in the atmosphere as a result of atmospheric chemical transformations that adversely affect public health, degrade visibility, form and deposit acids, toxics, and oxidants that damage crops and ecosystems, and modify clouds.

California's State Implementation Plan relies on predictions from atmospheric models that link emissions of nitrogen oxides (NO_x), volatile organic compounds (VOC), other gases and aerosols to ambient concentrations of O_3 and PM. The California Research at the Nexus of Air Quality and Climate Change (CalNex) field study was conducted throughout California in May, June and July of 2010 to test and evaluate these models. The study addressed issues of simultaneous relevance to atmospheric pollution and climate change, including (1) emission inventory assessment, (2) atmospheric transport and dispersion, (3) atmospheric chemical processing, and (4) cloud-aerosol interactions and radiative effects. This project adds to objectives 1, 2, and 3.

Past field campaigns in California have provided mostly information about pollutant concentrations inside the boundary layer. Little is known about pollution aloft, which can strongly modify the chemistry of O_3 and PM formation. This project has deployed the University of Colorado Airborne Multi AXis DOAS instrument (CU AMAX-DOAS) during 52 research flights over much of California to probe the horizontal and vertical distribution of nitrogen dioxide (NO_2), an O_3 precursor and radical sink. For selected case studies we further demonstrate innovative measurements of formaldehyde (HCHO), a carcinogen and a radical source, and glyoxal (CHOCHO), an air toxic, indicator of the rate of VOC oxidation, and precursor for secondary organic aerosol, SOA. These mobile column measurements help test and improve atmospheric models, and ultimately make more robust tools available to manage air resources.

Key findings from this project include:

- The comprehensive mapping of horizontal distributions of NO_2 vertical column densities (VCD, concentration integral over height below the aircraft) has provided over 18,000 NO_2 VCD measurements all over California. The mapping becomes possible with little error from remote-sensing measurements above the boundary layer (section 3.1).
- The comprehensive NO_2 dataset generated by this project has been considered in the construction of NO_x emissions in the CARB 2010 emission inventory (EI). We compare model predictions of NO_2 based on CARB 2010, and find agreement within 30% with our NO_2 VCD observations (section 3.3, 3.4). While the overall NO_x amounts agree within 30%, there is a mismatch in the location where NO_x emissions occur (section 3.3). Detailed analysis of mapping NO_x emission fluxes near Bakersfield shows that missing

NO_x emissions in the inventory are compensated by larger background NO_x emission over the entire region in the Central Valley.

- Our measurements provide vertical distributions of NO_2. Near surface concentrations agree well (within 10%) with ground-based CARB monitoring stations, and observations at Supersites. NO_2 is found to be layered, and varies strongly up to altitudes of several kilometers (sections 3.2, 3.6).
- Comparison of our NO_2 VCD measurements with coincident VCDs measured by OMI (NASA's NO_2 product v2.1) showed very good agreement (within 5%), suggesting that satellites can provide useful data to manage air resources over California during summer months. However, we also conclude that uncertain assumptions about vertical distributions and surface albedo lead to compensating errors in the satellite retrieval. The good agreement found thus applies only over areas with high surface albedo, like SCAB during summer, and does not necessarily extrapolate globally (section 3.2).
- This project brought into existence tools to measure mobile HCHO and CHOCHO VCDs. There had not been previous such measurements from aircraft. We demonstrate the feasibility, and for selected case studies present first maps of HCHO, CHOCHO, and the ratio of glyoxal to formaldehyde (R_{GF} = CHOCHO/HCHO VCD, section 3.5). R_{GF} is a useful metric to distinguish anthropogenic vs biogenic VOC influences in an air mass.
- We compare our HCHO and CHOCHO maps and profiles with predictions from different atmospheric models (section 3.5, 3.6). The models consistently and significantly under predict the abundance of both species compared to our observations. We also find evidence that refining VOC speciation in the inventory leads to an improved agreement in WRF-Chem predictions over Bakersfield. Vertical distributions show evidence for missing sources in the boundary layer, and in the residual layer aloft (section 3.6).
- In the South Coast Air Basin (SCAB) we observed lower O_3 on a very hot weekend in July. O_3 chemistry appears to be on the verge of transitioning to the NO_x limited regime during very hot days. Further reductions in NO_x in the future are likely to result in lower O_3 levels under such scenarios (see section 3.7). Spectra containing information about HCHO and CHOCHO are in principle available for all 52 flights, and provide an opportunity to further investigate the cause for the lower O_3 on hot weekends.
- We directly quantify O_x production rates (O_x = O_3 + NO_2) using the divergence flux approach for a case study flight near Bakersfield. The flux calculations are constrained also by Doppler-wind, and ozone/aerosol lidar measurements on the aircraft. We find higher O_x production rates over an area with active oil and natural gas production than over / downwind of an urban area. The results raise concerns whether emissions from oil and natural gas production are well represented in the emission inventory (section 3.3).
- The dataset provides opportunities to test models for missing VOC precursors, oxidative capacity, VOC speciation, uncertainties in VOC oxidation rates, with implications for secondary (inorganic and organic) aerosol formation rates. Maps of HCHO/NO_2 VCD ratios further assess directly the VOC/NO_x limitation of O_3 production (see section 6).

List of Figures:

List of Tables:

Abstract

The CU Airborne MAX-DOAS instrument was deployed in California aboard the NOAA Twin Otter research aircraft during May 19-July 19, 2010. A total of 52 flights were carried out covering the entire state but with a particular focus over South Coast Air Basin (SCAB) and the Sacramento area. CU AMAX-DOAS measured horizontal and vertical distributions of nitrogen dioxide (NO_2), formaldehyde (HCHO) and glyoxal (CHOCHO) during the campaign. Other instruments aboard the aircraft included NOAA TOPAZ lidar which measures vertical profiles of ozone (O_3) and aerosols, NCAS Doppler lidar which measures wind profiles, two radiometers to measure surface albedo, a radiometer to measure surface temperature, an in-situ O_3 monitor and temperature sensors.

The footprint of CU AMAX-DOAS measurements (~0.02 x 0.9 km^2 while flying at 4 km AGL) is similar to the spatial resolution of atmospheric model predictions (4 x 4 km^2), and our observations provide means to bridge between ground-based observations as part of measurement networks, Supersites, and satellites to improve atmospheric models used to manage air resources over California. Here, we start with an overview of the field deployment of the NOAA Twin Otter and then present various analyses of the data. Our analyses highlight the benefits of CU AMAX-DOAS observations for atmospheric model improvements, satellite retrievals and co-benefit of column/profile measurements of NO_2, OVOCs, O_3 and wind measurements aboard a research aircraft. We have further deployed two ground based MAX-DOAS instruments at the CARB measurement station in Fontana Arrows, and at the Caltech Supersite, and relocated one of the instruments for a period of time to the T1 site in Cool downwind of Sacramento. We have used these ground-based column observations to evaluate the uncertainty of mobile NO_2 VCD measurements from the aircraft during frequent overpasses with the aircraft. The agreement is found to be excellent (<7% error), and shows the data is useful to evaluate NO_x emissions with high accuracy. Our further analysis of the NO_x emissions from urban areas shows excellent agreement with the CARB 2010 emission inventory (within 30%). NO_x emission flux calculations over Bakersfield area also gave similar agreement. However, emissions from oil and gas operations were found to be missing in the emission inventory. These emissions also lead to significant O_3 production in the Bakersfield area.

We also present the assessment of the NASA OMI satellite NO_2 data over California during summer months. We show that uncertain vertical distributions and high surface albedo lead to compensating uncertainty in the NASA OMI satellite NO_2 product, which provides useful data over California during summer months to test atmospheric models over large spatial scale. We present new evidence that supports O_3 formation chemistry being near the peak or on verge of transitioning to NO_x limited conditions in the SCAB. Finally, we present case studies for HCHO and CHOCHO distributions in the SCAB and show that current atmospheric models significantly under predict these oxygenated VOCs (OVOC) with implications for O_3 as well as secondary (inorganic and organic) aerosol formation.

1. Introduction

Air pollution is one of the major problems in most urban areas around the world. It adversely affects human health as well as has environmental concerns such as causing acid rain, degrading visibility and damaging vegetation and materials. With half of the world population now living in urban areas, more people in the world are directly affected by air pollution today than at any time in the past. Further long-range transport of pollutants can affect areas far away from sources.

Human activities emit large number of chemical compounds into the atmosphere and are the main source for air pollution. Emission of nitrogen oxides (NO_x) and volatile organic compounds (VOC_S) are particularly important because of their ability to form tropospheric ozone (O_3). NO_x and VOCs can react in the presence of sunlight to produce tropospheric ozone. NO_x also form nitrate aerosols which is one of the major component of particulate matter (PM). NO_x, O_3 and PM are recognized by the U.S. Environmental Protection Agency (EPA) as criteria pollutants due to their health and environmental concerns. These criteria pollutants are regulated by air quality regulating agencies throughout the world by setting health based standards. The National Ambient Air Quality Standard (NAAQS) set by U.S. EPA are 75 ppb for O_3 (8 hour maximum), 53 ppb for NO_2 (annual mean) and 12 ug/m^3 and 15 ug/m^3 for primary and secondary $PM_{2.5}$ respectively (annual mean). Further O_3 and PM are relevant for climate discussions.

Ozone formation is a nonlinear process and is a function of NO_x and VOCs. Hence, reductions in the precursors can increase, decrease or leave the O_3 levels unchanged. The photochemical O_3 formation process has been extensively studied (e.g. Finlayson-Pitts and Pitts Jr, 2000, Seinfeld and Pandis, 2006). The only known reactions for O_3 formation in the troposphere is given by reactions R1-R3. Photolysis of NO_2 produces $O(^3P)$ radical which rapidly combines with O_2 molecule to form O_3 (R1 and R2). Ozone is then rapidly consumed in the subsequent reaction with NO to regenerate NO_2 (R3).

$$NO_2 + h\nu \rightarrow NO + O(^3P)\ (280 < \lambda < 430\ nm) \qquad (R1)$$

$$O(^3P) + O_2 + M \rightarrow O_3 + M \qquad (R2)$$

$$NO + O_3 \rightarrow NO_2 + O_2 \qquad (R3)$$

The null O_x-NO_x cycle represented by reactions R1-R3 establishes a steady-state O_3 concentration and does not lead to net formation or loss of O_3. Net ozone formation occurs when VOCs are considered. When a generic VOC molecule is oxidized by OH radical in the HO_x cycle (reaction R4-R6) to form RO_2, then HO_2 and subsequently regenerate OH, two NO molecules are oxidized to NO_2. The NO_2 molecules then yield O_3 via reaction R2 after undergoing photolysis (R1). Because in the presence of VOCs, NO molecules are oxidized to NO_2 via reactions R5 and R6 rather than via consumption of O_3 (R3), net photochemical O_3 production occurs.

$$RH + OH + O_2 \rightarrow RO_2 + H_2O \quad (R4)$$

$$RO_2 + NO + O_2 \rightarrow NO_2 + R'CHO + HO_2 \quad (R5)$$

$$HO_2 + NO \rightarrow NO_2 + OH \quad (R6)$$

NO_2 reacts readily with OH to form nitric acid (R7). This is one of the loss processes for NO_2 in the atmosphere. Though it is usually not a dominant loss process for NO_2, it is sufficiently fast to form significant HNO_3 during the day in polluted regions with relatively high NO_2 concentrations. HNO_3 can then react with ammonia to form ammonium nitrate particles (R8). The ammonium nitrate can exist as a solid particle or in solution and is in equilibrium.

$$NO_2 + OH \rightarrow HNO_3 \quad (R7)$$

$$NH_3 + HNO_3 \rightarrow NH_4NO_3 \quad (R8)$$

$$NH_4NO_3 \leftrightarrow NH_4^+(aq) + NO^{3-}(aq) \quad (R9)$$

Despite decades of pollution control measures, tropospheric O_3 along with particulate matter has remained a problem in many urban areas in California in particular the South Coast Air Basin (SCAB) and San Joaquin valley. Both NO_x and VOC levels in SCAB and California in general have gradually decreased over the last few decades and continue to decrease (Russell et al., 2010, Russell et al., 2012, Warneke et al., 2012, Pollack et al., 2013). However improvement in O_3 has slowed down in recent years and O_3 levels continue to exceed the air quality standards (Ryerson et al., 2013). Nitrates continue to form a large fraction of PM mass in California. More than 20% of PM_1 mass was found to be nitrates at the CalNex ground site in Pasadena, CA in summer 2010 (Hayes et al., 2013).

The CU AMAX-DOAS instrument was deployed aboard the NOAA Twin Otter during the CalNex campaign to probe horizontal and vertical distributions of ozone precursor molecule nitrogen dioxide (NO_2), formaldehyde (HCHO), which is a radical source and possibly measure the secondary organic aerosol (SOA) precursor gas glyoxal (CHOCHO) in California. The overall objective of the deployment was make the map of spatial distributions of these gases available to provide better opportunity and ability to test atmospheric models for the purpose of making improved models available for air resources management. The main elements of our project can be summarized as follows:

- To upgrade the CU AMAX-DOAS telescope pylon to add vertical profiling capability and deploy the modified instrument aboard the NOAA Twin Otter as part of the field campaign.
- To make maps of horizontal and vertical distribution of NO_2, HCHO and possibly CHOCHO available to test atmospheric models.

- To explore synergies between CU AMAX-DOAS, NOAA TOPAZ lidar and other instruments aboard the aircraft as well as integrate data from ground based super sites, satellites and atmospheric models.
- To report to CARB on our findings and publish scientific journal article.

This report is organized as follows: In Section 2 of this report we describe the field deployment of the CU AMAX-DOAS instrument. The key findings from this project are summarized in Section 3 of the report including three manuscripts that have been published in peer reviewed journal publications. Section 3 also presents findings from ongoing analyses. The publications and presentations originated from this project are listed in section 4. In section 5, we present the report summary and conclusions.

2. Field deployment

The CalNex (Ryerson et al., 2013) and CARES (Zaveri et al., 2012) field campaigns took place during summer 2010 in the Los Angeles Basin (LA Basin) and Sacramento Valley respectively. Fifty-two NOAA Twin Otter aircraft research flights, totaling 207 hours, took place between May 19 and July 19, 2010 as part of the two field intensives. Of these, 34 flights were based in Ontario, California as part of CalNex program (Fig. 2.1b), and 15 were based in Sacramento, California in coordination with the DOE CARES program (Fig. 2.1c) and three were transit flight to and from California. Table 2.1 lists and provides a brief description of all the NOAA Twin Otter flights during the two campaigns. These flights were supported by the California Air Resources Bureau (CARB) and the NOAA Air Quality Program. The NOAA Twin Otter aircraft provided an airborne remote–sensing capability and was equipped with the TOPAZ differential absorption lidar (DIAL) to measure vertically–resolved O3 and aerosol backscatter nadir profiles (Alvarez II et al., 2011, Langford et al., 2011), a scanning Doppler lidar to measure nadir wind fields (Pearson et al., 2009), and an airborne multi axis differential optical absorption spectrometer (AMAX–DOAS) to measure aerosol extinction and variety of trace gas column densities, among them nitrogen dioxide (NO_2), formaldehyde (HCHO), glyoxal (CHOCHO), and nitrous acid (HONO) (Volkamer et al., 2009, Baidar et al., 2013). The NOAA Twin Otter also carried an *in situ* O_3 sensor, a radiometer to measure surface temperature, and upward and downward irradiance sensors to retrieve surface albedo at 360, 479, 630, and 868 nm. Details about the instrumentation on the NOAA Twin Otter research aircraft is given in Table 2.2. Further details on the instrumentation can be found in Section 3. Its deployment and flight plans were focused on providing data to better understand the emissions sources of NO_x to the atmosphere, the 3-dimensional distribution of O_3, NO_2, HCHO, CHOCHO, and particulate matter in different regions of California, and the key transport processes affecting the spatial and temporal distributions of these pollutants. CU AMAX-DOAS NO_2 data from this deployment are available at http://chem.colorado.edu/volkamergroup/ and preliminary O_3 data are publicly available at http://www.esrl.noaa.gov/csd/lidar/calnex/data_archive.

Typically, the Twin Otter flew one of two generic flight plans lasting ~4 hours during the two campaigns. Maps with the overlaid Twin Otter flights are shown in Fig. 2.1. Morning flights (between 9-14 PST) were dedicated to mapping horizontal distributions of trace gases and obtaining high-resolution vertical profiles of trace gases and the aerosol extinction coefficient from the surface to 4 km ASL at selected locations in the Los Angeles Basin, including a coastal site, over the high desert, and in the Central and Sacramento Valleys. The morning observations were primarily aimed at constraining the boundary conditions of atmospheric models, characterizing pollutant concentrations aloft, and testing of satellite retrievals. During afternoon flights (between 14-19 PST) the plane stayed at one altitude, typically about 4 km ASL, to map out the ozone, wind and aerosol structure when photochemical production of ozone was high and to observe transport of O_3, NO_2, and aerosol into and out of the various air basins of California. Example morning and afternoon flight plans in the LA Basin are shown in Fig. 2.2.

Flight date in 2010	Description	Coordination & Overflights
Wed. May 19	Second leg of the transit flight from Broomfield, CO to Ontario; pollution survey over LA Basin	Pasadena
Sun. May 23	O_3 distribution over Southern California associated with a stratospheric intrusion	
Tue. May 25 A	Pollution survey over LA Basin	Pasadena
Tue. May 25 B	Pollution survey over LA Basin	Pasadena
Sat. May 29	O_3 distribution over LA Basin and Mojave Desert associated with a stratospheric intrusion	Pasadena
Sun. May 30	Day–into–night flight (6 PM–9:30 PM); pollutant distribution over LA Basin and LA Bight	NOAA P-3; Pasadena
Mon. May 31A	Pollution survey over LA Basin	Pasadena
Mon. May 31B	Pollution survey over eastern LA Basin; Doppler lidar test	
Tue. June 1	Outflow of pollution from LA Basin to Mojave Desert; NO_2 comparison with OMI satellite	Pasadena
Thu. June 3 A	Dawn flight, Pollution survey over LA Basin	Fontana Arrow
Thu. June 3 B	Pollution survey over LA Basin	Pasadena
Fri. June 4	Pollution survey over LA Basin; transport to Mojave Desert and Imperial Valley	Pasadena
Sat. June 5 A	Pollution survey over LA Basin	Pasadena
Sat. June 5 B	Pollution survey over LA Basin; transport to Mojave Desert and Imperial Valley	
Mon. June 7 A	Pollution survey over LA Basin	Pasadena
Mon. June 7 B	Pollution survey over LA Basin; transport to Mojave Desert and Imperial Valley	Pasadena
Wed. June 9	Aborted transit flight to Sacramento	
Tue. June 15 A	First leg of transit flight from Ontario to Sacramento; pollution survey over Bakersfield area; NO_2 comparison with OMI satellite	Bakersfield
Tue. June 15 B	Second leg of transit flight from Ontario to Sacramento; pollution survey over San Joaquin Valley	
Fri. June 18 A	Pollution survey over Sacramento area and northern San Joaquin Valley	WGC tower
Fri. June 18 B	Pollution survey over San Joaquin Valley	NOAA P-3; DOE G1; NASA B200; Bakersfield
Mon. June 21 A	Pollution survey over Sacramento and east of Bay Area	
Mon. June 21 B	Pollution survey over Sacramento, southern Bay Area, and northern San Joaquin Valley	
Tue. June 22 A	Pollution survey over Sacramento and east of Bay Area	WGC tower
Tue. June 22 B	Inflow of Asian pollution over Northern Coast and Sacramento Valley; NO_2 comparison with OMI satellite	
Wed. June 23	Pollution survey over Sacramento, east of Bay Area, and over Sierra Nevada Foothills	
Thu. June 24 A	Pollution survey over Sacramento and east of Bay Area	
Thu. June 24 B	Pollution survey over Sacramento, east of Bay Area, and over Sierra Nevada Foothills	
Sat. June 26	Pollution survey over Sacramento and east/south of Bay Area; transport to San Joaquin Valley, inflow of Asian pollution	WGC tower
Sun. June 27 A	Pollution survey over Sacramento and east of Bay Area	

Sun. June 27 B	Pollution survey over Sacramento, east of Bay Area, and over Sierra Nevada Foothills	WGC tower
Mon. June 28	Pollution survey over Sacramento and east of Bay Area	WGC tower
Tue. June 29 A	First leg of transit flight from Sacramento to Ontario; pollution survey near Point Reyes, north and east of Bay Area	WGC tower
Tue. June 29 B	Second leg of transit flight from Sacramento to Ontario; pollution survey near over San Joaquin Valley and Mojave Desert; transport of pollutants between air basins	
Wed. June 30 A	Pollution survey over Salton Sea, along Mexican border, and over portion of northern Mexico; cross-border pollution transport	
Wed. June 30 B	Pollution survey over San Diego, near Mexican border, and between San Diego and LA; cross-border pollution transport	
Fri. July 2	Pollution survey over LA Basin; transport to Mojave Desert and Imperial Valley	Pasadena
Sun. July 4	Pollution survey over LA Basin; transport to Mojave Desert and Imperial Valley	Pasadena
Mon. July 5 A	Pollution survey over LA Basin and transport to Mojave Desert; OMI	Pasadena
Mon. July 5 B	Pollution survey over LA Basin; transport to Mojave Desert and Imperial Valley	Pasadena
Tue. July 6	Pollution survey over LA Basin; transport to Mojave Desert and Imperial Valley	Pasadena
Mon. July 12	Pollution survey over LA Basin and transport to Mojave Desert; OMI?	Pasadena
Wed. July 14	Ontario to Monterey; pollution survey over San Joaquin Valley and Sierra Nevada; transport by mountain slope flows	Bakersfield
Thu. July 15 A	Day–into–night flight (7 PM–11 PM); Monterey to Ontario: pollution survey over San Joaquin Valley and Sierra Nevada; transport by mountain slope flows and low level jet	Bakersfield
Thu. July 15 B	Pollution survey over LA Basin and transport to Mojave Desert	Pasadena
Fri. July 16 A	Pollution survey over LA Basin; transport to Mojave Desert and Imperial Valley	Pasadena
Fri. July 16 B	Pollution survey over LA Basin; transport to Mojave Desert and Imperial Valley	Pasadena
Sat. July 17	Pollution survey over LA Basin; transport to Mojave Desert and Imperial Valley	Pasadena
Sun. July 18 A	Dawn flight; Pollution survey over LA Basin	Fontana Arrow
Sun. July 18 B	Pollution survey over San Diego, near Mexican border, and between San Diego and LA; cross-border pollution transport	
Mon. July 19 A	First leg of the transit flight from Ontario to Broomfield, CO; pollution transport from LA Basin to Mojave Desert and southern Nevada	
Mon. July 19 B	Second leg of the transit flight from Ontario to Broomfield, CO; Four Corners and San Juan Power plants	

Table 2.1: *NOAA Twin Otter flights during CalNex and CARES field campaigns.*

Measurement	Technique	Sample interval	Accuracy at high S/N (±1σ)	Precision at low S/N (±1σ)	References
NO2 vertical column density (VCD)	Differential Optical Absorption Spectroscopy (DOAS)	2-30s	~7%	$1.5x10^{15}$ molec. cm^{-2}	Baidar et al.[2013] and Oetjen et al.[2013]
HCHO and CHOCHO VCD	DOAS	2-30s		depends upon gas and averaging time	
NO2, HCHO and CHOCHO vertical profiles	DOAS	ascent/descent	~10%	depends upon gas and averaging time	Baidar et al.[2013]
Aerosol extinction profiles (360, 477 nm)	DOAS	ascent/descent	~5%	~0.01-0.03 km^{-1}	Baidar et al.[2013]
Surface Albedo	4-channel UV and vis irradiance	30s		~5%	Oetjen et al.[2013]
O3 profiles	Differential absorption lidar (DIAL)	10s	5-10% (up to 30% for low SNR)	<5% (up to 15% for low SNR)	Alvarez et al.[2011] and Langford et al.[2011]
Aerosol backscatter profiles (300 nm)	DIAL	10s	~10%	<30%	Davis et al. [2000] and White et al. [1999]
BL Height	DIAL	10s	~50 m	~50 m	Davis et al. [2000] and White et al. [1999]
Line of sight wind speed profiles (at 4 azimuth angles)	Doppler lidar	2-6s	0.1 m/s	up to 0.1 m/s	Pearson et al. [2009]
Relative aerosol backscatter profiles (1.6 μm)	Doppler lidar	1s	uncalibrated	uncalibrated	Pearson et al. [2009]
O3	UV light absorption	10s	1 ppbv/10%	1 ppbv/ 2%	www.twobtech.com/model_202.htm
Temperature	Thermistor	1s	<0.2 K	0.2 K	www.ti.com/lit/ds/symlink/lm35.pdf
Surface temperature	IR pyrometer	1s	0.06 K	0.5 K	www.heitronics.com/fileadmin/content/Prospekte/KT15IIP_e_V510.pdf

Table 2.2: *NOAA Twin Otter measurements during CalNex and CARES field campaigns.*

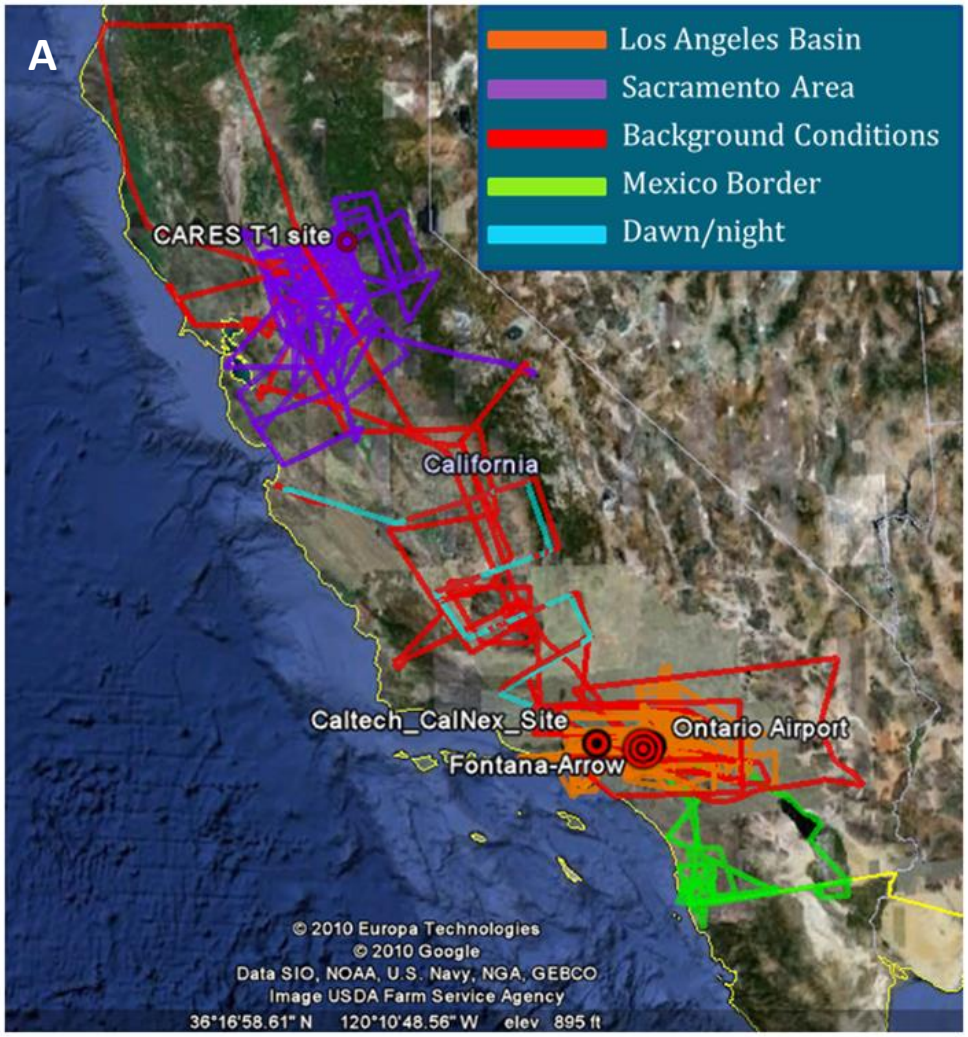
A
Los Angeles Basin
Sacramento Area
Background Conditions
Mexico Border
Dawn/night
CARES T1 site
California
Caltech_CalNex_Site
Ontario Airport
Fontana-Arrow
© 2010 Europa Technologies
© 2010 Google
Data SIO, NOAA, U.S. Navy, NGA, GEBCO
Image USDA Farm Service Agency
36°16'58.61" N 120°10'48.56" W elev 895 ft

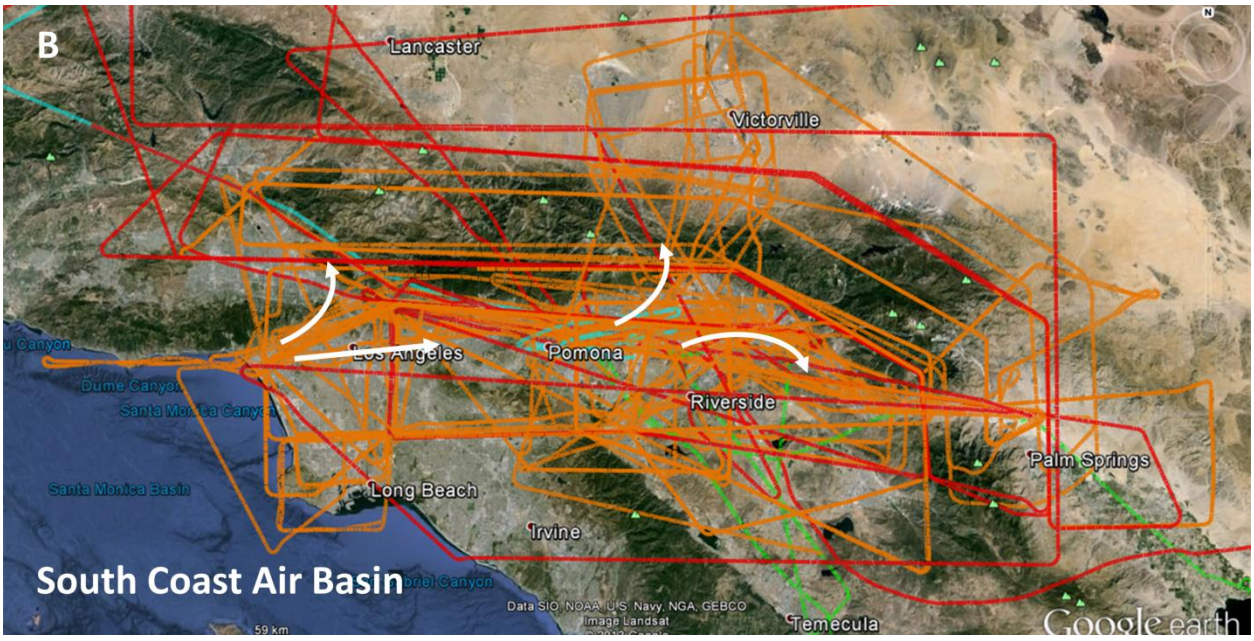
B
Lancaster
Victorville
Los Angeles
Pomona
Riverside
Palm Springs
Long Beach
Irvine
Temecula
South Coast Air Basin
Santa Monica Basin
Data SIO, NOAA, U.S. Navy, NGA, GEBCO
Image Landsat
Google earth

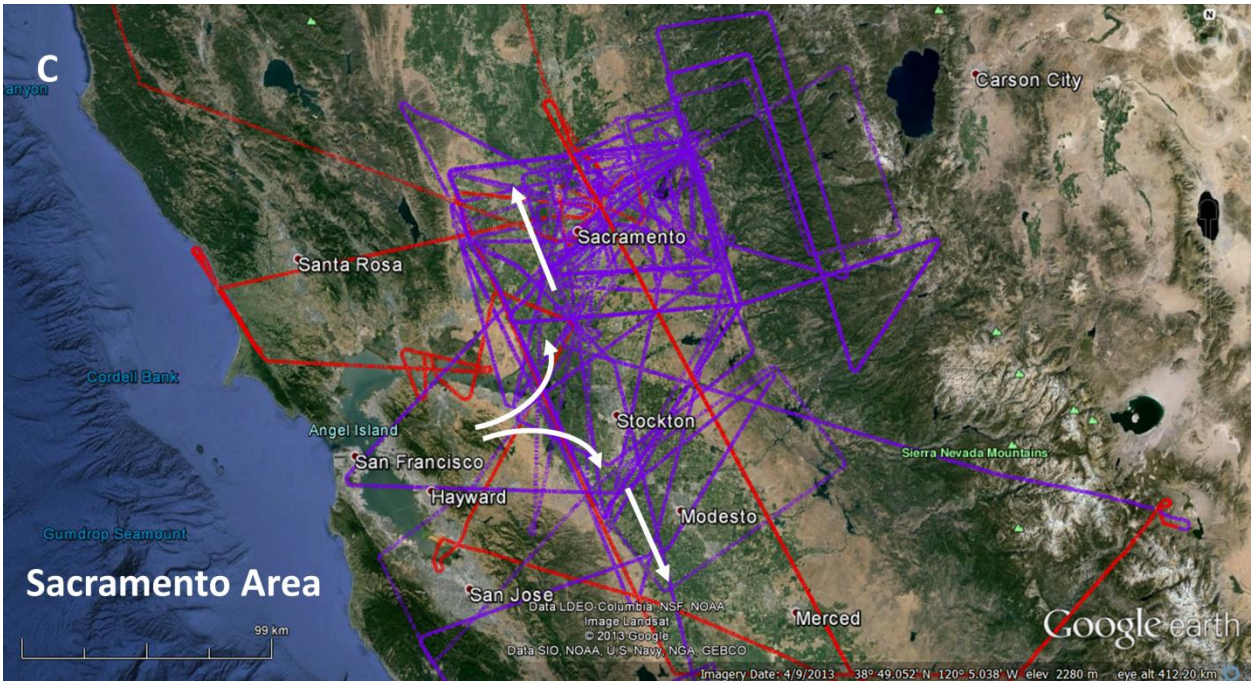

Figure 2.1: *(A) NOAA Twin Otter flights during CalNex and CARES field campaigns from May 19-July 19, 2010. (B) Same as A showing details of flights over the South Coast Air Basin. (C) Same as A showing details of flights over the Sacramento area. White arrows in (B) and (C) represent predominant wind flow during the day in summer months. Predominant wind patterns are shown to illustrate corridors for pollution transport and how the flight plans were designed to quantify this transport and are not true wind conditions for the measurement days.*

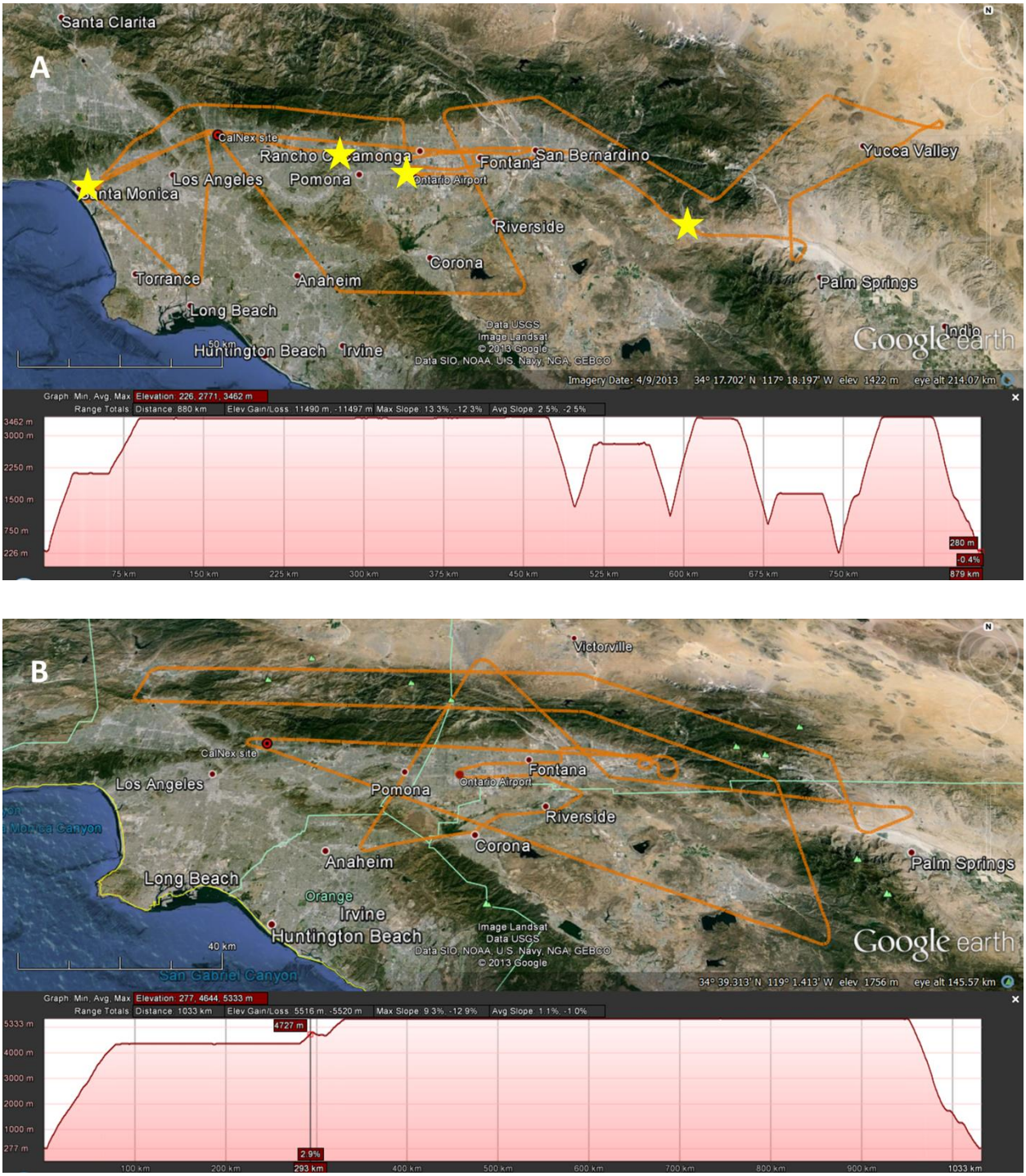

Figure 2.2: *Examples of NOAA Twin Otter flight plans in the South Coast Air Basin during (SCAB) the CalNex campaign: (A) Morning (9-14 PST) and (B) Afternoon (14-19 PST). Stars in (A) represent locations of vertical profiles inside the SCAB shown in Section 3.6.*

3. Data Analysis and Results

3.1 The CU Airborne MAX-DOAS instrument: vertical profiling of aerosol extinction and trace gases

Reproduced from: Baidar, S., H. Oetjen, S. Coburn, B. Dix, I. Ortega, R. Sinreich, and R. Volkamer (2013), The CU Airborne MAX-DOAS instrument: vertical profiling of aerosol extinction and trace gases, Atmos. Meas. Tech., 6, 719-739. doi:10.5194/amt-6-719-2013

The University of Colorado Airborne Multi Axis Differential Optical Absorption Spectroscopy (CU AMAX-DOAS) instrument uses solar stray light to detect and quantify multiple trace gases, including nitrogen dioxide (NO_2), glyoxal (CHOCHO), formaldehyde (HCHO), water vapor (H_2O), nitrous acid (HONO), iodine monoxide (IO), bromine monoxide (BrO), and oxygen dimers (O_4) at multiple wavelengths (absorption bands at 360 nm, 477 nm, 577 nm, 632 nm) simultaneously, in the open atmosphere. The instrument is unique, as it (1) features

-

zenith, and multiple elevation angles forward and below the plane by the same spectrometer/detector system. Sets of solar stray light spectra collected from nadir to zenith scans provide some vertical profile information within 2 km above and below the aircraft altitude, and the vertical column density (VCD) below the aircraft is measured in nadir view. Maximum information about vertical profiles is derived simultaneously for trace gas concentrations and aerosol extinction coefficients over similar spatial scales and with a vertical resolution of typically 250 m during aircraft ascent/descent.

The instrument is described, and data from flights over California during the CalNex and CARES air quality field campaigns is presented. Horizontal distributions of NO_2 VCDs (below the aircraft) maps are sampled with typically 1 km resolution, and show good agreement with two ground based MAX-DOAS instruments (slope 0.95±0.09, R^2=0.86). As a case study vertical profiles of NO_2, CHOCHO, HCHO, and H_2O concentrations and aerosol extinction coefficients, ε 477 from O_4 measurements from a low approach at Brackett airfield inside the South Coast Air Basin (SCAB) is presented. These profiles contain ~12 degrees of freedom (DOF) over a 3.5 km altitude range, an independent information approximately every 250 m. The boundary layer NO_2 concentration, and the integral aerosol extinction over height (aerosol optical depth, AOD) agrees well with nearby ground-based in-situ NO_2 measurement, and AERONET station. The detection limits of NO_2, CHOCHO, HCHO, H_2O_{442} ε_{360} ε_{477} for 30 seconds integration time spectra recorded forward of the plane are 5 ppt, 3 ppt, 100 ppt, 42 ppm, 0.004 km^{-1}, 0.002 km^{-1} in the free troposphere (FT), and 30 ppt, 16 ppt, 540 ppt, 252 ppm, 0.012 km^{-1}, 0.006 km^{-1} inside the boundary layer (BL), respectively. Mobile column observations of trace gases and aerosols are complimentary to in-situ observations, and help bridge the spatial scales probed by ground-based observations, satellites, and predicted by atmospheric models.

Conclusions:

- The University of Colorado Airborne MAX-DOAS instrument provides highly accurate and selective measurements of multiple trace gases and aerosols simultaneously by means of a single, portable instrument.

  comparison with an independent inertia system. We demonstrated the capability of the instrument to map horizontal and vertical distribution of trace gases.
- The CU AMAX-DOAS instrument is validated by comparison with NO_2 VCDs measured by ground-based MAX-DOAS. The agreement between the airborne and ground based instrument was very good for coincident measurements (slope: 1.05).
- Over southern California, where elevated surface albedo (~10% at 477 nm wavelength, measured aboard the plane) compensates for reduced sensitivity due to aerosols, the geometric approximation of Air Mass Factors is shown to be feasible with little error to convert NO_2 SCD to VCD below the plane. We estimate the error in the NO_2 vertical columns due 7%

  high altitude flights over low surface albedo.
- The available data set is of high quality to evaluate NO_x emissions over California.

Atmos. Meas. Tech., 6, 719–739, 2013
www.atmos-meas-tech.net/6/719/2013/
doi:10.5194/amt-6-719-2013

Atmospheric Measurement Techniques
Open Access

The CU Airborne MAX-DOAS instrument: vertical profiling of aerosol extinction and trace gases

S. Baidar[1,2], H. Oetjen[1,*], S. Coburn[1], B. Dix[1], I. Ortega[1], R. Sinreich[1], and R. Volkamer[1,2]

[1]Department of Chemistry and Biochemistry, University of Colorado, Boulder, CO 80309, USA
[2]Cooperative Institute for Research in Environmental Sciences (CIRES), Boulder, CO 80309, USA
[*]now at: UCLA/JPL Joint Institute for Regional Earth System Science and Engineering (JIFRESSE), Los Angeles, CA 90095, USA

Correspondence to: R. Volkamer (rainer.volkamer@colorado.edu)

Received: 2 August 2012 – Published in Atmos. Meas. Tech. Discuss.: 26 September 2012
Revised: 16 February 2013 – Accepted: 1 March 2013 – Published: 14 March 2013

Abstract. The University of Colorado Airborne Multi-Axis Differential Optical Absorption Spectroscopy (CU AMAX-DOAS) instrument uses solar stray light to detect and quantify multiple trace gases, including nitrogen dioxide (NO_2), glyoxal (CHOCHO), formaldehyde (HCHO), water vapor (H_2O), nitrous acid (HONO), iodine monoxide (IO), bromine monoxide (BrO), and oxygen dimers (O_4) at multiple wavelengths (absorption bands at 360, 477, 577, 632 nm) simultaneously in the open atmosphere. The instrument is unique as it (1) features a motion compensation system that decouples the telescope field of view from aircraft movements in real time ($< 0.35°$ accuracy), and (2) includes measurements of solar stray light photons from nadir, zenith, and multiple elevation angles forward and below the plane by the same spectrometer/detector system. Sets of solar stray light spectra collected from nadir to zenith scans provide some vertical profile information within 2 km above and below the aircraft altitude, and the vertical column density (VCD) below the aircraft is measured in nadir view. Maximum information about vertical profiles is derived simultaneously for trace gas concentrations and aerosol extinction coefficients over similar spatial scales and with a vertical resolution of typically 250 m during aircraft ascent/descent.

The instrument is described, and data from flights over California during the CalNex (California Research at the Nexus of Air Quality and Climate Change) and CARES (Carbonaceous Aerosols and Radiative Effects Study) air quality field campaigns is presented. Horizontal distributions of NO_2 VCD (below the aircraft) maps are sampled with typically 1 km resolution, and show good agreement with two ground-based MAX-DOAS instruments (slope = 0.95 ± 0.09, $R^2 = 0.86$). As a case study vertical profiles of NO_2, CHOCHO, HCHO, and H_2O concentrations and aerosol extinction coefficients, ε, at 477 nm calculated from O_4 measurements from a low approach at Brackett airfield inside the South Coast Air Basin (SCAB) are presented. These profiles contain ~ 12 degrees of freedom (DOF) over a 3.5 km altitude range, an independent information approximately every 250 m. The boundary layer NO_2 concentration, and the integral aerosol extinction over height (aerosol optical depth, AOD) agrees well with nearby ground-based in situ NO_2 measurement, and AERONET station. The detection limits of NO_2, CHOCHO, HCHO, H_2O_{442}, ε_{360}, ε_{477} for 30 s integration time spectra recorded forward of the plane are 5 ppt, 3 ppt, 100 ppt, 42 ppm, 0.004 km^{-1}, 0.002 km^{-1} in the free troposphere (FT), and 30 ppt, 16 ppt, 540 ppt, 252 ppm, 0.012 km^{-1}, 0.006 km^{-1} inside the boundary layer (BL), respectively. Mobile column observations of trace gases and aerosols are complimentary to in situ observations, and help bridge the spatial scales that are probed by satellites and ground-based observations, and predicted by atmospheric models.

1 Introduction

Airborne Differential Optical Absorption Spectroscopy (DOAS) measurements of different trace gases in the atmosphere by solar stray light started in late 1980s and has come a long way since then. Early studies were focused on

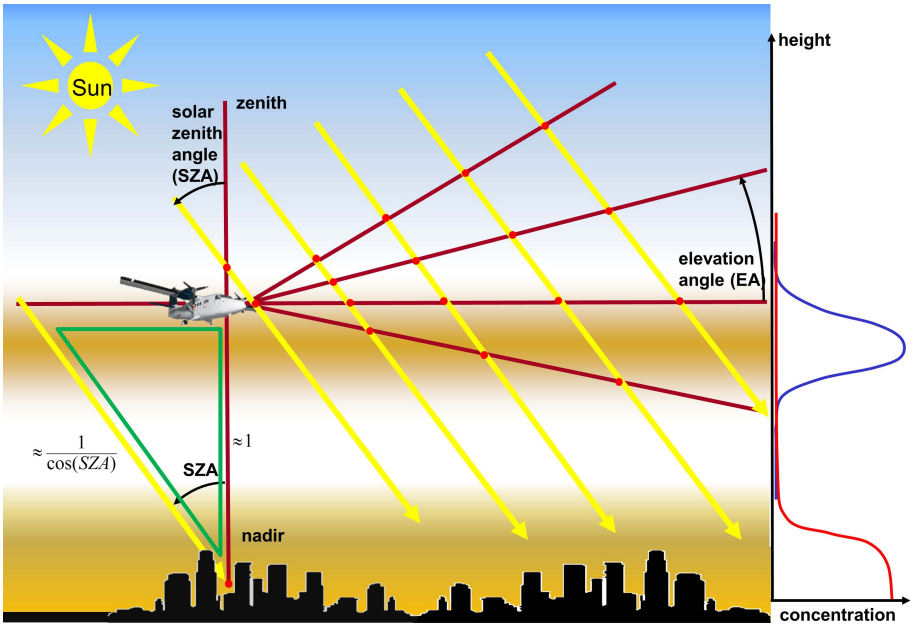

Fig. 1. Schematic of the AMAX-DOAS measurement principle. Individual EAs contain different amounts of information from different layers in the atmosphere. The inset (green triangle) illustrates the geometric approximation used to convert nadir dSCDs to VCDs.

obtaining column integrals of stratospheric trace gases like nitrogen dioxide (NO_2) (Wahner et al., 1990a), chlorine dioxide (OClO) (Schiller et al., 1990), and bromine oxide (BrO) (Wahner et al., 1990b) from zenith measurements. First retrievals of trace gas concentrations close to the aircraft altitude were reported by Petritoli et al. (2002) for stratospheric ozone (O_3). These studies were followed by the application of the AMAX-DOAS technique to obtain tropospheric columns for NO_2 (Melamed et al., 2003; Heue et al., 2005; Wang et al., 2005) and sulfur dioxide (SO_2) (Wang et al., 2006; Melamed et al., 2008) over polluted regions. These instruments used multiple telescopes, most notably zenith and nadir, to collect scattered sunlight. Over the past few years, building on the well-established limb observation technique (e.g., McElroy, 1988; Weidner et al., 2005 and references within) , the focus has shifted towards retrievals of vertical distribution of trace gases from the aircraft using several limb viewing telescopes. Figure 1 shows the conceptual viewing geometry of the so-called Airborne Multi-Axis DOAS (AMAX-DOAS) technique. Individual elevation angles (EAs) contain different amounts of information from different layers in the atmosphere and hence can be used to infer vertical distributions of trace gases. Bruns et al. (2006) first reported profiles of NO_2 over the Po valley from an airborne MAX-DOAS instrument with four telescopes pointing at fixed EAs. A boundary layer NO_2 profile was obtained by Dix et al. (2009) using multiple lines of sight (LOS) and a descent of an aircraft. Prados-Roman et al. (2011) used the LOS parallel to the plane and the aircraft descent to retrieve vertical profiles of BrO in the Arctic. Most recently, a limb scanning airborne DOAS instrument was developed at the Belgium Institute for Space Aeronomy (BIRA) to obtain vertical distribution of trace gases like NO_2 (Merlaud et al., 2011). Most airborne DOAS instruments use either a single or multiple fixed LOS and a spectrum collected from the same EA is used as the reference spectrum for DOAS analysis. However, these instruments lack active control of the viewing geometry of the telescope during the flight. Pitch and roll information from the aircraft is used during post-processing to calculate the true viewing angle at the time of measurement during the flight. This often leads to a range of EAs assigned to measurements, and results in a loss of sensitivity to a given layer in the atmosphere compared to when the EAs are actively controlled in order to retrieve vertical profile information of trace gases. Active control of EAs along with careful selection of EAs also allows for maximization of the degrees of freedom (DOF).

Here we describe the CU AMAX-DOAS instrument, a new and improved AMAX-DOAS instrument with capabilities to motion stabilize and collect spectra from multiple axes using a single telescope. The CU AMAX-DOAS instrument has the capability to access zenith, nadir and limb viewing geometry by means of a single, rotatable prism telescope that is coupled to a motion compensation system. The motion compensation system includes angle sensors to measure pitch and roll angles of the aircraft, and a feedback loop to correct the telescope position for pitch and roll angles in real time. This ensures a constant desired EA is maintained during spectra acquisition in flight. Isolation of the telescope from the aircraft movements enables us to systematically

probe the atmosphere with desired sets of EAs in order to retrieve vertical profiles of trace gases and aerosol extinction simultaneously, and with the highest possible information content. The use of a single telescope to collect spectra from zenith and other EAs (nadir, and forward of the plane) further enables the zenith spectra to be used as the Fraunhofer reference spectrum in the DOAS analysis. Zenith spectra usually contain the least amount of tropospheric absorbers, and the ability to record zenith spectra close in time to other EA spectra assures that absorbers above the plane are characterized with minimum difference in radiation fields, and makes the instrument inherently more sensitive to absorbers near and below the aircraft altitude (Volkamer et al., 2009a).

The CU AMAX-DOAS instrument was successfully deployed from 19 May–19 July 2010 as part of two air quality studies in California, namely the California Research at the Nexus of Air Quality and Climate Change (CalNex) (see the overview paper by Ryerson et al., 2013) and the Carbonaceous Aerosols and Radiative Effects Study (CARES) (see the overview paper by Zaveri et al., 2012). A total of 52 research flights were performed during this deployment and here we focus on results from one flight on 16 July 2010 to describe the technique and characterize instrument performance. In Sect. 2 the CU AMAX-DOAS instrument is described and the instrument configuration is introduced. Section 3 describes the DOAS analysis procedures, radiative transfer model (RTM) calculations, and algorithms to retrieve VCDs (vertical column densities) and vertical profiles of the trace gas concentrations and aerosol extinction. Section 4 demonstrates the capability of the new instrument. As a case study, vertical profiles of nitrogen dioxide (NO_2), glyoxal (CHOCHO), formaldehyde (HCHO), water vapor (H_2O) and aerosol extinction at 477 nm are retrieved from a low approach at Brackett airfield in the South Coast Air Basin (SCAB). Finally, as a validation, CU AMAX-DOAS NO_2 VCDs are compared with VCDs measured by two ground-based MAX-DOAS instruments that were regularly overpassed during flights, the boundary layer NO_2 concentration of the retrieved vertical profile is compared to a ground-based in situ sensor concentration, and the integral aerosol extinction over height, i.e., aerosol optical depth (AOD) is compared with data from an AERONET station.

Appendix A shows the glossary of frequently used abbreviations in the paper.

2 The CU AMAX-DOAS instrument

The CU-AMAX-DOAS instrument collects spectra of scattered sunlight between 330 and 720 nm at different EAs. The scattered sunlight spectra are analyzed for the presence of absorbers like NO_2, CHOCHO, HCHO, H_2O, HONO, IO, BrO, O_4 using the DOAS method (Platt and Stutz, 2008). NO_2, CHOCHO, HCHO, H_2O and O_4 data will exemplarily be presented in this paper. The instrument consists of

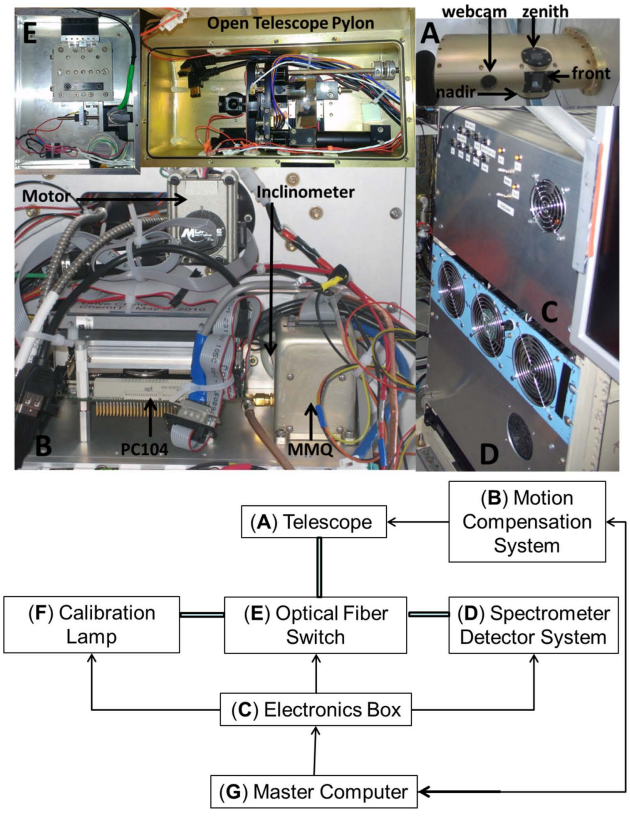

Fig. 2. CU AMAX-DOAS instrument setup aboard the NOAA Twin Otter during the CalNex and CARES campaigns.

a telescope pylon mounted outside of a window plate on a National Oceanic and Atmospheric Administration (NOAA) Twin Otter remote sensing research aircraft. The collected photons are transferred via optical fibers to two synchronized spectrometer/detector systems that are housed inside the aircraft fuselage. An optical fiber switch box is placed in between the light sources (telescopes and Hg calibration lamp) and the spectrometer/detector systems to select between different light sources at a given time. The Hg calibration lamp is used to characterize the optical resolution of the spectrometer/detector system. The instrumental setup is shown in Fig. 2.

2.1 Telescope system

The telescope is designed for high light throughput and a very narrow vertical field of view (FOV, $0.3° \times 5.89°$). It comprises a 1/2″ rotating prism, a 1/2″ lens tube with a 1/2″ f/4 lens and a stepper motor. All the telescope components are housed in a telescope pylon – an aluminum housing with quartz windows, which is mounted outside of a window plate on a NOAA Twin Otter research aircraft. The rotating prism is installed with 0° EA parallel to the aircraft heading and is driven by a stepper motor with an internal encoder to rotate vertically. The prism is capable of making a complete 360°

rotation and hence allows characterization of the air masses above, below and in front of the aircraft using the same telescope. Viewing directions behind the aircraft are not accessible due to the structural design of the pylon including the placement of viewing ports. An additional telescope with a fixed EA is therefore present in the pylon to reach some of the inaccessible viewing geometries of the rotating prism. This telescope was rarely used during the CalNex and CARES campaigns, and data from this telescope are not presented in this paper. The viewing ports on the pylon are heated to prevent formation of ice at higher altitudes. The pylon also includes two webcams: a downward and a forward looking one, to capture atmospheric conditions during the flight and to filter for clouds during post-processing of data. The light collected by the rotatable prism is focused via a lens tube onto a 12-m-long fiber bundle consisting of 72×145 µm fibers. The fiber bundle is configured into two rows of 36 fibers at the telescope end and a circular arrangement at the other. The end of the fiber bundle away from the telescope is connected to a custom-made optical fiber switch box.

2.2 Optical fiber switch box

The optical fiber switch box is used to select between different incoming light sources. It consists of a translational stage mounted to a stepper motor linear actuator. The fibers from the telescopes and Hg calibration lamp are connected to one end of the box. Hg spectra were taken before, after and at regular intervals during flights to check the stability of the spectrograph's optical resolution. A 10-m-long 1.7-mm-diameter silica monofiber, which is used as a mixing fiber to minimize polarization effects, is mounted on the translational stage opposite the incoming fibers from the light sources. The motor of the linear actuator drives the platform to place the monofiber directly in front of the desired fiber with the incoming light at a given time. The other end of the monofiber is connected to a bifurcated fiber bundle (72×145 µm) to deliver light to two spectrometers simultaneously. The bifurcated ends are aligned in a single row of 36 fibers to connect to the spectrograph entrance slit.

2.3 Spectrometer and detector system

Two spectrometers and their respective detectors are housed in a standard 19″ aluminum instrument rack ($19'' \times 22'' \times 10\,1/2''$) with modifications to the bottom and top plates for added stability. The spectrometers are Princeton Instrument Acton SP2150 Imaging Czerny-Turner spectrometers with PIXIS 400 back illuminated charge-coupled devices (CCDs) detectors. The first spectrometer (later referred to as the O_4 spectrometer) is equipped with a 500 grooves/mm grating, blazed at 330 nm. It covers 350–720 nm and is used to measure all four major O_4 absorption bands at 360, 477, 577 and 630 nm. The second spectrometer (later referred to as trace gas – TG – spectrometer) covers a wavelength range from 330–470 nm with a custom 1000 grooves/mm (250 nm blaze wavelength) grating. It is used to measure all other trace gases. The optical resolutions of the O_4 and TG spectrometers were ~ 2.2 nm (~ 7.7 pixels) and ~ 0.7 nm (~ 6.7 pixels), respectively, inferred from the full width at half maximum (FWHM) of a representative Hg line. The CCDs are cooled to $-30\,^{\circ}$C to reduce dark current. The temperatures of the spectrometers are actively controlled with heaters, while the instrument rack box temperature is actively cooled using peltier cooling units assuring a constant temperature over a range of varying ambient temperatures. Please refer to Coburn et al. (2011) for additional information on temperature stability, data acquisition and electronic and dark current correction for a comparable instrument. To suppress spectrometer stray light from longer wavelength (above 470 nm) and to gain maximum intensities in our regions of interest, i.e., between 330–470 nm, in the TG spectrometer, two filters – a BG3 and a BG38 – were placed immediately after the shutter.

2.4 Motion compensation system

The motion compensation system is used to correct the viewing geometry of the telescope for the aircraft pitch and roll effects during the flight. It consists of a PC104 computer connected to the prism motor and two angle sensors, a Systron Donner Inertial MMQ-G, and an electronic inclinometer. The MMQ-G is a small robust global positioning system (GPS) -based inertial navigation system (INS). It provides accurate 3-D position, time, velocity, and attitude. It is primarily used to measure the pitch and roll angles of the aircraft for our application, and has an angle accuracy of 5 mrad ($\sim 0.29°$). The information from the sensor is processed by custom LabVIEW software into the coordinate system along the horizon. It is then used to drive the stepper motor of the prism to a new position such that it corrects for the aircraft's movement and keeps the telescope at the desired EA. The software has capability for a 100 Hz loop rate, and was typically operated at 10 Hz. The stepper motor has a precision of 0.01° but is limited by the resolution of the internal encoder (0.2°) to precisely read back the position of the motor. The MMQ-G, inclinometer and the telescope prism are mounted on planes parallel to the ground such that the EA of the telescope and the pitch of the aircraft read zero simultaneously. The inclinometer is used as a backup during flights for situations when the GPS signal required for the MMQ-G is lost. The theoretical angle accuracy of the motion compensation system is 0.35°, considering the MMQ-G accuracy of $\sim 0.29°$ (1σ) and motor internal encoder resolution of 0.2°. The system is configured to reset the motor when it does not reach a given position within a desired tolerance level by a fixed time interval. The same motion compensation system has also been integrated as part of another telescope pylon designed for adaptation of the CU AMAX-DOAS instrument aboard the NSF/NCAR GV HIAPER aircraft.

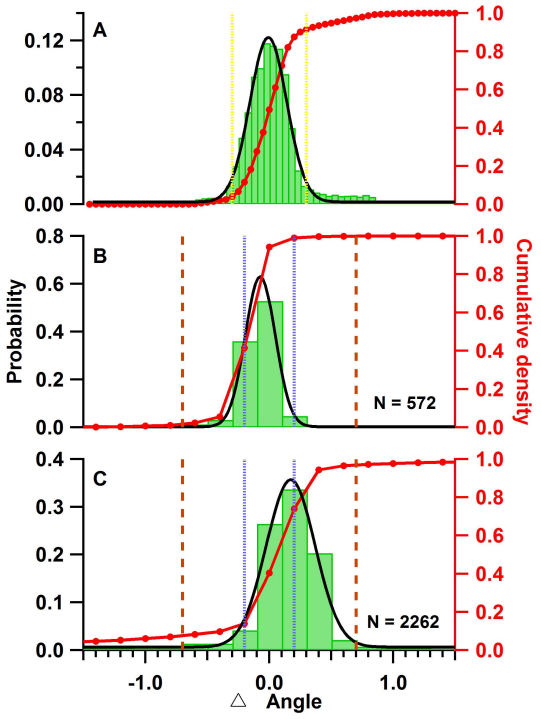

Fig. 3. (A) Distribution of difference in pitch angle of the aircraft measured at real time by the MMQ-G angle sensor of the CU-AMAX-DOAS and aircraft avionics system of NSF/NCAR GV HIAPER aircraft during a research flight on 24 February 2012. 1σ angle accuracy (0.29°) of the MMQ-G sensor is shown in yellow dotted lines. 1σ for the Gaussian fit (black line) is 0.15°. Distribution of elevation angle accuracy of the CU AMAX-DOAS telescope **(B)** from the above-mentioned flight on NSF/NCAR GV HIAPER flight and **(C)** during RF#46 aboard NOAA Twin Otter on 16 July 2010. 1σ for the Gaussian fits (black lines) are 0.12° and 0.2° for instrument aboard HIAPER and Twin Otter aircraft, respectively, and are within the resolution of the motor internal encoder (0.2°), shown in blue dotted lines. Brown dashed lines represent the motor tolerance level (0.7°) set in the software before an automatic reset of the motor position takes place. The red lines represent the cumulative densities.

2.5 Performance of the motion compensation system

Figure 3 shows the performance of the system during research flights aboard the GV HIAPER and Twin Otter aircrafts. GV HIAPER flights provide an excellent opportunity to test the system as the aircraft pitch and roll angles measured by the aircraft avionics system during the flight are recorded, while avionics data for the Twin Otter flights are not available. The histogram of differences in aircraft pitch angle recorded at 1 Hz frequency measured by NSF/NCAR GV HIAPER aircraft avionics and our MMQ-G recording during a research flight ($\sim$8 h) on 24 February 2012 is plotted as a probability density function in Fig. 3a. A Gaussian fit (black line) to the histogram has a 1σ deviation of 0.15°, which is less than the 1σ accuracy (0.29°, yellow line in Fig. 3a) of the MMQ-G pitch measurement. This shows that the MMQ-G measures the aircraft pitch and roll angles with sufficient accuracy, which are then being used for real-time pointing corrections. Figure 3b shows the difference in desired EA and the real-time EA read back from the motor internal encoder as a probability density for the same flight. The 1σ of the Gaussian fit to the histogram (0.12°) is smaller than the resolution of the motor internal encoder confirming that the telescope position was corrected for the aircraft movements within our ability to read back the motor position. The width of the histograms (Fig. 3b and c) is chosen based on the resolution of the motor internal encoder, i.e., 0.2°.

A similar plot from a research flight ($\sim$4 h) on 16 July 2010 aboard the NOAA Twin Otter is shown in Fig. 3c and the 1σ of the Gaussian fit is 0.2°. This slightly larger distribution is within the resolution of the motor internal encoder. The fact that the 1σ for both platforms is less than or equal to the ability with which we can accurately read the position of the motor demonstrates that this motion compensation is suitable for a wide range of moving platforms. Since the precision of the stepper motor is 0.01°, an order of magnitude better than resolution of the motor internal encoder, it is very likely that the difference between the real-time and desired EA is smaller than what is being read back from the internal encoder, and the overall angle accuracy (1σ) of the motion compensation system is better than 0.35°. The offset of 0.17° for the Gaussian fit in Fig. 3c is probably due to some remaining misalignment between the angle sensor and the motor, but is smaller than the accuracy of the angle sensor.

The tolerance level (brown dashed lines in Fig. 3b and c) above which the motor performs an automatic reset was set to 0.7° (2σ theoretical accuracy) for the campaigns described here. The statistical distribution of the EA difference indicates that the desired position of the motor was achieved after the reset.

2.6 Field deployment and operation during CalNex and CARES

The CU AMAX-DOAS instrument was deployed aboard the NOAA Twin Otter remote sensing research aircraft during the CalNex and CARES field campaigns from 19 May–19 July 2010 in California after test flights in 2008 and 2009. The pylon was modified significantly after 2009. The aircraft is an unpressurized twin-engine turboprop with an altitude ceiling of $\sim$4 km a.s.l. (above sea level) without supplemental cabin oxygen. It has a normal cruising speed of $\sim$65 m s^{-1} and ascent rate of $\sim$10 m s^{-1}, making it particularly suitable for surveying vertical and horizontal distributions of trace gases in a polluted urban environment. During CalNex, the NOAA Twin Otter aircraft was stationed at Ontario, CA, and joined the CARES campaign from 16–29 June 2010 at Sacramento, CA. The plane was equipped

with a suite of remote sensing instruments: the University of Colorado deployed the (1) CU AMAX-DOAS instrument and (2) two 4-channel radiometers (zenith and nadir viewing) to measure surface albedo (SA); further, NOAA/ESRL/CSD deployed (3) a nadir-pointing TOPAZ (Tunable Ozone Profiler for Aerosol and oZone) lidar (Alvarez II et al., 2011), which measures vertical distribution of ozone (O_3), and the (4) University of Leeds HALO Doppler lidar (Pearson et al., 2009), which measures 3-D wind fields, as well as (5) a nadir pointing infrared pyrometer and (6) an in situ O_3 monitor.

The purposes of the CU AMAX-DOAS deployment were the following: to measure horizontal and vertical distributions of NO_2, HCHO, CHOHO and aerosol extinction over California – particularly over the SCAB – to characterize boundary conditions for comparison with atmospheric models, and to probe for pollutant concentrations above the boundary layer (BL). NO_2, HCHO and CHOCHO play important roles in atmospheric chemistry and strongly influence air quality. NO_2 is a precursor molecule for tropospheric O_3 formation. Oxidation of nitrogen oxides ($NO_x = NO + NO_2$) in the atmosphere results in the formation of nitric acid and aerosol nitrates, causing acid deposition and visibility degradation. HCHO is the most abundant volatile organic compound (VOC) and produces HO_x radicals upon photolysis – a major oxidizer in the atmosphere, which sustains photochemical production of O_3 and secondary organic aerosols (SOA) (Griffin et al., 2004; Volkamer et al., 2010). CHOCHO also forms HO_x radicals upon photolysis and is a direct precursor for SOA. Studies conducted in Mexico City have suggested that CHOCHO could be responsible for 10–15 % of SOA formation in Mexico City (Volkamer et al., 2007). Aerosols directly affect human health and have been linked to increases in morbidity and mortality (Pope III et al., 2009). A total of 52 research flights, each lasting up to $\sim$ 4 h, were carried out over the two month period (206 flight hours). Flight plans were developed with the scientific objectives of mapping out horizontal and vertical distribution as well as characterizing transport of pollutants and validation of satellite retrievals. As this was the first deployment of this specific instrument pylon, different integration times and EA sequences were explored as well as the LabVIEW acquisition software was updated during the early portion of the campaign for optimization. Spectra were collected with 2 seconds integration time during the second half of the campaign, and all the data presented in this paper are 2 s data unless otherwise noted. The most commonly used EA sequence included EAs 90° (zenith), 20°, 10°, 5°, 2°, 0°, −2°, −5°, −10°, −20° and −90° (nadir) with 0° corresponding to a view parallel to the horizon. The FOV of the telescope at nadir viewing geometry gives a footprint of $\sim$ 0.55 km while flying at 4 km altitude. Typically, nadir spectra were recorded every 12–15 s, corresponding to a horizontal resolution of $\sim$ 1 km.

Table 1. List of trace gas references used for DOAS analysis.

No.	Molecule	Reference
1	NO_2 (220 K)	Vandaele et al. (1998)
2	NO_2 (294 K)	Vandaele et al. (1998)
3	O_3 (223 K)	Bogumil et al. (2003)
4	O_3 (243 K)	Bogumil et al. (2003)
5	O_4 (298 K)	Hermans (2002)
6	CHOCHO (298 K)	Volkamer et al. (2005)
7	HCHO (298 K)	Meller and Moortgat (2000)
8	H_2O	Rothman et al. (2005)
9	O_4	Greenblatt et al. (1990)

3 Data analysis

3.1 DOAS analysis

The measured spectra were analyzed for NO_2, CHOCHO, HCHO, H_2O and O_4 using the DOAS method (Platt and Stutz, 2008) implemented by the WinDOAS software (Fayt and Van Roozendael, 2001). In DOAS, measured spectra are analyzed against a Fraunhofer reference spectrum, and absorption cross sections of different absorbers in the atmosphere are fitted simultaneously in a selected wavelength interval applying a nonlinear least-square fitting routine. A low-order polynomial to account for scattering processes and broadband absorption in the atmosphere as well as broadband instrumental features, a Ring reference spectrum to account for the "filling-in" of Fraunhofer lines due to rotational Raman scattering (Grainger and Ring, 1962), and an additional intensity offset to account for instrumental stray light were also included in the fitting procedure. The Ring spectrum is calculated from the Fraunhofer reference (Bussemer, 1993). The Twin Otter aircraft being an unpressurized aircraft, the pressure in the cabin changed from 1010–665 mbar over a 3.5 km altitude range for typical flights (e.g., see Fig. 7). The change in the refractive index as well as any pressure differentials that could give rise to a wavelength shift equally affect the Fraunhofer lines and Earth atmospheric absorbers, and are accounted for by including a linear shift of the measurement spectrum during analysis. The observed shifts are up to 0.18 nm for the TG spectrometer between the spectra taken at the highest and the lowest altitude. A high-altitude ($\sim$ 4 km) zenith spectrum from a clean, cloud-free region of the same flight was included for the analysis of the individual flight data. The choice of the zenith spectrum as Fraunhofer reference spectrum minimizes the amount of tropospheric absorbers in the reference spectrum, allowing for the detection of trace gases more sensitively. Since measured spectra are analyzed with respect to a reference spectrum, the quantity retrieved from the DOAS analysis is a differential slant column density (dSCD), which is the integrated difference in concentration of the absorber along the light path length with respect to the reference. The trace gas absorption

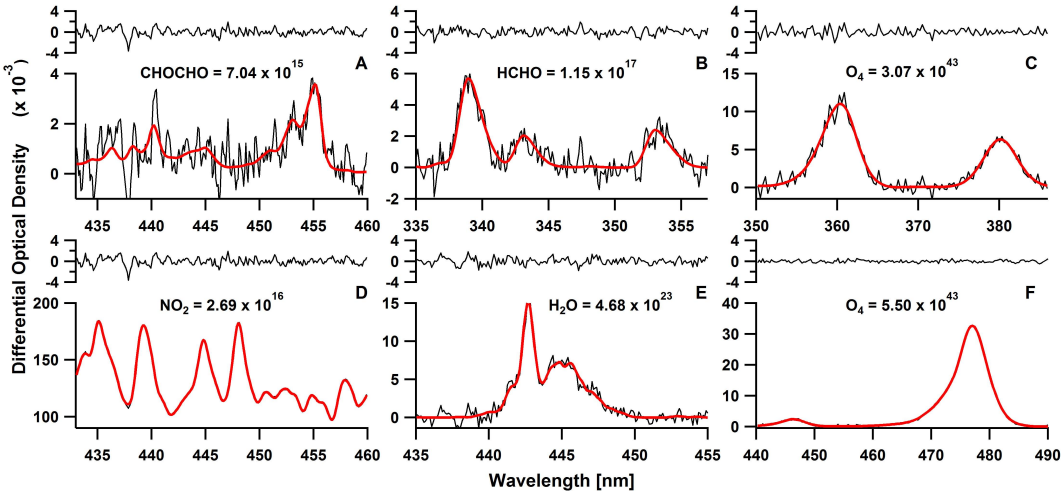

Fig. 4. Spectral proofs for the detection of **(A)** CHOCHO, **(B)** HCHO, **(C)** O_4 at 360 nm, **(D)** NO_2, **(E)** H_2O and **(F)** O_4 at 477 nm. CHOCHO and NO_2 fits are from 14 July 2010 at 22:08 UTC (SZA: $\sim 42°$) at ~ 150 m a.g.l. HCHO and H_2O fits are from 16 July 2010 at 20:19 UTC (SZA: $\sim 24°$) at ~ 600 m a.g.l. O_4 fits are from the same flight at 20:11 UTC (SZA: $\sim 23°$) at ~ 3000 m a.g.l. The black lines represent the measured spectra and red lines are fitted reference cross sections. Note that for NO_2 and O_4 at 477 nm, the absorption is so strong that the black lines are not visible. All the fits are for 0° EA. The units for retrieved dSCDs for CHOCHO, HCHO, NO_2 and H_2O are molecules cm^{-2} and for O_4 are molecules^2 cm^{-5}.

Table 2. Summary of DOAS analysis settings for different trace gases. 2 Rings (warm and cold) were fitted for HCHO retrievals, and spectra collected for SZA $< \sim 65°$ were only analyzed and hence BrO was not included in the fit.

Trace gas	Wavelength range (nm)	Fitted absorber	Polynomial order
NO_2	433–460	1, 2, 3, 6, 8, 9	3
CHOCHO	433–460	1, 2, 3, 6, 8, 9	3
HCHO	335–357	1, 2, 3, 4, 5, 7	3
H_2O	435–455	1, 2, 4, 5, 6, 8	3
O_4	350–386	1, 2, 3, 4, 5	3
O_4	440–490	1, 2, 4, 5, 8	5

Table 3. Detection limits of CU AMAX-DOAS instrument in the clean free troposphere and the boundary layer in polluted urban conditions like SCAB for different integration times. Detection limit was calculated as 1σ RMS detection limit for the aerosol scenario presented in the Fig. 10.

Trace gas	Free troposphere (FT) (ppt)		Boundary layer (BL) (ppt)	
	30 s	2 s	30 s	2 s
NO_2	5	30	30	120
CHOCHO	3	16	16	65
HCHO	98	290	540	1355
H_2O_{442nm} (ppm)	42	210	252	760
ε_{477nm} (km^{-1})	0.002	0.002	0.006	0.006
ε_{360nm} (km^{-1})	0.004	0.004	0.012	0.012

cross sections and other analysis settings for the retrievals of the different trace gases are listed in Tables 1 and 2, respectively. Examples for spectral fits of NO_2, CHOCHO, HCHO, O_4, and H_2O from the data measured during CalNex and CARES campaigns are shown in Fig. 4. Detection limit for CU AMAX-DOAS instrument in the clean free troposphere (FT) and polluted urban BL such as the SCAB for 30 and 2 s integration time is listed in Table 3. It is roughly equivalent to the 3σ DOAS fit error for typical clean FT (near Rayleigh atmosphere) and polluted urban BL atmospheric conditions (see Fig. 10b for aerosol extinction profile). Note that detection limit highly depends upon the atmospheric conditions during the time of measurement.

We included 2 Ring spectra (Bussemer, 1993), calculated for two different temperatures (298 and 230 K), in HCHO retrieval to account for the temperature dependence of rotational Raman scattering, which leads to the so-called "filling-in" of the Fraunhofer lines (Ring effect). The inclusion of a second Ring cross section in the HCHO retrieval (1) improved the HCHO fit, (2) minimized fitting residuals and (3) reduced scatter in the retrieved HCHO slant columns. A second Ring cross section was not needed to achieve comparable results for other trace gases where the Ring structures are relatively smaller. A new HCHO reference cross section has recently been reported by Chance and Orphal (2011). We compared the dSCDs retrieved with new cross section to the one from Meller and Moortgat (2000) (used in this work) and found the mean difference of 6.0×10^{14} molecules cm^{-2}, which is well below the DOAS fit error for our retrieval. For

a mean dSCD of 3.0×10^{16} molecules cm^{-2} for 0° EA at all flight altitudes for the exemplary flight presented here, the difference is only 2 %.

We used the O_4 cross section by Greenblatt et al. (1990) for NO_2 and CHOCHO retrievals. The O_4 cross section by Hermans (2002) has some nonphysical structures in the baseline around the weak O_4 absorption band at 446 nm, which seems to affect NO_2 and CHOCHO fits. The nonphysicality of these structures has been verified by our laboratory (Thalman and Volkamer, 2013). At the time of writing this manuscript, these new O_4 reference spectra were subject to ongoing measurements. Hence, for this particular wavelength range, we prefer using Greenblatt et al. (1990).

The quantity retrieved from a DOAS analysis, the dSCD is converted to tropospheric VCD (VCD_{trop}) by using an air mass factor (AMF). An AMF is a light path enhancement in the atmosphere for a particular viewing geometry relative to vertical path through the atmosphere. The VCD_{trop} is the integral absorber concentration per unit area in the troposphere.

$$VCD_{trop} = \frac{dSCD}{dAMF} \quad (1)$$

dAMF (differential air mass factor) is usually calculated with the help of a radiative transfer program to convert the measured dSCD to a VCD_{trop} and is a difference in AMF between the measured and the reference viewing geometry. It requires a priori knowledge of trace gas vertical concentrations and aerosol extinction coefficients along with other input parameters such as pressure, temperature, surface albedo (SA), aerosol asymmetry parameter g, and aerosol single scattering albedo (SSA). NO_2 concentrations, profile shapes and aerosol scenarios are highly variable in the SCAB because of the variable sources and hence could result in a significant amount of error in radiative transfer calculations of AMFs. Instead, we applied a simple geometric approximation for the nadir viewing geometry to convert dSCDs to VCDs. The geometric approach, its validity and error associated with this approximation are further discussed in Sect. 3.3.

3.2 Radiative transfer modeling

Since the AMAX-DOAS measurements are carried out in the open atmosphere using scattered sun light as the light source, the solar radiative transfer during the time of measurement needs to be modeled to interpret the retrieved data. The radiative transfer program McArtim (Monte Carlo atmospheric radiative transfer inversion model) (Deutschmann et al., 2011) used here is a fully spherical model and simulates radiative transfer in the atmosphere in the UV/vis/NIR spectral range using a Monte Carlo approach. In McArtim the 3-D atmosphere is simulated as a 1-D modeled atmosphere divided into concentric spherical shells. The atmospheric conditions during the time of measurement in each vertical layer are assumed to be horizontally and vertically homogeneous. McArtim has the capability to simulate Jacobians of trace gases and aerosols needed for the interpretation of AMAX-DOAS data. Auxiliary input parameters used in the radiative transfer program were either measured aboard the aircraft (i.e., SA), on the ground at the CalNex ground site (Ryerson et al., 2013) (i.e., aerosol SSA), at the California Air Resources Board (CARB) (http://www.arb.ca.gov/homepage.htm) monitoring stations or based on values from previous studies for urban environments (i.e., g-parameter, e.g., Dubovik et al., 2002).

3.3 Geometric approximation for conversion of dSCDs to VCDs

Under the geometric approximation, it is assumed that all the photons get scattered only once very close to the ground or are reflected from the surface before entering the telescope in nadir geometry. The geometric air mass factor (geoAMF) is then only a function of the solar zenith angle (SZA) and is given by

$$\text{geoAMF} = 1 + \frac{1}{\cos(\text{SZA})}. \quad (2)$$

The schematic of the geometric approximation is shown in the Fig. 1 inset.

In our DOAS analysis, a high-altitude zenith spectrum from a clean background area is used as reference spectrum. Assuming this background zenith spectrum has no tropospheric NO_2, the nadir dSCDs can be considered as tropospheric slant column densities (SCDs) for most flights performed at low SZA. At high SZA, stratospheric NO_2 contribution changes with SZA and hence requires independent removal. For such flights (18 out of 52), stratospheric NO_2 contribution was corrected by fitting a polynomial through all the zenith dSCDs above 1.8 km flight altitude and subtracting the polynomial from the nadir measurements. The resulting quantity is defined as the tropospheric SCDs. This quantity is then converted to VCD_{trop} ($VCD_{trop} = SCD_{trop}/\text{geoAMF}$), and is defined as VCD below the aircraft.

Sensitivity studies using the radiative transfer model (RTM) McArtim were performed to estimate uncertainties associated with the geometric approximation. A range of conditions that could potentially occur during the time of measurements were explored for this study. A representative sample of the results is summarized in Table 4, where the relative error in the geoAMF assumption compared to AMFs calculated using the RTM for different scenarios are specified. The results for most likely atmospheric state in the SCAB (surface albedo, SA = 0.1; single scattering albedo, SSA = 0.94; asymmetry parameter, g = 0.68; aerosol optical depth, AOD = 0.4; boundary layer height, BLH = 1.0 km; NO_2 mixing ratio = 10 ppb) is also shown in Table 4; it is based on ancillary measurements aboard the aircraft, CalNex ground site at Pasadena and CARB ground monitoring stations or climatology of urban aerosol. Thomson et al. (2012) reported an average value for SSA of 0.92 at 532 nm during the entire CalNex campaign at Pasadena. They found SSA

Table 4. Relative error of geometric approximation compared to AMF calculated for nadir viewing geometry at 455 nm using radiative transfer program McArtim under different scenarios.

Altitude [km]	Solar zenith angle (SZA)	Most probable conditions*	Boundary layer height [m]		NO_2 concentration [ppb]		Surface albedo (SA)		Single scattering albedo (SSA)		Aerosol optical depth (AOD)	
			500	1500	5	20	0.05	0.15	0.90	0.99	0.10	0.80
2 (low)	20	6.3	3.3	9.0	7.2	5.6	3.0	12.2	4.4	9.6	4.3	6.7
	40	4.7	1.0	5.6	5.1	3.2	5.7	9.4	1.1	6.9	2.9	2.6
	60	5.9	7.3	6.3	6.0	7.0	15.3	0.7	8.0	3.3	3.4	11.0
3.5 (high)	20	3.0	6.3	0.3	2.8	3.2	15.2	5.3	5.3	0.30	4.6	1.0
	40	5.4	8.6	3.1	4.1	5.1	15.9	2.8	7.6	2.1	6.9	4.9
	60	16.1	16.4	14.0	14.5	16.5	25.0	8.3	17.5	11.6	14.2	19.3

* Most probable atmospheric conditions in SCAB: surface albedo = 0.10, single scattering albedo = 0.94, g parameter = 0.68, aerosol optical depth = 0.4, boundary layer height = 1 km and NO_2 mixing ratio = 10.0 ppb.

values to be slightly higher during the day time, when our measurements were taken. AOD measured at the AERONET station at Pasadena showed AOD values to be lower than 0.4 at 440 nm for almost all of summer 2010, and the AOD of 0.4 likely represents an upper limit to provide a conservative estimate of relative error. The value of asymmetry parameter g is based on the climatology of urban aerosol (e.g., Dubovik et al., 2002) and agrees well with measurements at the AERONET station at Pasadena (range for the entire campaign: 0.63–0.80). AMFs calculated for this range of g values were within 3 % of AMF relative to $g = 0.68$. It should be noted that these quantities are wavelength dependent. The largest source of error was found to be SA (see Table 4), which is constrained using the measurement aboard the aircraft. Notably, our SA measurements also provide means to filter data for conditions where the error may exceed 10 %. The error from using the geoAMF compared to AMF calculated for most likely atmospheric state in SCAB is plotted as a function of SZA in Fig. 5. Based on this a SZA cutoff of 65° was used to constrain the error in the NO_2 vertical columns. With these filters the error in geoAMF is < 7 % for most conditions (85 % of flight time with SZA $< 65°$), and slightly larger (error < 25 % in all cases) for SZA $\sim 65°$ or during high-altitude flights over low SA. The error associated with the geoAMF is consistent with previous airborne DOAS studies that used the geometric approximation. Melamed et al. (2003) estimated the error in NO_2 VCD from the geometric approximation to be ~ 20 % based on the discrepancies between measured and modeled O_2 AMF. To the best of our knowledge, there have been no previous deployments of AMAX-DOAS with simultaneous SA measurements by independent sensors. The high SA value of ~ 10 % at 477 nm is found widespread in the SCAB, and has the favorable effect of reducing errors from the geoAMF assumption due to compensating effects in the radiative transfer calculations.

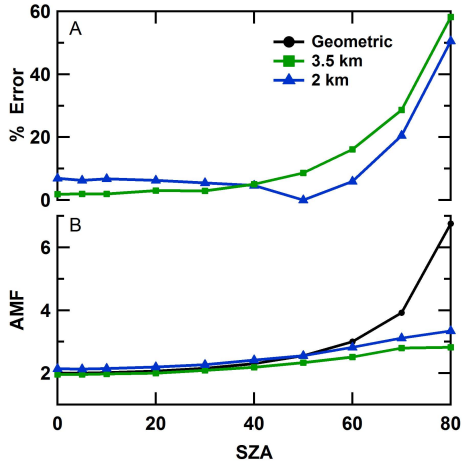

Fig. 5. (A) Relative error of geometric air mass factor (geoAMF) compared to AMF for nadir geometry calculated using RTM, McArtim for flight altitude of 3.5 km (green) and 2 km (blue) a.g.l., for most likely atmospheric conditions in South Coast Air Basin (SCAB). **(B)** AMF calculated using McArtim (green and blue) and geoAMF (black). Most likely atmospheric state in SCAB: surface albedo = 0.10, single scattering albedo = 0.94, g parameter = 0.68, aerosol optical depth = 0.4, boundary layer height = 1 km and NO_2 mixing ratio = 10.0 ppb.

3.4 Aerosol extinction profile retrieval

In the near-UV and visible wavelength range, under cloud free conditions, the change in photon path length compared to the Rayleigh atmosphere and hence the measured dSCDs of a trace gas depend mainly on the aerosol extinction profile. Thus, if the vertical distribution of an absorber is well known, the dSCD measurements of such species can be exploited to infer aerosol properties. The collisional complex of oxygen O_4 is one such species (Hönninger et al., 2004; Wagner et al., 2004; Wittrock et al., 2004; Clémer et al., 2010). The O_4 concentration varies with the pressure, temperature and square of

the concentration of O_2. Hence, the dSCD measurements of O_4 can be used to calculate the aerosol extinction profiles. O_4 dSCD measurements from ground-based and airborne MAX-DOAS have previously been used for aerosol extinction profile and AOD retrievals (Clémer et al., 2010; Merlaud et al., 2011 and references within). Aerosol inversion is a nonlinear problem and hence requires an iterative method. We used an iterative forward model approach to obtain the aerosol extinction profile. Under this approach a set of measured O_4 SCDs, $\boldsymbol{y}$, is related to the aerosol extinction vertical profile, $\boldsymbol{x}_i$, by forward model $\mathbf{F}$ such that

$$\boldsymbol{y} = \mathbf{F}\left(\boldsymbol{x}_i,\ \boldsymbol{b}\right) + \varepsilon, \tag{3}$$

where $\boldsymbol{b}$ are forward model parameters that are not retrieved, i represents the iteration index, and ε is the sum of measurement and model error. For 0° EA, i.e., parallel to the horizon, under cloud free conditions, the measurement is almost entirely sensitive to the altitude of measurement and nearly all of the vertical information contained in the SCD comes from that particular altitude. We exploit this property and retrieve the aerosol extinction profile by using a modified onion peeling algorithm using 0° EA O_4 SCD measurements. First the extinction above the highest altitude is constrained using upward EA scans performed at that altitude. Then the aerosol extinction values at the subsequent altitudes during the descent are determined iteratively using the set of 0° EA O_4 SCD measurements at those altitudes. Aerosol extinction below the lowest aircraft altitude is obtained using downward EA scans performed at the lowest altitude. This process is repeated to account for any information on O_4 SCDs for 0° EA at a given altitude from the O_4 column below the measurement altitude, until measured and modeled O_4 SCDs agree. The profile is then verified using other angles in the EA scans during the descent/ascent. It should be noted that this approach is feasible only due to the ability to maintain the desired EAs within a narrow error bound also during descent/ascent of the aircraft, as discussed in Sect. 2.5.

The relative error in O_4 SCDs at different altitudes in the atmosphere for different pointing uncertainties for a 0° EA is illustrated in Fig. 6. An uncertainty of 1–2° in pointing accuracy, which can easily happen on an airborne platform, could result in 20–80 % O_4 SCD error above 10 km. Even though the O_4 concentration is very small above 10 km (around 10 % of the near surface at 10 km), the SCD at 0° EA can still be measured with good signal-to-noise because of the much longer photon path lengths in the less-dense air. Hence, the high sensitivity towards the pointing accuracy is the limiting source of error. Considering a nonlinear relationship between O_4 SCD and aerosol extinction, this could result in even larger errors when O_4 SCDs are used to retrieve the aerosol extinction profile. This highlights the need for a motion compensation system to maintain pointing accuracy of the telescope.

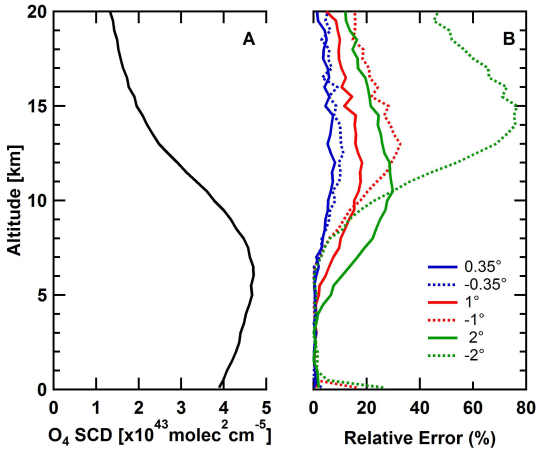

Fig. 6. (A) Vertical profile of O_4 SCDs calculated for 0° EA at 477 nm using McArtim (US standard atmosphere with exponential aerosol extinction profile with extinction of 0.2 km^{-1} at the ground and 2.5 km scale height). **(B)** Relative error in O_4 SCDs for 0.35° (blue), 1° (red) and 2° (green) pointing error of the telescope at 0° EA. The solid and dashed lines represent angles above and below the horizon, respectively.

3.5 Trace gas vertical profile retrieval

The trace gas vertical profile retrieval algorithm is based on the concept of optimal estimation (Rodgers, 2000). The use of this technique for profile retrieval from AMAX-DOAS measurements has been described in detail before (e.g., Bruns et al., 2004) and hence will only be introduced here briefly. A set of measurements, $\boldsymbol{y}$, which in our case are trace gas SCDs for different LOS can be related to a vertical distribution, $\boldsymbol{x}$, by the forward model $\mathbf{F}$ as shown in Eq. (3). Considering that we use a high-altitude clean-environment zenith reference spectrum, SCD of the reference spectrum is/can be considered to be negligible for tropospheric pollutants.

Equation (3) can be rewritten in a linearized form as

$$\boldsymbol{y} = \mathbf{K}\boldsymbol{x} + \varepsilon, \tag{4}$$

where $\mathbf{K}$ defined as $\frac{\partial \mathrm{SCD}_i}{\boldsymbol{x}_i}$ is the weighting function matrix that expresses the sensitivity of measurement $\boldsymbol{y}$ to $\boldsymbol{x}$. We used the maximum a posterior solution as described in Rodgers (2000) to solve Eq. (4):

$$\boldsymbol{x} = \boldsymbol{x}_\mathrm{a} + \left(\mathbf{K}^T\,\mathbf{S}_\varepsilon^{-1}\,\mathbf{K} + \mathbf{S}_\mathrm{a}\right)^{-1}\mathbf{K}^T\,\mathbf{S}_\varepsilon^{-1}\left(\boldsymbol{y} - \mathbf{K}\boldsymbol{x}_\mathrm{a}\right), \tag{5}$$

where $\boldsymbol{x}_\mathrm{a}$ is the a priori profile and $\mathbf{S}_\mathrm{a}$ and $\mathbf{S}_\varepsilon$ are the a priori error and measurement error covariance matrices, respectively. The a priori profile is used to constrain the above described problem as it is generally ill-posed. $\mathbf{S}_\varepsilon$ was constructed using the square of the DOAS fit error as the diagonal elements of the matrix, the nondiagonal elements were set to 0. The apriori error covariance matrix, $\mathbf{S}_\mathrm{a}$, was used as a

tuning parameter, maximizing the information content while avoiding spurious oscillations in retrieved profiles (Schofield et al., 2004). The nondiagonal elements in $\mathbf{S}_a$ matrix accounts for correlation of trace gas values between different altitude layers and were included as the Gaussian function shown in Eq. (5) (Barret et al., 2002; Hendrick et al., 2004):

$$\mathbf{S}_{a_{ij}} = \sqrt{\mathbf{S}_{a_{ii}}\,\mathbf{S}_{a_{jj}}}\,\exp\left(-\ln 2\left(\frac{z_i - z_j}{\quad}\right)^2\right), \tag{6}$$

where z_i and z_j are the altitudes of the i-th and j-th layers respectively and is the half width at half maximum (HWHM). The value of was set to half the width of vertical grid considered for inversion (Hendrick et al., 2004).

The solution given by Eq. (5) is a weighted mean of the a priori profile and the information from the measurement. This weight is given by the averaging kernel matrix $\mathbf{A}$

$$\mathbf{A} = \left(\mathbf{K}^T\,\mathbf{S}_\varepsilon^{-1}\mathbf{K} + \mathbf{S}_a\right)^{-1}\mathbf{K}\mathbf{T}\mathbf{S}_\varepsilon^{-1}\mathbf{K}. \tag{7}$$

The retrieval at any layer is an average of the whole profile weighted by the row of the averaging kernel matrix corresponding to that layer. The averaging kernel matrix also contains information about the number of independent pieces of information retrieved, and an estimate of the vertical resolution of the retrieved profile at a given level. The trace of the averaging kernel matrix, $\mathbf{A}$, gives the DOF, i.e., number of independent pieces of information retrieved. The FWHM of the main peak of an averaging kernel at any layer gives the estimate of the vertical resolution of the retrieved profile at that layer. For an ideal retrieval scenario, $\mathbf{A}$ is an identity matrix, the DOF equals the number of retrieved profile layers, and the averaging kernels peak at their corresponding altitudes. In reality, the retrieved profile is a smoothed version of the true profile.

EA scans at flight altitude can be used to retrieve vertical profiles (e.g., Bruns et al., 2004), but the sensitivity of such scans are limited to mostly 2 km above and below the plane. Box AMF calculations for EAs 5° and 10° above and below the horizon show that the sensitivity of these EAs falls below 50 % of the peak value above and below 2 km of the aircraft. Roscoe and Hill (2002) showed that vertical resolution can be improved by oversampling, provided that the random error is degraded. Sensitivity can be improved by combining EA scan with aircraft ascent/descent. We exemplarily present vertical profiles from actively controlled EA scans during an aircraft descent at Brackett airfield in the Los Angeles Basin, CA.

3.6 Error analysis

Measurement noise, forward model parameter (e.g., SA) uncertainties and smoothing error due to finite resolution of the inversion grid contribute to the uncertainties in the retrieved profiles. The actual model error itself is neglected here as these uncertainties are very small (Hendrick et al., 2006; Wagner et al., 2007). Thus, the total error in the retrieved profile is given by

$$\mathbf{S}_{\text{total}} = \mathbf{S}_m + \mathbf{S}_f + \mathbf{S}_s, \tag{8}$$

where $\mathbf{S}_m$ is retrieval noise covariance, $\mathbf{S}_f$ is forward model parameter covariance, and $\mathbf{S}_s$ is smoothing error covariance matrices. Since the a priori covariance matrix $\mathbf{S}_a$ is used as a tuning parameter, the smoothing error is also not considered, but could be estimated from the averaging kernel matrix $\mathbf{A}$.

The error due to measurement noise is given by the retrieval noise covariance

$$\mathbf{S}_m = \mathbf{G}^T\,\mathbf{S}_\varepsilon^{-1}\mathbf{G}, \tag{9}$$

where

$$\mathbf{G} = \left(\mathbf{K}^T\,\mathbf{S}_\varepsilon^{-1}\mathbf{K} + \mathbf{S}_a\right)^{-1}\mathbf{K}\mathbf{T}\mathbf{S}_\varepsilon^{-1} \tag{10}$$

is the gain matrix and expresses the sensitivity of retrieved profile to measured SCDs.

Sensitivity studies were performed in order to estimate the error in the retrieved profiles due to uncertainties in forward model parameters including EA accuracy. For each forward model parameter, $\boldsymbol{b}$, we retrieved a new profile, $\boldsymbol{x}'$, such that

$$\boldsymbol{y} = \mathbf{F}(\boldsymbol{x}',\ \boldsymbol{b}'), \tag{11}$$

where $\boldsymbol{b}'$ is the perturbation to the forward model parameter $\boldsymbol{b}$.

The difference between retrieved profiles $\boldsymbol{x}$ with forward model parameter $\boldsymbol{b}$, and $\boldsymbol{x}'$ with $\boldsymbol{b}'$, gives an estimate of the forward model error caused by uncertainties in parameter $\boldsymbol{b}$. The square of the differences constitutes the diagonal element of the corresponding forward model parameter covariance matrix $\mathbf{S}_f$.

We studied the effects of uncertainties in SA, SSA, asymmetry parameter, temperature, and EA on aerosol extinction coefficients at 477 nm. Results from the study are summarized in Table 5. The asymmetry parameter uncertainty ($g = 0.68 \pm 0.07$) could result in as much as 10 % relative error in extinction values. A 5 °C temperature uncertainty

Table 5. Uncertainty in aerosol extinction coefficient due to uncertainty in model input parameters.

Parameter	Uncertainty in parameter	Uncertainty in extinction coefficient
Surface albedo	±0.05	< 2 %
Single scattering albedo	±0.05	< 2 %
Asymmetry parameter	± 0.07	up to 10 %
Temperature	± 5 °C	up to 10 %
Pointing accuracy	±0.35°	mostly in transition layer

could also result in similar relative error as the O_4 concentration in the atmosphere is temperature dependent (density effect). We used temperature measured aboard the aircraft to minimize this error. Angle accuracy uncertainty was found to result in large extinction errors ($> 0.01\,km^{-1}$) in the transition layer at the top of the boundary layer and around elevated layers. It points to the possibility of uncertainty in altitude of aerosol layers in the extinction profile and results in a blurring effect (Kritten et al., 2010). Angle accuracy uncertainties are often not considered for error estimates for vertical profiles from airborne DOAS measurements, but it could be the most important and largest source of error in the retrieved profiles, especially for transition layers. The error bars in the aerosol extinction profile (Fig. 10b) reflect uncertainty due to measurement error, and uncertainty in SSA, *g* parameter, SA and EA.

Uncertainties in aerosol extinction coefficients and EA were only considered as a forward model parameter affecting the retrieved trace gas profiles as other forward model parameters (e.g., SA) have already been considered in aerosol extinction coefficient retrieval.

4 Results and discussion

4.1 Nadir observations

4.1.1 Horizontal distribution of NO_2

As an example, a map of NO_2 VCD distribution in the SCAB from RF#46 on 16 July 2010 (10:30–14:10 PDT) is shown in Fig. 7. The small footprint (~ 1 km along the flight track) of the measurement allows us to clearly identify local hotspots and pollution sources. The NO_2 map in Fig. 7 reflects our understanding of the NO_x sources and its relatively short life time (~ 4 h). Clear NO_2 hotspots can be observed around downtown Los Angeles and Ontario, along the major highway, State Route 210, and at intersections of major highways. In contrast, very little NO_2 is seen in the eastern part of the basin, and over the High Desert to the northeast, where there are no significant local sources of NO_x. The footprint of CU AMAX-DOAS is comparable to air quality models, and smaller than that of current solar stray light satellite observations, which also measure VCDs of trace gases; this makes this data set an excellent opportunity to evaluate emissions in air quality models and validate satellite observations. A first application of CU AMAX-DOAS to test NASA NO_2 VCD retrievals from the OMI/AURA satellite instrument is currently under review (Oetjen et al., 2013).

4.1.2 Validation of NO_2 vertical column

To validate the retrieval of our NO_2 VCDs by CU AMAX-DOAS using the geometric approximation, we compared our observations with NO_2 VCDs from ground-based MAX-DOAS instruments. Two MAX-DOAS instruments (Sinreich et al., 2010; Coburn et al., 2011) were deployed at the CalNex ground site (Ryerson et al., 2013) in Pasadena, the Fontana Arrows CARB monitoring network station and the CARES T1 (Zaveri et al., 2012) site in Cool, CA at various times of the campaign. MAX-DOAS operates on the same principle as AMAX-DOAS. Spectra measured at off-axis angles were analyzed for NO_2 using a closest zenith reference spectrum in time. The retrieved NO_2 dSCDs for 20° EA were converted to VCDs using a dAMF calculated by McArtim. This EA was chosen to minimize the effect of uncertainties in model parameters – especially magnitude and shape of NO_2 profile and aerosols. Sensitivity studies were performed to estimate the error in calculated dAMF due to model parameter uncertainties and is estimated to be around 8 %. Considering ~ 3 % dSCD retrieval error and ~ 8 % dAMF error, we estimate the overall error in MAX-DOAS VCDs to be around 10 %. Further details about MAX-DOAS measurements during the CalNex and CARES campaigns can be found in Ortega et al. (2013). MAX-DOAS instruments at Pasadena and Fontana Arrows were pointing in both east and west directions, while the one at the CARES T1 site was facing both north and south. Those MAX-DOAS instruments are capable of making a full 180° EA scan.

The NOAA Twin Otter was frequently routed over these ground sites. The correlation plot between the CU AMAX-DOAS and MAX-DOAS instruments is shown in Fig. 8. Correlations showed sensitivity to filtering data by criteria such as the distance of the plane and ground site, the relative azimuth angle between plane heading and ground viewing, and inhomogeneous air mass. The inhomogeneity of air mass was measured by MAX-DOAS, which observed differences in NO_2 VCDs in the east and west view of up to 2.5×10^{16} molecules cm^{-2}. Figure 7 gives an idea of the NO_2 VCD variability as mapped by CU AMAX-DOAS. Filtering for data within 5 km radius of the ground site, clouds (via two webcams installed on the aircraft), SZA $< 65°$ aircraft altitude < 4 km, and $< 1.5 \times 10^{16}$ molecules cm^{-2} NO_2 VCD difference in east/west view of MAX-DOAS instruments in SCAB, as well as coincident measurements within 10 min of the aircraft overpass, resulted in a correlation with slope of 0.86 ± 0.03, and offset in VCD of $-0.8 \pm 3.7 \times 10^{14}$ molecules cm^{-2} ($R^2 = 0.96$) (grey dots in Fig. 8). The slope of the linear fit line is skewed by the measurements at CARES T1 site that are near or below the detection limit of both the instruments, but nevertheless still a very good agreement between the two instruments. If only measurements in SCAB are considered, and filtering is further constrained (relative azimuth angle between plane heading and ground viewing $< \pm 15°$, and variability in NO_2 VCD for both instruments $< 8 \times 10^{15}$ molecules cm^{-2}), the slope increases to 0.95 ± 0.09, offset in VCD of $2.5 \pm 1.4 \times 10^{15}$ molecules cm^{-2} ($R^2 = 0.86$) (Fig. 8). This sensitivity to filtering criteria reflects upon the inhomogeneity of the SCAB air mass and also points to the validity

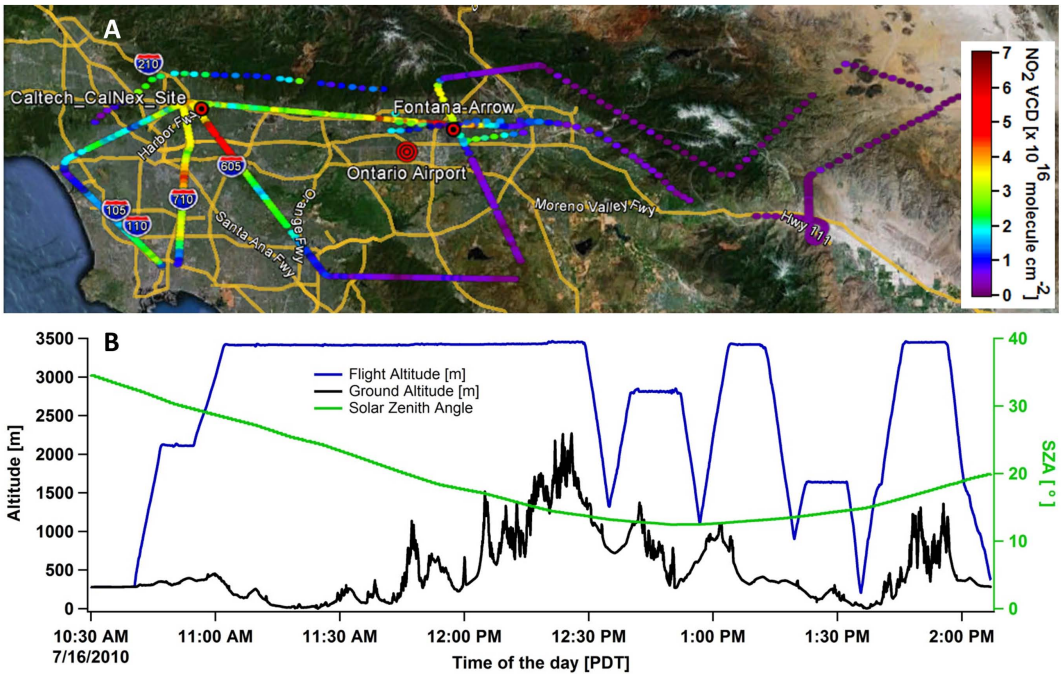

Fig. 7. (A) Map showing horizontal distribution of NO_2 VCDs below the aircraft derived from nadir measurements from RF#46 on 16 July 2010 (10:30–14:10 PDT – Pacific Daylight Time) in the SCAB. MAX-DOAS instruments deployment sites and the base airport for the Twin Otter are shown as red targets. **(B)** Time trace of flight altitude (blue), ground altitude (black) and SZA (green) from the same flight.

of geometric approach under horizontally inhomogeneous conditions.

4.2 Limb observations

Vertical profiles of aerosol extinction coefficient and trace gas concentrations were retrieved for a low approach at Brackett airfield, CA during RF#46. The aircraft was flying at ∼3.1 km a.g.l. (above ground level), made a slow descent to an altitude of ∼0.6 km a.g.l. at the airport, and then ascended again. The telescope was scanning a set of EAs (−90°, −5°, −2°, 0°, 2°, 5°, 90°) during the low approach. A complete set of EAs was also measured at the highest altitude just before the descent and at the lowest point before starting to ascend in order to characterize the air mass above and below the aircraft. The descent portion of the low approach took ∼8 min. Low approach is a maneuver over an airport in which the pilot intentionally does not make contact with the runway.

4.2.1 Determination of O_4 SCD in the reference spectrum

The scale height of O_4 in the atmosphere is ∼4 km and as our measurements were usually performed below 4 km altitude, it is important to quantify the O_4 SCD contained in the reference spectrum (SCD_{ref}) in order to accurately retrieve the aerosol extinction profile. Merlaud et al. (2011) used a linear regression between measured dSCD and calculated SCD for airborne measurements above 5.5 km in the Arctic to determine SCD_{ref} and the dSCD correction factor, :

$$\text{SCD} = \quad \times \text{dSCD} + \text{SCD}_{\text{ref}}. \tag{12}$$

The dSCD correction factor ( ) has been used to scale measured O_4 dSCDs to bring inferences of aerosol extinction into agreement with other sensors, such as AERONET (e.g., Clémer et al., 2010). It is an empirical observation that some MAX-DOAS applications find measured O_4 dSCDs to be too large compared to modeled O_4 dSCDs for a Rayleigh atmosphere. The nonphysicality of , different from unity, is a subject of ongoing debate in the DOAS community. For example, the value for the correction factor is different between different environments and research groups, wavelength, and ranges from 0.75 to 0.89 (Wagner et al., 2009; Clémer et al., 2010; Merlaud et al., 2011; Zieger et al., 2011). It has been speculated that the need for could be due to the temperature dependence of the O_4 absorption cross section (Wagner et al., 2009; Cleémer et al., 2010). Indeed, a temperature uncertainty in the O_4 absorption cross section has been reported (Blickensdorfer and Ewing, 1969; Wagner et al., 2002 and references within).

We employed the same approach as Merlaud et al. (2011) to determine SCD_{ref} and . Temperature and pressure as measured on the plane were used to prescribe the vertical distribution of O_4 in the model. Temperature and pressure

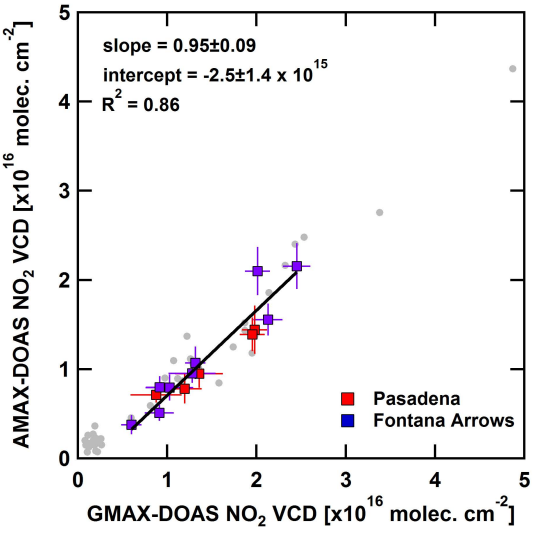

Fig. 8. Correlation plot of NO_2 VCDs between CU AMAX-DOAS and two MAX-DOAS instruments deployed in California during the CalNex and CARES field campaigns. Grey dots represent all data from both CalNex and CARES campaigns (see text for filtering conditions). Data from CalNex further constrained for relative azimuth between plane heading and MAX-DOAS viewing geometry $< \pm 15°$ and NO_2 VCD variability $< 8x \times 10^{15}$ molecules cm^{-2} are shown in red and blue. Black line is the linear fit through the colored points.

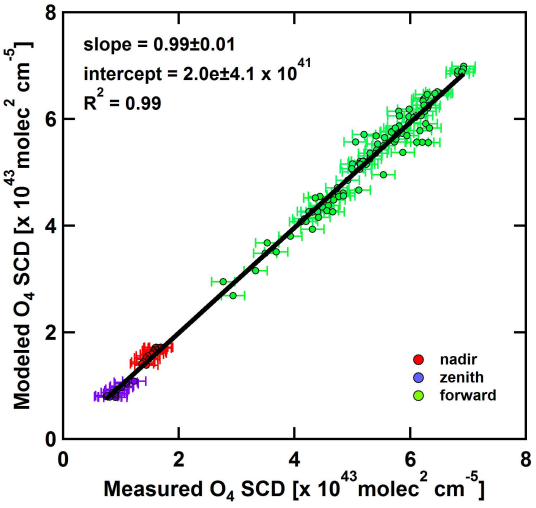

Fig. 9. Correlation plot of modeled and measured O_4 SCDs at 477 nm for the case study shown in Fig. 10b. SCD of the zenith reference (9×10^{42} molecules^2 cm^{-5}) has been added to the measured O_4 dSCDs. Forward viewing geometry includes 0°, ±2°, ±5° EAs.

profiles were extrapolated to the ground using the lapse rate and scale height determined from the measurements, respectively. The temperature was 36.7 °C and the pressure was 966 mbar at the ground. Comparison of extrapolated temperature and pressure values at the ground with measurements at the nearest CARB monitoring stations showed good agreement within ±2 °C and ±10 mbar, respectively. Profiles above the aircraft were extrapolated based on the mean temperature and pressure profiles measured at Joshua Tree, CA. The O_3 profile was also constructed similarly and was measured by the NOAA TOPAZ lidar aboard the plane. Based on the regression analysis shown in Fig. 9, between simulated and measured O_4 SCDs at 477 nm for the low approach at Brackett airfield during RF#46 (see more details below), we determine $= 0.99 \pm 0.01$ for 477 nm. Hence, it is concluded that a scaling factor is not needed to explain our measurements. An O_4 reference SCD of 9×10^{42} molecule^2 cm^{-5} based on the regression has been added to the measured dSCDs to convert them to SCDs.

4.2.2 Aerosol extinction coefficient profiles

The aerosol extinction coefficient vertical distribution retrieved at 477 nm is shown in Fig. 10b. The extinction profile was retrieved by iteratively minimizing the residual between measured and simulated O_4 SCDs; see Sect. 3.4. Figure 10a illustrates the agreement between the measured and modeled O_4 SCDs at 477 nm for 0° EA. The corresponding aerosol extinction profile is presented in Fig. 10b. The aerosol extinction profile in Fig. 10b indicates that most of the aerosols are located inside the BL (up to 0.9 km, indicated by the decrease in NO_2 and aerosol) with a 500-m-thick elevated layer at ∼ 2.5 km. The error contribution in retrieved extinction due to EA uncertainty of 0.35° is shown in Fig. 10c, and it illustrates that pointing accuracy is needed especially to minimize error in transition layers and elevated layers.

Integration of the extinction coefficient profile over altitude gives AOD – the total load of aerosols in the atmosphere. AOD at 477 nm from the profile in Fig. 10b is 0.16 ± 0.03 and agrees well with 0.18 ± 0.02 at 500 nm measured by the AERONET station located at Pasadena. The AOD values for the AERONET station reported here are hourly averages and standard deviations for the hour of the low approach. Pasadena is located 30 km west of the Brackett airfield; the telescope was pointing towards the west during our low approach, and measurements inherently average over spatial scales of typically few 10 km. Based on the Koschmieder visibility formula for the visible wavelength region – visibility = 3.91/extinction coefficient (see e.g., Horvath, 1971) – the visibility at 477 nm during the time of our measurement would be ∼ 39 km. The excellent agreement between the AOD calculated from our profiles and AERONET station adds confidence to our retrieval approach and accuracy of the retrieved profile. To our knowledge this is the first demonstration of quantitative retrieval of aerosol extinction from O_4 dSCD observations that does not require a correction factor.

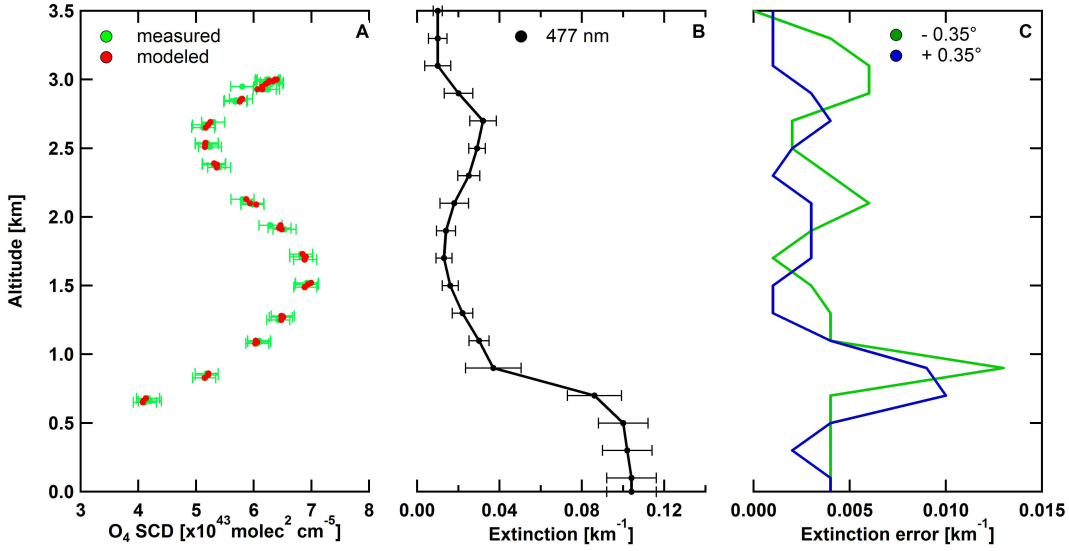

Fig. 10. (A) Measured (green) and simulated (red) vertical profiles of O_4 SCDs for 0° EA at 477 nm from the low approach at Brackett airfield during RF#46 on 16 July 2010 in SCAB. **(B)** Corresponding aerosol extinction vertical profile retrieved at 477 nm. **(C)** Error contribution in extinction due to angle uncertainty of ±0.35°. Note that the aircraft only flew down to ∼ 600 m a.g.l. during the low approach, and a set of downward EAs at that altitude was used to probe the lower altitudes.

4.2.3 Trace gas vertical profiles

Figure 11 shows the retrieved NO_2, CHOCHO, HCHO and H_2O mixing ratio profiles from the same low approach. The NO_2, CHOCHO, and HCHO vertical profiles have a very similar shape, with most of the trace gases located inside the BL. This is not surprising since most of the sources for these gases are close to the surface. On the other hand, the H_2O profile is almost linearly decreasing with altitude. The retrieved NO_2 profile shows an average urban BL value of 14.2 ± 1.3 ppb (at the surface: $1\,\text{ppb} \cong 2.46 \times 10^{10}$ molecules cm^{-3} at sea level, and 298 K temperature). The hourly NO_2 data recorded at the nearest CARB monitoring station at Pomona, CA are 13 ppb. Pomona station is located ∼ 3 km south of the Brackett airfield. Our retrieved NO_2 surface mixing ratio agrees well with the measurement at the ground station. The CHOCHO profile shows a BL value of 274 ± 28 ppt. It also exhibits an elevated layer of CHOCHO with $\sim 33 \pm 8$ ppt at around 2.5 km (Fig. 11b). The lower error bars in the FT compared to the BL is due to two reasons: (1) with both the reference spectrum and the measured spectrum taken under very similar conditions, i.e., FT with lower aerosol load compared to BL, the DOAS retrieval error is smaller in the FT compared to BL. (2) In our low approach, the aircraft only descended down to an altitude of ∼ 600 m a.g.l. , and a set of downward EAs at that altitude was used to probe the lower altitudes. Hence, the measurement has relatively lower sensitivity below 600 m (see Fig. S1 in the Supplement). The observation of 33 ppt CHOCHO in a layer aloft that is decoupled from the boundary layer coincides with the altitude where a layer of enhanced aerosol is observed in the aerosol extinction profile (Fig. 10b). The coexistence of CHOCHO and aerosol aloft could indicate the in situ production of CHOCHO from oxidation of VOCs that have been transported along with the aerosols. Laboratory studies show consistent evidence of CHOCHO uptake by aerosols forms SOA (Liggio et al., 2005; Volkamer et al., 2009b; Trainic et al., 2011). However, if this process is partly reversible, the collocation of CHOCHO and aerosol could also point to aerosols as a source of CHOCHO aloft (Kroll et al., 2005; Kampf et al., 2013). It should be noted that while CHOCHO dSCDs at the elevated layers are close to the detection limit for our 2 s data, this detection limit can be improved by longer averaging times. An elevated layer of O_3 is also observed in the NOAA TOPAZ lidar data at the same altitude (C. Senff, CIRES & NOAA, personal communication, 2012) and is included in the RTM calculations for aerosol extinction and trace gas inversion. The water vapor mixing ratio inside the BL corresponds to a relative humidity, $\text{RH} = 23 \pm 5$ %. Coincident measurements of RH at nearby CARB monitoring stations varied from RH = 23 % (Ontario International Airport) to RH = 34 % (Upland, CA). The good agreement of RH demonstrates control of radiation fields in the inversion. HCHO vertical profile was retrieved using aerosol extinction profile independently obtained using O_4 dSCD measurements at 360 nm (see Fig. S2 in the Supplement).

A 250 m altitude grid was chosen for the retrieval of trace gases. This grid height was chosen based on the FOV of the telescope, rate of aircraft descent and time it took to complete one EA scan cycle during the descent. The averaging kernels for all the trace gases indicate a constant sensitivity

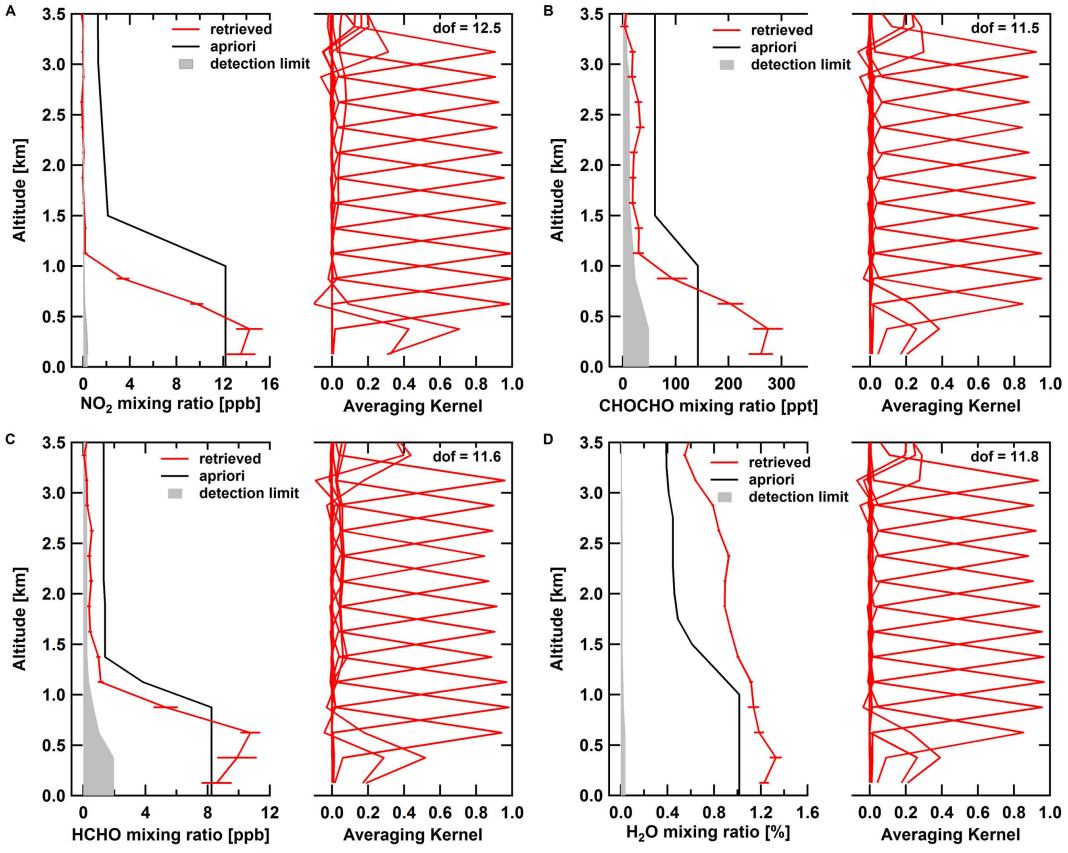

Fig. 11. Retrieved vertical profiles and corresponding averaging kernels for **(A)** NO_2, **(B)** CHOCHO, **(C)** HCHO and **(D)** H_2O from the low approach at Brackett airfield. NO_2, CHOCHO and HCHO profiles show most of the trace gases are located close to the source region inside the BL. Averaging kernels indicate almost constant sensitivity for all trace gases over the entire altitude range. Grey shaded area represents detection limit for each profile.

for the whole low approach except the lowest layer at the surface. The DOF are 12.5, 11.5, 11.6, and 11.8 for NO_2, CHOCHO, HCHO, and H_2O, respectively confirming the presence of independent information approximately every 250 m. The sensitivity of the retrieved profile to different a priori profiles was also tested, and the lowest layer inside the BL was found to be the most susceptible (up to 20 %), which is the layer with the least measurement sensitivity. The lower averaging kernels below 600 m are explained from the observing geometry of the low approach (see above). While this decrease in sensitivity for other EAs compared to 0° for a given atmospheric layer does not appear to limit our ability to infer meaningful information near the surface (see this section above), it highlights the benefit of capabilities to maintain 0° EA during aircraft ascent/descent to systematically probe the atmosphere with maximum sensitivity and vertical resolution.

The averaging kernels (Fig. 11) appear as if there were no other EAs but 0° EA used for the profile retrievals. In fact, they peak at the altitude of 0° EA measurements. This highlights the fact that 0° EA is the most sensitive EA during ascent and descent of the aircraft and provides the most independent information. This has also been reported by Merlaud et al. (2011). Bruns et al. (2004) performed theoretical sensitivity study regarding choice of EA for maximizing DOF while flying at a constant altitude. Based on the study by Bruns et al. (2004) and our experiment, we recommend maintaining 0° EA actively aligned during descent/ascent and scanning only at the lowest and highest point during the ascent/descent to maximize DOF.

5 Conclusions

An airborne MAX-DOAS instrument equipped with a motion-stabilized scanning telescope to collect solar stray light photons provides accurate means to probe atmospheric composition in terms of the horizontal and vertical distributions of multiple trace gases and aerosols simultaneously and sensitively by means of a single, portable instrument.

The CU AMAX-DOAS instrument is validated by comparison with NO_2 VCDs measured by ground-based MAX-DOAS. A sensitivity study using radiative transfer modeling

reveals that the geometric approximation is a viable option to convert NO_2 SCD to VCD for measurements below the plane. This approximation is found to be accurate over southern California, where elevated SA ($\sim 10\,\%$ at 477 nm wavelength, measured aboard the plane) compensates for reduced sensitivity due to aerosols. We estimate the error in the NO_2 vertical columns due to the geometric approximation to be less than 7 % under most conditions for SZA $< 65°$; a slightly larger error ($< 25\,\%$ in all cases) is found for SZA $\sim 65°$ or during high-altitude flights over low SA. These results emphasize benefits of measuring SA and AOD by independent sensors.

For a case study, vertical profiles of NO_2, CHOCHO, HCHO, H_2O, and aerosol extinction coefficient at 477 nm showed that trace gases and aerosols are located mostly inside the BL, though the presence of an elevated pollution layer was observed as well. Sensitivity studies show that the main error sources in the retrieved vertical profiles of aerosol extinction are due to the asymmetry parameter of aerosol scattering. Further, sensitivity studies highlight the need of pointing accuracy of the telescope on moving platforms like an aircraft to accurately retrieve vertical distributions of trace gases and aerosol extinction coefficients. The accuracy of our motion compensation is found to be $< 0.35°$ by comparison with an independent inertia system.

An $\sim$500-m-thick layer at around 2.5 km altitude a.g.l. was observed that was decoupled from the BL, and contained 33 ± 8 ppt CHOCHO, NO_2 below the detection limit (30 ppt, for 2 s integration time), 545 ± 114 ppt HCHO, $0.029 \pm 0.004\,km^{-1}$ ε_{477}, corresponding to a partial vertical columns of $4.14 \pm 1.12 \times 10^{13}$ molecules cm^{-2} CHOCHO, $7.10 \pm 1.75 \times 10^{14}$ molecules cm^{-2} HCHO, and partial AOD of 0.047 ± 0.007 at 477 nm. This elevated layer contained ratios of CHOCHO/HCHO of 0.06 ± 0.02, compared to 0.027 ± 0.006 inside the BL. The concurrent location of elevated aerosol extinction at the same altitude indicates either collocated CHOCHO sources from VOC oxidation, or the release of CHOCHO that was initially taken up as SOA back to the gas phase. The increase in the CHOCHO/HCHO ratio with altitude appears to be outside error bars, and the cause for this altitude dependence deserves further investigation.

The capabilities of CU AMAX-DOAS are not limited to the parameters presented here, and also include measurements of reactive species such as halogen oxide radicals (e.g., Dix et al., 2013), and aerosols at other wavelengths. The absence of sampling lines, and inherent averaging over extended spatial scales enable the AMAX-DOAS technique to bridge between ground-based networks, atmospheric models, and satellites, and holds as yet unexplored potential to advance airborne atmospheric observations, and improve our understanding of the processes taking place in the atmosphere. The CU AMAX-DOAS deployment during the CalNex and CARES field campaigns makes a 10-week-long data set available that we plan to apply for such studies.

Appendix A

Table A1. List of frequently used abbreviations.

a.g.l.	above ground level
AMAX-DOAS	airborne multi-axis differential optical absorption spectroscopy
AMF	air mass factor
AOD	aerosol optical depth
BL	boundary layer
BLH	boundary layer height
CalNex	California Research at the Nexus of Air Quality and Climate Change
CARB	California Air Resources Board
CARES	Carbonaceous Aerosols and Radiative Effects Study
dAMF	differential air mass factor
dSCD	differential slant column density
DOF	degrees of freedom
EA	elevation angle
FOV	field of view
FT	free troposphere
FWHM	full width at half maximum
geoAMF	geometric air mass factor
LOS	lines of sight
MAX-DOAS	multi-axis differential optical absorption spectroscopy
RF	research flight
RTM	radiative transfer model
SA	surface albedo
SCD	slant column density
SCAB	South Coast Air Basin
SOA	secondary organic aerosol
SSA	single scattering albedo
SZA	solar zenith angle
VCD	vertical column density

Supplementary material related to this article is available online at: http://www.atmos-meas-tech.net/6/719/2013/amt-6-719-2013-supplement.pdf.

Acknowledgements. This work was supported by the California Air Resource Board (CARB) contract 09-317, the National Science Foundation CAREER award ATM-847793, CU startup funds (RV) and an ESRL-CIRES Graduate Fellowship (SB). The authors thank Dr. Jochen Stutz for providing AERONET data at the Caltech site. The authors like to thank Tim Deutschmann, University of Heidelberg for the radiative transfer code, McArtim, David Thomson for the software support, Caroline Fayt and Michel van Roozendael for the WinDOAS software and the NOAA Twin Otter research flight crew.

Edited by: J. Stutz

References

Alvarez II, R. J., Senff, C. J., Langford, A. O., Weickmann, A. M., Law, D. C., Machol, J. L., Merritt, D. A., Marchbanks, R. D., Sandberg, S. P., Brewer, W. A., Hardesty, R. M., and Banta, R. M.: Development and Application of a Compact, Tunable, Solid-State Airborne Ozone Lidar System for Boundary Layer Profiling, J. Atmos. Ocean. Tech., 28, 1258–1272, doi:10.1175/JTECH-D-10-05044.1, 2011.

Barret, B., De Maziere, M., and Demoulin, P.: Retrieval and characterization of ozone profiles from solar infrared spectra at the Jungfraujoch, J. Geophys. Res.-Atmos., 107, 4788, doi:10.1029/2001JD001298, 2002.

Blickendsdorfer, R. P. and Ewing, G. E.: Collision-Induced Absorption Spectrum of Gaseous Oxygen at Low Temperatures and Pressures, II. The Simultaneous Transitions $^1\Delta_g + {}^1\Delta_g < - {}^3\sum_g\!\!\left(+ {}^3\sum_g\right.\!\!\left($ and $^1\Delta_g + {}^1\sum_g\!\!\left(+ < - {}^3\sum_g\!\!\left(+ {}^3\sum_g\right.\right.\!\!\left.\right)$, J. Chem. Phys., 51, 5284–5289, doi:10.1063/1.1671946, 1969.

Bogumil, K., Orphal, J., Homann, T., Voigt, S., Spietz, P., Fleischmann, O., Vogel, A., Hartmann, M., Kromminga, H., Bovensmann, H., Frerick, J., and Burrows, J.: Measurements of molecular absorption spectra with the SCIAMACHY pre-flight model: instrument characterization and reference data for atmospheric remote-sensing in the 230-2380 nm region, J. Photoch. Photobio. A, 157, 167–184, doi:10.1016/S1010-6030(03)00062-5, 2003.

Bruns, M., Buehler, S. A., Burrows, J. P., Heue, K. P., Platt, U., Pundt, I., Richter, A., Rozanov, A., Wagner, T., and Wang, P.: Retrieval of Pro?le Information from Airborne Multi AxisUV/visible Skylight Absorption Measurements, Appl. Optics, 43, 4415–4426, doi:10.1364/AO.43.004415, 2004.

Bruns, M., Buehler, S. A., Burrows, J. P., Richter, A., Rozanov, A., Wang, P., Heue, K. P., Platt, U., Pundt, I., and Wagner, T.: NO_2 Profile retrieval using airborne multi axis UV-visible skylight absorption measurements over central Europe, Atmos. Chem. Phys., 6, 3049–3058, doi:10.5194/acp-6-3049-2006, 2006.

Bussemer, M.: Der Ring-Effekt: Ursachen und Einfluß auf die spektroskopische Messung stratosphärischer Spurenstoffe, Diploma Thesis thesis/masters, University of Heidelberg, Heidelberg, Germany, 1993.

Chance, K. and Orphal, J.: Revised ultraviolet absroption cross sections of H_2CO for the HITRAN database, J. Quant. Spectrosc. Ra., 112, 1509–1510, doi:10.1016/j.jqsrt.2011.02.002, 2011.

Clémer, K., Van Roozendael, M., Fayt, C., Hendrick, F., Hermans, C., Pinardi, G., Spurr, R., Wang, P., and De Mazière, M.: Multiple wavelength retrieval of tropospheric aerosol optical properties from MAXDOAS measurements in Beijing, Atmos. Meas. Tech., 3, 863–878, doi:10.5194/amt-3-863-2010, 2010.

Coburn, S., Dix, B., Sinreich, R., and Volkamer, R.: The CU ground MAX-DOAS instrument: characterization of RMS noise limitations and first measurements near Pensacola, FL of BrO, IO, and CHOCHO, Atmos. Meas. Tech., 4, 2421–2439, doi:10.5194/amt-4-2421-2011, 2011.

Deutschmann, T., Beirle, S., Friess, U., Grzegorski, M., Kern, C., Kritten, L., Platt, U., Prados-Roman, C., Pukite, J., Wagner, T., Werner, B., and Pfeilsticker, K.: The Monte Carlo atmospheric radiative transfer model McArtim: Introduction and validation of Jacobians and 3D features, J. Quant. Spectrosc. Ra., 112, 1119–1137, doi:10.1016/j.jqsrt.2010.12.009, 2011.

Dix, B., Brenninkmeijer, C. A. M., Frieß, U., Wagner, T., and Platt, U.: Airborne multi-axis DOAS measurements of atmospheric trace gases on CARIBIC long-distance flights, Atmos. Meas. Tech., 2, 639–652, doi:10.5194/amt-2-639-2009, 2009.

Dix, B., Baidar, S., Bresch, J. F., Hall, S. R., Schmidt, K. S., Wang, S., and Volkamer, R.: Detection of Iodine Monoxide in the Tropical Free Troposphere, Proc. Natl. Acad. Sci., 110, 2035–2040, doi:10.1073/pnas.1212386110, 2013.

Dubovik, O., Holben, B., Eck, T. F., Smirnov, A., Kaufman, Y. F., King, M. D., Tanré, D., and Slutsker, I.: Variability of absorption and optical properties of key aerosol types observed in worldwide locations, J. Atmos. Sci., 59, 590–608, doi:10.1175/1520-0469(2002)059<0590:VOAAOP>2.0.CO;2, 2002.

Fayt, C. and Van Roozendael, M.: WinDOAS 2.1, Software User Manual, available at: http://bro.aeronomie.be/WinDOAS-SUM-201b.pdf, last access: 29 May 2012, Belgian Institute for Space Aeronomy, Brussels, Belgium, 2001.

Grainger, J. and Ring, J.: Anomalous Fraunhofer Line Profiles, Nature, 193, p. 762, doi:10.1038/193762a0, 1962.

Greenblatt, G. D., Orlando, J. J., Burkholder, J. B., and Ravishankara, A. R.: Absorption-Measurements of Oxygen between 330 nm and 1140 nm, J. Geophys. Res., 95, 18577–18582, doi:10.1029/JD095iD11p18577, 1990.

Griffin, R. J., Revelle, M. K., and Dabdub, D.: Modeling the oxidative capacity of the atmosphere of the south coast air basin of California, 1. Ozone formation metrics, Environ. Sci. Technol., 38, 746–752, doi:10.1021/es0341283, 2004.

Hendrick, F., Barret, B., Van Roozendael, M., Boesch, H., Butz, A., De Mazière, M., Goutail, F., Hermans, C., Lambert, J.-C., Pfeilsticker, K., and Pommereau, J.-P.: Retrieval of nitrogen dioxide stratospheric profiles from ground-based zenith-sky UV-visible observations: validation of the technique through correlative comparisons, Atmos. Chem. Phys., 4, 2091–2106, doi:10.5194/acp-4-2091-2004, 2004.

Hendrick, F., Van Roozendael, M., Kylling, A., Petritoli, A., Rozanov, A., Sanghavi, S., Schofield, R., von Friedeburg, C., Wagner, T., Wittrock, F., Fonteyn, D., and De Mazière, M.: Intercomparison exercise between different radiative transfer models used for the interpretation of ground-based zenith-sky and multi-axis DOAS observations, Atmos. Chem. Phys., 6, 93–108, doi:10.5194/acp-6-93-2006, 2006.

Hermans, C.: Measurement of absorption cross sections and spectroscopicmolecular parameters: O_2 and its collisional induced absorption, available at: http://spectrolab.aeronomie.be/o2.htm (last access: 29 May 2012), 2002.

Heue, K.-P., Richter, A., Bruns, M., Burrows, J. P., v. Friedeburg, C., Platt, U., Pundt, I., Wang, P., and Wagner, T.: Validation of SCIAMACHY tropospheric NO_2-columns with AMAXDOAS measurements, Atmos. Chem. Phys., 5, 1039–1051, doi:10.5194/acp-5-1039-2005, 2005.

Hönninger, G., von Friedeburg, C., and Platt, U.: Multi axis differential optical absorption spectroscopy (MAX-DOAS), Atmos. Chem. Phys., 4, 231–254, doi:10.5194/acp-4-231-2004, 2004.

Horvath, H.: Applicability of Koschmieder Visibility Formula, Atmos. Environ., 5, 177–184, doi:10.1016/0004-6981(71)90081-3, 1971.

Kampf, C. J., Waxman, E. M., Slowik, J. G., Dommen, J., Pfaffenberger, L., Praplan, A., Prevot, A., Baltensperger, U., Hoffmann, T., and Volkamer, R.: Direct effective Henry's law constant measurements for glyoxal in model aerosols containing sulfate, Environ. Sci. Technol., submitted, 2013.

Kritten, L., Butz, A., Dorf, M., Deutschmann, T., Kühl, S., Prados-Roman, C., Pukite, J., Rozanov, A., Schofield, R., and Pfeilsticker, K.: Time dependent profile retrieval of UV/vis absorbing radicals from balloon-borne limb measurements – a case study on NO_2 and O_3, Atmos. Meas. Tech., 3, 933–946, doi:10.5194/amt-3-933-2010, 2010.

Kroll, J. H., Ng, N. L., Murphy, S. M., Varutbangkul, V., Flagan, R. C., and Seinfeld, J. H.: Chamber studies of secondary organic aerosol growth by reactive uptake of simple carbonyl compounds, J. Geophys. Res.-Atmos., 110, D23207, doi:10.1029/2005JD006004, 2005.

Liggio, J., Li, S., and McLaren, R.: Reactive uptake of glyoxal by particulate matter, J. Geophys. Res., 110, D10304, doi:10.1029/2004JD005113, 2005.

McElroy, C. T.: Stratospheric Nitrogen-Dioxide Concentrations as Determined from Limb Brightness Measurements made on June 17, 1983, J. Geophys. Res.-Atmos., 93, 7075–7083, doi:10.1029/JD093iD06p07075, 1988.

Melamed, M. L., Solomon, S., Daniel, J. S., Langford, A. O., Portmann, R. W., Ryerson, T. B., Nicks, D. K. J., and and McKeen, S. A.: Measuring reactive nitrogen emissions from pointsources using visible spectroscopy from aircraft, J. Environ. Monit., 5, 29–34, doi:10.1039/B204220G, 2003.

Melamed, M. L., Langford, A. O., Daniel, J. S., Portmann, R. W., Miller, H. L., Eubank, C. S., Schofield, R., Holloway, J., and Solomon, S.: Sulfur dioxide emission flux measurements from point sources using airborne near ultraviolet spectroscopy during the New England Air Quality Study 2004, J. Geophys. Res., 113, D02305, doi:10.1029/2007JD008923, 2008.

Meller, R. and Moortgat, G.: Temperature dependence of the absorption cross sections of formaldehyde between 223 and 323 K in the wavelength range 225–375 nm, J. Geophys. Res., 105, 7089–7101, doi:10.1029/1999JD901074, 2000.

Merlaud, A., Van Roozendael, M., Theys, N., Fayt, C., Hermans, C., Quennehen, B., Schwarzenboeck, A., Ancellet, G., Pommier, M., Pelon, J., Burkhart, J., Stohl, A., and De Mazière, M.: Airborne DOAS measurements in Arctic: vertical distributions of aerosol extinction coefficient and NO_2 concentration, Atmos. Chem. Phys., 11, 9219–9236, doi:10.5194/acp-11-9219-2011, 2011.

Oetjen, H., Baidar, S., Krotkov, N. A., Lamsal, L. N., and Volkamer, R.: Testing the NASA OMI tropospheric NO_2 product over California for summer 2010 using airborne MAX-DOAS measurements, J. Geophys. Res.-Atmos., submitted, 2013.

Ortega, I., Baidar, S., Coburn, S., Dix, B., Oetjen, H., Sinreich, R., and Volkamer, R.: Comparison of regularization and optimal estimation inversion techniques to retrieve trace gas profiles from ground-based MAX-DOAS, in preparation, 2013.

Pearson, G., Davies, F., and Collier, C.: An Analysis of the Performance of the UFAM Pulsed Doppler Lidar for Observing the Boundary Layer, J. Atmos. Ocean. Tech., 26, 240–250, doi:10.1175/2008JTECHA1128.1, 2009.

Petritoli, A., Ravegnani, F., Giovanelli, G., Bortoli, D., Bonafe, U., Kostadinov, I., and Oulanovsky, A.: Off-axis measurements of atmospheric trace gases by use of an airborne ultraviolet-visible spectrometer, Appl. Optics, 41, 5593–5599, doi:10.1364/AO.41.005593, 2002.

Platt, U. and Stutz, J.: Differential Optical Absorption Spectroscopy: Principles and Applications, Springer Verlag, Heidelberg, 2008.

Pope III, C. A., Ezzati, M., and Dockery, D. W.: Fine-Particulate Air Pollution and Life Expectancy in the United States, N. Engl. J. Med., 360, 376–386, doi:10.1056/NEJMsa0805646, 2009.

Prados-Roman, C., Butz, A., Deutschmann, T., Dorf, M., Kritten, L., Minikin, A., Platt, U., Schlager, H., Sihler, H., Theys, N., Van Roozendael, M., Wagner, T., and Pfeilsticker, K.: Airborne DOAS limb measurements of tropospheric trace gas profiles: case studies on the profile retrieval of O_4 and BrO, Atmos. Meas. Tech., 4, 1241–1260, doi:10.5194/amt-4-1241-2011, 2011.

Rodgers, C. D.: Inverse Methods for Atmospheric Sounding: Theory and Practice, World Scientific, Singapore, 2000.

Roscoe, H. K. and Hill, J. G. T.: Vertical resolution of oversampled limb-sounding measurements from satellites and aircraft, J. Quant. Spectrosc. Ra., 72, 237–248, doi:10.1016/S0022-4073(01)00121-2, 2002.

Rothman, L., Jacquemart, D., Barbe, A., Benner, D., Birk, M., Brown, L., Carleer, M., Chackerian, C., Chance, K., Coudert, L., Dana, V., Devi, V., Flaud, J., Gamache, R., Goldman, A., Hartmann, J., Jucks, K., Maki, A., Mandin, J., Massie, S., Orphal, J., Perrin, A., Rinsland, C., Smith, M., Tennyson, J., Tolchenov, R., Toth, R., Vander Auwera, J., Varanasi, P., and Wagner, G.: The HITRAN 2004 molecular spectroscopic database, J. Quant. Spectrosc. Ra., 96, 139–204, doi:10.1016/j.jqsrt.2004.10.008, 2005.

Ryerson, T. B., Andrews, A. E., Angevine, W. M., Bates, T. S., Brock, C. A., Cohen, R. C., Cooper, O. R., de Gouw, J. A., Fehsenfeld, F. C., Ferrare, R. A., Fischer, M. L., Flagan, R. C., Goldstein, A. H., Hair, J. W., Hardesty, R. M., Hostetler, C. A., Jimenez, J. L., Langford, A. O., McCauley, E., McKeen, S. A., Molina, L. T., Nenes, A., Oltmans, S. J., Parrish, D. D., Pederson, J. R., Pierce, R. B., Prather, K., Quinn, P. K., Seinfeld, J. H., Senff, C., Sorooshian, A., Stutz, J., Surratt, J. D., Trainer, M., Volkmer, R., Williams, E. J., and Wofsy, S. C.: The 2010 California Research at the Nexus of Air Quality and Climate Change (CalNex) field study, J. Geophys. Res.-Atmos., submitted, 2013.

Schiller, C., Wahner, A., Platt, U., Dorn, H. P., Callies, J., and Ehhalt, D. H.: Near Uv Atmospheric Absorption-Measurements of Column Abundances during Airborne Arctic Stratospheric Expedition, January–February 1989, 2. Oclo Observations, Geophys. Res. Lett., 17, 501–504, doi:10.1029/GL017i004p00501, 1990.

Schofield, R., Connor, B. J., Kreher, K., Johnston, P. V., and Rodgers, C. D.: The retrieval of profile and chemical information from ground-based UV-visible spectroscopic measurements, J. Quant. Spectrosc. Ra., 86, 115–131, doi:10.1016/s0022-4073(03)00278-4, 2004.

Sinreich, R., Coburn, S., Dix, B., and Volkamer, R.: Ship-based detection of glyoxal over the remote tropical Pacific Ocean, Atmos. Chem. Phys., 10, 11359–11371, doi:10.5194/acp-10-11359-2010, 2010.

Thalman, R. and Volkamer, R.: Temperature Dependent Absorption Cross-Sections of O_2-O_2 collision pairs between 340 and 630 nm at atmospheric pressure, submitted, 2013.

Thomson, J., Hayes, P. L., Jimenez, J. L., Adachi, K., Zhang, X., Liu, J., Weber, R. J., and Buseck, R. R.: Aerosol Optical Properties at Pasadena, CA During CalNex 2010, Atmos. Environ., 55, 190–200, doi:10.1016/j.atmosenv.2012.03.011, 2012.

Trainic, M., Abo Riziq, A., Lavi, A., Flores, J. M., and Rudich, Y.: The optical, physical and chemical properties of the products of glyoxal uptake on ammonium sulfate seed aerosols, Atmos. Chem. Phys., 11, 9697–9707, doi:10.5194/acp-11-9697-2011, 2011.

Vandaele, A., Hermans, C., Simon, P., Carleer, M., Colin, R., Fally, S., Merienne, M., Jenouvrier, A., and Coquart, B.: Measurements of the NO_2 absorption cross-section from 42 000 cm^{-1} to 10 000 cm^{-1} (238–1000 nm) at 220 K and 294 K, J. Quant. Spectrosc. Ra., 59, 171–184, doi:10.1016/S0022-4073(97)00168-4, 1998.

Volkamer, R., Spietz, P., Burrows, J., and Platt, U.: High-resolution absorption cross-section of glyoxal in the UV-vis and IR spectral ranges, J. Photoch. Photobio. A, 172, 35-46, doi:10.1016/j.jphotochem.2004.11.011, 2005.

Volkamer, R., Martini, F. S., Molina, L. T., Salcedo, D., Jimenez, J. L., and Molina, M. J.: A missing sink for gas-phase glyoxal in Mexico City: Formation of secondary organic aerosol, Geophys. Res. Lett., 34, L19807, doi:10.1029/2007GL030752, 2007.

Volkamer, R., Coburn, S., Dix, B., and Sinreich, R.: MAX-DOAS observations from ground, ship, and research aircraft: maximizing signal-to-noise to measure "weak" absorbers, Proc. SPIE, 7462, 746203, doi:10.1117/12.826792, 2009a.

Volkamer, R., Ziemann, P. J., and Molina, M. J.: Secondary Organic Aerosol Formation from Acetylene (C_2H_2): seed effect on SOA yields due to organic photochemistry in the aerosol aqueous phase, Atmos. Chem. Phys., 9, 1907–1928, doi:10.5194/acp-9-1907-2009, 2009b.

Volkamer, R., Sheehy, P., Molina, L. T., and Molina, M. J.: Oxidative capacity of the Mexico City atmosphere – Part 1: A radical source perspective, Atmos. Chem. Phys., 10, 6969–6991, doi:10.5194/acp-10-6969-2010, 2010.

Wagner, T., von Friedeburg, C., Wenig, M., Otten, C., and Platt, U.: UV-visible observations of atmospheric O_4 absorptions using direct moonlight and zenith-scattered sunlight for clear-sky and cloudy sky conditions, J. Geophys. Res., 107, 4424, doi:10.1029/2001JD001026, 2002.

Wagner, T., Dix, B., von Friedeburg, C., Friess, U., Sanghavi, S., Sinreich, R., and Platt, U.: MAX-DOAS O_4 measurements: A new technique to derive information on atmospheric aerosols – Principles and information content, J. Geophys. Res., 109, D22205, doi:10.1029/2004JD004904, 2004.

Wagner, T., Burrows, J. P., Deutschmann, T., Dix, B., von Friedeburg, C., Frieß, U., Hendrick, F., Heue, K.-P., Irie, H., Iwabuchi, H., Kanaya, Y., Keller, J., McLinden, C. A., Oetjen, H., Palazzi, E., Petritoli, A., Platt, U., Postylyakov, O., Pukite, J., Richter, A., van Roozendael, M., Rozanov, A., Rozanov, V., Sinreich, R., Sanghavi, S., and Wittrock, F.: Comparison of box-air-mass-factors and radiances for Multiple-Axis Differential Optical Absorption Spectroscopy (MAX-DOAS) geometries calculated from different UV/visible radiative transfer models, Atmos. Chem. Phys., 7, 1809–1833, doi:10.5194/acp-7-1809-2007, 2007.

Wagner, T., Deutschmann, T., and Platt, U.: Determination of aerosol properties from MAX-DOAS observations of the Ring effect, Atmos. Meas. Tech., 2, 495–512, doi:10.5194/amt-2-495-2009, 2009.

Wahner, A., Callies, J., Dorn, H. P., Platt, U., and Schiller, C.: Near Uv Atmospheric Absorption-Measurements of Column Abundances during Airborne Arctic Stratospheric Expedition, January–February 1989, 1. Technique and No_2 Observations, Geophys. Res. Lett., 17, 497–500, doi:10.1029/GL017i004p00497, 1990a.

Wahner, A., Callies, J., Dorn, H. P., Platt, U., and Schiller, C.: Near Uv Atmospheric Absorption-Measurements of Column Abundances during Airborne Arctic Stratospheric Expedition, January–February 1989, 3. Bro Observations, Geophys. Res. Lett., 17, 517–520, doi:10.1029/GL017i004p00517, 1990b.

Wang, P., Richter, A., Bruns, M., Rozanov, V. V., Burrows, J. P., Heue, K.-P., Wagner, T., Pundt, I., and Platt, U.: Measurements of tropospheric NO_2 with an airborne multi-axis DOAS instrument, Atmos. Chem. Phys., 5, 337–343, doi:10.5194/acp-5-337-2005, 2005.

Wang, P., Richter, A., Bruns, M., Burrows, J. P., Scheele, R., Junkermann, W., Heue, K.-P., Wagner, T., Platt, U., and Pundt, I.: Airborne multi-axis DOAS measurements of tropospheric SO_2 plumes in the Po-valley, Italy, Atmos. Chem. Phys., 6, 329–338, doi:10.5194/acp-6-329-2006, 2006.

Weidner, F., Bösch, H., Bovensmann, H., Burrows, J. P., Butz, A., Camy-Peyret, C., Dorf, M., Gerilowski, K., Gurlit, W., Platt, U., von Friedeburg, C., Wagner, T., and Pfeilsticker, K.: Balloon-borne limb profiling of UV/vis skylight radiances, O_3, NO_2, and BrO: technical set-up and validation of the method, Atmos. Chem. Phys., 5, 1409–1422, doi:10.5194/acp-5-1409-2005, 2005.

Wittrock, F., Oetjen, H., Richter, A., Fietkau, S., Medeke, T., Rozanov, A., and Burrows, J. P.: MAX-DOAS measurements of atmospheric trace gases in Ny-Ålesund – Radiative transfer studies and their application, Atmos. Chem. Phys., 4, 955–966, doi:10.5194/acp-4-955-2004, 2004.

Zaveri, R. A., Shaw, W. J., Cziczo, D. J., Schmid, B., Ferrare, R. A., Alexander, M. L., Alexandrov, M., Alvarez, R. J., Arnott, W. P., Atkinson, D. B., Baidar, S., Banta, R. M., Barnard, J. C., Beranek, J., Berg, L. K., Brechtel, F., Brewer, W. A., Cahill, J. F., Cairns, B., Cappa, C. D., Chand, D., China, S., Comstock, J. M., Dubey, M. K., Easter, R. C., Erickson, M. H., Fast, J.

D., Floerchinger, C., Flowers, B. A., Fortner, E., Gaffney, J. S., Gilles, M. K., Gorkowski, K., Gustafson, W. I., Gyawali, M., Hair, J., Hardesty, R. M., Harworth, J. W., Herndon, S., Hiranuma, N., Hostetler, C., Hubbe, J. M., Jayne, J. T., Jeong, H., Jobson, B. T., Kassianov, E. I., Kleinman, L. I., Kluzek, C., Knighton, B., Kolesar, K. R., Kuang, C., Kubátová, A., Langford, A. O., Laskin, A., Laulainen, N., Marchbanks, R. D., Mazzoleni, C., Mei, F., Moffet, R. C., Nelson, D., Obland, M. D., Oetjen, H., Onasch, T. B., Ortega, I., Ottaviani, M., Pekour, M., Prather, K. A., Radney, J. G., Rogers, R. R., Sandberg, S. P., Sedlacek, A., Senff, C. J., Senum, G., Setyan, A., Shilling, J. E., Shrivastava, M., Song, C., Springston, S. R., Subramanian, R., Suski, K., Tomlinson, J., Volkamer, R., Wallace, H. W., Wang, J., Weickmann, A. M., Worsnop, D. R., Yu, X.-Y., Zelenyuk, A., and Zhang, Q.: Overview of the 2010 Carbonaceous Aerosols and Radiative Effects Study (CARES), Atmos. Chem. Phys., 12, 7647–7687, doi:10.5194/acp-12-7647-2012, 2012.

Zieger, P., Weingartner, E., Henzing, J., Moerman, M., de Leeuw, G., Mikkilä, J., Ehn, M., Petäjä, T., Clémer, K., van Roozendael, M., Yilmaz, S., Frieß, U., Irie, H., Wagner, T., Shaiganfar, R., Beirle, S., Apituley, A., Wilson, K., and Baltensperger, U.: Comparison of ambient aerosol extinction coefficients obtained from in-situ, MAX-DOAS and LIDAR measurements at Cabauw, Atmos. Chem. Phys., 11, 2603–2624, doi:10.5194/acp-11-2603-2011, 2011.

3.2 Airborne MAX-DOAS measurements over California: Testing the NASA OMI tropospheric NO2 product

Reproduced from: Oetjen, H., S. Baidar, N. A. Krotkov, L. N. Lamsal, M. Lechner, and R. Volkamer (2013), Airborne MAXDOAS measurements over California: Testing the NASA OMI tropospheric NO2 product, J. Geophys. Res. Atmos., 118, 7400–7413, doi:10.1002/jgrd.50550.

Airborne Multi-AXis Differential Optical Absorption Spectroscopy (AMAX-DOAS) measurements of NO_2 tropospheric vertical columns were performed over California for two months in summer 2010. The observations are compared to the NASA Ozone Monitoring Instrument (OMI) tropospheric vertical columns (data product v2.1) in two ways: (1) Median data were compared for the whole time period for selected boxes, and the agreement was found to be fair ($R = 0.97$, slope = 1.4 ± 0.1, $N= 10$). (2) A comparison was performed on the mean of coincident AMAX-DOAS measurements within the area of the corresponding OMI pixels with the tropospheric NASA OMI NO_2 assigned to that pixel. The effects of different data filters were assessed. Excellent agreement and a strong correlation ($R = 0.85$, slope = 1.05 ± 0.09, $N= 56$) was found for (2) when the data were filtered to eliminate large pixels near the edge of the OMI orbit, the cloud radiance fraction was <50%, the OMI overpass occurred within 2 h of the AMAX-DOAS measurements, the flight altitude was >2 km, and a representative sample of the satellite footprint was probed by the AMAX-DOAS instrument. The AMAX-DOAS and OMI data sets both show a reduction of NO_2 tropospheric columns on weekends by $38 \pm 24\%$ and $33 \pm 11\%$, respectively. The assumptions in the tropospheric satellite air mass factor simulations were tested using independent measurements of surface albedo, aerosol extinction, and NO_2 profiles over Los Angeles during July 2010, indicating an uncertainty of 12%.

Conclusions:

- The uncertainty of the NASA OMI tropAMF is estimated to be 12% for summer over the Los Angeles area. Notably, the area probed is characterized by a rather high surface albedo (here 10% at 479 nm) and low AOD. Our results indicate that a generalization of the satellite uncertainty over areas with a different surface albedo may not be straightforward.
- Fair agreement was found for the temporally and spatially averaged data comparison. The application of successive selection criteria such as pixel number in OMI swath, cloud radiance fraction significantly improved the agreement. The removal of large OMI pixel from the comparison was found to be the main driver. Large OMI pixels at the side of the swath combined with the SCAB being surrounded by relatively unpolluted areas is the cause for this bias. Thus, it is very important to consider the size of the OMI pixel and representative sampling of individual pixels for comparison with satellite data.
- Sensitivity studies on the satellite AMF showed that the radiative transfer is rather independent of the range of aerosol load as encountered during the campaign, but highly dependent on the surface albedo and the trace gas a priori profile shape.

Airborne MAX-DOAS measurements over California: Testing the NASA OMI tropospheric NO_2 product

Hilke Oetjen,[1,5] Sunil Baidar,[1,2] Nickolay A. Krotkov,[3] Lok N. Lamsal,[3,4] Michael Lechner,[1,3] and Rainer Volkamer[1,2]

Received 1 November 2012; revised 13 May 2013; accepted 2 June 2013; published 10 July 2013.

[1] Airborne Multi-AXis Differential Optical Absorption Spectroscopy (AMAX-DOAS) measurements of NO_2 tropospheric vertical columns were performed over California for two months in summer 2010. The observations are compared to the NASA Ozone Monitoring Instrument (OMI) tropospheric vertical columns (data product v2.1) in two ways: (1) Median data were compared for the whole time period for selected boxes, and the agreement was found to be fair ($R = 0.97$, slope $= 1.4 \pm 0.1$, $N = 10$). (2) A comparison was performed on the mean of coincident AMAX-DOAS measurements within the area of the corresponding OMI pixels with the tropospheric NASA OMI NO_2 assigned to that pixel. The effects of different data filters were assessed. Excellent agreement and a strong correlation ($R = 0.85$, slope $= 1.05 \pm 0.09$, $N = 56$) was found for (2) when the data were filtered to eliminate large pixels near the edge of the OMI orbit, the cloud radiance fraction was $<50\%$, the OMI overpass occurred within 2 h of the AMAX-DOAS measurements, the flight altitude was >2 km, and a representative sample of the footprint was taken by the AMAX-DOAS instrument. The AMAX-DOAS and OMI data sets both show a reduction of NO_2 tropospheric columns on weekends by $38 \pm 24\%$ and $33 \pm 11\%$, respectively. The assumptions in the tropospheric satellite air mass factor simulations were tested using independent measurements of surface albedo, aerosol extinction, and NO_2 profiles for Los Angeles for July 2010 indicating an uncertainty of 12%.

Citation: Oetjen, H., S. Baidar, N. A. Krotkov, L. N. Lamsal, M. Lechner, and R. Volkamer (2013), Airborne MAX-DOAS measurements over California: Testing the NASA OMI tropospheric NO_2 product, *J. Geophys. Res. Atmos.*, *118*, 7400–7413, doi:10.1002/jgrd.50550.

1. Introduction

[2] Nitrogen dioxide (NO_2) is a regulated air pollutant, and monitoring is needed to assess the effects of reduction measures. Satellites provide the opportunity for global measurements of tropospheric vertical column densities (tropVCDs) on the basis of nadir measurements of ultraviolet (UV) and visible scattered sunlight. There is/was a number of satellite instruments available for measuring NO_2 tropVCDs starting in the mid-90s of the last century: GOME on ERS-2 [*Burrows et al.*, 1999], SCIAMACHY on ENVISAT [*Bovensmann et al.*, 1999], Ozone Monitoring Instrument (OMI) on AURA [*Levelt et al.*, 2006], and GOME-2 on MetOp-A [*Munro et al.*, 2006]. Although satellites today only have a relatively coarse resolution of ca. 10 to 100 s of kilometers and usually only provide a global picture every 1 – 6 days, those measurements are useful tools for trend analyses [e.g., *Richter et al.*, 2005; *Lamsal et al.*, 2011], to infer NO_x emissions by inverse modeling [e.g.,, *Miyazaki et al.*, 2012; *Lin*, 2012], as assimilation data for air quality forecasting [e.g., *Wang et al.*, 2011; *Petritoli et al.*, 2011], and to deduce NO_2 surface concentrations [e.g., *Lamsal et al.*, 2008; *Lee et al.*, 2011]. However, tropVCDs from different research groups do not always agree [e.g., *Lamsal et al.*, 2010; *Bucsela et al.*, 2008; *Boersma et al.*, 2008]. Differences result mainly from differences in the assumptions in the radiative transfer calculation and in the way the stratospheric NO_2 is removed from the total column density. The uncertainty of satellite retrievals for polluted environments is dominated by the uncertainty in the radiative transfer calculations and originates from the necessary assumptions made to describe the surface albedo, the NO_2 and aerosol extinction a priori profile shapes as well as insufficient information about clouds [*Boersma et al.*, 2004; *Richter and Burrows*, 2002]. Therefore, regular validation

Additional supporting information may be found in the online version of this article.

[1]Department of Chemistry and Biochemistry, University of Boulder, Boulder, Colorado, USA.
[2]Cooperative Institute for Research in Environmental Sciences, University of Boulder, Boulder, Colorado, USA.
[3]NASA Goddard Space Flight Center, Greenbelt, Maryland, USA.
[4]Goddard Earth Sciences Technology and Research, Universities Space Research Association, Columbia, Maryland, USA.
[5]Now at the UCLA/JPL Joint Institute for Regional Earth System Science and Engineering, Los Angeles, California, USA.

Corresponding author: R. Volkamer, Department of Chemistry and Biochemistry, University of Colorado Boulder, Boulder, CO 80309, USA. (rainer.volkamer@colorado.edu)

2169-897X/13/10.1002/jgrd.50550

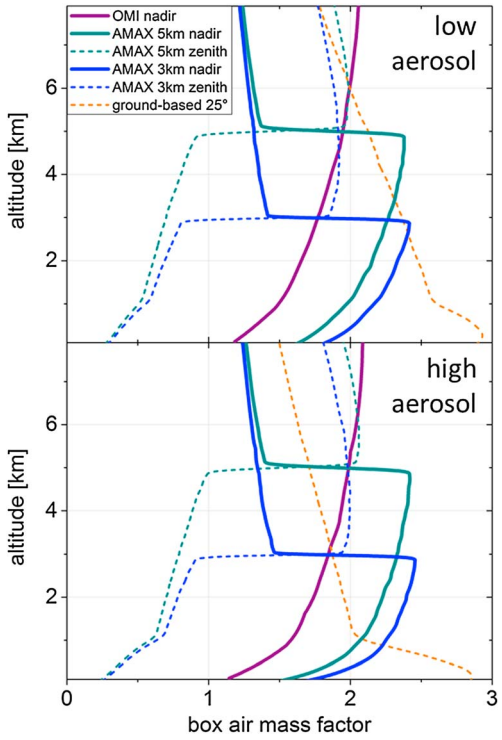

Figure 1. BAMFs for satellite and aircraft geometries for a SZA of 17° (time of OMI/AURA overpass over North America). Aircraft BAMF was calculated for aircraft altitudes of 3 km and 5 km. The BAMFs have been calculated for 435 nm for OMI and otherwise for 446 nm (center wavelengths of the NO_2 fitting windows). Aerosol optical depths are 0.2 and 0.5 and have a negligible effect on the nadir observations. The nonzero zenith BAMF below the aircraft highlights the need for choosing a reference spectrum with low trace gas concentration.

under a variety of conditions and also spanning the entire area of a satellite footprint is important.

[3] We present an NO_2 validation study using the University of Colorado Airborne Multi-Axis Differential Optical Absorption Spectroscopy (CU-AMAX-DOAS) instrument, which is optimized to obtain tropVCDs of trace gases as well as detailed profile information for trace gases and aerosol extinction when flying so-called low approaches [*Baidar et al*., 2013]. We recorded data in California from 19 May – 19 July 2010 flying on a NOAA Twin Otter aircraft (http://www.aoc.noaa.gov/aircraft_otter.htm) and compared the data to the NASA OMI tropospheric NO_2 product. The sampling area contained pollution hotspots like the Los Angeles Metropolitan Area as well as background conditions, e.g., over the High Desert. These measurements were part of the California Research at the Nexus of Air Quality and Climate Change (CalNex, campaign overview by *Ryerson et al.* [2013]) and Carbonaceous Aerosols and Radiative Effects Study (CARES, campaign overview by *Zaveri et al.* [2012]) campaigns. We also deployed a set of upward and downward pointing radiometers to measure surface albedo. Hence, the key parameters for the solar radiative transfer calculation, i.e., surface albedo, aerosol extinction profiles, and trace gas profiles, were measured quasi-simultaneously with the NO_2 tropVCD. Since the AMAX-DOAS instrument measures in a similar wavelength range as the UV/visible satellite spectrometers, the same absorbers can be retrieved which makes this technique applicable to the validation of other species as well, e.g., glyoxal or formaldehyde.

[4] Satellite instruments and the CU-AMAX-DOAS instrument measure with a similar viewing geometry, i.e., nadir or near nadir. Hence, they exhibit similar vertical sensitivities. Figure 1 compares box air mass factors (BAMFs; BAMFs are equivalent to weighting functions for optically thin absorbers, and they express the average light path enhancement with respect to the vertical thickness of a layer) for a typical scenario during CalNex/CARES at the solar zenith angle (SZA) of the OMI overpass. AMAX-DOAS measurements are on average about 50 – 36% more sensitive than OMI to the lowest 1 km in the atmosphere for an aircraft altitude of 3 – 5 km, respectively, but the shapes of the BAMFs are very similar. The aerosol extinction in these examples is rather at the extremes: AERONET measurements at CalTech, Pasadena indicate a mean aerosol optical depth (AOD) of 0.19 ± 0.08 and a median AOD of 0.18 with 0.14 being the 25th percentile and 0.24 being the 75th percentile at 440 nm over the time period of 19 May – 19 July 2010. As can be seen from Figure 1, the differences in the BAMFS for the two different AODs are negligible for the nadir observations (compare top and bottom panel).

[5] Tropospheric NO_2 satellite validation has been performed with airborne or ground-based chemiluminescence NO_x analyzers, but also with airborne or ground-based remote-sensing instruments.

[6] When comparing ground-based concentrations with column densities measured from space, assumptions of the profile shape have to be made either by using models [*Petritoli et al*., 2004; *Ordóñez et al*., 2006; *Blond et al*., 2007; *Lamsal et al*., 2010] or mixing depth from climatologies [*Boersma et al*., 2009] or as done by *Schaub et al.* [2006], using NO_2 measurements from different altitudes in the Alps to construct a profile. The chemiluminescence NO_x analyzers applied in the above studies use a heated molybdenum oxide surface to reduce NO_2 to detectable NO. These analyzers are known to suffer from interferences: species such as nitric acid or peroxyacetyl nitrate also convert to NO [e.g., *Steinbacher et al*., 2007; *Dunlea et al*., 2007], and correction factors have to be applied [e.g., *Ordóñez et al*., 2006]. Discrepancies between the different measurements can partly be attributed to the nonrepresentativeness of point measurements [e.g., *Ordóñez et al*., 2006; *Schaub et al*., 2006; *Celarier et al*., 2008; *Boersma et al*., 2009]. Hence, ground-based in situ monitor validation is best performed for background sites [e.g., *Lamsal et al*., 2010]. Especially at urban hotspots, the traditional and localized ground-based validation attempt fails [e.g., *Lamsal et al*., 2010].

[7] In situ measurements of NO_2 on an aircraft make profile measurements possible when the altitude of the aircraft is changed. Usually, spiral flight patterns are performed for this. The concentrations can then be integrated to yield partial column densities. However, missing layers have to be interpolated and the layers above maximum flight altitude or below the minimum extrapolated to obtain a tropVCD to compare with satellite products [*Heland et al*., 2002; *Ladstätter-Weißenmayer et al*., 2003; *Martin et al*.,

2004; *Bucsela et al*., 2008; *Boersma et al*., 2008; *Hains et al*., 2010]. This approach is prone to introduce errors for the bottom layer where most of the NO_2 resides and an aircraft is not allowed to fly, at least not if not taking off or landing at an airport.

[8] Ground-based multi-axis (MAX) DOAS measurements have been used for comparison with satellites since those instruments not only provide tropVCDs, but also surface concentrations for comparison with NO_x analyzers [e.g., *Brinksma et al*., 2008]. Measurements usually agree within the limits of the uncertainties. But the quality of agreement is variable depending on satellite product, but also season and location. MAX-DOAS tropVCDs at highly polluted areas seem to indicate that also those measurements, similar to the ground-based in situ sensors, are more sensitive to local emissions and yield higher columns than the satellite (Figure 1) [e.g., *Irie et al*., 2008; *Brinksma et al*., 2008; *Ma et al*., 2013; *Irie et al*., 2012]. Other remote-sensing ground-based techniques that have been used for satellite validation include Lidar [*Volten et al*., 2009], zenith-sky DOAS measurements [*Petritoli et al*., 2004; *Chen et al*., 2009], and direct-sun DOAS [*Wenig et al*., 2008].

[9] Although airborne DOAS NO_2 measurements have been performed for several years [e.g., *Melamed et al.*, 2003; *Wang et al*., 2005; *Merlaud et al*., 2011], only in three studies, NO_2 tropVCDs were compared to satellite measurements but with very limited data from only one day of measurements each [*Heue et al*., 2005, 2008; *Bruns et al*., 2006; *Walter et al*., 2012]. Knowledge of the horizontal variability of tropVCDs can also be obtained by ground-based mobile MAX-DOAS, and those tropVCDs were compared to OMI but again only for a few days of measurements [*Wagner et al*., 2010; *Shaiganfar et al*., 2011].

[10] The advantages of using the CU-AMAX-DOAS measurements recorded during summer 2010 over California for NASA OMI NO_2 tropVCD validation are the vast amount of data collected over a time period of two months (overall 206 h) spanning an area covering Los Angeles and surroundings (and to a lesser extent Sacramento and surroundings).

2. Instrumentation and Measurements

[11] The CU-AMAX-DOAS measurements used for this validation study were recorded during the CalNex and CARES campaigns, both took place in California in summer 2010. The CU-AMAX-DOAS instrument and albedo sensors were mounted to the NOAA Twin Otter remote-sensing aircraft which was based out of Ontario International Airport during CalNex from 19 May – 15 June and 30 June – 19 July and for a shorter time period (16 – 29 June), McClellan Airport in Sacramento during CARES. The majority of the measurements were performed over the Greater Los Angeles Area and its relatively unpolluted surroundings. Hence, measurements of the study presented here provide a large range of NO_x conditions from background to highly polluted.

2.1. CU-AMAX-DOAS Instrument and NO_2 tropVCD Retrievals

[12] The instrument and its performance during CalNex and CARES are described in detail in *Baidar et al*. [2013]. Briefly, a telescope pylon is window-plate-mounted pointing parallel to the flight direction. A motor-mounted prism in the telescope permits scanning in forward, upward, and downward directions under discrete elevation angles with a field of view (FOV) of $0.3° \times 5.9°$. Independently of the movement of the aircraft, the angle is held constant with respect to horizontal by means of an angle sensor coupled to a motor adjusted with controller times of ~20 Hz and an overall 1 sigma angle accuracy of 0.35°. The collected light is transmitted by a split glass fiber bundle into two temperature-stabilized spectrometer/CCD detector systems. In this study, spectra only from one of the systems are used with a wavelength range of 330 – 470 nm and a resolution of 0.7 nm full-width half-maximum (FWHM). The spectra are analyzed with the well-known DOAS technique [e.g., *Platt and Stutz*, 2008]. Here, the WinDOAS software [*Fayt and Van Roozendael*, 2001] was used to retrieve NO_2 slant column densities (SCDs) in a wavelength range from 433 to 460 nm applying two NO_2 absorption cross sections at 220 K and 294 K [*Vandaele et al*., 2002], and further including cross sections for the oxygen dimer [*Greenblatt et al*., 1990], ozone [*Bogumil et al*., 2001], glyoxal [*Volkamer et al*. 2005], and water vapor [*Rothman et al*., 2005]. A ring cross section was calculated with the MFC software [*Gomer et al*., 1993] from the zenith reference spectrum and taken into account as a pseudo-absorber in the DOAS fit. A polynomial of the order of three was used and a straylight correction (see *Fayt and Van Roozendael*, 2001) applied. All spectra of one flight were analyzed in comparison to one common zenith reference spectrum recorded during that particular flight in a clean environment and flying at relatively high altitudes, i.e., ca. 3 – 5 km. The results are trace gas differential SCDs (dSCDs), i.e., the integrated absorber density along the average photon path from the sun to the telescope, and *differential* with regards to the amount of NO_2 present in the reference spectrum.

[13] In the following, only nadir and zenith spectra are investigated, for other geometries see *Baidar et al*. [2013]. Stratospheric NO_2 concentrations are relatively stable but undergo photochemical reactions resulting in a distinct diurnal pattern with higher NO_2 towards higher SZAs. In addition, the dSCDs also increase towards higher SZAs due to the longer light path through the stratosphere. Therefore, for some early or late measurements, fast changes in the stratospheric NO_2 over the course of a flight occurred. This change is a smooth function with time of day for a certain location. However, changing the location of the aircraft also changes the local SZA. A polynomial of the order of three was fitted through all the zenith dSCDs (the frequency for zenith measurements varied, but was up to every 30 s towards the latter half of the campaign, see also below) of such a flight with aircraft altitudes of 1800 m above sea level (ASL) or more. This polynomial was then subtracted from the nadir dSCDs which yields an effective tropospheric SCD (tropSCD). The polynomial approach was chosen instead of a linear interpolation of the zenith dSCDs in order to better account for slight variations in the possible residual tropospheric NO_2 originating from possible tropospheric NO_2 above the flight altitude as well as changes in stratospheric NO_2 due to the slight changes in the local SZA. This leads to a relatively high uncertainty of $0.5 – 2.0 \times 10^{15}$ molecule cm ^{2} in the stratospheric correction when the polynomial had to be

applied to the measurements. For many flights, the nadir dSCDs can be directly interpreted as a tropSCD assuming that the zenith reference spectrum, obtained at altitudes 3 km, only contains stratospheric NO_2 and that the change in stratospheric NO_2 is negligible during a 4 h flight. Of 41 flights, 18 indicated a changing stratospheric NO_2 load during parts of the flight, and those were corrected with a polynomial.

[14] The original or corrected tropSCD is then converted to a tropVCD with a geometric air mass factor (*geoAMF*):

$$tropVCD = \frac{tropSCD}{geoAMF} = \frac{tropSCD}{\sec SZA + 1} \quad (1)$$

[15] For this geoAMF, the assumption is made that the photons reach the telescope after being reflected from the Earth's surface in the nadir point. Hence, the slant column in comparison to the vertical column is weighted by the secant function of the SZA plus unity for the part of the lightpath from the nadir point into the telescope. The aircraft height and hence the integration height is implicitly included in this equation by applying the trigonometric function of a right-angled triangle. After extensive radiative transfer calculations simulating a range of possible scenarios for NO_2 mixing ratios and mixing heights, optical aerosol parameters, AOD, and surface albedo, the geometric approximation was found to be an adequate approximation and chosen here to be independent of climatology or model NO_2 profile data which would be needed as a priori in radiative transfer simulated AMFs. *Baidar et al*. [2013] have shown that this geometric conversion yields reliable results within 10% comparing with ground-based MAX-DOAS instruments. The error due to the use of geoAMF depends on the SZA and is accurate to within 6% for SZA $<20°$, 10% for SZA $<50°$, and 20% for SZA $<60°$ when compared to radiative transfer simulation performed with the McArtim code [*Deutschmann et al*., 2011] for the predominant conditions encountered during the CalNex/CARES campaigns [*Baidar et al*., 2013]. Most flights were conducted at SZA $<60°$. The uncertainty on the NO_2 cross section is ca. 5% depending on the temperature [*Vandaele et al*., 2002]. For the nadir dSCD, the 1 sigma DOAS fitting error is ca. 3% and the limit of detection ca. 3.2×10^{15} molecule cm ^{2} for 2 s integration time. In addition, the uncertainty in the geoAMF (see above) and the uncertainty of $0.5 - 2.0 \times 10^{15}$ molecule cm ^{2} in the stratospheric correction have to be taken into account. An overall estimate for the uncertainty of the tropVCD is 10 – 20% depending on the SZA. Please note that the overpass of the AURA satellite occurs at about 17° SZA over California and therefore at a time closest to the minimum uncertainty of the AMAX-DOAS measurements.

[16] The CU-AMAX-DOAS data acquisition software was improved over the course of the two months resulting in integration times of 2 s for the latter half of the campaigns. The scanning sequence when flying at altitudes above 2 km above ground level (AGL) included the angles 90°, 2°, 5°, 10°, 20°, 90°, 0°, 2°, 5°, 10°, and 20° (positive angles upward and negative downward), with a larger number of observations on the downward looking angles. Typically, nadir spectra were recorded every 12 – 15 s. With a typical aircraft speed of 65 m s ^{1}, this corresponds to a horizontal translation of about 900 m. The FOV of the telescope gives a nadir footprint of ~20 m across and ~550 m along the track while flying at 4 km altitude for 2 s integration times.

2.2. NASA OMI Instrument and NO_2 tropVCD Retrievals

[17] OMI flies on the NASA Aura satellite which was launched into a near-polar sun-synchronous orbit in 2004 [*Levelt et al*., 2006]. The crossing of the equator occurs at 13:45 local time. Two-dimensional CCD detectors span the wavelength range from 270 nm to 500 nm (FWHM 0.45 nm – 1.0 nm) in one dimension, and the other dimension is binned to monitor 60 different ground footprints perpendicular to the flight direction in a push broom manner. The width of the resulting swath is ca. 2600 km, and global coverage is obtained within one day. The size of the ground footprint varies across the swath from 13×24 km^2 at nadir to ~40×160 km^2 for the edge of the orbit due to the optical aberrations and asymmetric alignment. Due to the so-called row anomaly caused by partially blocked entrance optics, some of the 60 pixels have to be excluded in the further analysis.

[18] The NO_2 tropVCDs data product used here (v2.1) is the standard NASA OMI NO_2 product and is based on the algorithm described in *Bucsela et al*. [2013]. Briefly, the recorded spectra are analyzed with the DOAS method in a fitting window from 405 nm to 465 nm applying the *Vandaele et al*. [2002] NO_2 absorption cross section and a reference solar irradiance spectrum. The obtained SCDs are then corrected for instrumental artifacts. This is called destriping since the effect varies across the orbital track. To separate stratospheric and tropospheric components, application of stratospheric AMFs to destriped SCDs yield initial VCDs. Areas of tropospheric contamination in the stratospheric NO_2 field are identified using monthly mean tropospheric NO_2 columns from GMI simulations. Those regions are then masked, and the residual field of the stratospheric VCDs measured outside the masked regions is interpolated to estimate stratospheric NO_2 columns for each measurement. The stratospheric SCDs are subsequently subtracted from the original SCDs yielding the tropSCDs. The tropospheric AMFs (tropAMF) are calculated using a precomputed scattering-weight table from TOMRAD [*Davé*, 1965] and monthly mean NO_2 profiles from the GMI simulation. The algorithm uses OMI-based reflectivity [*Kleipool et al*., 2008], a cloud fraction and cloud pressure derived as described by *Acarreta et al*. [2004], temperature profiles from the GEOS-5 meteorological field, and the ETOPO5 topography. The tropopause height is obtained from GEOS-5 monthly tropopause pressures. The effects of aerosols on the OMI NO_2 retrieval is implicitly accounted for through the use of the OMI-derived surface reflectivity which is usually larger than the true surface reflectivity due to scattering from aerosols [*Torres et al*., 2007], and through the OMI cloud parameters [*Boersma et al*., 2011].

[19] The uncertainty in the SCDs is ca. 10^{15} molecule cm ^{2} which corresponds to about 10% of the total slant column for polluted regions, and the stratospheric corrections leads to an uncertainty of ca. 2×10^{14} molecule cm ^{2} [*Bucsela et al*., 2013]. Stratospheric AMFs have an

uncertainty of 1 – 2% and the tropAMF uncertainties range from ca. 20% for low cloud fraction to 30 – 80% for high cloud fraction, but are highly dependent on the NO_2 profile shape [*Wenig et al*., 2008; *Bucsela et al*., 2013]. The overall error on the tropVCD is <30% under clear-sky conditions and typical polluted conditions ($>1\times10^{15}$ molec cm ^{2}) [*Boersma et al*., 2009; *Hains et al*., 2010; *Irie et al*., 2012; *Bucsela et al*., 2013].

2.3. Albedo Sensor

[20] The University of Colorado albedo instrument consists of two four channel radiation sensors (Skye instruments SKR 1850) mounted to the top and the bottom of the NOAA Twin Otter research aircraft pointing straight upwards and downwards. Each of the four telescopes is equipped with a custom interference filter with ~10 nm wide transmission centered at 361 nm, 479 nm, 629 nm, and 868 nm. The sensors are fitted with a cosine correcting diffuser plate to measure irradiance from the hemispherical distribution. To ensure the upward and downward facing channel pairs at any given wavelength are directly comparable, a calibration factor for each channel was determined by simultaneous zenith measurement of solar radiation during a bright sunny day. 1 Hz data were recorded during all flights. The ratio of the normalized up-welling counts to the normalized down-welling counts is defined as the surface albedo. Atmospheric backscatter for higher flight altitudes was corrected as follows: Radiative transfer simulations show that outside the aerosol layer, up-welling and down-welling radiation is a linear function of sensor altitude. Surface albedo measurements from high altitude flights were corrected for the base altitude of 1100 m AGL which was assumed to be just outside the aerosol layer. After this correction, surface albedo measured during high altitude flights showed good agreement with low altitude flights (<1000 m, See Figure 7), which were conducted to minimize the need for atmospheric correction. During postprocessing, the 1 Hz radiation data from the two sensors were averaged for 30 s to maximize signal to noise. The overall uncertainty on the surface albedo is ±5%. The instantaneous footprint of hemispherical irradiance measurements is a circle with ~2.5 km radius, while flying at 2.5 km, which is smaller than the OMI pixel size (see section 2.2).

2.4. Flight Planning and Measurements

[21] The Twin Otter flight plan included usually a *morning* flight (ca. 10 – 14 h local Pacific Daytime Time) with emphasis on a combination of low approaches to obtain profile information and constant flight altitude at ca. 2 – 2.5 km AGL, just outside the boundary layer, followed by an *afternoon* flight (ca. 15 – 19 h) with a constant flight altitude of ~3.5 – 4 km AGL. Overall, we performed 51 research flights on 30 days over the two month period, but only 41 flights took place on the same days as OMI measurements. This is due to the row anomaly of this instrument (see section 2.2). Coordination with satellite overpasses was not the primary focus of the flight planning. Rather, the frequent OMI overpasses coupled with the large swath width of the OMI instrument result in a high number of flights that are suitable for satellite validation.

3. Satellite Validation

3.1. Comparison of All Data

[22] In a first step, tropVCDs are grouped to calculate the median values for specific regions over California covering the whole two months, i.e., individual measurements of the two observational platforms are not directly compared, but rather the respective medians of distributions within a specific region. The regions, as outlined by boxes in Figure 2, are chosen at locations with sufficient data points of AMAX-DOAS measurements. These mainly urban areas include the Greater Los Angeles Area (boxes 1 – 5), Bakersfield (boxes 6 – 7), and Sacramento (boxes 8 – 10). OMI tropVCDs are selected when the center of a pixel is located within a box on the same day a Twin Otter flight took place over this box. Days on which either data set is not available are excluded. There is no other temporal coincidence criterion applied resulting in possible time differences between the AMAX-DOAS measurements of up to 7 h before and 5 h after the satellite overpass. Figure 3 shows the medians split by region for the two instruments. Both data sets follow a similar trend: high NO_2 tropVCDs are observed over the Los Angeles Metropolitan Area (boxes 1 and 2) where many major motorways intersect. The Los Angeles International Airport (LAX) and the Port of Los Angeles are both situated in box 2. The Inland Empire also displays very high NO_2 (box 3). Lowest NO_2 is found west of Bakersfield (box 7). In general, the regions around Bakersfield and Sacramento are cleaner than the Greater Los Angeles Area. As expected, NO_2 amounts are closely related to population and transportation. The population of the Greater Los Angeles Area is 17,877,006 (2010 US census, http://2010.census.gov/2010census/data/). In comparison, the population of Sacramento is 466,488 and Bakersfield 347,483. In the so-called South Coast Air Basin (SCAB), a geopolitical area defined for the purpose of air quality management and delimited by the Pacific Ocean to the west and mountain ranges in all other directions, on-road motor vehicles and other mobile sources together account for 91% of the total NO_x emissions (Emission data for 2008 by California Air Resources Board: http://www.arb.ca.gov/app/emsinv/fcemssumcat2009.php).

[23] The satellite data are lower than the AMAX-DOAS measurements for enhanced NO_2, see boxes 1 and 3. This is also reflected in the slope of 1.4 ± 0.1 for the linear regression analysis of the two data sets (Figure 4, CU-AMAX-DOAS vs. NASA OMI, Pearson correlation coefficient $R=0.97$, offset $0.7\pm0.5\times10^{15}$ molecule cm ^{2}). If the data from boxes 1 and 3 are omitted, the slope is reduced to 0.9 ± 0.1 and hence insignificantly different from 1. The Pearson correlation coefficient is 0.96 and the offset $0.4\pm0.3\times10^{15}$ molecule cm ^{2}. Please note, the simple linear regression does not take the uncertainty of the individual data points into account, and these offsets are much smaller than the range of the 25th and 75th percentile of the data (see Figure 3) or the uncertainty of the stratospheric correction. The reason for the underestimation of the OMI data for enhanced NO_2 most likely originates from the selection criteria for the satellite pixels. As stated above, the center of the ground footprint has to be within the box. Furthermore, also pixels at the side of the OMI swath are included and those can be up to 160 km wide. This results in a bias to

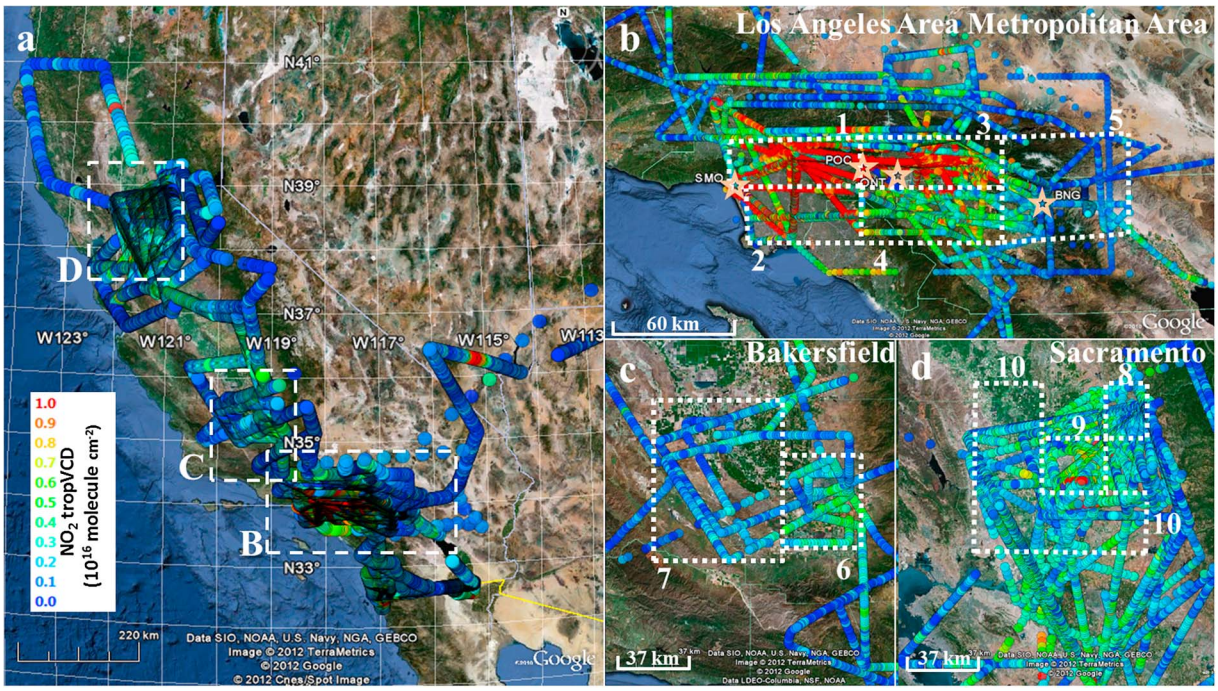

Figure 2. Overview of CU-AMAX-DOAS NO_2 tropVCDs over California 19 May – 19 July 2010. To show the variation in the background NO_2, the color scale was set to a range up to 1×10^{16} molecule cm ^{2}, but highest observed NO_2 was ~3×10^{16} molecule cm ^{2}. White dashed boxes in panel a mark the outlines of panels b–d. The dotted boxes (1–10) in b–d outline the areas for which the data were averaged for comparison with NASA OMI NO_2 averages as summarized in Figures 3 and 4. Stars in panel b mark the location of profiles as presented in Figure 8; from west to east: Santa Monica, Brackett, Ontario, and Banning airports.

background values since the actual area sampled by OMI included in the average will extend beyond the delimiters of the boxes by up to 80 km. Especially, the highly polluted boxes are surrounded by cleaner areas, e.g., box 3 is adjacent to the San Gabriel Mountains and the High Desert located to the north and west.

[24] Only for the Greater Los Angeles Area (boxes 1 – 5), statistics were good enough to separate the data into weekend and weekday measurements. A clear decrease can be observed (see Figure 3) which is caused by a reduction of heavy-duty diesel-fueled vehicles and is consistent with previous studies for California [e.g., *Marr and Harley*, 2002; *Chinkin et al.*, 2003; *Pollack et al.*, 2012 and references therein]: the NO_2 is lower by 38 ± 24% and 33 ± 11% for AMAX-DOAS and OMI, respectively. In the regression analysis (see Figure 4), the slope for the weekday data of 1.8 ± 0.3 is clearly larger than the 1:1-line, whereas the weekend regression with a slope of 1.1 ± 0.2 is consistent with a slope of unity. Both offsets are insignificantly different from zero. However, the two slopes are statistically different indicating as already mentioned above, the overestimation of the AMAX-DOAS data in comparison to the OMI measurements is nonlinear. The reason for this is the exponential increase of the satellite pixels towards the edge of the swath.

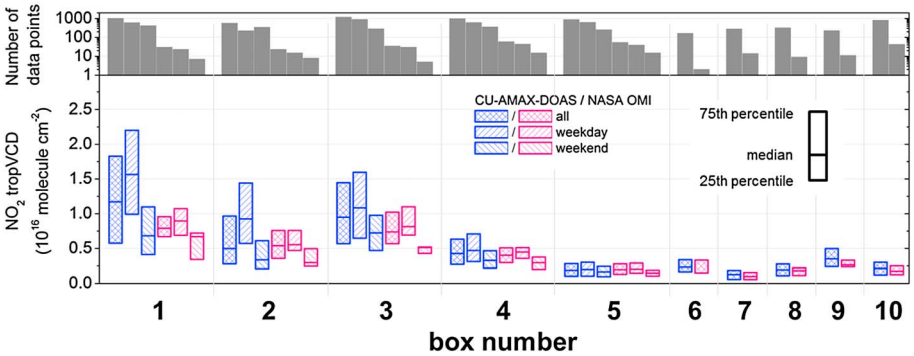

Figure 3. Comparison of NASA OMI and CU-AMAX-DOAS median tropVCDs. Data were averaged over two months and within the boxes 1–10 as indicated in Figures 2b–d. Boxes 1–5 are located over the Greater Los Angeles Area, 6–7 over Bakersfield, and 8–10 over Sacramento. A linear regression analysis was performed on the median of the data, and the results are shown in Figure 4.

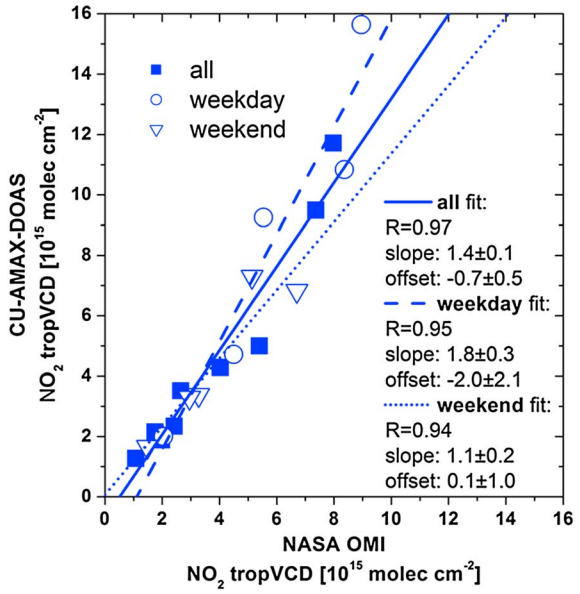

Figure 4. Linear regression analysis for data from Figure 3. The correlation coefficient R and the slopes and offsets are given in the legend. The offset has to be multiplied by [10^{15} molecule cm ^{2}].

3.2. Comparison Based on Individual OMI Pixels

[25] The large number of data points of the CU-AMAX-DOAS instrument allows for a validation of the NASA OMI data on a pixel level. Figure 5 shows an example flight on 1 June 2010 where the AMAX-DOAS tropVCDs are plotted on top of the gridded OMI data. The individual AMAX-DOAS measurements can be combined within the area of a satellite pixel to calculate a mean AMAX-DOAS NO_2 tropVCD which can then be compared to the specific OMI tropVCD. In order to identify the AMAX-DOAS data points within that area that is given by the four corner points of the OMI pixel, the so-called point-in-polygon problem was approached with a ray-casting algorithm. The flight presented in Figure 5 is from earlier in the campaign where the detector exposure times were 20 s. Nevertheless, there are up to four AMAX-DOAS measurements per OMI pixel.

[26] Several factors can affect the quality of the comparison exercise. In the following, we discuss five key parameters: (1) Since the NO_2 lifetime is in the range of a few hours and also transport can take place, the time difference between the measurements is very important. (2) Although most sources of NO_2 are close to the surface, our vertical profile measurements during this campaign have shown that the NO_2 can be mixed in the BL up to ca. 2 km [*Baidar et al.*, 2013] and hence the aircraft altitude determines the fraction of the NO_2 tropospheric column sampled by the AMAX-DOAS. (3) As was observed above, the quality of the comparison suffers when the large pixels at the sides of the swath are included, and hence this parameter is tested here as well. (4) Obviously, the cloud radiance fraction determines how representative the measured OMI column is for the whole pixel. In general, the cloud radiance fraction during the campaign was rather low though.

[27] (5) Further, we define a quantity we call the normalized distance to assess the representativeness of the AMAX-DOAS measurements within a pixel with respect to the sampled area. The OMI pixels are divided into similarly sized subgrid cells with a side length of ~7.5 km each resulting in 3×2 to 20×4 dimensional subgrids. This variation is due to the increasing footprint of the OMI measurements from the middle to the side of the swath. In a first step, it is checked whether the above defined subgrid cells contain any data points. Matrices with the dimension of the subgrid are defined for each of these individual cells.

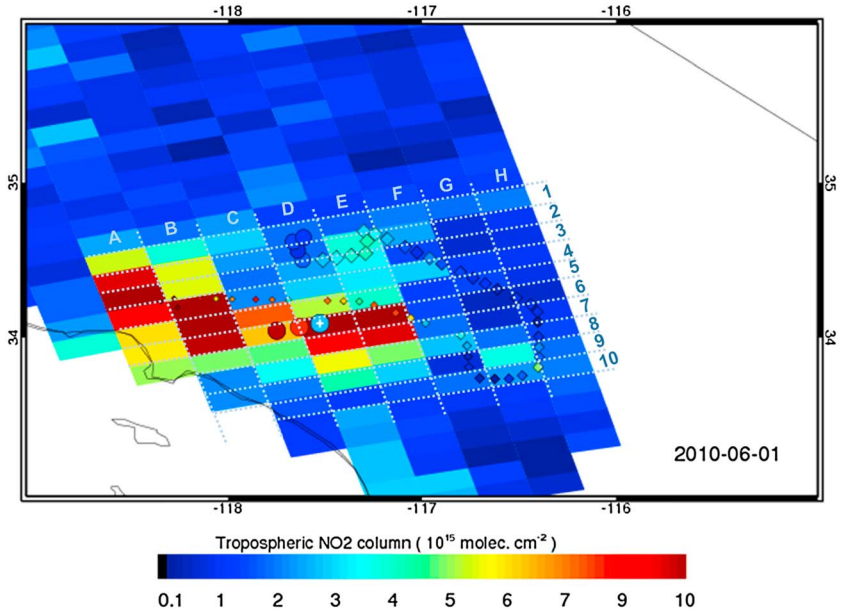

Figure 5. CU-AMAX-DOAS NO_2 vertical columns plotted on top of a NO_2 NASA OMI swath for a selected flight on 1 June 2010. The white plus indicates the AMAX-DOAS measurement recorded at the time of the OMI measurement, circles indicate a time difference <30 min, diamonds >30 min, and the size of the symbols is inversely proportional to the time difference.

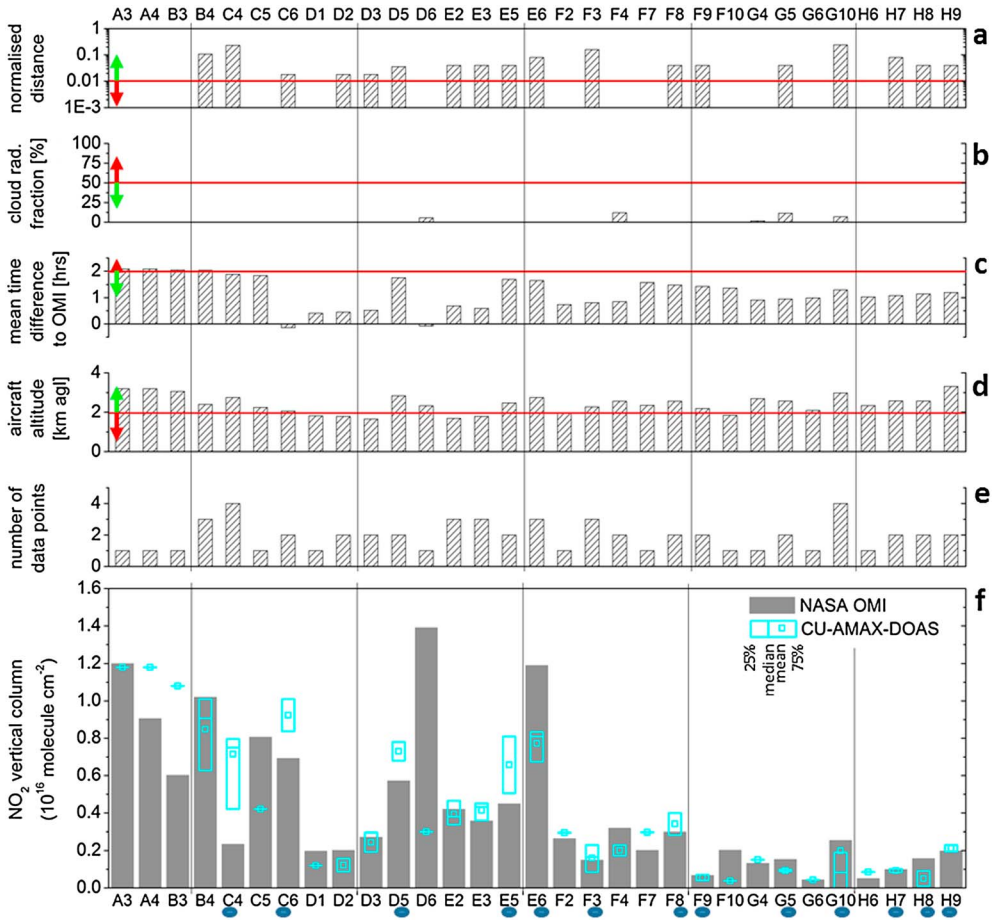

Figure 6. Panel f summarizes the data from Figure 5. The letter and number combination of the x-axis indicates the location of the individual OMI pixel in the grid of Figure 5. Panel a: normalized distance (see text and Figure A1), panel b: cloud radiance fraction of the OMI measurement, panel c: mean time difference between the AMAX-DOAS and the OMI measurement, panel d: Twin Otter altitude, panel e: number of individual AMAX-DOAS data points that were in the average of panel f. The red lines and associated arrows (green: good, red: less optimal) indicate chosen thresholds for the selection criteria, and the blue dots below panel f mark the good data points based on the selection criterion which contributed to the regression analysis shown in Table 2.

The step distance between occupied subgrid cells are assigned as the matrix elements for the individual occupied cell matrix. For example, the distance between adjacent occupied cells is 1, between diagonally adjacent occupied cells 2, a knight's move distance is 3, etc. These individual elements are summed up and divided by the value of the best case scenario, i.e., every subgrid cell contains at least one data point. Consequently, the normalized distance is a number between 0 and 1 and an approximate measure for the distribution of the AMAX-DOAS data points within an OMI pixel. How to obtain the normalized distance is sketched in Figure A1 for an example of three occupied cells of a 3×2 subgrid. This normalized distance is less dependent on the actual number of data points which varied during the campaign due to different integration times.

[28] The data for the example flight of Figure 5 are summarized in Figure 6f with each spatially coincident measurement identified by a letter and number coordinate as defined in Figure 5. Figures 6a – e show the key parameters as described above: The normalized distance of the AMAX-DOAS data points (Figure 6a), the OMI cloud radiation fraction (Figure 6b), the mean time difference between the AMAX-DOAS measurements and the OMI measurement (Figure 6c), the aircraft altitude (Figure 6d), and the number of AMAX-DOAS data points (Figure 6e). During this example flight, the included data points are from the OMI pixel numbers 18 to 24 (with 30 and 31 being the center of the orbit) within the OMI swath. With a combination of selection criteria as indicated by the horizontal red lines in Figures 6a – d (normalized distance >0.01, cloud radiance fraction $<50\%$, OMI overpass within ± 2 h, flight altitude >2 km), the initial 31 data points are reduced to 13 as indicated by the blue marks below panel f. The resulting slope of the linear correlation is 0.8 ± 0.2, with a moderately strong correlation coefficient of $R = 0.78$ and an offset of $1.1 \pm 0.9 \times 10^{15}$ molecule cm ^{2}. Please note the uncertainties of the measurements are neglected in the regression since the uncertainty for each individual data point is unknown (see sections 2.1 and 2.2). This and all following regression results are based on the AMAX-DOAS data acting as ordinate and the OMI data as abscissa in the Cartesian coordinate system.

Table 1. Regression Analysis for All Data on the Pixel Level[a]

Scenario[b]	Slope	Offset [10^{15} molec/cm^2]	N OMI Pixels (AMAX-DOAS Data Points)	R	Standard Deviation of Fit[d] [10^{15} molec/cm^2]
All data	1.12 ± 0.04	0.67 ± 0.13	1016 (34,058)	0.69	2.9
Pixels[c]:					
6–55	1.07 ± 0.04	0.25 ± 0.14	546 (10,555)	0.78	2.4
11–50	1.04 ± 0.04	0.35 ± 0.19	363 (5300)	0.78	2.6
16–45	1.06 ± 0.05	0.37 ± 0.20	284 (3507)	0.79	2.5
Normalized distance:					
>0.01	1.17 ± 0.04	0.36 ± 0.15	602 (28,559)	0.78	2.5
>0.05	1.21 ± 0.05	0.23 ± 0.24	312 (20,649)	0.80	2.8
>0.1	1.30 ± 0.08	0.09 ± 0.35	187 (14,756)	0.79	3.0
Cloud radiance fraction:					
<50%	1.14 ± 0.04	0.51 ± 0.14	908 (32,153)	0.70	2.8
<30%	1.14 ± 0.04	0.51 ± 0.11	848 (28,135)	0.70	2.8
OMI overpass:					
±2 h	1.18 ± 0.07	0.69 ± 0.23	382 (12,607)	0.66	3.1
±1 h	1.30 ± 0.12	0.23 ± 0.36	131 (3248)	0.69	2.8
Flight altitude:					
>2 km	1.05 ± 0.04	0.58 ± 0.13	830 (27,994)	0.69	2.5
>3 km	1.12 ± 0.06	0.31 ± 0.20	391 (12,208)	0.72	2.8
>4 km	1.39 ± 0.08	0.27 ± 0.26	126 (4177)	0.84	2.0

[a]AMAX-DOAS data acting as ordinate and the OMI data as abscissa in a Cartesian coordinate system.
[b]See section 3 for details.
[c]Numbers refer to the pixel number in the OMI swath.
[d]The standard deviation of the fit = $\sqrt{\frac{1}{N-1}\sum_i [y_i - (Bx_i + A)]^2}$ with N being the number of measurements, x_i and y_i the measurements themselves, and A and B the intercept and slope of the regression, respectively.

[29] In the following, this kind of regression analysis is applied to all of the available data. As before, the initial selection criterion is that the NASA OMI and the CU-AMAX-DOAS measurements were performed on the same day. This results in 1016 individual OMI measurements being initially included in the comparison and 34,058 colocated AMAX-DOAS measurements for the two months of the measurement period. For the comparison of the two data sets,

Table 2. Regression Analysis Results for All Data on the Pixel Level for a Combination of the *Best-Off*-Scenarios Based on Table 1[a]

Scenario[b]	Slope	Offset [10^{15} molec/cm^2]	N OMI Pixel (AMAX-DOAS Points)	R	Standard Deviation of Fit[d] [10^{15} molec/cm^2]
All data	1.12 ± 0.04	0.67 ± 0.13	1016 (34,058)	0.69	2.9
Pixels 11–50[c]	1.04 ± 0.04	0.35 ± 0.19	363 (5300)	0.78	2.6
Pixels 11–50[c] + Norm. distance >0.01	1.03 ± 0.04	0.35 ± 0.16	282 (5021)	0.86	2.0
Pixels 11–50[c] + Norm. distance >0.01 + Cloud rad. fraction <50%	1.01 ± 0.04	0.30 ± 0.17	252 (4671)	0.86	2.0
Pixels 11–50[c] + Norm. distance >0.01 + Cloud rad. fraction <50% + OMI overpass ± 2 h	1.06 ± 0.08	0.20 ± 0.37	81 (1220)	0.82	2.3
Pixels 11–50[c] + Norm. distance >0.01 + Cloud rad. fraction <50% + OMI overpass ± 2 h + Flight altitude >2 km	1.03 ± 0.09	0.14 ± 0.43	56 (632)	0.85	2.3

[a]AMAX-DOAS data acting as ordinate and the OMI data as abscissa in a Cartesian coordinate system.
[b]See section 3 for details.
[c]Numbers refer to the pixel number in the OMI swath.
[d]The standard deviation of the fit = $\sqrt{\frac{1}{N-1}\sum_i [y_i - (Bx_i + A)]^2}$ with N being the number of measurements, x_i and y_i the measurements themselves, and A and B the intercept and slope of the regression, respectively.

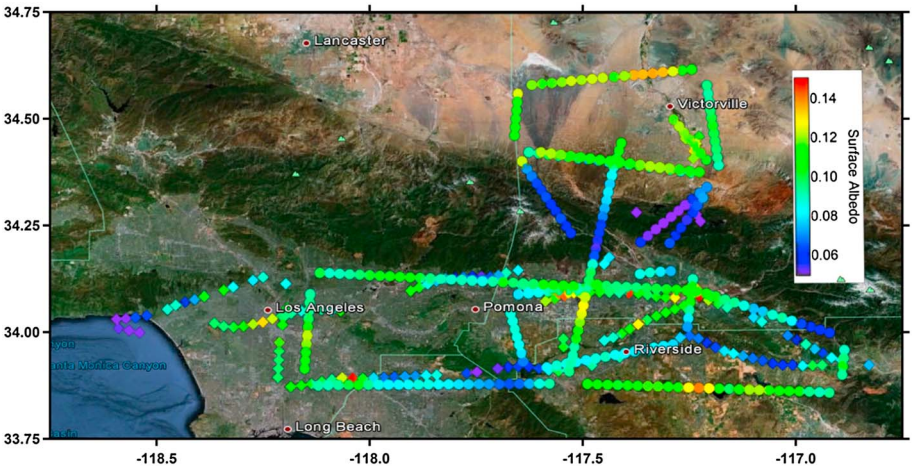

Figure 7. Surface albedo at 479 nm as measured by the radiometers on board the NOAA Twin Otter on 31 May 2010 (symbol: diamonds) and 12 July 2010 (symbol: discs) in the Los Angeles region.

the AMAX-DOAS measurements are first averaged within the subgrid cells as defined for the calculation of the normalized distance, and the resulting mean values are then again averaged. This two-step calculation of the mean is done to avoid any weighting towards heavily sampled areas of the OMI pixel. Table 1 shows the results for the linear regression analysis for the averaged AMAX-DOAS measurements compared to the OMI data and how the results change when constraining the above described key parameters.

[30] In general, the correlation coefficient increases with more stringent limits and so does the slope up to values significantly higher than 1 (see Table 1), i.e., the AMAX-DOAS measurements are higher than the NASA OMI ones (by up to 39 ± 8%). The only exception to the increase of the slope with stricter coincidence criteria is when removing the large OMI pixels at the sides of the swaths from the comparison; then the slope actually decreases (although not significantly within the uncertainty range). The offset does not seem to follow a certain pattern, but is mostly positive. However, the numbers are smaller than the uncertainty on the stratospheric correction of $0.5 - 2 \times 10^{15}$ molecule cm ^{2} for the CU-AMAX-DOAS measurements and 0.2×10^{15} molecule cm ^{2} for the NASA OMI. This somewhat surprising trend in the slope can be explained when viewed in relation to the results described in the following exercise.

[31] Table 2 and Figure A2 summarize the effect of successively applying the weakest selection criteria to the full data set of the initial 1016 OMI pixels again. The weakest criteria were chosen to leave sufficient data points for good statistics. After removing the sides of the swath, adding any other limitation results in a strong correlation of $R \geq 0.82$ and does not change the slope significantly from 1. In the end, for the remaining pixels, the agreement is excellent, and the concluding slope is 1.03 ± 0.09. After removing the large pixels of the side of the swath, constraining the normalized distance decreases the standard deviation of the fit and increases the correlation coefficient showing that the normalized distance is indeed an important factor. Limiting the cloud radiance fraction only results in negligible effects since the pixels had more or less already a very low cloud fraction to start with. Reducing the difference in the OMI overpass time to ±2 h within the AMAX-DOAS measurements removed many of the data points, and the results are not very conclusive anymore. The standard deviation of the fit as well as the uncertainty on the slope significantly increased. The consecutive removal of measurements with an aircraft altitude <2 km does not change the picture anymore which suggests that most of the NO_2 is below 1.8 km, the initial selection criterion.

[32] As mentioned above, these results seem to be in contrast to Table 1 where the individual limiting criteria mostly increased the slope, i.e., the AMAX-DOAS data seem to overestimate the NO_2 in comparison to the OMI pixel. This previous regression analysis was performed including all pixels of the OMI swath. The area of the footprint of a nadir AMAX-DOAS pixel is 0.011 km^2 when flying at 4 km altitude and integrating for 2 s (see section 2.1 last paragraph). This is relatively small in comparison to the OMI footprint area of 312–6400 km^2. This indicates that in combination with the small FOV of the AMAX-DOAS instrument, the NOAA Twin Otter is not fast enough to

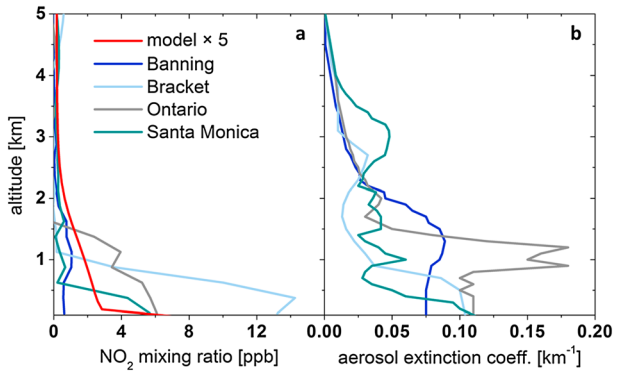

Figure 8. Profiles for NO_2 (panel a) and the aerosol extinction coefficient at 477 nm (panel b) as derived from CU-AMAX-DOAS measurements on 16 July 2010 [*Baidar et al.*, 2013]. The locations of these profiles are marked in Figure 2b, and they span the SCAB in roughly east-west direction from the Banning mountain pass to the coast (Santa Monica Airport). The profiles were normalized to 0 m ASL. The red line shows the NO_2 GMI model profile for Los Angeles for July 2010 multiplied by factor 5.

Table 3. Satellite tropAMF Sensitivity Studies for 17° SZA and 435 nm[a]

	NO_2 Profile									
Scenario	Banning	Model	Brackett	Model	Ontario	Model	Santa Monica	Model	**Ø[a] Measurements**	**Ø[a] Model**
Albedo 0.083, no aerosols	1.28	1.36[b]	1.21	1.36	1.12	1.36	1.10	1.36	**Ø[a] 1.18**	**1.36[b]**
Albedo 0.1, aerosol extinction from Figure 8b	1.38[c]	1.45	1.32[c]	1.46	1.33[c]	1.46	1.21[c]	1.45	**Ø[a] 1.31[c]**	**Ø[a] 1.46**
Albedo 0.1, no aerosols[d]	1.37	1.44	1.32	1.44	1.23	1.44	1.22	1.44	**Ø[a] 1.29**	**1.44**

[a]Ø: mean.
[b]tropAMF calculated with the same NO_2 profile and same settings for the aerosol/surface albedo parameterization as the actual OMI tropAMF calculations.
[c]tropAMF calculated using the Twin-Otter-measured average aerosol extinction, average NO_2 profiles (Figures 8a and 8b), and albedo.
[d]Scenario to illustrate that aerosols have only little influence.

representatively sample the large OMI pixels in a sufficiently short time interval. Since the flight tracks were mainly over polluted areas, the MAX-DOAS measurements are automatically biased to the enhanced NO_2. In order to verify this, even more satellite data are needed so that the regression presented in Table 1 could be amended to only include OMI data with pixel numbers of 6–55 or even 11–50. However, OMI pixels in the same swath and adjacent swaths are measured almost simultaneously. Hence, to improve on this validation technique, extended time periods of measurements, several aircrafts measuring simultaneously, a larger FOV of the AMAX-DOAS instrument, faster aircrafts, or a combination of the four is needed.

4. Sensitivity Studies on the Satellite AMF

[33] In this section, the assumptions of the satellite radiative transfer are tested with available auxiliary measurements of trace gas profiles, aerosol extinction profiles, and surface albedo. As can be seen from Figure 1, the sensitivity of the measurements towards the actual NO_2 profile changes with altitude. Hence, the *tropAMF* depends on the a priori trace gas profile:

$$tropAMF = \frac{\sum_i BAMF_i \quad VCD_i^{a\ priori}}{tropVCD^{a\ priori}} \tag{2}$$

with $BAMF_i$ and $VCD_i^{a\ priori}$ being the BAMF and the trace gas a priori partial vertical column of the layer i and $tropVCD^{a\ priori}$ the integrated a priori profile. The summation is performed from the surface to the tropopause for discrete layers. If the true profile is different from the a priori profile, this can introduce significant errors in the tropVCD retrieved with this tropAMF.

[34] As mentioned above, the satellite retrieval uncertainty is dominated by the uncertainty in the tropAMF calculation and there the most important parameters are trace gas concentration profile and surface albedo [*Boersma et al*., 2004; *Richter and Burrows*, 2002]. By using independent profile observations measured by the AMAX-DOAS instrument while flying low approaches over airports [see *Baidar et al*., 2013] as well as surface albedo by the radiometers, sensitivity studies were performed to test the assumptions made in the NASA OMI retrievals. As mentioned above, the radiative transfer calculation of the OMI retrievals parameterizes the aerosol load in the atmosphere in combination with the surface albedo by applying the so-called effective albedo calculated from the measurement itself. Here, a case was chosen for an OMI nadir pixel for Los Angeles for July 2010 which was deemed as relatively low cloud by the OMI retrieval algorithm having an effective albedo of 0.083. The corresponding NO_2 profile is given in Figure 8a and was obtained from the GSFC GMI CTM model. The resulting tropAMF is 1.41 at 435 nm.

[35] Figure 7 shows the surface albedo as measured from the Twin Otter in summer 2010 over the Greater Los Angeles Area, parts of the High Desert and over the San Bernardino Mountains. Mostly, the surface albedo is around 0.10 ± 0.02. Only over some of the mountain ranges and the Pacific Ocean, the surface albedo is lower: ca. 0.03 – 0.07. Figures 8a and 8b show the NO_2 and the 477 nm aerosol extinction profiles measured during four low approaches over the Greater Los Angeles Area (location marked in Figure 2b) on 16 July 2010. Both shape and absolute values of the trace gas profiles differ significantly from the model profile.

[36] Here, tropAMFs are calculated for the OMI nadir viewing geometry at a SZA of 17° for a clear-sky scenario. Simulations are performed for the five different NO_2 profiles from Figure 8a. The McArtim code is employed because aerosol extinction can be treated explicitly. The aerosol optical properties were chosen as 0.94 for the single scattering albedo, typical for wavelengths >400 nm, and 0.68 as asymmetry parameter, typical for polluted environments. These are the setting used for retrieving the NO_2 and aerosol profiles shown in Figure 8 using the same radiative transfer model McArtim. The aerosol extinction profiles corresponding to the NO_2 profiles at the four different locations are applied (see Figure 8b). Calculations were also performed for a Rayleigh atmosphere with 0.083 (corresponds to the effective albedo) and 0.1 surface albedo. Profiles for pressure, temperature, and ozone were taken from the US standard atmosphere to be consistent with what was used during the profile retrievals [*Baidar et al*., 2013]. However, using the GEOS-5 meteorological field (which drives the GMI model) pressure and temperature profiles increases the tropAMFs by ~1 – 2%. The tropAMF obtained by mimicking the OMI retrievals by using the albedo settings (i.e., effective albedo of 0.083 and no aerosols) and the NO_2 model profile results in a tropAMF of 1.36 which is within 4% of the actual OMI tropAMF applied to the measured slant columns. The aim of these radiative transfer calculation comparisons is not to reproduce the exact OMI tropAMF, but rather to study the differences to the standard scenario, i.e., 1.36 tropAMF in order to identify the main contributors as well as obtaining an estimate for the satellite tropAMF uncertainty.

[37] Table 3 summarizes the results for the different scenarios. On average, the GMI model profile results in a larger tropAMF in comparison to the measured NO_2 profile

tropAMF by 11–15%. An increase in the surface albedo of 20% results in an average tropAMF increase of 9% for the measured profiles. When using the GMI model profile in combination with the different measured aerosol extinction profiles, the tropAMF changes by ≲1%. The weak dependence of the satellite (but also the AMAX-DOAS) tropAMF on the aerosol extinction profile was already explained in the introduction. Using a combination of the Twin Otter measurements for surface albedo, aerosol extinction profile, and NO_2 profile and giving equal weights to the four individual profile combinations yields on average a tropAMF of 1.31. This value is about 4% lower than the tropAMF of 1.36 using the OMI settings, i.e., an effective albedo of 0.083 in combination with a Rayleigh atmosphere, and the model NO_2 profile. Looking at the individual measured profiles, the maximum deviation is for the coastal profile at Santa Monica with 12%. It is worth noting that this value of 12% is smaller than the differences caused by only using the different NO_2 profiles, i.e., up to 15%. Applying the measured effective albedo seems to partly offset the nonideal choice of the model trace gas profile.

[38] In summary, the NASA OMI tropAMF for the Los Angeles area for July 2010 is only as good as the estimate for the albedo and especially the trace gas profile. Considering the assumptions in the simulations and the range of values, a tripling of the average difference seems to be appropriate to estimate the satellite tropAMF uncertainty for the Los Angeles area for the summer to be 12%. This is much better than the estimate described in section 2.2 for OMI retrievals in general (ca. 20% for low cloud fraction, 30 – 80% for high cloud fraction [*Wenig et al*., 2008; *Bucsela et al*., 2013]), but is consistent with the results of the linear regression study in the previous section.

5. Additional Error Sources

[39] Error sources in the OMI and the AMAX-DOAS data products which have not been discussed so far in this manuscript are the effect of the orography on the field in the RTM calculations, the temperature dependence in the NO_2 absorption cross section, and the contribution to the NO_2 column from above the aircraft altitude: The radiative transfer models used in this study treat the atmosphere and the surface elevation as isotropic. However, the terrain height of the SCAB is highly variable. On the other hand, areas with highest NO_2 are usually not in the foothills of the surrounding mountains. Also, this effect should become significant only for large SZAs in combination with the position of the sun in the direction of a mountain range. Hence, the influence is most likely negligible, especially when investigating statistical ensembles of data. A detailed study is beyond the scope of this manuscript.

[40] The AMAX-DOAS analysis was performed with a combination of two NO_2 cross sections at 220 K and 294 K. When using only the cross section at 294 K in the analysis, the differences in those dSCDs to the dSCDs obtained with the combination of the two absorption cross sections are negligible. However, using the 220 K cross section yields 20% smaller dSCDs. This highlights the need for treating the temperature dependence of the NO_2 absorption cross section in the two retrievals in a similar way for a meaningful comparison. In the satellite algorithm, the temperature dependence of the cross section is treated explicitly by assimilating a temperature profile and calculating a correction factor for the cross section [*Bucsela et al*., 2013]. The average temperature in the lowest kilometer in the model profile for July over California is 295 K and therefore close to the value in the AMAX-DOAS retrievals.

[41] NO_2 can be produced in the free troposphere from lightning, but California was mainly cloud free during the campaign. However, the GMI model profile yields a partial column of 4×10^{14} molecule cm ^{2} from 5 km to the tropopause. This partial column above the aircraft is comparable to the offsets found in Table 1.

[42] The CU-AMAX-DOAS retrieval error is already low, but could possibly be improved for higher SZA by using optimal estimation to obtain a vertical column including observations from additional viewing angles. This will be examined in a follow-up research paper.

6. Summary and Conclusions

[43] In this paper we presented (1) a comparison of NASA OMI with CU-AMAX-DOAS NO_2 median tropVCDs over 2 months for defined areas and a comparison on an individual OMI pixel basis over California in summer 2010, and (2) sensitivity studies on the satellite AMF. The results can be summarized as follows:

[44] 1. Fair agreement was found for the temporally and spatially averaged data comparison (section 3.1). The slope between the tropVCDs of the two instruments is 1.4 ± 0.1 and the correlation coefficient 0.97. This is caused by a combination of large OMI pixels at the side of the swath and the SCAB being surrounded by relatively unpolluted areas. Therefore, large pixels should be excluded if the coincidence criterion is based on pixel center coordinates.

[45] 2. The mean AMAX-DOAS tropVCDs were calculated for coincident OMI pixels. A regression analysis was performed and the successive application of a combination of individual selection criteria to the data (i.e., pixel number in the OMI swath, normalized distance, cloud radiance fraction, satellite overpass time, and aircraft altitude) led to a strong correlation of 0.85 and a slope of 1.03 ± 0.09 in the end showing good agreement. The main driver seems to be the removal of the large pixels from the comparison. The AMAX-DOAS footprint area of ~0.011 km^2 is relatively small in comparison to the OMI footprint area of 312–6400 km^2. Optimizing the normalized distance is also important. The cloud radiance fraction and the aircraft altitude have only minor impacts on the results since the former is very low anyways over Los Angeles in summer and in the latter case since most of the tropospheric NO_2 seems to be confined below 1800 m.

[46] 3. The statistics of this validation technique can be improved by extending the time periods of measurements, coordinating several aircrafts at the same time, developing an AMAX-DOAS instrument with a larger FOV, deploying a faster aircraft or a combination of the four.

[47] 4. Sensitivity studies on the satellite AMF showed that the radiative transfer is rather independent of the range of aerosol load as encountered during the campaign, but highly dependent on the surface albedo and the trace gas a priori profile shape.

[48] 5. The uncertainty of the NASA OMI tropAMF is estimated to be 12% for summer over the Los Angeles area. Notably, the area probed is characterized by a rather high surface albedo (here 10% at 479 nm) and low AOD. A generalization of the satellite uncertainty over areas with a different surface albedo may not be straightforward.

[49] 6. The observed weekly cycle of the NO_2 is consistent with previous studies. A decrease of $38 \pm 24\%$ and $33 \pm 11\%$ for AMAX-DOAS and OMI measurements, respectively, is found for the weekend in comparison to weekdays. While the effects on ozone are not the subject of this study, we note that this decrease in NO_2 leads to higher ozone during weekends in June (consistent with *Pollack et al*. [2012], and references therein), but lower ozone during a hot weekend case in July [*Baidar et al*., 2012].

[50] The aircraft observations reported here were only partially intended for satellite validation. Purposeful validation, flying grids coincident in time and space with the satellite overpass, and adjustments to the actual AMAX-DOAS instrument could provide a more detailed data set. All this said, it can be concluded that (1) CU-AMAX-DOAS is well suited for satellite validation when the above precautions are taken into account, and the data collected over California are a valuable data set to validate other satellite instruments and (2) the NASA OMI tropospheric NO_2 product (v2.1) delivers high quality data for the Californian summer season.

[51] **Acknowledgments.** This study was supported by the California Air Resource Board contract 09-317, the National Science Foundation CAREER award ATM-847793, CU start-up funds (RV) and an ESRL-CIRES graduate fellowship (SB). We thank T. Deutschmann (University of Heidelberg, Germany) for providing McArtim, C. Fayt and M. v. Roozendael (IASB-BIRA, Belgium) for WinDOAS, S.-W. Kim, A. O. Langford, and C. J. Senff (NOAA, Boulder) for discussions, A. Schneider for the GPS visualizer (http://www.gpsvisualizer.com/), and the NOAA Twin Otter flight crew for their support during the campaigns. We acknowledge Jochen Stutz for providing AERONET data from the Caltech site.

References

Acarreta, J. R., J. F. de Haan, and P. Stammes (2004), Cloud pressure retrieval using the O_2-O_2 absorption band at 477 nm, *J. Geophys. Res.*, *109*, D05204, doi:10.1029/2003JD003915.

Baidar, S., H. Oetjen, C. Senff, R. Alvarez II, M. Hardesty, A. Langford, S.-W. Kim, M. Trainer, and R. Volkamer (2012), Observation of a reverse ozone weekend effect in the South Coast Air Basin (SoCAB) during summer 2010, Abstract A11F-0107 presented at 2012 Fall Meeting, AGU, San Francisco, Calif., 3-7 Dec.

Baidar, S., H. Oetjen, S. Coburn, B. Dix, I. Ortega, R. Sinreich, and R. Volkamer (2013), The CU Airborne MAX-DOAS instrument: Vertical profiling of aerosol extinction and trace gases, *Atmos. Meas. Tech.*, *6*, 719–739, doi:10.5194/amt-6-719-2013 .

Blond, N., K. F. Boersma, H. J. Eskes, R. J. van der A, M. Van Roozendael, I. De Smedt, G. Bergametti, and R. Vautard (2007), Intercomparison of SCIAMACHY nitrogen dioxide observations, in situ measurements and air quality modeling results over Western Europe, *J. Geophys. Res.*, *112*, D10311, doi:10.1029/2006jd007277.

Boersma, K. F., H. J. Eskes, and E. J. Brinksma (2004), Error analysis for tropospheric NO_2 retrieval from space, *J. Geophys. Res.*, *109*, D04311, doi:10.1029/2003jd003962.

Boersma, K. F., D. J. Jacob, H. J. Eskes, R. W. Pinder, J. Wang, and R. J. van der A (2008), Intercomparison of SCIAMACHY and OMI tropospheric NO(2) columns: Observing the diurnal evolution of chemistry and emissions from space, *J. Geophys. Res.*, *113*, D16S26, doi:10.1029/2007jd008816.

Boersma, K. F., D. J. Jacob, M. Trainic, Y. Rudich, I. DeSmedt, R. Dirksen, and H. J. Eskes (2009), Validation of urban NO_2 concentrations and their diurnal and seasonal variations observed from the SCIAMACHY and OMI sensors using in situ surface measurements in Israeli cities, *Atmos. Chem. Phys.*, *9*(12), 3867–3879, doi:10.5194/acp-9-3867-2009.

Boersma, K. F., et al. (2011), An improved tropospheric NO_2 column retrieval algorithm for the Ozone Monitoring Instrument, *Atmos. Meas. Tech.*, *4*, 1905–1928, doi:10.5194/amt-4-1905-2011.

Bogumil, K., J. Orphal, J. P. Burrows, and J. M. Flaud (2001), Vibrational progressions in the visible and near-ultraviolet absorption spectrum of ozone, *Chem. Phys. Lett.*, *349*(3–4), 241–248, doi:10.1016/s0009-2614(01)01191-5.

Bovensmann, H., J. P. Burrows, M. Buchwitz, J. Frerick, S. Noël, V. V. Rozanov, K. V. Chance, and A. P. H. Goede (1999), SCIAMACHY: Mission Objectives and Measurement Modes, *J. Atmos. Sci.*, *56*(2), 127–150, doi:10.1175/1520-0469(1999)056<0127:smoamm >2.0.co;2.

Brinksma, E. J., et al. (2008), The 2005 and 2006 DANDELIONS NO_2 and aerosol intercomparison campaigns, *J. Geophys. Res.*, *113*, D16S46, doi:10.1029/2007jd008808.

Bruns, M., S. A. Buehler, J. P. Burrows, A. Richter, A. Rozanov, P. Wang, K. P. Heue, U. Platt, I. Pundt, and T. Wagner (2006), NO_2 Profile retrieval using airborne multi axis UV-visible skylight absorption measurements over central Europe, *Atmos. Chem. Phys.*, *6*(10), 3049–3058, doi:10.5194/acp-6-3049-2006.

Bucsela, E. J., et al. (2008), Comparison of tropospheric NO_2 from in situ aircraft measurements with near-real-time and standard product data from OMI, *J. Geophys. Res.*, *113*, D16S31, doi:10.1029/2007jd008838.

Bucsela, E. J., et al. (2013), A new stratospheric and tropospheric NO_2 retrieval algorithm for nadir-viewing satellite instruments: application to OMI, *Atmos, Meas. Tech. Discuss.*, *6*(6), 1361–1407, doi:10.5194/amtd-6-1361-2013.

Burrows, J. P., et al. (1999), The global ozone monitoring experiment (GOME): Mission concept and first scientific results, *J. Atmos. Sci.*, *56*(2), 151–175, doi:10.1175/1520-0469(1999)056<0151:tgomeg>2.0.co;2.

Celarier, E. A., et al. (2008), Validation of ozone monitoring instrument nitrogen dioxide columns, *J. Geophys. Res.*, *113*, D15S15, doi:10.1029/2007JD008908.

Chen, D., B. Zhou, S. Beirle, L. M. Chen, and T. Wagner (2009), Tropospheric NO_2 column densities deduced from zenith-sky DOAS measurements in Shanghai, China, and their application to satellite validation, *Atmos. Chem. Phys.*, *9*, 3641–3662, doi:10.5194/acp-9-3641-2009.

Chinkin, L. R., D. L. Coe, T. H. Funk, H. R. Hafner, P. T. Roberts, P. A. Ryan, and D. R. Lawson (2003), Weekday versus weekend activity patterns for ozone precursor emissions in California's South Coast Air Basin, *J. Air Waste Manage. Assoc.*, *53*(7), 829–843, doi:10.1080/10473289.2003.10466223.

Davé, J. V. (1965), Multiple scattering in a non-homogeneous Rayleigh atmosphere, *J. Atmos. Sci.*, 22(3), 273–289, doi:10.1175/1520-0469(1965)022<0273:msianh>2.0.co;2.

Deutschmann, T., et al. (2011), The Monte Carlo atmospheric radiative transfer model McArtim: Introduction and validation of Jacobians and 3D features, *J. Quant. Spectrosc. Radiat. Transfer*, *112*(6), 1119–1137, doi:10.1016/j.jqsrt.2010.12.009.

Dunlea, E. J., et al. (2007), Evaluation of nitrogen dioxide chemiluminescence monitors in a polluted urban environment, *Atmos. Chem. Phys.*, *7*(10), 2691–2704, doi:10.5194/acp-7-2691-2007.

Fayt, C., and M. Van Roozendael (2001), WinDOAS 2.1: Software User Manual, http://bro.aeronomie.be/WinDOAS-SUM-210b.pdf.

Gomer, T., T. Brauers, F. Heintz, J. Stutz, and U. Platt (1993), MFC User Manual, Vers.1.98, Inst. für Umweltphys., Univ. Heidelberg, Heidelberg, Germany.

Greenblatt, G. D., J. J. Orlando, J. B. Burkholder, and A. R. Ravishankara (1990), Absorption measurements of oxygen between 330 and 1140 nm, *J. Geophys. Res.*, *95*(D11), 18,577–18,582, doi:10.1029/JD095iD11p18577.

Hains, J. C., et al. (2010), Testing and improving OMI DOMINO tropospheric NO_2 using observations from the DANDELIONS and INTEX-B validation campaigns, *J. Geophys. Res.*, *115*, D05301, doi:10.1029/2009JD012399.

Heland, J., H. Schlager, A. Richter, and J. P. Burrows (2002), First comparison of tropospheric NO_2 column densities retrieved from GOME measurements and in situ aircraft profile measurements, *Geophys. Res. Lett.*, *29*(20), 1983, doi:10.1029/2002GL015528.

Heue, K. P., A. Richter, M. Bruns, J. P. Burrows, C. v. Friedeburg, U. Platt, I. Pundt, P. Wang, and T. Wagner (2005), Validation of SCIAMACHY tropospheric NO_2-columns with AMAXDOAS measurements, *Atmos. Chem. Phys.*, *5*(4), 1039–1051, doi:10.5194/acp-5-1039-2005.

Heue, K. P., T. Wagner, S. P. Broccardo, D. Walter, S. J. Piketh, K. E. Ross, S. Beirle, and U. Platt (2008), Direct observation of two dimensional trace gas distributions with an airborne Imaging DOAS instrument, *Atmos. Chem. Phys.*, *8*(22), 6707–6717, doi:10.5194/acp-8-6707-2008.

Irie, H., Y. Kanaya, H. Akimoto, H. Tanimoto, Z. Wang, J. F. Gleason, and E. J. Bucsela (2008), Validation of OMI tropospheric NO_2 column data using MAX-DOAS measurements deep inside the North China Plain in June 2006: Mount Tai Experiment 2006, *Atmos. Chem. Phys.*, *8*(22), 6577–6586, doi:10.5194/acp-8-6577-2008.

Irie, H., K. F. Boersma, Y. Kanaya, H. Takashima, X. Pan, and Z. F. Wang (2012), Quantitative bias estimates for tropospheric NO_2 columns retrieved from SCIAMACHY, OMI, and GOME-2 using a common standard for East Asia, *Atmos. Meas. Tech.*, *5*, 2403–2411, doi:10.5194/amt-5-2403-2012.

Kleipool, Q. L., M. R. Dobber, J. F. de Haan, and P. F. Levelt (2008), Earth surface reflectance climatology from 3 years of OMI data, *J. Geophys. Res.*, *113*, D18308, doi:10.1029/2008JD010290.

Ladstätter-Weißenmayer, A., J. Heland, R. Kormann, R. von Kuhlmann, M. G. Lawrence, J. Meyer-Arnek, A. Richter, F. Wittrock, H. Ziereis, and J. P. Burrows (2003), Transport and build-up of tropospheric trace gases during the MINOS campaign: comparision of GOME, in situ aircraft measurements and MATCH-MPIC-data, *Atmos. Chem. Phys.*, *3*, 1887–1902, doi:10.5194/acp-3-1887-2003.

Lamsal, L. N., R. V. Martin, A. van Donkelaar, M. Steinbacher, E. A. Celarier, E. Bucsela, E. J. Dunlea, and J. P. Pinto (2008), Ground-level nitrogen dioxide concentrations inferred from the satellite-borne Ozone Monitoring Instrument, *J. Geophys. Res.*, *113*, D16308, doi:10.1029/2007JD009235.

Lamsal, L. N., R. V. Martin, A. van Donkelaar, E. A. Celarier, E. J. Bucsela, K. F. Boersma, R. Dirksen, C. Luo, and Y. Wang (2010), Indirect validation of tropospheric nitrogen dioxide retrieved from the OMI satellite instrument: Insight into the seasonal variation of nitrogen oxides at northern midlatitudes, *J. Geophys. Res.*, *115*, D05302, doi:10.1029/2009JD013351.

Lamsal, L. N., R. V. Martin, A. Padmanabhan, A. van Donkelaar, Q. Zhang, C. E. Sioris, K. Chance, T. P. Kurosu, and M. J. Newchurch (2011), Application of satellite observations for timely updates to global anthropogenic NO x emission inventories, *Geophys. Res. Lett.*, *38*, L05810, doi:10.1029/2010GL046476.

Lee, C. J., J. R. Brook, G. J. Evans, R. V. Martin, and C. Mihele (2011), Novel application of satellite and in-situ measurements to map surface-level NO_2 in the Great Lakes region, *Atmos. Chem. Phys.*, *11*(22), 11,761–11,775, doi:10.5194/acp-11-11761-2011.

Levelt, P. F., E. Hilsenrath, G. W. Leppelmeier, G. H. J. van den Oord, P. K. Bhartia, J. Tamminen, J. F. de Haan, and J. P. Veefkind (2006), Science objectives of the Ozone Monitoring Instrument, *IEEE Trans. Geosci. Remote Sens.*, *44*(5), 1199–1208, doi:10.1109/tgrs.2006.872336.

Lin, J. T. (2012), Satellite constraint for emissions of nitrogen oxides from anthropogenic, lightning and soil sources over East China on a high-resolution grid, *Atmos. Chem. Phys.*, *12*(6), 2881–2898, doi:10.5194/acp-12-2881-2012.

Ma, J. Z., S. Beirle, J. L. Jin, R. Shaiganfar, P. Yan, and T. Wagner (2013), Tropospheric NO_2 vertical column densities over Beijing: Results of the first three years of ground-based MAX-DOAS measurements (2008–2011) and satellite validation, *Atmos. Chem. Phys.*, *13*, 1547–1567, doi:10.5194/acp-13-1547-2013.

Marr, L. C., and R. A. Harley (2002), Spectral analysis of weekday-weekend differences in ambient ozone, nitrogen oxide, and non-methane hydrocarbon time series in California, *Atmos. Environ.*, *36*(14), 2327–2335, doi:10.1016/S1352-2310(02)00188-7.

Martin, R. V., D. D. Parrish, T. B. Ryerson, D. K. Nicks Jr., K. Chance, T. P. Kurosu, D. J. Jacob, E. D. Sturges, A. Fried, and B. P. Wert (2004), Evaluation of GOME satellite measurements of tropospheric NO_2 and HCHO using regional data from aircraft campaigns in the southeastern United States, *J. Geophys. Res.*, *109*, D24307, doi:10.1029/2004JD004869.

Melamed, M. L., S. Solomon, J. S. Daniel, A. O. Langford, R. W. Portmann, T. B. Ryerson, D. K. Nicks, and S. A. McKeen (2003), Measuring reactive nitrogen emissions from point sources using visible spectroscopy from aircraft, *J. Environ. Monit.*, *5*(1), 29–34, doi:10.1039/b204220g.

Merlaud, A., et al. (2011), Airborne DOAS measurements in Arctic: vertical distributions of aerosol extinction coefficient and NO_2 concentration, *Atmos. Chem. Phys.*, *11*(17), 9219–9236, doi:10.5194/acp-11-9219-2011.

Miyazaki, K., H. J. Eskes, and K. Sudo (2012), Global NO_x emission estimates derived from an assimilation of OMI tropospheric NO_2 columns, *Atmos. Chem. Phys*, *12*(5), 2263–2288, doi:10.5194/acp-12-2263-2012.

Munro, R., M. Eisinger, C. Anderson, J. Callies, E. Corpaccioli, R. Lang, A. Lefebvre, Y. Livschitz, and A. P. Albinana (2006), GOME-2 on MetOp, paper presented at 2006 EUMETSAT Meteorological Satellite Conference, EUMETSAT, Helsinki, 12–16 June.

Ordóñez, C., A. Richter, M. Steinbacher, C. Zellweger, H. Nüß, J. P. Burrows, and A. S. H. Prevot (2006), Comparison of 7 years of satellite-borne and ground-based tropospheric NO(2) measurements around Milan, Italy, *J. Geophys. Res.*, *111*, D05310, doi:10.1029/2005JD006305.

Petritoli, A., P. Bonasoni, G. Giovanelli, F. Ravegnani, I. Kostadinov, D. Bortoli, A. Weiss, D. Schaub, A. Richter, and F. Fortezza (2004), First comparison between ground-based and satellite-borne measurements of tropospheric nitrogen dioxide in the Po basin, *J. Geophys. Res.*, *109*, D15307, doi:10.1029/2004JD004547.

Petritoli, A., E. Palazzi, G. Giovanelli, W. Di Nicolantonio, G. Ballista, C. Carnevale, G. Finzi, E. Pisoni, and M. Volta (2011), Combined use of space-borne observations of NO_2 and regional CTM model for air quality monitoring in Northern Italy, *Int. J. Environ. Pollut.*, *47*(1-4), 158–166, doi:10.1504/11.47332.

Platt, U., and J. Stutz (2008), *Differential Optical Absorption Spectroscopy: Principles and Applications*, 597 pp., Springer, Berlin.

Pollack, I. B., et al. (2012), Airborne and ground-based observations of a weekend effect in ozone, precursors, and oxidation products in the California South Coast Air Basin, *J. Geophys. Res.*, *117*, D00V05, doi:10.1029/2011JD016772.

Richter, A., and J. P. Burrows (2002), Tropospheric NO_2 from GOME measurements, *Adv. Space Res.*, *29*(11), 1673–1683, doi:10.1016/S0273-1177(02)00100-X.

Richter, A., J. P. Burrows, H. Nüß, C. Granier, and U. Niemeier (2005), Increase in tropospheric nitrogen dioxide over China observed from space, *Nature*, *437*(7055), 129–132, doi:10.1038/nature04092.

Rothman, L., et al. (2005), The HITRAN 2004 molecular spectroscopic database, *J. Quant. Spectrosc. Radiat. Transfer*, *772*(96), 139–204, doi:10.1016/j.jqsrt.2004.10.008.

Ryerson, T. B., et al. (2013), The 2010 California research at the Nexus of air quality and climate change (CalNex) field study, *J. Geophys. Res.*, doi:10.1002/jgrd.50331, in press.

Schaub, D., K. F. Boersma, J. W. Kaiser, A. K. Weiss, D. Folini, H. J. Eskes, and B. Buchmann (2006), Comparison of GOME tropospheric NO_2 columns with NO_2 profiles deduced from ground-based in situ measurements, *Atmos. Chem. Phys.*, *6*(11), 3211–3229, doi:10.5194/acp-6-3211-2006.

Shaiganfar, R., S. Beirle, M. Sharma, A. Chauhan, R. P. Singh, and T. Wagner (2011), Estimation of NO_x emissions from Delhi using Car MAX-DOAS observations and comparison with OMI satellite data, *Atmos. Chem. Phys.*, *11*(21), 10,871–10,887, doi:10.5194/acp-11-10871-2011.

Steinbacher, M., C. Zellweger, B. Schwarzenbach, S. Bugmann, B. Buchmann, C. Ordonez, A. S. H. Prevot, and C. Hueglin (2007), Nitrogen oxide measurements at rural sites in Switzerland: Bias of conventional measurement techniques, *J. Geophys. Res.*, *112*, D11307, doi:10.1029/2006JD007971.

Torres, O., A. Tanskanen, B. Veihelmann, C. Ahn, R. Braak, P. K. Bhartia, P. Veefkind, and P. Levelt (2007), Aerosols and surface UV products from Ozone Monitoring Instrument observations: An overview, *J. Geophys. Res.*, *112*, D24S47, doi:10.1029/2007JD008809.

Vandaele, A. C., C. Hermans, S. Fally, M. Carleer, R. Colin, M. F. Mérienne, A. Jenouvrier, and B. Coquart (2002), High-resolution Fourier transform measurement of the NO_2 visible and near-infrared absorption cross sections: Temperature and pressure effects, *J. Geophys. Res.*, *107*(D18), 4348, doi:10.1029/2001JD000971.

Volkamer, R., P. Spietz, J. Burrows, and U. Platt (2005), High-resolution absorption cross-section of glyoxal in the UV-vis and IR spectral ranges, *J. Photochem. Photobiol. A*, *172*(1), 35–46, doi:10.1016/j.jphotochem.2004.11.011.

Volten, H., E. J. Brinksma, A. J. C. Berkhout, J. Hains, J. B. Bergwerff, G. R. Van der Hoff, A. Apituley, R. J. Dirksen, S. Calabretta-Jongen, and D. P. J. Swart (2009), NO_2 lidar profile measurements for satellite interpretation and validation, *J. Geophys. Res.*, *114*, D24301, doi:10.1029/2009JD012441.

Wagner, T., O. Ibrahim, R. Shaiganfar, and U. Platt (2010), Mobile MAX-DOAS observations of tropospheric trace gases, *Atmos. Meas. Tech.*, *3*(1), 129–140, doi:10.5194/amt-3-129-2010.

Walter, D., K. P. Heue, A. Rauthe-Schöch, C. A. M. Brenninkmeijer, L. N. Lamsal, N. A. Krotkov, and U. Platt (2012), Flux calculation using CARIBIC DOAS aircraft measurements: SO2 emission of Norilsk, *J. Geophys. Res.*, *117*, D11305, doi:10.1029/2011JD017335.

Wang, P., A. Richter, M. Bruns, V. V. Rozanov, J. P. Burrows, K. P. Heue, T. Wagner, I. Pundt, and U. Platt (2005), Measurements of tropospheric NO_2 with an airborne multi-axis DOAS instrument, *Atmos. Chem. Phys.*, *5*(2), 337–343, doi:10.5194/acp-5-337-2005.

Wang, X. N., V. Mallet, J. P. Berroir, and I. Herlin (2011), Assimilation of OMI NO_2 retrievals into a regional chemistry-transport model for improving air quality forecasts over Europe, *Atmos. Environ.*, *45*(2), 485–492, doi:10.1016/j.atmosenv.2010.09.028.

Wenig, M. O., A. M. Cede, E. J. Bucsela, E. A. Celarier, K. F. Boersma, J. P. Veefkind, E. J. Brinksma, J. F. Gleason, and J. R. Herman (2008), Validation of OMI tropospheric NO_2 column densities using direct-Sun mode Brewer measurements at NASA Goddard Space Flight Center, *J. Geophys. Res.*, *113*, D16S45, doi:10.1029/2007JD008988.

Zaveri, R. A., et al. (2012), Overview of the 2010 Carbonaceous Aerosols and Radiative Effects Study (CARES), *Atmos. Chem. Phys.*, *12*(1), 7647–7687, doi:10.5194/acp-12-7647-2012.

3.3 Combining Active and Passive Airborne Remote Sensing to Quantify NO_2 and Ox Production near Bakersfield, CA

Reproduced from: Baidar, S., R. Volkamer, R. Alvarez, A. Brewer, F. Davies, A. Langford, H. Oetjen, G. Pearson, C. Senff, and R.M. Hardesty (2013), Combining Active and Passive Airborne Remote Sensing to Quantify NO_2 and O_x Production near Bakersfield, CA, British Journal for Environmental and Climate Change, 3 (4), 566-586. doi:10.9734/BJECC/2013/5740

A research flight on June 15, 2010 was conducted over Bakersfield, CA and nearby areas with oil and natural gas production. Three remote sensing instruments, namely the University of Colorado AMAX-DOAS, NOAA TOPAZ lidar, and NCAS Doppler lidar were used to quantify production rates of nitrogen dioxide (NO_2) and O_x' (background corrected O_3 + NO_2) using the horizontal flux divergence approach by flying closed loops near Bakersfield, CA. By making concurrent measurements of the trace gases as well as the wind fields, we have reduced the uncertainty due to wind field in production rates. We find that the entire region is a source for both NO_2 and O_x'. NO_2 production is highest over the city (1.35 kg hr^{-1} km^{-2} NO_2), and about 30 times lower, though non-zero, at background sites (0.04 kg hr^{-1} km^{-2} NO_2). NO_x emissions as represented in the CARB 2010 emission inventory generally agree well with our measurements over Bakersfield city (within 30%). However, emissions upwind of the city are significantly underestimated. The O_x' production is less variable and widespread throughout the region, and accounts for 7.4 kg hr^{-1} km^{-2} O_x' at background sites. Interestingly, the maximum of 17.1 kg hr^{-1} km^{-2} O_x' production was observed upwind of the city. A plausible explanation for the efficient O_x' production upwind of Bakersfield, CA are favorable volatile organic compound (VOC) to NO_x ratios for O_x' production, that are affected by emissions from large oil and natural gas operations in that area.

Conclusions:

- An innovative approach to quantify and locate NO_x emissions, and to quantify the O_x production rates from an urban area is presented. There is no similar such measurements reported in the literature. The approach has the potential to also measure OVOC fluxes.
- The largest NO_x emissions are found over the city of Bakersfield, while the highest O_x' production was observed upwind of the city, over areas with large oil and gas operation. VOC emissions from oil and gas operations create a favorable VOC to NO_x ratio for O_3 production, and are likely the cause for the observed high O_x' production rate. Elevated O_x' production is widespread, and rather uniform throughout the region.
- NO_x emissions are non-zero also at background sites in the Central Valley. The overall NO_x emissions from the city of Bakersfield are well represented in the CARB 2010 emission inventory (within 30%), though differences in the location of emissions are observed. NO_x emissions from oil and natural gas operations are currently missing in the emission inventory.

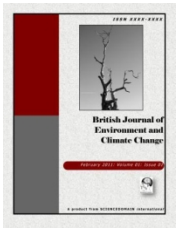

SCIENCEDOMAIN

Original Research Article

Aims: The objective of this study is to demonstrate the integrated use of passive and active remote sensing instruments to quantify the rate of NO_x emissions, and investigate the O_x production rates from an urban area.
Place and Duration of Study: A research flight on June 15, 2010 was conducted over Bakersfield, CA and nearby areas with oil and natural gas production.
Methodology: Three remote sensing instruments, namely the University of Colorado AMAX-DOAS, NOAA TOPAZ lidar, and NCAS Doppler lidar were deployed aboard the NOAA Twin Otter during summer 2010. Production rates of nitrogen dioxide (NO_2) and O_x' (background corrected O_3 + NO_2) were quantified using the horizontal flux divergence approach by flying closed loops near Bakersfield, CA. By making concurrent measurements of the trace gases as well as the wind fields, we have reduced the uncertainty due to wind field in production rates.
Results: We find that the entire region is a source for both NO_2 and O_x'. NO_2 production

is highest over the city (1.35 kg hr^{-1} km^{-2} NO_2), and about 30 times lower at background sites (0.04 kg hr^{-1} km^{-2} NO_2). NO_x emissions as represented in the CARB 2010 emission inventory agree well with our measurements over Bakersfield city (within 30%). However, emissions upwind of the city are significantly underestimated. The O_x' production is less variable, found ubiquitous, and accounts for 7.4 kg hr^{-1} km^{-2} O_x' at background sites. Interestingly, the maximum of 17.1 kg hr^{-1} km^{-2} O_x' production was observed upwind of the city. A plausible explanation for the efficient O_x' production upwind of Bakersfield, CA are favorable volatile organic compound (VOC) to NO_x ratios for O_x' production, that are affected by emissions from large oil and natural gas operations in that area.

Conclusion: The NO_2 and O_3 source fluxes vary significantly, and allow us to separate and map NO_x emissions and O_x production rates in the Central Valley. The data is probed over spatial scales that link closely with those predicted by atmospheric models, and provide innovative means to test and improve atmospheric models that are used to manage air resources. Emissions from oil and natural gas operations are a source for O_3 air pollution, and deserve further study to better characterize effects on public health.

Keywords: Active and passive remote sensing; LIDAR; AMAX-DOAS; fluxes, air pollution;

1. INTRODUCTION

Ozone (O_3) and nitrogen oxides (NO_x = NO + NO_2) are trace gases that are important components of air pollution. Health concerns of O_3 and NO_2 are related to respiratory illnesses such as chest pain, reduced lung function, asthma, emphysema whereas environmental concerns include reduced vegetation growth and acid rain. Due to these concerns both trace gases are recognized as air pollutants by air quality regulating agencies around the world, and are regulated by air quality standards and guidelines. The World Health Organization (WHO) air quality guideline recommends the standard to be set at 100 µg m^{-3} (~51 ppb) for O_3 (8 hour mean) and 40 µg m^{-3} (~21 ppb) for NO_2 (annual mean) [1]. The National Ambient Air Quality Standard (NAAQS) set by U.S. Environmental Protection Agency are 75 ppb for O_3 (8 hour maximum) and 53 ppb for NO_2 (annual mean) [2]. Similarly, the current air quality standard for the European Union are 120 µg m^{-3} (~61 ppb) for O_3 (8 hour maximum) and 40 µg m^{-3} (~21 ppb) for NO_2 (annual mean) [3]. Further, O_3 is a greenhouse gas that is relevant to climate discussions [4]. The lifecycles of O_3 and NO_x are intimately coupled, because NO_2 photolysis by sunlight drives photochemical O_3 production, while emissions of NO destroy O_3 to form NO_2. The sum of O_3 and NO_2 is called O_x, and is a conserved quantity as it implicitly accounts for the destruction of O_3 by NO (O_3 titration). Excess O_x is formed from the oxidation of volatile organic compounds (VOCs) in the presence of NO_x [5-7]. Fig. 1 shows a schematic diagram of photochemical O_3 production and evolution of NO, NO_2, O_3 and O_x concentrations upwind (I), within city limits (II) and downwind (III and IV) of an urban area. Different chemistry in these regions results in the characteristic spatial patterns in NO_x-O_3 distributions depicted in Fig. 1, which are: (1) Background O_3 present in the upwind region (I). (2) Emission of NO_x in the city limits (II), which leads to (3) O_3 removal via reaction with NO to produce NO_2 (titration reaction). (4) Photochemical production of O_3 from VOC/NO_x chemical cycles, which dominates downwind of the city center (III) and results in O_3 concentrations to accumulate. Further (5) the O_3 concentration does no longer accumulate in some distance downwind (IV), when NO_x has been oxidized to NO_y. NO_y is efficiently deposited or lost to aerosols resulting in insufficient NO_x to drive VOC-NO_x chemical cycles (NO_x limited region). Ultimately O_3 removal by photolysis and dry deposition leads to a slowly decreasing O_3 concentration here [6-8].

Due to their importance for air quality and human health, NO_2 and O_3 plumes from point sources and urban areas have been extensively studied. Previous studies have estimated NO_2 emission rates from point sources like power plants [9], urban areas [10-13], O_3 production rates in urban plumes [14,15], the amount of O_3 transported from urban areas and its impact on regional background O_3 [15], and the relationship between O_3, NO and NO_2 as function of NO_x in urban areas [16]. However, despite decades of research, models that predict O_3 formations have not been constrained by observations at the scale of cities and immediately downwind of cities. The comparison at the local scale is important, because of uncertain and changing emission of VOCs [17], NO_x [18], complicated transport [19-21] over cities and downwind of cities, and also uncertainties in non-linear chemistry that couples VOCs, NO_x and O_3. Such chemistry is heavily parameterized in current atmospheric models used to predict O_3. The net O_3 production by VOC oxidation is related to the conversion of NO to NO_2 by organic peroxy-and hydro peroxy radicals that are formed during the airborne oxidation of VOCs by atmospheric oxidants like OH, NO_3, O_3, and Cl radicals [22]. Under high NO_x conditions, the rate of O_3 production is limited by the availability of VOCs, while availability of NO_x controls the rate of O_3 production under low NO_x conditions [22-25]. For example, the testing of detailed chemical mechanisms of VOC oxidation using simulation chamber data [26,27], and field observations [28-31] often predict lower O_3 formation rates than that are actually being observed. The uncertainty in the chemistry of O_3 formation can be of similar relevance as uncertainties in emissions, and transport [30]. Further, transport of O_x across city, state and international borders causes possible non-attainment of O_3 levels at sites downwind [15,20,32] and the changing boundary conditions complicates enforcement of regulations.

Over the course of the last decade, emission control policies aimed at reducing ambient O_3 levels have resulted into NO_x reductions in North America and Europe [18,33-38]. NO_x sources in the troposphere are primarily related to anthropogenic emissions from on-road motor vehicles and power plants. With more than half of the world population now living in urban areas, cities have developed into hotspots for NO_x sources [18,33,34] and provide opportunities for NO_x reductions that are relevant on the global scale. This trend towards urbanization on global scales is unique in the history of mankind, and has the potential to change the planet. There is an increasing need for the development of analytical approaches that are effective at quantifying emissions of NO_x, provide experimental constraints to O_x production rates, and transport in order to refine atmospheric models that are used to manage air resources.

The primary objective of this study is to demonstrate the potential and feasibility of integrated use of passive and active remote sensing instruments and column observations to estimate the rate of NO_x emissions, and investigate the O_x production from an urban area. We use the mass conservation approach to estimate source strength for NO_2, and O_x from an urban area. Recently, ground based mobile differential optical absorption spectroscopy (DOAS) measurements have been used to estimate NO_x emissions from urban areas using this approach [10,11,13]. A similar approach has also been used to probe NO_x emission from megacities using satellites [12]. We have made simultaneous measurements of NO_2 vertical columns, O_3 and wind profiles for the first time from a research aircraft. The data set provides an opportunity to estimate production of individual species and investigate the conserved quantity, O_x, which could be significantly impacted by O_3 titration in NO_x source areas such as city centers. As a case study, data from a research flight on June 15, 2010 over Bakersfield, California is presented.

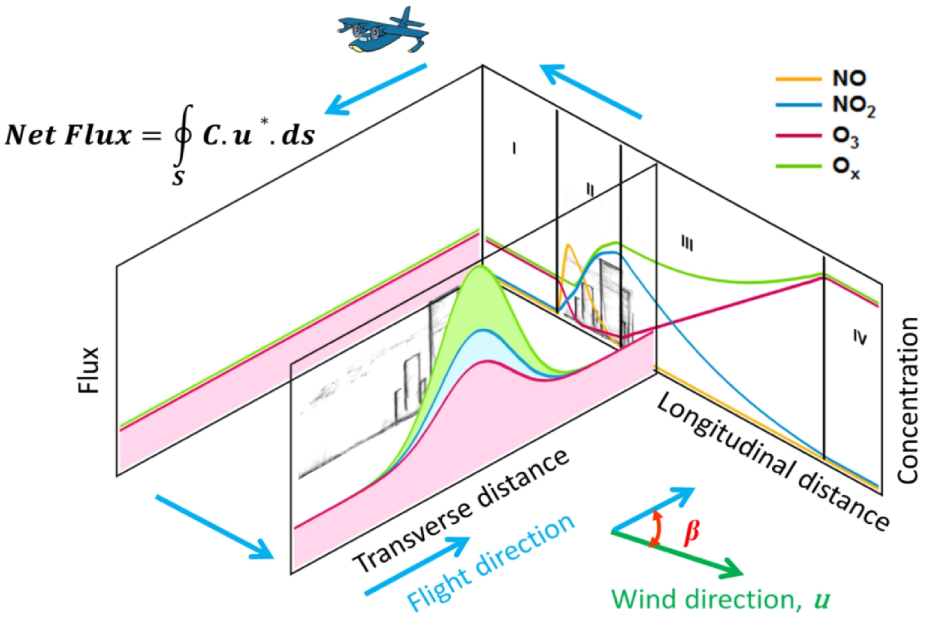

Fig. 1. Schematic diagram showing cross-section of ozone formation in an urban area under steady wind conditions and horizontal flux divergence measurements in a closed loop for source strength calculations. Evolution of NO (orange), NO_2 (blue), O_3 (maroon) and O_x (green) over different urban regions: (I) upwind, (II) urban center, (III) downwind and (IV) further downwind are also illustrated.

2. METHODOLOGY

We use a mass conservation approach to estimate the emission and production source strength of NO_2 and O_x. Neglecting the molecular diffusivity term in the mass conservation equation, the NO_2 and O_x source strengths within a given volume can be estimated from their time rate of change within the volume and the horizontal flux divergence across the boundaries enclosing the volume. We have conducted measurements of vertical columns of NO_2, O_3, and wind profiles aboard a research aircraft that flew box patterns over and near an urban area. Fig. 1 shows a conceptual schematic illustrating our approach for measuring NO_2 and O_x production rates.

Three remote sensing instruments namely (1) the University of Colorado Airborne Multi-Axis Differential Absorption Spectroscopy instrument (CU AMAX-DOAS), (2) the National Oceanic and Atmospheric Administration (NOAA) Tunable Optical Profiler for Aerosol and Ozone (TOPAZ) lidar and (3) the National Center for Atmospheric Science (NCAS) Doppler lidar were deployed aboard the NOAA Twin Otter research aircraft. The configuration of the three instruments aboard the Twin Otter is shown in Fig. 2. A total of 52 research flights were conducted over the course of two months (May 19-July 19, 2010) as part of the California Research at the Nexus of Air Quality and Climate Change (CalNex) [39] and the Carbonaceous Aerosol and Radiative Effects Study (CARES) [40] field campaigns in California during summer 2010. Most of the flights were focused on the Los Angeles basin

and Greater Sacramento area. More details on the individual Twin Otter research flights can be found in Ryerson et al. [39]. One of the foci of this deployment was to constrain the emission and production of NO_2 and O_3 upwind, within and downwind of urban areas.

2.1 AMAX-DOAS

The CU AMAX-DOAS instrument [41,42] uses scattered sunlight as the light source (passive remote sensing). The scattered sunlight spectra are analyzed for the presence of absorbers like NO_2, glyoxal (CHOCHO), formaldehyde (HCHO) and oxygen dimer (O_4) among others using the DOAS method [43]. The instrument and its performance during CalNex and CARES field campaigns are described in detail in Baidar et al. [42]. Briefly, a telescope pylon is mounted on the outside of the window plate of the aircraft and includes a rotatable prism to collect scattered photons from different elevation angle (EA) i.e. angle relative to the horizon. Spectra collected from different EA contain information from different layers in the atmosphere and hence can be used to obtain information about vertical distribution of trace gases. The collected photons are transferred to a spectrometer / charge coupled device (CCD) detector system via optical glass fiber bundle. Here we will only present data from nadir viewing geometry from the flight over Bakersfield.

The measured spectra were analyzed, for NO_2 in a wavelength range from 433 to 460 nm, against a fixed zenith reference spectrum recorded during the same flight in a clean environment and flying at relatively high altitudes (3 – 5 km; 3.5 km for this flight). Zenith spectra were recorded frequently, and are used to correct for stratospheric NO_2 contributions and NO_2 above the aircraft. The nadir NO_2 differential slant column densities (dSCDs) are observed below the plane and correspond to the average integrated difference in concentration of the absorber along the light path with respect to the reference. Since most of the NO_2 sources in an urban environment are located close to the surface, the retrieved nadir dSCD was considered to be the boundary layer slant column ($dSCD_{bl}$). NO_2 nadir measurements were performed every 20-25 s and hence NO_2 data points are available every ~1.5 km horizontally. For the conversion of nadir NO_2 $dSCD_{bl}$ into boundary layer vertical column densities, VCD_{bl}, the geometric Air Mass Factor (AMF_{geo}) approximation was applied.

$$\mathrm{AMF_{geo}} = \frac{1}{1+\frac{1}{\cos(\mathrm{SZA})}} = \frac{\mathrm{SCD_{bl}}}{\mathrm{VCD_{bl}}} \qquad (1)$$

Here, SZA refers to solar zenith angle at the time of the measurement. This approach is in good agreement with explicit radiative transfer calculations for California while flying between 2 and 4 km. Radiative transfer calculations for the conditions of the Bakersfield case study (flight altitude: 2 km, SZA: <25º), and comparisons with ground based vertical columns consistently reveal the uncertainty in AMF_{geo} to be less than 7% [42]. The overall uncertainty in NO_2 VCD for the Bakersfield case study is estimated to be around 9% (AMF_{geo} : <7%, NO_2 cross-section: ~5%, DOAS fit: ~3%) [42,44].

2.2 TOPAZ

NOAA's nadir-looking TOPAZ differential absorption lidar is a compact, solid-state-laser-based O_3 lidar that emits pulsed laser beams at three tunable wavelengths in the UV spectral region between about 285 and 300 nm [45]. The differential attenuation of the three wavelengths due to O_3 permits the retrieval of O_3 concentration profiles along the laser beam path [46]. TOPAZ O_3 profiles were computed every 10 s (or about 600 m horizontally) with a

vertical resolution of 90 m. The ozone profiles extend from about 400 m beneath the plane to near the ground. O_3 values in the lowest two measurement bins (lowest 180m) above ground level (AGL) are typically not used because of poor signal to noise ratio.

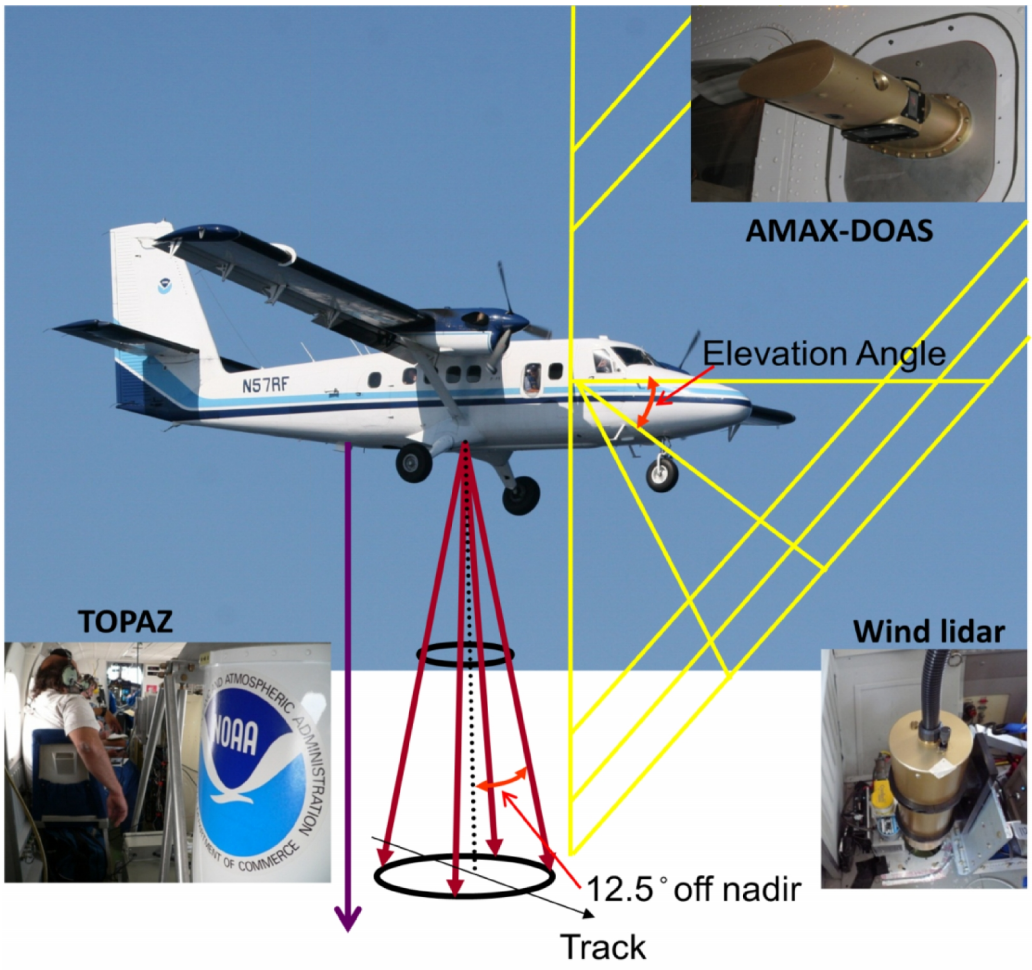

Fig. 2. Instrumental setup of CU AMAX-DOAS, NOAA TOPAZ lidar and NCAS Doppler wind lidar aboard the NOAA Twin Otter research aircraft during CalNex and CARES field campaigns. The yellow, purple and maroon lines represent viewing geometry of CU AMAX-DOAS, NOAA TOPAZ lidar and NCAS Doppler wind lidar respectively. The three instruments are also shown in the insets.

The TOPAZ lidar also provided aerosol backscatter profiles for the longest (and least absorbed by O_3) of the three emitted wavelengths near 300 nm. The time resolution of the aerosol backscatter profile measurements is the same as for O_3, but the vertical resolution is much finer at 6 m. We used these highly resolved lidar backscatter profile data to retrieve boundary layer height (BLH) by employing a Haar wavelet technique [47]. This approach is based on the (often valid) assumption that the aerosol concentration is higher in the boundary layer (BL) than in the lower free troposphere (FT). The altitude at which the strongest aerosol gradient is found by the wavelet technique is used as an estimate of the

BLH. At times, the contrast in aerosol backscatter between the BL and the overlying FT is not sufficient to yield reliable results, and the BLH is not reported for such scenarios.

We used the BLH estimates and O_3 profiles measured with the TOPAZ lidar to compute O_3 column data integrated over the depth of the BL. To fill in data gaps in the O_3 profiles close to the ground, we averaged the ozone measurements in the lowest two gates with usable data (typically 200 - 300 m AGL) and extrapolated this value to the ground. We then integrated these extrapolated ozone profiles from the surface to the top of the BL to yield BL O_3 column density along the flight track at 10-s resolution. When BLH estimates were not available from the backscatter profile for a given O_3 profile, BLH was interpolated from adjacent measurements to compute O_3 vertical column over the BLH. TOPAZ O_3 measurements have been extensively compared to and agree well (±2-9%) with in situ airborne O_3 observations [48].

2.3 Doppler Wind Lidar

Information on the wind structure below the aircraft was provided by the NCAS Doppler lidar [49] mounted in the Twin Otter cabin. The lidar measures the Doppler shift of radiation scattered from atmospheric aerosol particles to estimate the component of wind along the lidar line of sight. Typical precision of the lidar radial wind measurements under acceptable aerosol loading is better than a few tens of cm s^{-1}. The lidar was mounted in the cabin with the beam transmitted vertically through a small camera port located on the underside of the aircraft (Fig. 2). In order to measure the horizontal component of the winds a rotatable refractive wedge mounted in the port directed the beam to 12.5º off nadir. The original scanner design included two wedges, which provides greater beam deflection and enables vertical pointing; however poor optical quality of the wedges forced us to eliminate the second wedge to reduce total attenuation through the scanner.

During flight operations the wedge was rotated to four different azimuth angles (45, 135, 225, 315º) relative to the flight track. Dwell time at each azimuth angle was 1 s for most of the Doppler measurements during CalNex. A complete rotation among the four azimuths required 8 s, including the time required to rotate the wedge to a new position. At the nominal Twin Otter speed of 60 m s^{-1} a complete 4-beam scan was completed about every 500 m. Vertical resolution of the lidar wind measurements was roughly 50 m.

Information on aircraft speed and orientation was obtained from the CU AMAX-DOAS motion compensation system [42]. Additionally, we used the surface return at the four look angles, for which the only Doppler shift results from motion of the aircraft, to provide additional information on aircraft orientation and velocity. For the case described here, a 19-beam running average of the radial wind estimates at each of the four azimuth angles was computed to improve precision of measurements. After removal of the Doppler shift induced by aircraft motion, the velocities from the four azimuth angles were combined in a least-squares type algorithm to estimate the mean wind speed and direction in each of the 50 m range gates where backscatter was high enough to provide a strong signal. The wind speed and direction were averaged up to the BLH before further calculations of horizontal flux. The uncertainty in the wind measurement is estimated to be around 6% based on the difference between wind retrievals from a longer (19-beam) and a shorter (3-beam) running average wind fits.

2.4 Bakersfield Case Study

Bakersfield is a city located in the southern part of the Central Valley, CA, surrounded mostly by agricultural area and oil and natural gas operations. In the summer months, wind blows predominantly from the northwest down the valley providing steady wind conditions necessary for the method presented here. The Bakersfield area also makes for an interesting case study to probe NO_2 and O_x production from a large city influenced by intense agriculture and petrochemical production. In particular, we have probed (i) background air unaffected by urban anthropogenic emissions, (ii) air upwind, influenced by agricultural and petrochemical production, (iii) urban emissions from the city, and, (iv) the chemical evolution downwind, after it is perturbed by urban emission inputs.

The flight plan of the Twin Otter on June 15, 2010 (see Fig. 3) was designed to interrogate NO_x emissions and constrain the O_3 production from different source regions enclosed by "boxes" by applying the horizontal flux divergence approach. The flight plan included an enclosed box, over areas with no major emission sources, in the northwest of Bakersfield to characterize the background conditions (Box A; see Fig. 4). Two boxes (Box C and D; D is twice the size of C) were flown over the city of Bakersfield to constrain emissions/productions from the city. In order to contrast NO_2 and O_3 production upwind and downwind of Bakersfield, two additional boxes (Box B and E) were created by interpolating the measured NO_2, O_3 and wind data for the western legs (shown as diamonds in Fig. 4). A larger trapezoid (Box F) was flown, connecting the three boxes, and enclosing the entire greater Bakersfield region. It took approximately 15, 13 and 18 minutes to complete boxes A, C and D respectively while the larger Box F took ~75 minutes. The entire box patterns were flown at a constant altitude (~2000 m above sea level), well above the BL. Details related to the times and meteorological conditions encountered for each boxes are summarized in Table 1.

Table 1. Meteorological conditions on June 15, 2010 for the closed boxes flown near Bakersfield, CA

Box	Area (km x km)	Time (UTC)	Wind speed (m/s)	Wind direction (º)	Boundary layer height (m, AGL)	
			mean ± sdev	mean ± sdev	min	max
A	20 x 14	20:24-20:38	5.6 ± 1.7	283 ± 44	1005	1548
B	20 x 19		4.3 ± 1.6	314 ± 41	760	1425
C	20 x 9	19:41-19:54	4.1 ± 1.5	317 ± 49	936	1425
D	20 x 18	21:07-21:25	4.7 ± 0.9	317 ± 26	1049	1481
E	20 x 18		3.0 ± 0.8	328 ± 27	1066	1450
F	67 x 56	19:54-21:11	3.3 ± 1.8	313 ± 41	760	1524

2.5 Horizontal Flux and Source Strength

For each transect, the gas flux at a point, *x* along the flight path is obtained by multiplying the column measurement at that location, *column(x)* by the corresponding wind speed averaged over the BLH, $u^*_{avg}(x)$ [10,11]. The flux calculation through a surface area, *A* is shown in equation 2:

$$\int \vec{f}.d\vec{A}_{area} = \int_{x1}^{x2}\int_{0}^{BLH} conc(z).u^*(z).dzdx = \int_{x1}^{x2} u^*_{avg}(x).column(x)dx \quad (2)$$

Where *J* corresponds to flux at any location, *x* to the flight direction, *z* to the altitude, *u** to the wind speed orthogonal to the flight direction *(x)* and is assumed to be constant over the BLH, u^*_{avg} to wind speed averaged up to the BLH, and

$$column = \int_0^{BLH} conc(z).dz \quad (3)$$

$$u^* = u.\sin(\beta) \quad (4)$$

Here *u* is wind speed and *β* is angle between wind direction and flight heading.

Flux measurement in a closed loop can be used to estimate source strength within the enclosed volume [10,11]. The general continuity equation in the integral form is given in equation (5) and is the basis for the source strength calculation. It involves three terms: source, flux divergence and rate of change of concentration.

$$Q_{net} = \oint_S \vec{J}.d\vec{A}_{area} + \int_{Vol} \frac{\partial conc}{\partial t} dV_{vol} \quad (5)$$

i.e. the net source strength of an enclosed volume, Q_{net} is the sum of fluxes through all areas along the closed loop (incoming and outgoing) and change in concentration inside the volume.

We assumed that the time dependence of concentration in the enclosed volume is zero over the time scale of our measurement. Our measurements were performed during the midday when rate of change of NO_2 and O_3 concentration in the Bakersfield area is very small (see Fig. 5). Hence, we neglected the second term on the right hand side in equation (5). We also assumed that the net vertical exchange and deposition are negligible over the timescale of our measurement. Hence, the net flux i.e. the difference in fluxes entering and leaving the enclosed volume through the walls gives the source strength for the species of the particular enclosed area at the time of the measurement.

2.6 Daily NO_x Emission

Daily NO_x emission was estimated based on the computed NO_2 source strength, diurnal profile of NO_2 and the NO_x to NO_2 ratio measured at the California Air Resource Board (CARB) monitoring station at Bakersfield. It is computed as:

$$NO_x\ emssion\ = \sum_{t=10}^{20} E.\frac{[NO_2(t)]}{[NO_2(t_0)]}.\frac{[NO_x(t)]}{[NO_2(t)]} \quad (6)$$

Where *E* is the computed NO_2 production rate from (5), *t* is hour of the day, t_0 is the hour of our measurement. Therefore, the daily NO_x emission is the sum of product of measured NO_2 emission rate at time t_0, ratio of NO_2 at time *t* and t_0 and ratio of NO_x to NO_2 at time *t* over the course of the day. In order to minimize potential bias created due NO_x accumulation overnight, we only calculated daily NO_x emission for the period when NO_2 and NO_x measurements at the CARB station were stable (10:00-20:59 PST). Fig. 5 shows NO_2, NO_x and O_3 mixing ratios measured hourly at the Bakersfield CARB monitoring station on that day. The time period of our measurement and time frame for the daily NO_x emission calculation are also shown in Fig. 5.

3. RESULTS AND DISCUSSION

The measurement on June 15, 2010 over Bakersfield, CA was performed at mid-day when the change in NO_2 and O_3 concentration is very small, providing chemically stable conditions most suitable for source strength calculations. This is supported by NO_2 and O_3 measurements at the CARB monitoring station at Bakersfield (see Fig. 5). Column O_3, BLH from the NOAA TOPAZ lidar, column NO_2 from the CU AMAX-DOAS, and wind speed and direction from NCAS Doppler lidar are shown in Fig. 3. Fig. 3a shows the BLH at the time of the measurement retrieved from TOPAZ backscatter profiles. In general, the highest O_3 and NO_2 VCDs were measured in the southeastern corners of the boxes especially for boxes with significant emission sources (Fig. 3b and 3c), consistent with the prevailing wind conditions. We calculated NO_2 and O_x production rates for the six boxes.

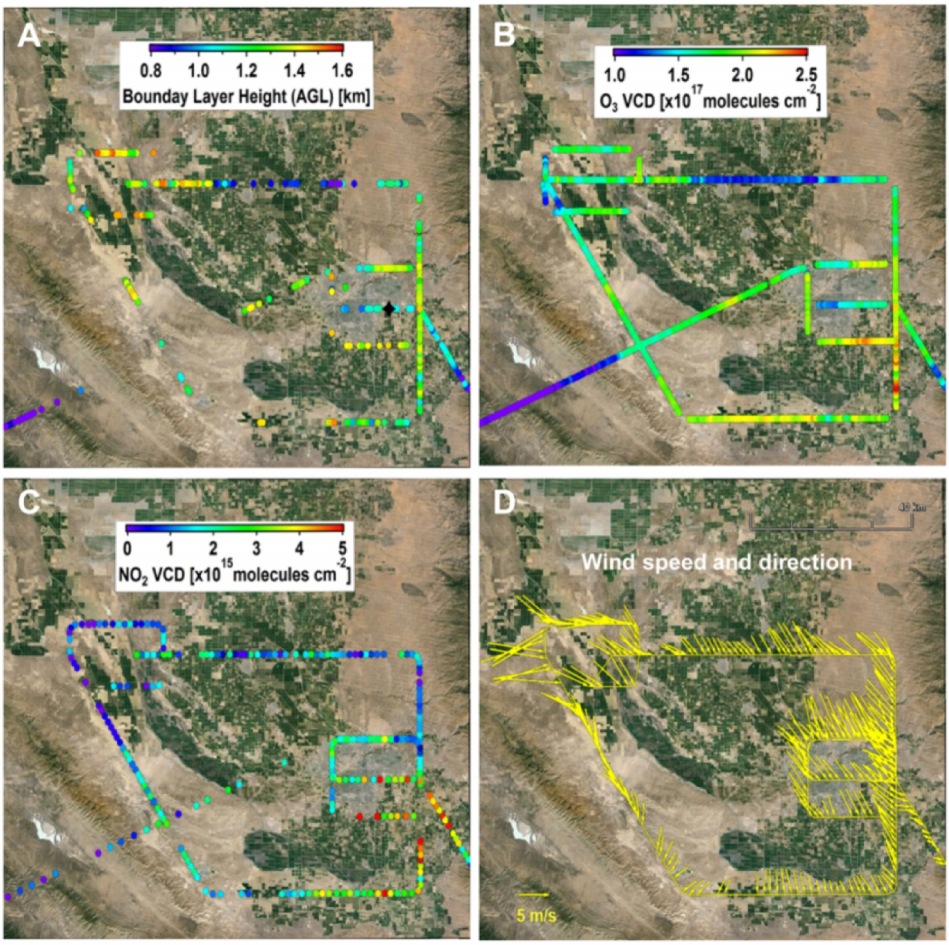

Fig. 3. Maps of (A) Boundary layer height (BLH) above ground level, (B) O_3 vertical columns up to the BLH, (C) NO_2 vertical columns and (D) wind speed and direction from the flight over Bakersfield, CA on June 15, 2010. BLH and O_3 columns were measured by NOAA TOPAZ lidar, NO_2 vertical columns by CU AMAX-DOAS and wind speed and direction by NCAS Doppler wind lidar. Black diamond on A shows the location of CalNex Bakersfield supersite.

The wind speed and direction and BLH during the time of measurements for different boxes are given in Table 1. The wind was blowing predominantly from the northwest and provided ideal conditions as horizontal flux divergence measurements require steady wind fields (also see Fig. 3d). The variability in wind speed and direction was larger for upwind boxes (A and B) compared to downwind boxes (D and E). The BLH range for boxes D and E were also smaller compared to other boxes. The observed BLH variability is most likely a combination of land use changes (irrigated fields vs. dry land vs. urban heat island) and the fact that upslope flow over the foothills east of Bakersfield favor BLH growth, while strong subsidence over the middle of the valley acts to suppress BL growth. We use the BLH variability to estimate the amount of BL air column susceptible to exchange with the FT (see Section 3.1.). Since all the parameters needed to quantify flux are constrained by measurements here, the horizontal variability in BLH does not pose a limitation to our approach. Notably, the variability of BLH remains difficult to predict by atmospheric models, and warrants further investigation.

Background corrected O_x (O_x' from here on) column up to the BLH, computed as the sum of NO_2 and background corrected O_3 columns, is shown in Fig. 4. Background correction for O_3 is needed as we are interested in the source strength of the area at the time of measurement i.e. the amount that is being produced locally. The background correction also minimizes any potential biases due to BL-FT exchange in case of strongly varying BLH. If BLH is constant over a box, then background correction is not necessary, because incoming and outgoing background fluxes are the same and cancel each other. Note that we measure column amount of O_3 and NO_2. Background O_3 levels were calculated based on the mean O_3 concentration over the BLH in the northwestern corner of the Box A (see Fig. 4). We note that 'background' air in the Central Valley is affected by transport of pollution emitted upwind; indeed we find significant production of O_x' in Box A. However, low and similar amounts of NO_2 are transported into and out of Box A, and net production of measured species is the lowest observed anywhere. We find no evidence for major emission sources within Box A. The mean and the standard deviation of the background O_3 concentration was $1.20 \pm 0.03 \times 10^{12}$ molecules cm^{-3} (48.8 ± 1.2 ppbv, 1ppbv = 2.46×10^{10} molecules cm^{-3}). It was assumed that this background O_3 concentration is representative of the entire area. A background O_3 column was calculated for each measurement point along the flight track by multiplying this O_3 concentration with BLH at that location. This background column was then subtracted from the measured O_3 column to determine O_3', which corresponds to the excess O_3 column at each point along the flight track. NO_2 VCDs were used without further corrections as they were below the detection level over that area (4.2×10^{14} molecules cm^{-2}, ~130 pptv). The average column NO_2 to O_x' partition ratio increased from 2% over the background site to 7% over the city of Bakersfield. Thus, NO_2 gas forms a significant portion of O_x' over the urban area and would result in a bias if O_3 production rates were calculated instead of O_x. By investigating O_x' we eliminate the uncertainty due to titration of O_3 by NO to form NO_2 in the NO_x source regions.

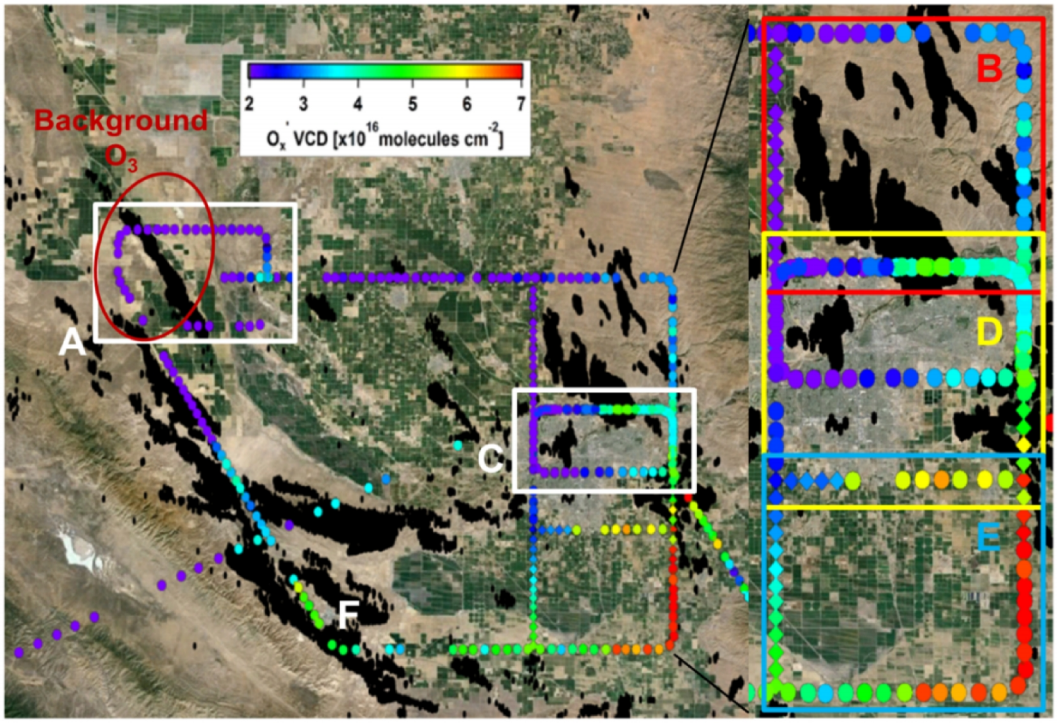

Fig. 4. Map of O_x' vertical columns up to the BLH. Rectangles represent different boxes flown over Bakersfield: (A) upwind background area, (C) over the city, and (F) over the entire area. Colored rectangles in the inset highlight three boxes: (B) upwind, (D) over the city, and (E) downwind. Box B and E were created for comparison purposes by interpolating the western legs. Interpolated data are shown as diamonds. Black areas in the map show active oil and gas wells in the region.

The minimum, maximum and mean mixing ratios of NO_2 and O_3 for each box are also given in Table 2. The average NO_2 and O_3 concentrations were lowest for the background box. The NO_2 concentrations show higher variation within a box as well as between the boxes, indicating highly local NO_2 sources in the area. The mean O_3 does not vary much between the boxes (see Table 2). Notably, the maximum O_3 concentrations were observed to be generally related to the O_x' production rates in the box upwind of a given box, which is expected. Both O_3 and NO_2 showed the highest average concentration over the downwind box (E). Considering that the production rates are lower compared to the boxes upwind (B and D), there could be some accumulation of NO_2 and O_3 taking place in this box.

The enclosed areas are sources for both NO_2 and O_x' for all the boxes investigated. The NO_2 and O_x' production rates calculated for different boxes are given in Table 2. The production rates were calculated using equation (5) and have been normalized for the area of the boxes so that they can be directly compared to each other. As expected, the background, Box A, has the lowest production rate for both NO_2 and O_x'. The NO_2 production rate in the background box was 0.04 kg hr^{-1} km^{-2}. The NO_2 production rate was highest for Box D and amounts to 1.35 kg hr^{-1} km^{-2} above Bakersfield. This is consistent with the present knowledge that urban city limits are the dominant source for NO_x emissions in California [18].

Boxes C and E, located in the northern half of Box D, and immediately downwind of Box D respectively, show about 13 times lower NO_2 production rate, indicating that the NO_2 sources from the urban area are highly localized. Interestingly, the site upwind of Bakersfield (Box B) was also found to be a significant source for NO_2 compared to the downwind site (Box E).

Table 2. NO_2 and O_3 mixing ratios and NO_2 and O_x' production rates normalized by area of the boxes for each box near Bakersfield, CA on June 15, 2010

Box	Mixing ratio[1]		Production rates[4]	
	NO_2 (pptv)	O_3 (ppbv)	NO_2[2]	O_x'[3]
	min / max / mean	min / max / mean	($x10^{-2}$ kg hr^{-1} km^{-2})	(kg hr^{-1} km^{-2})
A	22 / 864 / 298	45 / 59 / 51	4 ± 8	7.4 ± 0.6
B	38 / 951 / 497	47 / 62 / 58	60 ± 6	17.1 ± 0.8
C	145 / 2425 / 852	47 / 67 / 58	11 ± 15	11 ± 2
D	149 / 1554 / 694	52 / 68 / 60	135 ± 12	13 ± 1
E	563 / 1948 / 1183	56 / 76 / 66	12 ± 10	11 ± 1
F	22 / 1948 / 582	45 / 76 / 59	39 ± 1	9.4 ± 0.1

[1]Mixing ratio is calculated assuming that the NO_2 and O_3 are uniformly distributed over the boundary layer. Conversion: 1 pptv = 2.46 x 10^7 molecules cm^{-3} and 1 ppbv = 2.46 x 10^{10} molecules cm^{-3}.
[2]Molecular weight of NO_2 (MW_{NO2}) =46 g/mole
[3]Molecular weight of O_x ($MW_{Ox'}$) = 48 g/mole
[4]Error in the production rates represents total propagated measurement uncertainty. Details are provided in Section 3.1.

The O_x' production rate for the background box was 7.4 kg hr^{-1} km^{-2}, the lowest of all boxes. Box A likely represents the O_x' production rates for regions in the Bakersfield area that are not affected directly by the urban emissions. Notably, the NO_2 production from within box A was the lowest we have observed in this case study. However, our approach does not attempt to make a correction for NO_2 losses due to photochemistry and deposition, and as such the reported NO_2 production has to be considered a lower limit. While the measured NO_2 flux was essentially zero within error of the measurements, this indicates that comparable amounts of NO_2 enter and exit the box, and that enough NO_x was present to produce O_3. This was confirmed by our observations of elevated O_x production in box A. Interestingly, the O_x' production rates over the Bakersfield city limit (Box C and D) and downwind site (Box E) only showed small enhancement (< factor of 1.75) over the background O_x' production rate. This indicates that even though the NO_2 levels in the wider area surrounding Bakersfield are relatively small (~330 pptv), there is enough NO_x to sustain photochemical O_x' production in the entire region. Surprisingly, the upwind box (Box B) was found to have the largest O_x' production rate (17.1 kg hr^{-1} km^{-2}, 2.3 times that of Box A). The O_x' production rate in Box B was 133% that of urban Box D while the NO_2 production was only about 40% of the urban box. A plausible explanation for our observation of efficient and high O_x' production from Box B could be from enhanced VOC levels due to large oil and natural gas operations in the area, creating favorable conditions for enhanced O_3 production (high VOC/NO_x ratio). Oil and natural gas production is a source for atmospheric methane, a greenhouse gas, and other more reactive hydrocarbons as well as NO_x. The observed elevated emissions of NO_x in box B indicate emissions are active in this area. While higher NO_2 is likely to contribute to the higher O_3 production rate, additional VOC emissions are needed to explain such a high increase in the O_3 production rate. We are unable to conclude about additional VOC sources from our data at this point, but note that some emissions of reactive hydrocarbons are expected from the oil and natural gas production in the area that

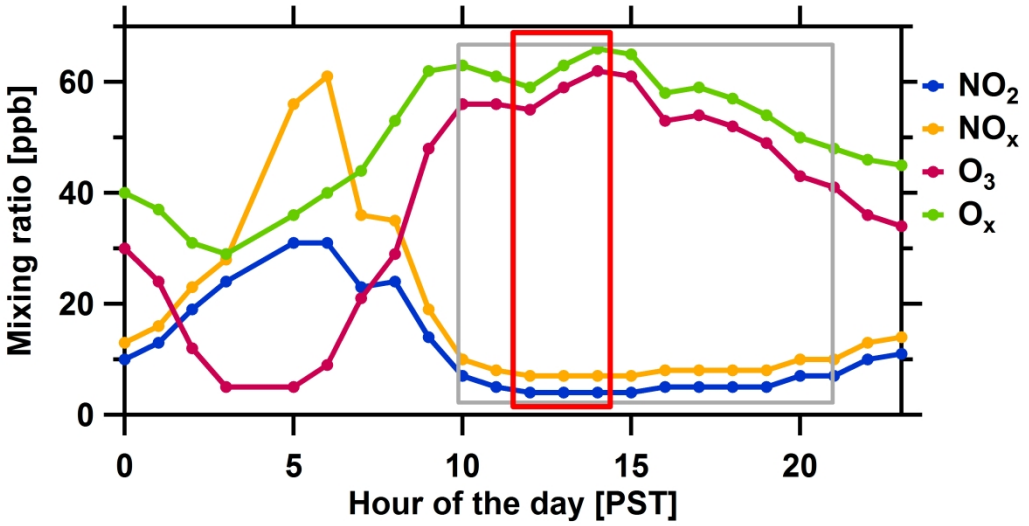
Mixing ratio [ppb]
0
20
40
60
0
5
10
15
20
Hour of the day [PST]
NO2
NOx
O3
Ox

for all the boxes except for the upwind box, B. Considering that the daily emission estimates are in better agreement compared to the hour of measurement, there is a discrepancy in the timing of NO_x emission in the emission inventory. The diurnal profile of NO_2 and the NO_x to NO_2 ratio varies between days as well as seasons and hence we do not attempt to scale up to the yearly NO_x emission. However with regular flights over different times of the day and course of different seasons, the combination of active and passive remote sensing has the potential to constrain and improve NO_x emissions in emission inventories.

Table 3. Daily and hourly NO_x emissions calculated for June 15, 2010 from (i) using derived NO_2 production rate and NO_x and NO_2 diurnal profiles measured at CARB monitoring station at Bakersfield, CA and (ii) NO_X emissions from CARB 2010 emission inventory for that day. Errors represent error due to uncertainty in NO_2 production rates

Box	NO_x Emissions[1] (metric tons)			
	This work		CARB 2010 emission inventory	
	Daily[2]	Hourly[3]	Daily[2]	Hourly[3]
A	0.2 ± 0.5	0.02 ± 0.04	1.1	0.11
B	5.1 ± 0.5	0.40 ± 0.04	1.1	0.11
C	0.4 ± 0.6	0.03 ± 0.05	10.6	1.05
D	10.7 ± 0.9	0.85 ± 0.07	13.5	1.33
E	0.9 ± 0.8	0.07 ± 0.06	2.2	0.22
F	32.1 ± 0.9	2.56 ± 0.07	29.2	2.91

[1]Molecular weight of NO_x (MW_{NOx}) = 46 g/mole.
[2]Daily = 10:00-20:59 PST.
[3]Hourly = hour of our measurement

3.1 Error Estimates

Error in calculated fluxes and source strengths are a function of uncertainties in the measurements of individual species, winds, uncertainties about sinks (dry deposition and oxidation), and the variability of atmospheric state. Previous source strength calculations have found the uncertainty in the wind to be the largest source of error as it was not measured concurrently [10,11]. The uncertainty in the wind measurements is estimated to be around 6%. Thus, the uncertainty in the wind measurement itself has a relatively small effect on the production rates in our study. This uncertainty is very likely not representative of wind variability within the boxes but the variability in wind are captured as part of individual wind measurements.

The overall uncertainty in NO_2 VCD is ~9%. The contributions of different error sources in NO_2 VCD uncertainty is given in Section 2.1. It is assumed that all of NO_2 were located inside the BL. Based on the amount of NO_2 above the BL in the vertical profile through the city center (see Fig. 6) we estimate this leads to a systematic error of around a few percent. The lidar O_3 profile measurements at 90 m vertical resolution have an error of typically 6-10% and can be improved by integration and averaging [45,48]. O_3 data were integrated vertically (~10 points) and horizontally (2-3 points) for flux calculations at each location. As a result, the statistical uncertainties in the integrated O_3 are reduced to ~2%. O_3 data to the ground were extrapolated from measurement at lowest two gates assuming a well-mixed BL (see section 2.3). Based on the difference between measurement at the CARB stations and extrapolated values, we estimate this systematic error to be around 5%. The uncertainty in BLH retrieval for TOPAZ backscatter profile is ~7%. Considering the standard deviation of

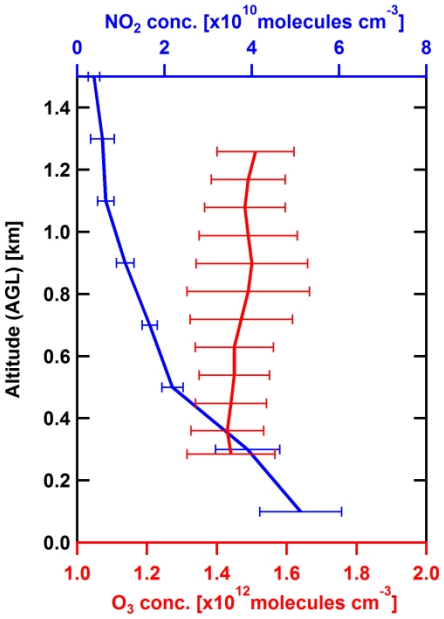
NO2 conc. [x10^10 molecules cm^-3]
0
2
4
6
8
Altitude (AGL) [km]
0.0
0.2
0.4
0.6
0.8
1.0
1.2
1.4
1.0
1.2
1.4
1.6
1.8
2.0
O3 conc. [x10^12 molecules cm^-3]

10% in the O_x' and ~1% in the NO_2 production rates. For an air mass transport time of 1 hour (between production and measurement), Ibrahim et al. [10] estimated the error in the production rate due to chemical transformation of NO_x, based on average atmospheric NO_x lifetime, to be around 10%. Considering that the transport time for our conditions is around 0.5 hour, we estimate the error due to chemical transformation of NO_2 to be less than 5%. The atmospheric lifetime of O_3 is more than 3 times that of NO_x. Hence, we estimate the error in O_x' production rate due to chemical transformation to be smaller than 2%. Thus, the potential error due to entrainment, dry deposition and chemical transformation is in the same order as the total measurement uncertainty in the production rates.

We observed very high local variation in BLH and this could also potentially result in error in the calculated production rates. The BLH variability makes the air column susceptible to exchange with the FT via horizontal transport. We have tried to bind the magnitude of this exchange in two ways: Method A calculates it as a product of the relative amount of air column (with respect to the average) susceptible to this exchange based on the difference in the average BLH measured for the upwind and downwind legs and our measured production rates; Method B calculates the same number based on the maximum and minimum BLH, assuming they occur equally frequent within each box. This is likely an upper limit estimate of such transport, since BLH is something in between most of the time. Note that we only know the BLH along the edge of the boxes and not within the boxes. We find that the uncertainty due to this potential FT exchange accounts for 1-8% (method A) of the overall horizontal flux. Method B yields 15-30% as an upper limit for FT exchange. To our knowledge the horizontally variable BLH as a mechanism for BL-FT exchange has not previously been studied, and deserves further investigation. We consider the error in horizontal fluxes from method A to be most likely representative of uncertainty in the production rates listed in Table 2 due to such an exchange.

4. CONCLUSION AND OUTLOOK

We demonstrated the feasibility of co-deployed active and passive remote sensing instruments aboard a research aircraft to study NO_x emissions and O_x production rates out of an urban area. NO_2 vertical column, O_3 vertical profile and wind profile measurements aboard the aircraft were used to calculate NO_2 and O_x' fluxes from source areas along the flight track.

The advantages to co-deployment of these three remote sensing instruments on a mobile platform for this kind of study are as follows:

1. The flux calculations are fully experimentally constrained. In particular, measurements of wind and BLH along the flight track decouple horizontal and vertical transport; column measurements integrate pollutant concentrations over the BLH, and are inherently insensitive to vertical inhomogeneity.
2. Measurements constrain NO_2, O_3, O_x (O_3+NO_2), enabling studies of NO_x emissions and O_x production rates also over NO_x source areas, i.e., under conditions when O_3 concentrations are reduced due to NO emissions (O_3 titration to form NO_2).
3. Colocation of all three sensors on a single platform minimizes error, and makes the flux calculation straightforward by assuring sampling on similar temporal and spatial scales.

The horizontal flux divergence approach presented here for a case study in the Bakersfield area has comparatively small error for the largest box (Box F) and larger error for the

smallest box (Box C). The overall measurement uncertainty in the individual flux measurement is in the order of 10-11%. The potential error due to entrainment, dry deposition and chemical transformation is of a similar magnitude, and can in the future be further reduced through coupling with atmospheric models. Our measured NO_2 and O_x' production rates reveal higher O_3 production upwind of Bakersfield in an area with active oil and natural gas production. This finding is highly significant within experimental error, and spatially well separated from urban source areas. Comparison of NO_x emissions with the CARB 2010 emission inventory suggest that the NO_x emissions from the urban area are well represented in the inventory. However, the location and timing of the NO_x emissions within the urban area could be improved. In contrast, NO_x emissions over areas with active oil and natural gas production were found to be significantly underestimated; higher background emissions compensate for these local effects over the entire study area. The atmospheric impacts of emissions from oil and natural gas production deserve further investigation.

Models that predict O_3 formation have not previously been constrained by observations at the scale of cities and immediately downwind of cities. The synergistic benefit of combining active and passive remote sensing instruments demonstrated here holds great potential as an innovative tool to improve NO_x emission inventories (emitted amounts and location) as well as constrain O_x production rates experimentally, and over extended areas. The local variations in BLH deserve further investigation as to their role in the exchange of air between the BL and the FT. Further, other trace gases (e.g., formaldehyde and glyoxal) can be measured by AMAX-DOAS and hold largely unexplored potential to extend this approach to the study of VOC oxidation rates. The co-deployment of AMAX-DOAS, TOPAZ lidar and Doppler wind lidar during 51 remaining flights provide a valuable dataset to locate and constrain NO_x emissions over much of California especially the South Coast Air Basin, the Bay area, as well to assess the transport of NO_2 and O_x across the US-Mexican border.

ACKNOWLEDGEMENTS

The authors thank Stuart McKeen (NOAA ESRL, Boulder) for providing the CARB 2010 emission inventory data and the NOAA Twin Otter pilots and flight crew for their support during the campaigns. F.D. acknowledges Halo-Photonics for their help in re-configuring the NCAS Doppler lidar. The scanner for the Doppler lidar was developed with support from CIRES IRP grant to R.M.H. S.B. is recipient of a ESRL/CIRES graduate fellowship. R.V. acknowledges financial support from the California Air Resources Board contract 09-317.

COMPETING INTERESTS

The authors declare no competing interests.

REFERENCES

1. World Health Organisation: Air Quality and Health. 2011; Available at: http://www.who.int/mediacentre/factsheets/fs313/en/. Accessed 09/25, 2013.
2. U.S. Environmental Protection Agency: National Ambient Air Quality Standard (NAAQS). 2012; Available at: http://www.epa.gov/air/criteria.html. Accessed 09/25, 2013.
3. European Commission: Air Quality Standards. 2013; Available at: http://ec.europa.eu/environment/air/quality/standards.htm. Accessed 09/25, 2013.

4. IPCC, 2007: Summary for Policymakers. In: Climate Change 2007: The Physical Science Basis. Contribution of Working Group I to the Fourth Assessment Report of the Intergovernmental Panel on Climate Change [Solomon, S., Qin, D., Manning, M., Chen, Z., Marquis, M., Averyt, K.B., Tignor, M., and Miller, H.L.(eds.)]. Cambridge, United Kingdom and New York, NY, USA: Cambridge University Press.
5. Haagensmit AJ. Chemistry and Physiology of Los-Angeles Smog. Ind. Eng. Chem. 1952;44(6):1342-6.
6. Finlayson-Pitts BJ, Pitts Jr JN. Chemistry of the Upper and Lower Atmosphere. San Diego, CA: Academic Press; 2000.
7. Seinfeld JH, Pandis SN. Atmospheric Chemistry and Physics: from air pollution to climate change. 2nd ed. Hoboken, New Jersey: Wiley-Interscience; 2006.
8. Stedman DH. Photochemical Ozone Formation, Simplified. Environ. Chem. 2004;1(2):65-6.
9. Melamed ML, Solomon S, Daniel JS, Langford AO, Portmann RW, Ryerson TB, et al. Measuring reactive nitrogen emissions from point sources using visible spectroscopy from aircraft. J. Environ.Monit. 2003;5:29-34.
10. Ibrahim O, Shaiganfar R, Sinreich R, Stein T, Platt U, Wagner T. Car MAX-DOAS measurements around entire cities: quantification of NOx emissions from the cities of Mannheim and Ludwigshafen (Germany). Atmos. Meas. Tech. 2010;3(3):709-21.
11. Wang S, Zhou B, Wang Z, Yang S, Hao N, Valks P, et al. Remote sensing of NO2 emission from the central urban area of Shanghai (China) using the mobile DOAS technique. J. Geophys. Res. 2012;117:D13305.
12. Beirle S, Boersma KF, Platt U, Lawrence MG, Wagner T. Megacity Emissions and Lifetimes of Nitrogen Oxides Probed from Space. Science. 2011;333(6050):1737-9.
13. Shaiganfar R, Beirle S, Sharma M, Chauhan A, Singh RP, Wagner T. Estimation of NOx emissions from Delhi using Car MAX-DOAS observations and comparison with OMI satellite data. Atmos. Chem. Phys. 2011;11(21):10871-87.
14. Kleinman LI, Daum PH, Imre D, Lee YN, Nunnermacker LJ, Springston SR, et al. Ozone production rate and hydrocarbon reactivity in 5 urban areas: A cause of high ozone concentration in Houston. Geophys.Res.Lett. 2002;29(10):1467.
15. Senff CJ, Alvarez RJ,II, Hardesty RM, Banta RM, Langford AO. Airborne lidar measurements of ozone flux downwind of Houston and Dallas. J. Geophys. Res. 2010;115:D20307.
16. Clapp L, Jenkin M. Analysis of the relationship between ambient levels Of O-3, NO2 and NO as a function of NOx in the UK. Atmos.Environ. 2001;35(36):6391-405.
17. Warneke C, de Gouw JA, Holloway JS, Peischl J, Ryerson TB, Atlas E, et al. Multi year trends in volatile organic compounds in Los Angeles, California: Five decades of decreasing emissions. J. Geophys. Res. 2012;117:D00V17.
18. Kim S.-W., Heckel A, Frost GJ, Richter A, Gleason J, Burrows JP, et al. NO2 columns in the western United States observed from space and simulated by a regional chemistry model and their implications for NOx emissions. J. Geophys. Res. 2009;114:D11301.
19. Langford AO, Brioude J, Cooper OR, Senff CJ, Alvarez RJ, II, Hardesty RM, et al. Stratospheric influence on surface ozone in the Los Angeles area during late spring and early summer of 2010. J. Geophys. Res. 2012;117:D00V06.
20. Langford AO, Senff CJ, Alvarez RJ,II, Banta RM, Hardesty RM. Long-range transport of ozone from the Los Angeles Basin: A case study. Geophys. Res. Lett. 2010;37:L06807.
21. Neuman JA, Trainer M, Aikin KC, Angevine WM, Brioude J, Brown SS, et al. Observations of ozone transport from the free troposphere to the Los Angeles basin. J. Geophys. Res. 2012;117:D00V09.

22. Sillman S. The relation between ozone, NOx and hydrocarbons in urban and polluted rural environments.Atmos.Environ. 1999;33(12):1821-45.
23. Liu SC, Trainer M, Fehsenfeld FC, Parrish DD, Williams EJ, Fahey DW, et al. Ozone Production in the Rural Troposphere and the Implications for Regional and Global Ozone Distributions. J. Geophys. Res. 1987;92(D4):4191-207.
24. Lin X, Trainer M, Liu SC. On the Nonlinearity of the Tropospheric Ozone Production. J. Geophys. Res. 1988;93(D12):15879-88.
25. Kleinman LI, Daum PH, Lee JH, Lee YN, Nunnermacker LJ, Springston SR, et al. Dependence of ozone production on NO and hydrocarbons in the troposphere. Geophys. Res. Lett. 1997;24(18):2299-302.
26. Carter WPL, Lurmann FW. Evaluation of a Detailed Gas-Phase Atmospheric Reaction-Mechanism using Environmental Chamber Data. Atmos. Environ. 1991;25(12):2771-806.
27. Carter WPL. Computer modeling of environmental chamber measurements of maximum incremental reactivities of volatile organic-compounds. Atmos. Environ. 1995;29(18):2513-27.
28. Ren XR, Harder H, Martinez M, Lesher RL, Oliger A, Simpas JB, et al. OH and HO2 chemistry in the urban atmosphere of New York City. Atmos. Environ. 2003;37(26):3639-51.
29. Volkamer R, Sheehy P, Molina LT, Molina MJ. Oxidative capacity of the Mexico City atmosphere - Part 1: A radical source perspective. Atmos. Chem. Phys. 2010;10(14):6969-91.
30. Sheehy PM, Volkamer R, Molina LT, Molina MJ. Oxidative capacity of the Mexico City atmosphere - Part 2: A ROx radical cycling perspective. Atmos. Chem. Phys. 2010;10(14):6993-7008.
31. Cazorla M, Brune WH, Ren X, Lefer B. Direct measurement of ozone production rates in Houston in 2009 and comparison with two estimation methods. Atmos. Chem. Phys. 2012;12(2):1203-12.
32. Pusede SE, Cohen RC. On the observed response of ozone to NOx and VOC reactivity reductions in San Joaquin Valley California 1995-present. Atmos. Chem. Phys. 2012;12(18):8323-39.
33. Richter A, Burrows JP, Nuss H, Granier C, Niemeier U. Increase in tropospheric nitrogen dioxide over China observed from space. Nature. 2005;437(7055):129-32.
34. van der A RJ, Eskes HJ, Boersma KF, van Noije TPC, Van Roozendael M, De Smedt I, et al. Trends, seasonal variability and dominant NOx source derived from a ten year record of NO(2) measured from space. J. Geophys. Res. 2008;113(D4):D04302.
35. Kim S-W, Heckel A, McKeen SA, Frost GJ, Hsie E-Y, Trainer MK, et al. Satellite-observed US power plant NOx emission reductions and their impact on air quality. Geophys. Res. Lett. 2006;33(22):L22812.
36. Konovalov IB, Beekmann M, Burrows JP, Richter A. Satellite measurement based estimates of decadal changes in European nitrogen oxides emissions. Atmos. Chem. Phys. 2008;8(10):2623-41.
37. Russell AR, Valin LC, Bucsela EJ, Wenig MO, Cohen RC. Space-based Constraints on Spatial and Temporal Patterns of NOx Emissions in California, 2005-2008. Environ. Sci. Technol. 2010;44(9):3608-15.
38. Russell AR, Valin LC, Cohen RC. Trends in OMI NO2 observations over the United States: effects of emission control technology and the economic recession. Atmos. Chem. Phys. 2012;12(24):12197-209.
39. Ryerson T, Andrews AE, Angevine WM, Bates TS, Brock CA, Cairns B, et al. The 2010 California research at the Nexus of air quality and climate change (CalNex) field study. J. Geophys. Res. 2013;118:5830-66.

40. Zaveri RA, Shaw WJ, Cziczo DJ, Schmid B, Ferrare RA, Alexander ML, et al. Overview of the 2010 Carbonaceous Aerosols and Radiative Effects Study (CARES). Atmos. Chem. Phys. 2012;12(16):7647-87.
41. Volkamer R, Coburn S, Dix B, Sinreich R. MAX-DOAS observations from ground, ship, and research aircraft: maximizing signal-to-noise to measure 'weak' absorbers. Proc. SPIE. 2009;7462-746203.
42. Baidar S, Oetjen H, Coburn S, Dix B, Ortega I, Sinreich R, et al. The CU Airborne MAX-DOAS instrument: vertical profiling of aerosol extinction and trace gases. Atmos. Meas. Tech. 2013;6(3):719-39.
43. Platt U, Stutz J. Differential Optical Absorption Spectroscopy: Principles and Applications. Heidelberg: Springer Verlag; 2008.
44. Oetjen H, Baidar S, Krotkov NA, Lamsal LN, Lechner M, Volkamer R. Airborne MAX-DOAS measurements over California: Testing the NASA OMI tropospheric NO2 product. J. Geophys. Res. Atmos. 2013;118:7400-13.
45. Alvarez RJ,II, Senff CJ, Langford AO, Weickmann AM, Law DC, Machol JL, et al. Development and Application of a Compact, Tunable, Solid-State Airborne Ozone Lidar System for Boundary Layer Profiling. J. Atmos. Ocean. Technol. 2011;28(10):1258-72.
46. Browell EV, Ismail S, Shipley ST. Ultraviolet Dial Measurements of O-3 Profiles in Regions of Spatially Inhomogeneous Aerosols. Appl. Opt. 1985;24(17):2827-36.
47. Davis KJ, Gamage N, Hagelberg CR, Kiemle C, Lenschow DH, Sullivan PP. An objective method for deriving atmospheric structure from airborne lidar observations. J. Atmos. Ocean. Technol. 2000;17(11):1455-68.
48. Langford AO, Senff CJ, Alvarez RJ, II, Banta RM, Hardesty RM, Parrish DD, et al. Comparison between the TOPAZ Airborne Ozone Lidar and In Situ Measurements during Tex AQS 2006. J. Atmos. Ocean. Technol. 2011;28(10):1243-57.
49. Pearson G, Davies F, Collier C. An analysis of the performance of the UFAM Pulsed Doppler Lidar for observing the boundary layer. J. Atmos. Ocean. Technol. 2009;26(2):240-50.
50. California Department of Conservation: GIS Mapping. 2013; Available at: http://www.conservation.ca.gov/dog/maps/Pages/GISMapping2.aspx. Accessed 09/25, 2013.
51. California Air Resource Board: 2010 CalNex Modeling Inventory. Available at: http://orthus.arb.ca.gov/calnex/data/. Accessed 09/25, 2013.
52. Hauglustaine DA, Granier C, Brasseur GP, Megie G. The Importance of Atmospheric Chemistry in the Calculation of Radiative Forcing on the Climate System. J. Geophys. Res. 1994;99(D1):1173-86.

Peer-review history:
The peer review history for this paper can be accessed here:
http://www.sciencedomain.org/review-history.php?iid=323&id=10&aid=2531

Addendum Section 3.3

Comment 1: For the calculation of O_3 production rates, why was the average wind speed over the entire column used instead of pairing height dependent wind speed with height dependent O_3 concentration? Also for the calculation of NO_2 production rate, it was assumed that the wind speed up to the BLH was constant. Was this true during the campaign? How would the results vary if vertical profiles for NO_2 (e.g. calculated based on VCD) and O_3 and the height dependent wind speed were used in the calculations?

The O_3 profiles over the BLH for this flight were relatively flat (see Fig. 3.3.6 in page 65). The vertical variability in O_3 mixing ratio over the BLH is smaller compared to the uncertainty in the O_3 measurements. The wind speed profiles varied along the flight track, and we use the average instantaneous wind over the BLH to calculate the flux because this average wind is very well known. Notably, any vertical variability in horizontal winds does not affect the flux calculation given the O_3 profile is constant. The standard error in the wind speed over the BLH is 0.14 ms^{-1} (average value for the flight) which is smaller compared to the wind measurement uncertainty (6%). Given the flatness of the O_3 profiles, considering the profiles for O_3 and wind speed would not change the results shown here.

For NO_2 the vertical distribution shows significant variability over the height of the air column. We have measured this distribution during a low approach over Bakersfield (see Fig. 3.3.6 in page 65), and several other case studies (see Fig. 3.2.8 in page 44 for the variability in NO_2 profiles within the LA basin). We use the average wind speed over the BLH corresponding to each NO_2 measurement for NO_2 production rate calculations, rather than extrapolating the NO_2 profiles and using altitude dependent wind profiles. The profile in Fig. 3.3.6 was flown traversing Box D shortly after the completion of that box. For this profile ~80% of the NO_2 is located below 800m, and virtually all NO_2 is located below 1.5km. Given that BLH was higher than 800m on average, we expect an error ~10% in the flux calculations. This is comparable or smaller to other error sources. Finally, some angle scans were conducted at regular intervals during this (and other) flight(s), and the spectra from these scans in principle facilitate information that can be used to assess the variability of NO_2 profiles along the flight track. However, this data was not leveraged in the present analysis due to time limitations and the scope of the paper. A further refined analysis that leverages angle scans could in principle be used in conjunction with vertically resolved wind measurements to further improve the results.

Notably, NO_2 makes a minor contribution (few percent) to the O_x production rates. Thus, considering the profiles of NO_2, O_3 and wind speed will not change our conclusions about O_x fluxes.

Comment 2: In instances where the aerosol backscatter signal is low – the BLH cannot be determined accurately – what is used in the calculations for the production rates? Since the average column densities are used, the flux through a given segment of a box would be highly sensitive to the BLH estimate. Is this uncertainty incorporated in estimates for production rates?

For instances where BLH could not be retrieved from aerosol backscatter signal, the BLH was interpolated from adjacent measured BLH. Uncertainty in the retrieval of BLH was incorporated

in the error calculation for production rates but uncertainty due to interpolation of BLH is not included. Please refer to section 3.1 of the manuscript (Page 64) for discussion on uncertainty related to BLH variability in flux calculations.

Comment 3: In Table 1, why are times of the flights for boxes B and E not included?

Boxes B and E were created for comparison purposes by interpolating measured NO_2, O_3 and wind data for the western legs. These boxes were only partly flown, and therefore the times are not included in Table 1. Please refer to section 2.4 of the manuscript.

Comment 4: In Table 1, the boundary layer height varies greatly between min and max values for most of the boxes (factor of 1.5 – 2). Is this variation over the course of the flight? Are separate BLH's used for different segments of each box in the calculation of production rates? Some further detail in how these rates were calculated would help the reader.

The minimum and maximum boundary layer heights given in Table 1 are variation in BLH along the flight track for each individual box flown. The BLH measured at each point along the flight track was used to calculate the O_3 vertical column and average wind speed and direction up to the BLH at that point. BLH was interpolated where no BLH retrievals were possible. We used NO_2 and O_3 vertical columns measured at that particular location to compute the O_x VCD. The NO_2 and O_x columns are then multiplied by the corresponding wind measurements to derive flux at each location along the flight track. The calculation of production rates is based on sum of individual flux measurements along a closed loop. The calculation of production rates is described in detail in section 2.5 of the manuscript (page 57).

3.4. Airborne MAX-DOAS measurements over California: Evaluation of NO_x emission inventories in atmospheric models.

3.4.1. Introduction

Better quality of life in large cities and urban areas are often offset by a severe degradation of air quality. Atmospheric chemistry models are used by air quality regulating agencies to forecast air quality and warn people of impending adverse conditions. Along with the meteorology and chemistry of pollutants, emission inventories of the pollutants are major components of these models. Emission inventories often lag behind by few years and are one of the main sources of uncertainty in the model results. In addition, with new stricter regulations, emissions of pollutants such as nitrogen oxides (NO_x = NO + NO_2) and volatile organic compounds (VOCs) have been decreasing steadily over the last few decades in urban areas such as South Coast Air Basin (SCAB) (e.g. Russell et al., 2010, Warneke et al., 2012, Pollack et al., 2013). Thus, the emission inventories need to be constantly updated and evaluated in order to improve the model performances.

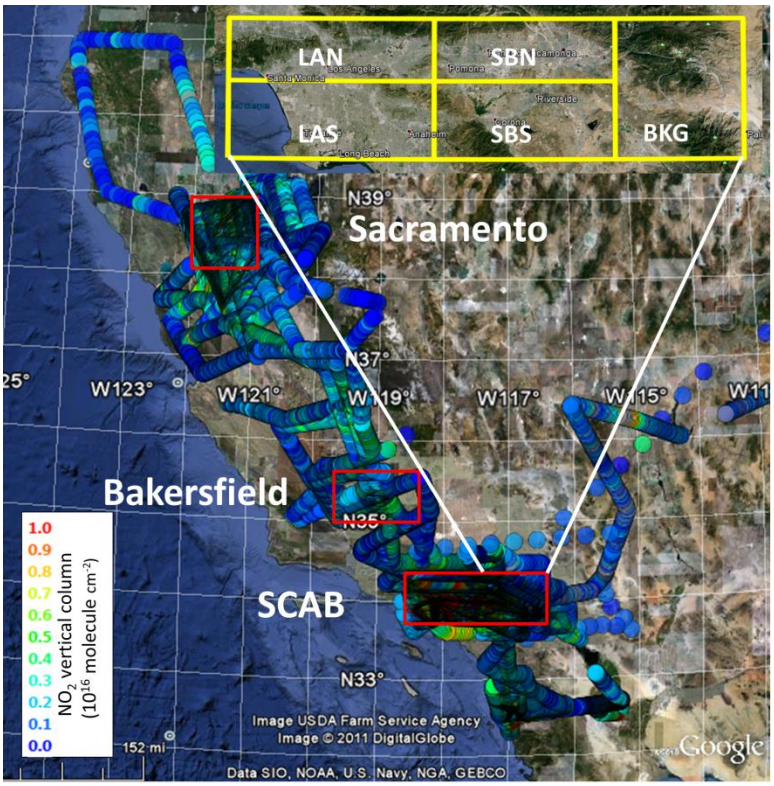

Figure 3.4.1: *Map of California showing all the NO_2 vertical columns measured by CU AMAX-DOAS during CalNex and CARES 2010 field campaigns. The three rectangles highlight the study areas namely the South Coast Air Basin (SCAB), Sacramento valley and Bakersfield for the model comparison. The five sub-division of the SCAB is shown in the inset.*

Here we compared our NO_2 vertical column measurements with NO_2 vertical column outputs from two different atmospheric chemistry models with three different NO_x emission inventories; (1) Weather Research and Forecasting - Chemistry (WRF-Chem) model with NEI-2005 emission inventory and (2) Community Multi-scale Air Quality (CMAQ) model with (i) CARB draft 2005/2008 (referred to as CARB 2008 from here on) and (ii) CARB 2010 emission inventories. Brief details about the two models can be found in Table 3.4.1.

3.4.2. Methods

The CU AMAX-DOAS measurement of NO_2 vertical columns during the CalNex and CARES campaigns in summer 2010 has been described in detail in section 3.1 and 3.2. The measured NO_2 vertical columns have a spatial foot print of ~1km which is comparable the spatial scale predicted by air quality models. This makes the CU AMAX-DOAS data collected during CalNex and CARES field campaigns an ideal dataset to evaluate emissions in air quality models over a large spatial region. The small footprint of the measurement also allows us to clearly identify local NO_2 hotspots and pollution sources.

We compared the NO_2 vertical columns below the aircraft flight altitude from the models outputs corresponding to the CU AMAX-DOAS observations along the flight tracks. The comparisons were made over three different urban areas in California namely the South Coast Air Basin, the Sacramento valley and Bakersfield. Further, to understand the spatial variability within the South Coast Air Basin, it was sub-divided into 5 regions: Los Angeles Basin North (LAN) (34.00-34.20 N, 117.8-118.6 W) and Los Angeles Basin South (LAS) (33.75-34.00 N, 117.8-118.6 W) at the coast, San Bernardino Valley North (SBN) (34.00-34.20 N, 117.1-117.8 W) and San Bernardino Valley South (SBS) (33.75-34.20 N, 117.1-117.8 W) in the inland and the background region to the further east (33.75-34.20 N, 117.1-116.6 W). Figure 3.4.1 show the three study areas overlaid on the map of the measured NO_2 vertical columns by CU AMAX-DOAS during the two campaigns in California. The sub-division of the SCAB is shown in the Fig 3.4.1 inset. The Los Angeles basin north included city of Los Angeles, Pasadena, as well as Los Angeles International Airport. City of Anaheim, Long Beach, Port of Long Beach are in the Los Angeles basin south. The San Bernardino basin north encompassed the Riverside-San Bernardino-Ontario metropolitan areas and the main thorough fare between the east and the west region of SCAB. The box designated as “background” (BKG) does not include any major sources of NO_x. Observed and modeled NO_2 vertical columns in each region were also segregated into weekday and weekend to study the weekday-weekend trend in NO_2 in the area. For Sacramento and Bakersfield areas, weekend observations were very limited and hence only weekday data were compared. The observed and modeled mean/median NO_2 column amounts for each area were compared.

	CMAQ		WRF-Chem
Version	4.7.1	5.0.1	3.1
Domain	4km x 4km	4km x 4km	4km x 4km
# of vertical levels	30	30	60
Boundary conditions	RAQMS	MOZART-4	NCEP GFS
Biogenic emissions	BEIGIS	MEGANv2.04	BEIS3.13
Anthropogenic emissions	CARB 2005/2008	CARB 2010	EPA NEI 2005
Chemical mechanism	SAPRC 999	SAPRC 07T	RACM

Table 3.4.1: *Details about the CMAQ and WRF-CHEM atmospheric chemistry models used for the study.*

3.4.3. Results and Discussion

3.4.3.1 South Coast Air Basin (SCAB)

The average NO_2 vertical column observed by CU AMAX-DOAS over the SCAB region was $8.8x10^{15}$ molecules cm^{-2}. The observed average value is consistent with the decrease in NO_2 VCD by $1.1x10^{15}$ molecules cm^{-2} per year for the basin based on OMI satellite observations from 2005-2008 reported by Russell et al. (2010). The average model predictions using NEI 2005 and CARB 2008 were $2.9x10^{16}$ and $1.9x10^{16}$ molecules cm^{-2} respectively for the area, a factor of ~2-3 larger than the observation. The model predictions with the newest CARB emission inventory, CARB 2010 ($1.1x10^{16}$ molecules cm^{-2}) is in very good agreement with our measurements.

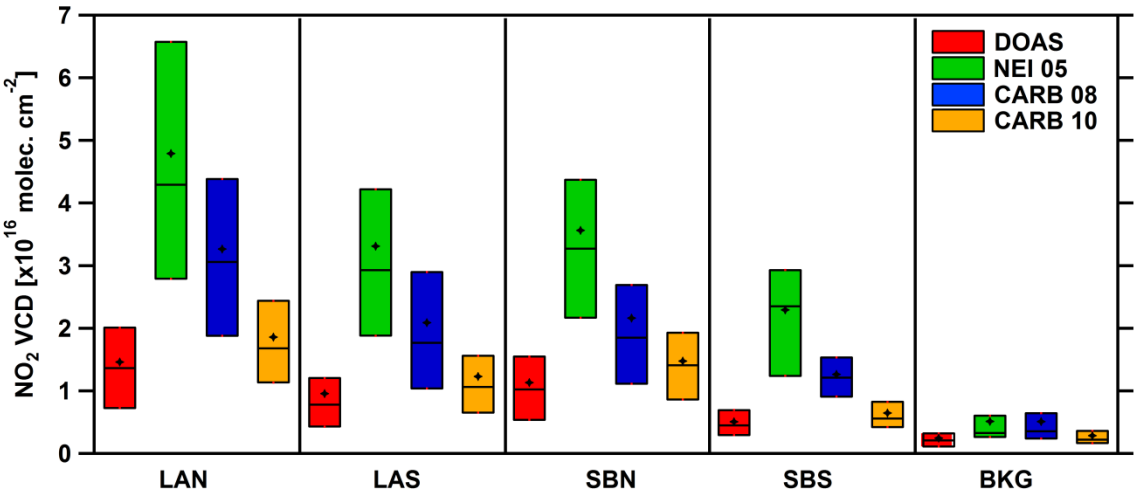

Figure 3.4.2: *Spatial trend in measured (red) and modeled (green: NEI 2005, blue: CARB 2008 and orange: CARB 20010) NO_2 vertical columns in the South Coast Air Basin. The bottom, middle and top lines of the box represent the 25^{th}, 50^{th} and 75^{th} percentile of the data. The average values are indicated by the stars.*

i) Spatial trend in NO_2 across the basin

Figure 3.4.2 shows the spatial trend in observed and modeled NO_2 across the SCAB. As expected, higher NO_2 was observed in the western part over the Los Angeles basin north which includes major NO_x sources like city of Los Angeles, and Los Angeles International airport and decreased towards the eastern and southern part of the basin. The background region with no major local sources of NO_x had the least amount of NO_2 (~17% of LAN) and is similar to what was observed in the Sacramento and Bakersfield area (see Fig. 3.4.4 and 3.4.5). The NO_2 columns in the LAS, SBN and SBS were 35%, 22% and 65% lower respectively compared to the Los Angeles basin. All the model results suggested similar spatial trend of decreasing NO_2 to the east and south. The relative decrease in NO_2 columns were very well captured in the models especially with the CARB 2010 emission inventory (within 2% for the mean and 10% for the median). Further, all model results indicated 85-90% decrease in NO_2 for the background region compared to LAN.

ii) Weekday-weekend trend in NO_2

Due to the reduction in heavy-duty diesel engine trucks on weekends, lower NO_x emissions have been observed on the weekends in California (Chinkin et al., 2003, Harley et al., 2005). This has been attributed to be the major reason for the weekend ozone effect in the SCAB (Pollack et al., 2012 and references within). We observed 20-40% lower NO_2 on weekend compared to weekdays in various regions in the SCAB and this decrease is consistent with the previous studies (e.g. Pollack et al., 2012). The decrease was larger over the source regions (LAN, LAS and SBN). Figure 3.4.3 shows the weekend to weekday ratio in NO_2 vertical columns observed over the SCAB.

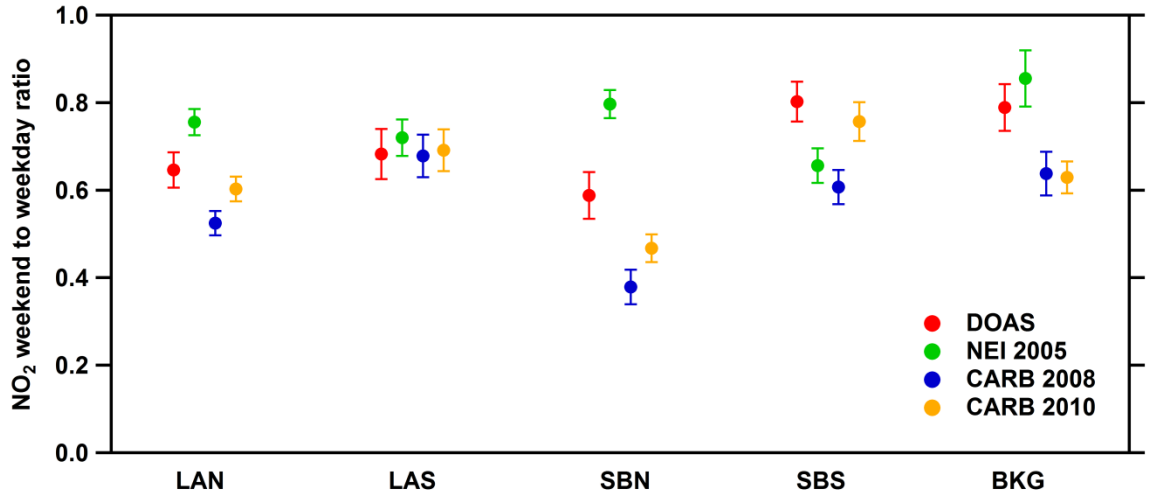

Figure 3.4.3: *Weekend to weekday ratio of measured (red) and modeled (green: NEI 2005, blue: CARB 2008, and orange: CARB 2010) NO_2 vertical columns in the South Coast Air Basin.*

All the models results showed decrease in NO_2 over the weekend. However the extent of reduction varied between the different emissions inventories in the model. Again, CARB 2010 results were in better agreement with the measurements compared to the older emission inventories. CMAQ simulations with both CARB 2008 and CARB 2010 predicted much larger reductions (50-60% and 25-55% respectively) whereas WRF-chem results with NEI 2005 were only lower by 15-35% across the SCAB. CMAQ results also showed larger reductions in the eastern part of the basin (see SBN and BKG in Fig 3.4.3). Further studies would be required to pinpoint if this mismatch is related to oxidative capacity, transport or emission inventory in the model. In general, observations and model simulations were consistent with the regions with the largest reduction in NO_2 over the weekend. LAN and SBN were predicted to experience the largest reduction in NO_2 on weekends.

3.4.3.2 Sacramento Valley

Significantly lower NO_2 was observed over the Sacramento Valley area compared to the SCAB. The average observed NO_2 in the area was 2.7×10^{15} molecules cm^{-2}. Figure 3.4.4 shows the box plot of NO_2 in the Sacramento area as observed by the CU AMAX-DOAS and predicted by the model simulations. The model predictions were higher (factor of 1.1 (CARB 2010) – 2 (NEI 2005)) but much closer to observations in comparison to the SCAB.

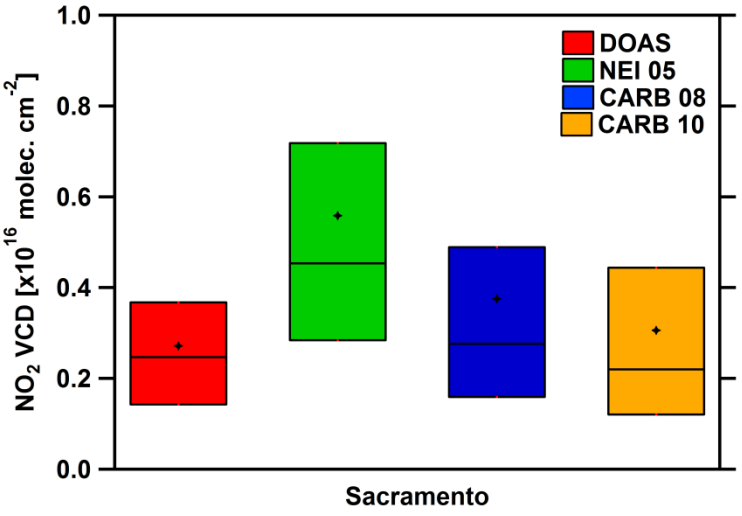

Figure 3.4.4: *Box plot showing measured (red) and modeled (green: NEI 2005, blue: CARB 2008 and orange: CARB 2010) NO_2 vertical columns in the Sacramento valley. The bottom, middle and top lines of the box represent the 25^{th}, 50^{th} and 75^{th} percentile of the data. The average values are indicated by the stars.*

3.4.3.3 Bakersfield area

We had only four flights that passed over the Bakersfield area, one in the morning and three in the afternoon. The box plot of the observed and modeled NO_2 vertical columns for these limited flights is shown in Fig. 3.4.5. The average NO_2 column measured by the CU AMAX-DOAS over the region was $2.3x10^{15}$ molecules cm^{-2} and is similar in magnitude to the Sacramento area and the background box (BKG) in SCAB. Again, results with CARB 2010 EI (mean: $2.3x10^{15}$ molecules cm^{-2}) showed excellent agreement with the observations. Model results with NEI 2005 and CARB 2008 showed large difference between the mean and the median indicating likely presence of large isolated NO_x sources or plumes. This also highlights potential bias created due to limited data set over Bakersfield. However, this issue is not present with the new emissions inventory.

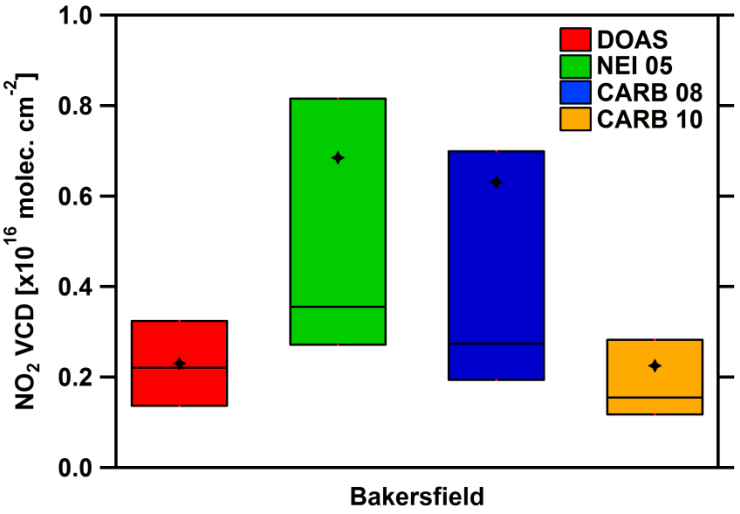

Figure 3.4.5: *Box plot showing measured (red) and modeled (green: NEI 2005, blue: CARB 2008 and orange: CARB 2010) NO_2 vertical columns in the Bakersfield area, CA. The bottom, middle and top lines of the box represent the 25^{th}, 50^{th} and 75^{th} percentile of the data. The average values are indicated by the stars.*

3.4.4. Conclusion

NO_2 vertical columns measured by CU AMAX-DOAS during the CalNex and CARES campaigns in 2010 were compared with WRF-Chem (with NEI 2005) and CMAQ (with CARB 2008 and 2010 emission inventories) model simulation results to evaluate the NO_x emission inventories used in the atmospheric chemistry models. Comparisons were performed over the South Coast Air Basin, Sacramento valley and Bakersfield. The model results were on average a factor of 2-3 larger compared to the observations with NEI 2005 and CARB 2008. In contrast,

CMAQ simulation results with CARB 2010 emission inventory was in very good agreement with the observations (within 30% in the SCAB and 10% in Sacramento and Bakersfield).

The SCAB was sub-divided into five regions to evaluate the spatial variation. Higher NO_2 was observed in the northwestern part of the basin and decreased to the east and south. All the models predictions were consistent with the observation on the relative decrease in NO_2 columns to the east and south despite the difference in absolute magnitude. Lower NO_2 columns (20-40%) were observed during weekends compared to weekday in the SCAB. This trend was well captured by the models though the extent of decrease varied by emission inventory. Model results with both CARB 2008 and 2010 showed a larger relative reduction in NO_2 compared to observation, in particular to the eastern part of the basin. Further studies would be needed to pin point the cause for this mismatch. We find model results for NO_2 in California to have significantly improved with the new CARB 2010 emission inventory.

3.5 Measurements of formaldehyde and glyoxal vertical columns in South Coast Air Basin

3.5.1 Introduction

Formaldehyde (HCHO) and glyoxal (CHOCHO) play important roles in atmospheric chemistry as tracer molecules for photochemistry. HCHO photolysis produces HO_x radicals, a major oxidizer in the atmosphere, which sustains photochemical production of ozone (O_3) and secondary organic aerosols (SOA) (Finlayson-Pitts and Pitts Jr, 2000). Sources of HCHO include direct emissions from biomass burning (Lee et al., 1997), vehicular exhaust, industrial activities (Anderson et al., 1996, Parrish et al., 2012) as well as secondary production from hydrocarbons like alkanes and alkenes (Finlayson-Pitts and Pitts Jr, 2000, Parrish et al., 2012). Contributions of primary vs secondary sources for HCHO differ greatly by location. For example, Garcia et al. (2006) reported >30% contribution from primary sources in Mexico City. In contrast, the contribution from primary sources was only around 5% in Houston, TX (Parrish et al., 2012). It is very important to differentiate primary and secondary sources of HCHO for regulatory purposes in order to identify appropriate control measures. Because of its relatively large secondary source, HCHO is also used as a proxy for VOC oxidation.

Glyoxal, the simplest alpha dicarbonyl, is a novel indicator molecule for active photochemistry (Volkamer et al., 2005). Sources for CHOCHO in the atmosphere are dominated by secondary productions from oxidation of precursor hydrocarbons with two or more carbon atoms (Calvert et al., 2002, Volkamer et al., 2007). Our knowledge on the primary sources of CHOCHO is currently very limited but minor amounts have been reported in tailpipe emissions (Grosjean et al., 2001, Kean et al., 2001). CHOCHO is a known direct precursor for SOA (Liggio et al., 2005a, Liggio et al., 2005b, Volkamer et al., 2007, Volkamer et al., 2009). The role of SOA as a source of CHOCHO is currently an active field of research in atmospheric chemistry (e.g. Washenfelder et al., 2011, Waxman et al., 2013). Recent results show that uptake of CHOCHO to SOA could be reversible (Kroll et al., 2005, Kampf et al., 2013). Glyoxal is a short lived species with average atmospheric life time of ~3 hours (Fu et al., 2008, Myriokefalitakis et al., 2008) and hence airborne measurements of CHOCHO can be used to identify photochemical hot spots for VOC oxidation and SOA formation.

CU AMAX-DOAS (Volkamer et al., 2009, Baidar et al., 2013) measurements during CalNex (Ryerson et al., 2013) and CARES (Zaveri et al., 2012) field campaigns in summer 2010 provided an opportunity of retrieve high resolution maps of HCHO and CHOCHO in California especially in the South Coast Air Basin (SCAB) and Sacramento area. Here, we present a case study from two morning flights on July 16 and 17, 2010 in the SCAB to demonstrate the potential and feasibility of HCHO and CHOCHO vertical column retrieval from CU AMAX-DOAS measurements. Brief discussions on the retrieval technique, horizontal distribution of the two species and glyoxal to formaldehyde ratio are presented. We also compared model HCHO

and CHOCHO outputs from two atmospheric models namely CMAQ (EI: CARB 2010) and WRF-Chem (EI: NEI 2005 and CARB 2010) with the measured vertical columns.

3.5.2 Data Retrieval

Analysis of the CU AMAX-DOAS measured atmospheric absorption spectra for HCHO and CHOCHO was performed using the DOAS method (Platt and Stutz, 2008). Briefly, the DOAS approach relies on the separation of the narrow band absorption signatures of trace gases from broad band absorption and scattering features. A quantity known as differential slant column density (dSCD) of trace gases are retrieved in a set wavelength window by simultaneously fitting the absorption cross-sections of the known absorbers in that window using a non-linear least square fitting procedure. For HCHO dSCD retrievals, a spectral region of 335-357 nm was chosen and absorption cross-sections of NO_2 (at 220 K and 294 K), O_3 (at 223 K and 243 K), O_4 and HCHO, a Ring spectrum and a third order polynomial was included in the fit. Absorption cross-section of NO_2 (at 220 K and 294 K), O_3 (223 K), O_4, H_2O, and CHOCHO, a Ring spectrum and a third order polynomial was fitted in the wavelength window of 433-460 nm for CHOCHCO dSCD retrievals. 3-10 spectra with 2 seconds integration time for each EA were averaged to improve the signal to noise for HCHO and CHOCHO DOAS retrievals.

The retrieved HCHO and CHOCHO dSCDs were converted to vertical column densities (VCDs) using the concept of optimal estimation by Rogers (2000). This technique was also used to retrieve vertical profiles of trace gases (NO_2, CHOCHCO, HCHO and H_2O) from CU AMAX-DOAS measurements during low approaches and is described in detail in Baidar et al. (2013). Generally, dSCDs are converted into VCDs using the quantity known as differential air mass factor (dAMF; dAMF = dSCD/VCD). Calculation of dAMF requires knowledge of vertical distribution of trace gas of interest as well as aerosol. Since the magnitude as well as vertical distribution of pollutants such as HCHO and CHOCHO is highly variable in the polluted urban environment like Los Angeles Basin, we used the elevation angle (EA) scans performed at flight altitude >1500 m above ground level (agl) to constrain the problem and retrieve the VCD using the inversion based on optimal estimation. Sensitivity studies showed that vertical columns could be retrieved very reliably using this technique (see Section 3). The EA scan at flight altitude usually included the following angles; ±90, ±20, ±10, ±5, ±2, and 0 with +90 being the zenith view and -90 being the nadir view. A set of EA scan containing all or some of these angles were used to retrieve the vertical columns of HCHO and CHOCHO.

The vertical column retrieval algorithm builds on the algorithm used to retrieve vertical profiles and hence will only be introduced here briefly. In the linearized form, a set of measured trace gas SCDs, $\boldsymbol{y}$ is related to the trace gas vertical profile, $\boldsymbol{x}$ such that

$$\boldsymbol{y} = \mathbf{K}\boldsymbol{x} + \varepsilon \qquad (1)$$

where **K** is the weighting function matrix that expresses the sensitivity of measurement ***y*** to true profile ***x***. The maximum a posterior solution to the above problem using optimal estimation is given by

( ) ( ) (2)

where $\boldsymbol{x_a}$ is the a priori profile, and $\mathbf{S_\varepsilon}$ and $\mathbf{S_a}$ are the measurement error and a priori error covariance matrices respectively. A priori profile is used to constrain the problem as it is generally ill-posed. $\mathbf{S_\varepsilon}$ was constructed using the square of the DOAS fit error as the diagonal elements and the non-diagonal elements were set to 0 assuming the errors are uncorrelated. The a priori error covariance matrix, $\mathbf{S_a}$ was constructed with the diagonal elements defined as

$$\mathbf{S_a}[i, i] = (\alpha \,.\, \boldsymbol{x_{a\,[i]}})^2 \qquad (3)$$

Here, α is the turning parameter used to minimize the residual between the measured and modeled SCDs using the retrieved profiles while avoiding spurious oscillations in the retrieved profiles. The value of α was determined by L curve method (e.g. Hansen, 1992, Steck, 2002). L curve method is a popular technique to determine the regularization parameter in Phillips-Tikhonov regularization. In this work, L curve was constructed by the residual norm, $\|\boldsymbol{y} - \mathbf{K}\boldsymbol{x}\|$ and the error norm of the solution, $\|\boldsymbol{x_e}\|$. The residual norm decreases monotonically with α while the error norm increases monotonically with each iteration. Thus, the curve formed by the error norm of the solution vs the residual norm has a characteristic L shape. Figure 3.5.1 shows the points of L-curve from the sensitivity studies (see section 3). The point with the maximum curvature balances the minimization of the residual norm and the error norm and provides the optimal solution. We used the triangle method (Castellanos et al., 2002) to determine the optimal solution for α. The non-diagonal elements of $\mathbf{S_a}$ is defined as described in Baidar et al. (2013).

The vertical column is then the sum of the individual element of the retrieved profile and is given by

$$\sum \qquad (4)$$

where $\boldsymbol{x_i}$ is the trace gas concentration at retrieval grid, i and ΔH_i is the height of that retrieval grid.

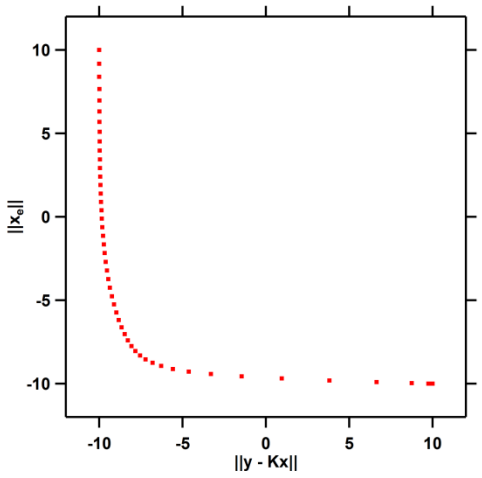

Figure 3.5.1: *Example of L curve formed by the residual norm vs the solution error norm used to determine the optimal value of α.*

3.5.3 Sensitivity Studies

Sensitivity studies using the radiative transfer model (RTM) McArtim (Deutschmann et al., 2011) were performed to validate the technique to retrieve the vertical columns as well as estimate uncertainties due to a priori profile, and aerosol load. Six CHOCHO profiles of various shapes with vertical columns ranging from $2.5x10^{14}$ to $2.5x10^{16}$ molecules cm^{-2}, five different aerosol scenarios with AOD ranging from 0 to 0.5 was considered for the study. The different CHOCHO profiles used for this study are shown in Fig. 3.5.2. CHOCHO SCDs for different EAs were simulated for each CHOCHO profile under the scenario with AOD=0.3 using McArtim. A 10% Gaussian noise was added to the SCDs before using them as the input SCDs in the inversion algorithm to retrieve vertical columns. Vertical columns were retrieved for the above mentioned five aerosol conditions using the six CHOCHO profiles as a priori.

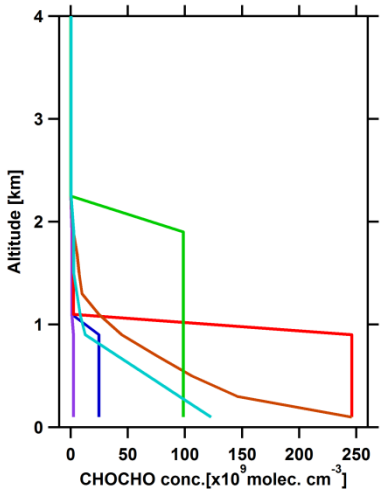

Figure 3.5.2: *Different CHOCHO profiles used for the sensitivity studies. The vertical columns for the profiles range from $2.5x10^{14}$ – $2.5x10^{16}$ molecules cm^{-2}.*

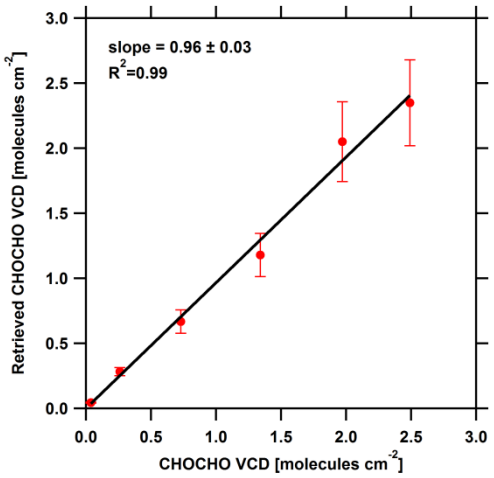

Figure 3.5.3: *Correlation plot of mean retrieved CHOCHO vertical columns for the different aerosol and a priori conditions (see Fig. 3.5.2) and true CHOCHO vertical columns. Error bars represent standard deviation of the retrieved vertical columns for the different conditions.*

The correlation between the mean retrieved CHOCHO vertical columns for all the aerosol load and a priori conditions (n=30 for each point) and true CHOCHO vertical columns is shown in Figure 3.5.3. The linear least square fit through the origin has a slope of 0.96 and a correlation coefficient of 0.99 indicating that the technique is well suited for retrieval of vertical columns of trace gases. The error bars in the y-axis represents the standard deviation of the retrieved vertical columns and is in the order of 9-14%. The variability between the retrieved vertical columns for a given aerosol scenario using different a priori CHOCHO profiles provides insight to the uncertainty due to a priori conditions. Similarly, the variability in VCDs for a given a priori profile but various aerosol loads gives uncertainty due to aerosol conditions. The a priori is the larger source of uncertainty (~12%), while the aerosol load has ~7% contribution in the total uncertainty. Uncertainties due to other parameters such as surface albedo, single scattering albedo are expected to be very small (<2%) (Baidar et al., 2013).

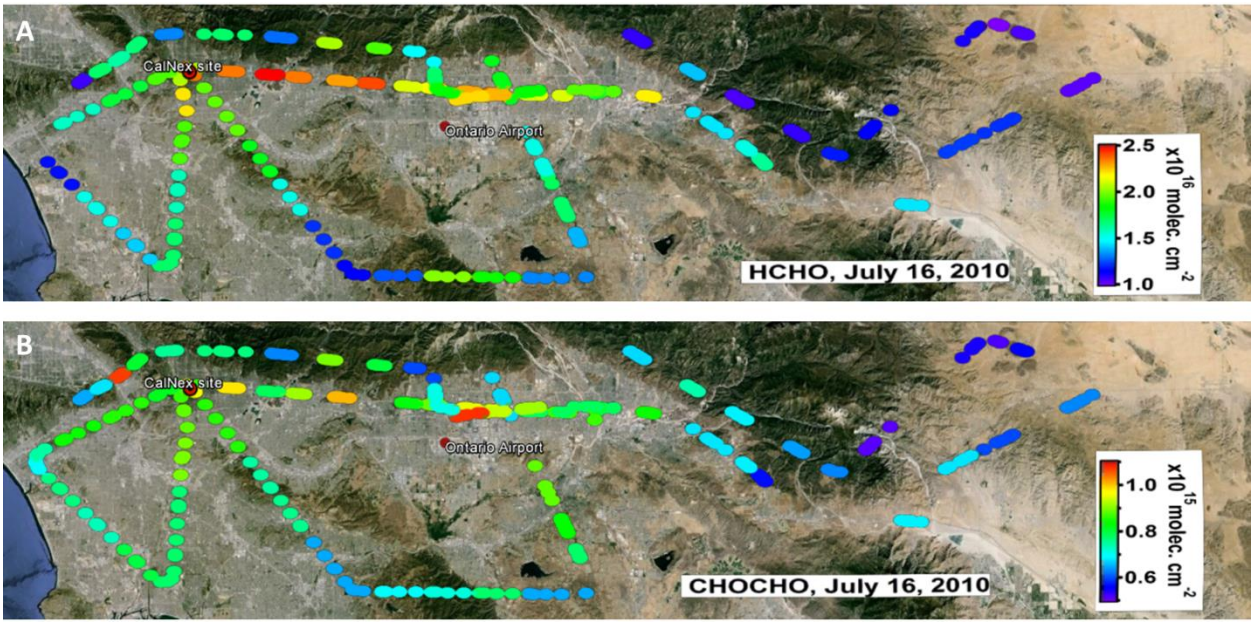

Figure 3.5.4: *Vertical columns of (A) HCHO and (B) CHOCHO measured over the South Coast Air Basin during a flight on July 16, 2010.*

3.5.4 Results

Figure 3.5.4 and 3.5.5 show maps of HCHO and CHOCHO VCD distribution in the SCAB from RF#46 on July 16, 2010 (10:30-14:10 PDT) and RF#48 on July 17, 2010 (10:30-14:10 PDT) respectively. Since the individual spectra were averaged for DOAS analysis of HCHO and CHOCHO, the horizontal footprint is larger compared to NO_2 VCDs. However, the maps reveal a clear trend in the spatial distribution of HCHO and CHOCHO inside the basin. Higher column amounts were observed over the western and central part of the basin especially along the foothills. The foothills in the SCAB is a major thoroughfare for both the vehicular traffic as well as the pollutants and this is very clear from the maps. Further, the column amounts of HCHO are smaller along the foothills on July 17, a Saturday, when vehicular traffic is relatively lower compared to the weekday on July 16. In contrast, the eastern part of the basin show comparatively lower amount of HCHO and CHOCHO for both days. The horizontal footprint of CU AMAX-DOAS measurement of HCHO and CHOCHO VCD (~12 km) is comparable to air quality models (4 km^2) and satellite observations (~13 x 24 km^2). This makes the current dataset an excellent opportunity of evaluate air quality models and assess the value of satellite observations of HCHO and CHOCHO as a data source for air quality regulation over California.

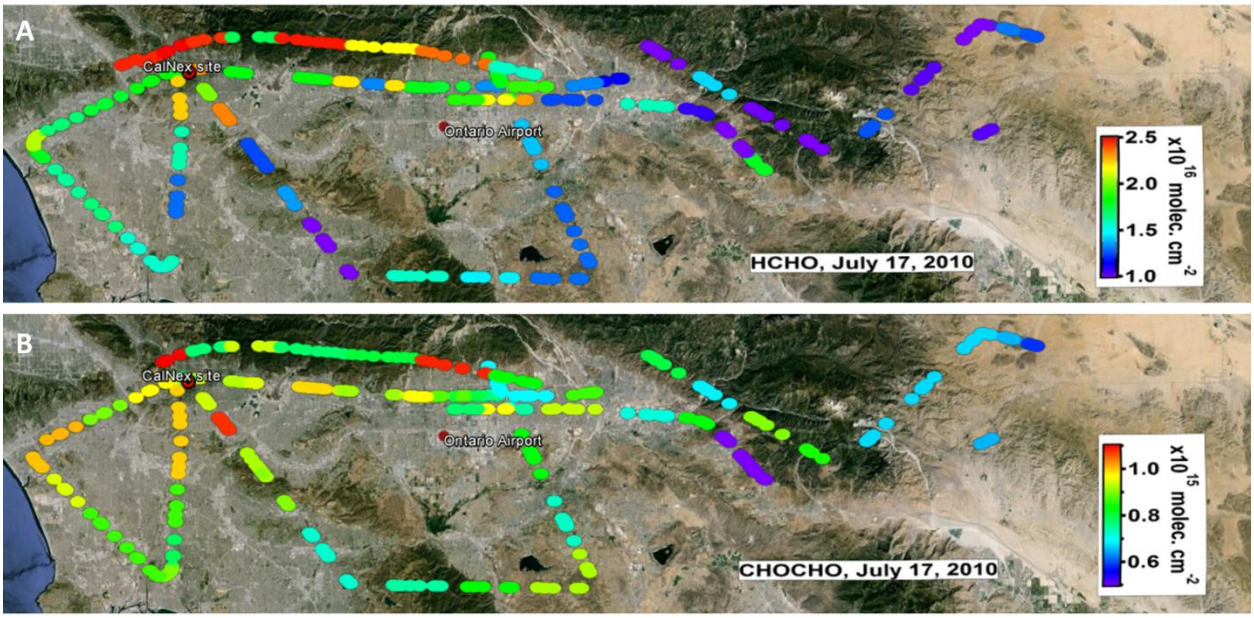

Figure 3.5.5: *Vertical columns of (A) HCHO and (B) CHOCHO measured over the South Coast Air Basin during a flight on July 17, 2010.*

3.5.5 Comparison with model

3.5.5.1 HCHO

Figure 3.5.6 show time series of measured (black) and modeled HCHO vertical columns (red: WRF-Chem with CARB 2010 EI, green: WRF-Chem with NEI 2005 EI and orange: CMAQ with CARB 2010 EI) respectively for the two flights on (A) July 16 and (B) on July 17, 2010. Note that the large variability is mostly due to the large spatial area covered by the Twin Otter during the flights. In general, the overall spatial trend as well as magnitude is better captured by the WRF-Chem simulations compared to CMAQ. Considering one of the WRF-Chem simulations used the same emission inventory as the CMAQ simulations, the difference in the two model outputs is likely due to the different VOC chemistry in the models.

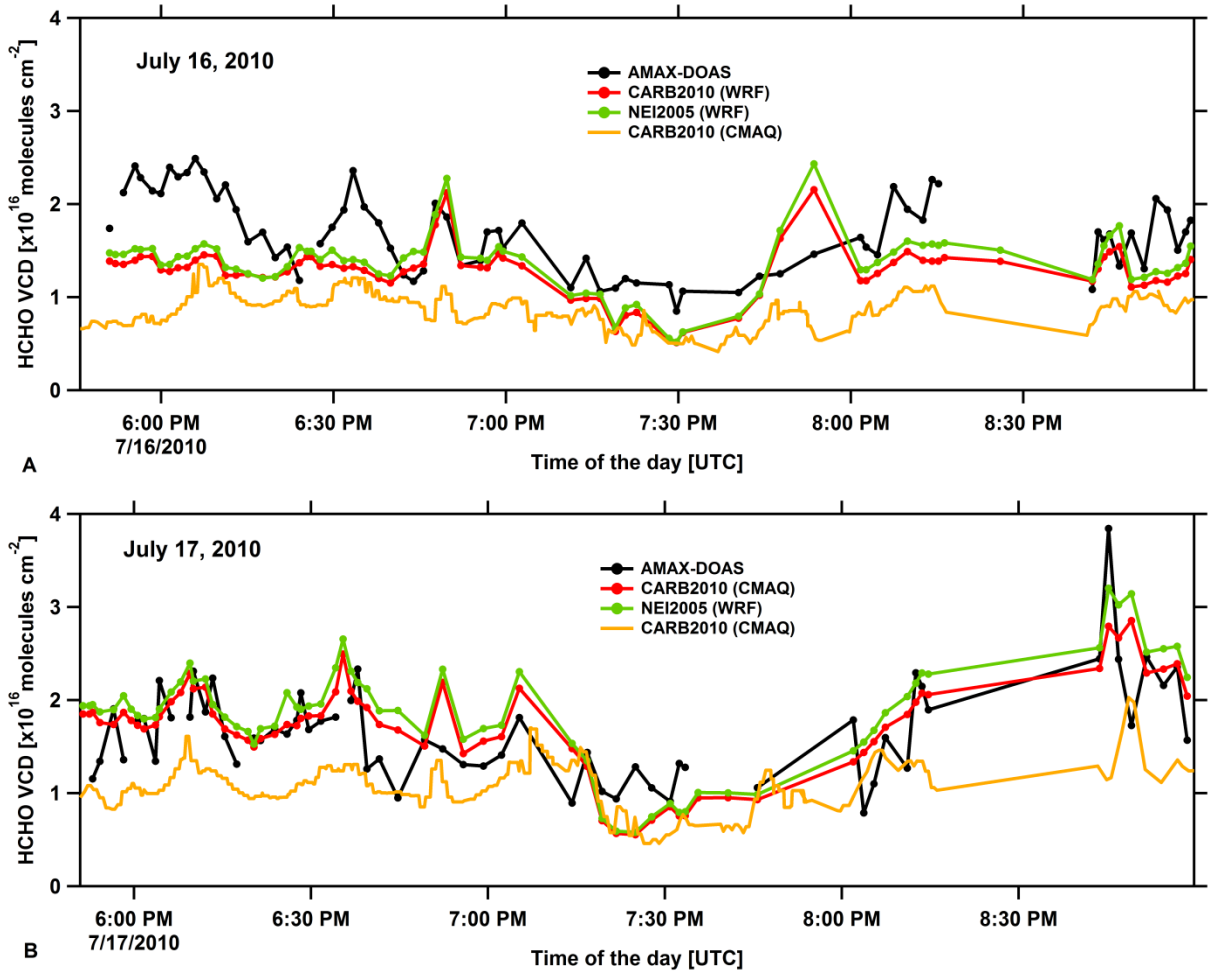

Figure 3.5.6: *Time series of HCHO vertical columns measured (black) and modeled (red: WRF-Chem with CARB 2010 EI, green: WRF-Chem with NEI 2005 EI and orange: CMAQ with CARB 2010 EI) over the South Coast Air Basin during a flight on (A) July 16 and (B) July 17, 2010.*

3.5.5.2 CHOCHO

Figure 3.5.7 show the same plots as Fig. 3.5.6 but for CHOCHO. The model outputs seems to capture the spatial trend to some extent but is largely under predicted by both the models. Again, the WRF-Chem simulations are closer to the measurements. Interestingly, the WRF-Chem results with NEI 2005 EI are in better agreement with the measurements than CARB 2010 indicating that the VOC emissions might not have decreased as expected from 2005 to 2010. The missing VOC source and chemistry in the models could have larger impacts on both O_3 production and SOA formation in the models.

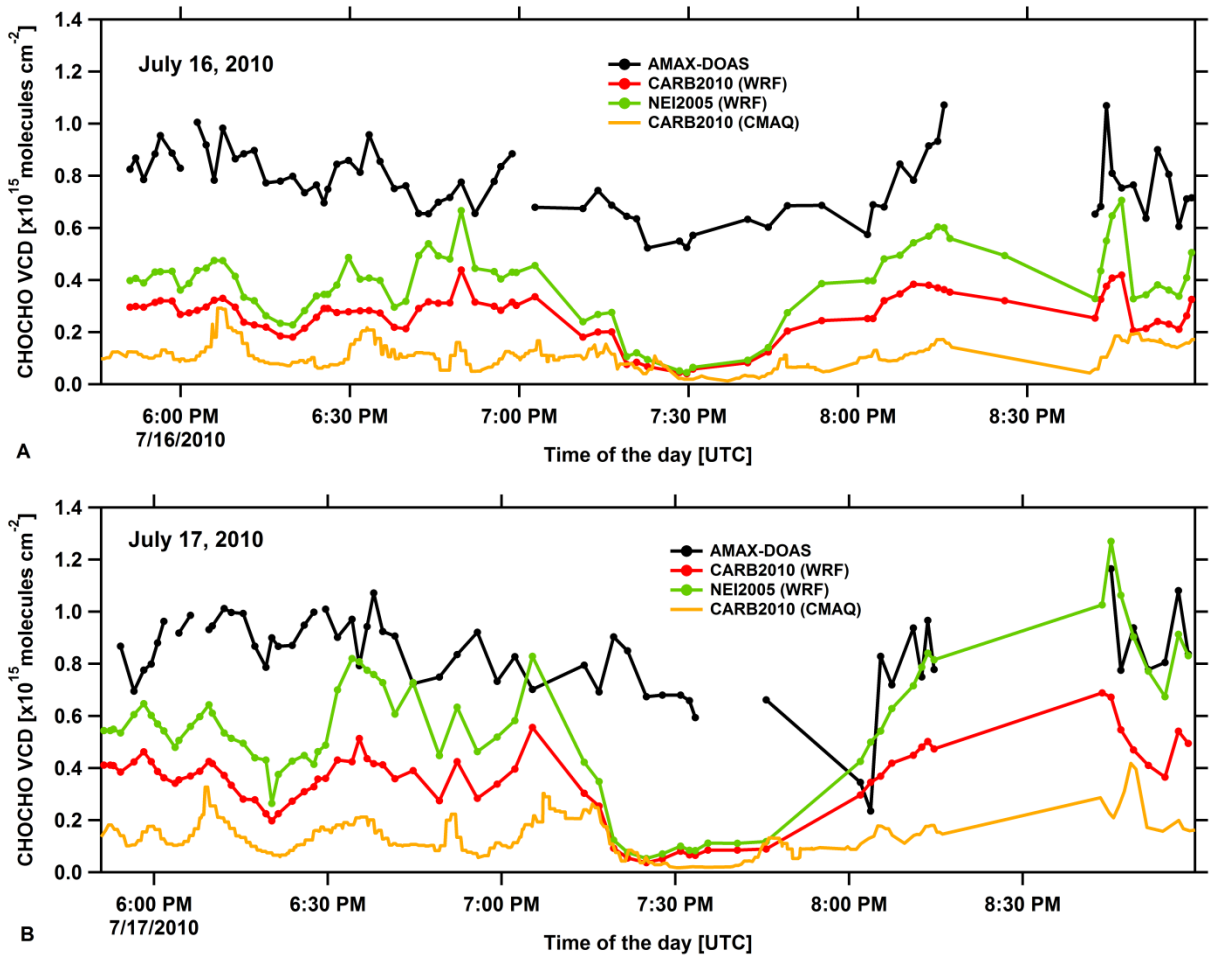

Figure 3.5.7: *Time series of CHOCHO vertical columns measured (black) and modeled (red: WRF-Chem with CARB 2010 EI, green: WRF-Chem with NEI 2005 EI and orange: CMAQ with CARB 2010 EI) over the South Coast Air Basin during a flight on (A) July 16 and (B) July 17, 2010.*

3.5.6 Glyoxal to Formaldehyde ratio, R_{GF}

The ratio of CHOCHO to HCHO, R_{GF} depends upon the relative contribution of biogenic and anthropogenic VOC sources. A ratio between 0.04 and 0.06 has been reported for areas dominated by biogenic emissions based on satellite measurements of HCHO and CHOCHO (Vrekoussis et al., 2009, Vrekoussis et al., 2010). Lower values of R_{GF} have been observed over polluted areas such as Mexico City. However, recent in-situ measurements in the forests over Sierra Nevada and Rocky Mountain regions indicated the opposite, i.e. lower R_{GF} for biogenic emissions (DiGangi et al., 2012). Thus, there is an unresolved issue about R_{GF} in current scientific literature.

Figure 3.5.8 shows the maps of R_{GF} for the flights on July 16 and 17, 2010. For large part of the basin, the R_{GF} was found to be between 0.04 and 0.06. R_{GF} close to or less than 0.04 is observed

along the foothills of San Gabriel Mountains and downtown Los Angeles where we also observed higher NO_2 vertical columns (see Fig 3.7.3). Thus, our observations support satellite observed $R_{GF,}$ i.e. increased influence of anthropogenic emission lowers R_{GF}. This is also corroborated by the R_{GF} from the vertical profiles of HCHO and CHOCHO over four different locations in SCAB, Bakersfield, CA and high desert in Arizona. Table 3.5.1 show the R_{GF} for the six profiles (see Section 3.6 for the vertical profiles). The lowest R_{GF} is observed for Brackett, the site in the middle of the SCAB, which also shows the highest NO_2 concentration and the highest value is seen over the high desert.

The basin wide average R_{GF} for the two days is 0.05. This value is larger than 0.041 reported by Vrekoussis et al. (2010) for Los Angeles based on GOME-2 measurements for a two year period from 2007 to 2008. A plausible explanation for the higher value could be that the biogenic VOC emissions during the summer season are relatively higher. There could also be bias in the sampling between the two measurements due to large spatial scale covered by satellite pixels. The spatial variability in R_{GF} over a relatively small area is intriguing by itself and deserves further investigation.

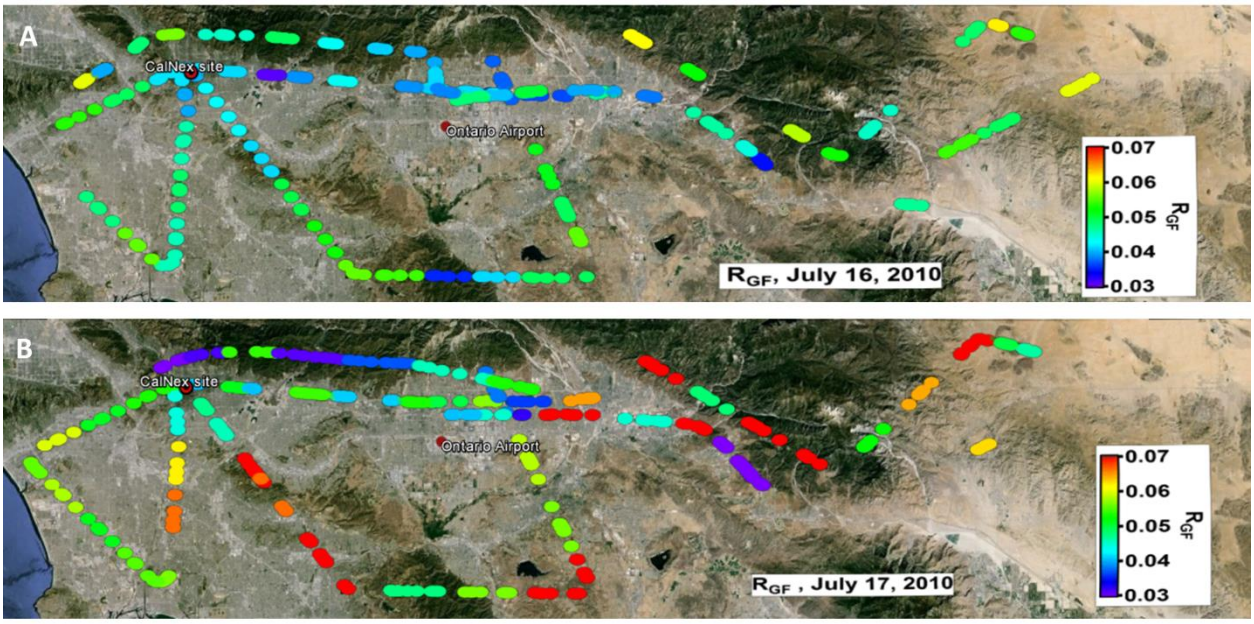

Figure 3.5.8: *Ratio of glyoxal to formaldehyde, R_{GF} for the flights over the South Coast Air Basin on (A) July 16, 2010 and (B) July 17, 2010.*

Vrekoussis et al. (2010) also reported an anti-correlation between R_{GF} and NO_2 column amounts i.e. R_{GF} decreases with increasing NO_2 amounts, based on two years of GOME-2 data. Figure 3.5.9 shows the RGF as a function of NO_2 VCD for the two flights and six profiles. There is clearly a correlation between R_{GF} and NO_2 amount in SCAB and R_{GF} decreases with increasing NO_2. It would be interesting to investigate the correlation between observed R_{GF} and ozone production in the basin.

Site	R_{GF}
Page, AZ	0.050 ± 0.008
Bakersfield, CA	0.029 ± 0.003
Santa Monica, CA	0.048 ± 0.004
Brackett, CA	0.027 ± 0.003
Ontario, CA	0.039 ± 0.001
Banning, CA	0.044 ± 0.003

Table 3.5.1: *Ratio of glyxoal to formaldehyde, R_{GF} for the vertical profiles at six different locations in California and Arizona (see section 3.6 for details).*

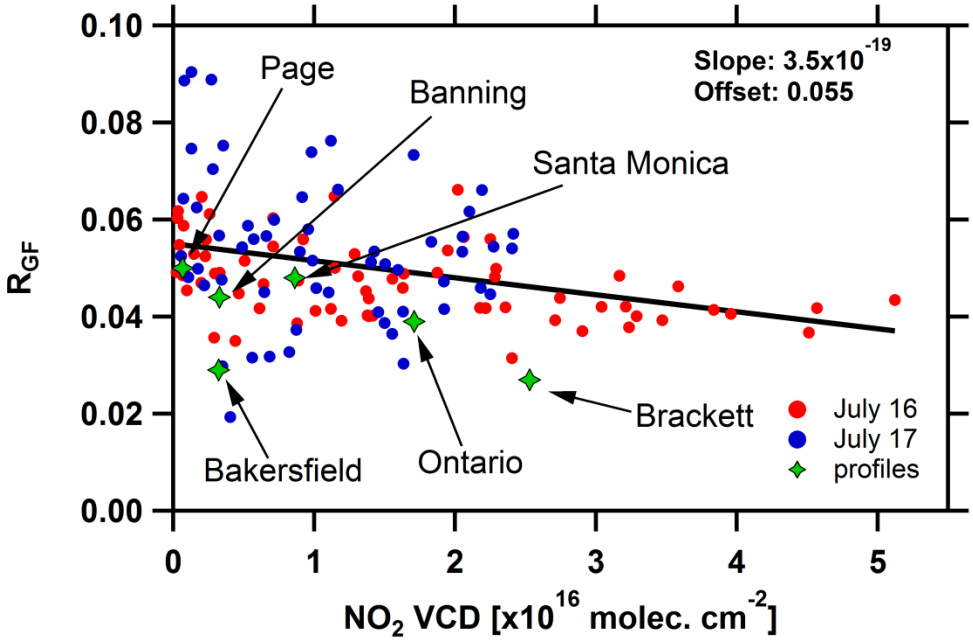

Figure 3.5.9: *R_{GF} as a function of NO_2 vertical column.*

3.5.7 Conclusion

Retrievals of HCHO and CHOCHO VCDs along the flight track using the EA scans of the CU AMAX-DOAS instrument are feasible and provide a means to obtain high spatial resolution maps of the two trace gases. Maps in the SCAB showed higher amount of HCHO and CHOCHO in the western and central part of the basin especially along the foothills. The ratio of glyoxal to formaldehyde also indicated the foothills region to be more anthropogenic emission influenced compared to the other parts of the basin, where biogenic influences are significant. Our measurements supported the satellite interpretation of $R_{GF,}$ i.e. R_{GF} decreases with increasing

anthropogenic influence. Comparison of model outputs with different emission inventories showed that the models generally under estimate the amount of these gases, particularly CHOCHO. This is likely due to (i) missing VOC chemistry and (ii) lower VOC emission in the emission inventories.

HCHO and CHOCHO are indicator molecules for VOC oxidation chemistry. Maps of HCHO and CHOCHO provide powerful indicators to pinpoint location of active VOC photochemistry. Further, the ratio of glyoxal to formaldehyde allows us to identify areas with dominant biogenic and anthropogenic VOC emissions. The existing CU AMAX-DOAS dataset has the potential to retrieve high resolution maps of vertical columns of HCHO and CHOCHO for the identification of regions of active photochemistry and constrain VOC emission in California. These maps would also be very valuable in evaluating current atmospheric models and assessing the value of satellites as a source for data to assess air quality regulations over California.

3.6. Vertical Profiles of NO_2, HCHO, and CHOCHO

Another focus of our study was the investigation of vertical distributions of nitrogen dioxide (NO_2), formaldehyde (HCHO) and glyoxal (CHOCHO) over different parts of California, especially over the South Coast Air Basin. Vertical profiles of trace gases other than ozone and water vapor are usually not readily available. We performed low approaches (up to ~0.2 km AGL) over various airports to obtain vertical distributions of these trace gases. The vertical profile retrieval algorithm from CU AMAX-DOAS measurements is based on the Optimal Estimation technique by Rodgers (2000) and is described in detail in (Baidar et al., 2013).

Here, we present case studies of vertical profiles over four different locations within the South Coast Air Basin (SCAB), over Bakersfield city center and over the high desert in Page, Arizona. We compare our retrieved profiles to results from the CMAQ model using CARB 2010 emission inventory. (Model results were provided by Chenxia Cai, CARB)

Figure 3.6.1-3.6.4 show example vertical profiles of NO_2, HCHO and CHOCHO at four different locations (Santa Monica, Brackett, Ontario, and Banning respectively) inside the SCAB on July 16, 2010 (see Fig 2.2a for the locations of the vertical profiles inside the SCAB). Most of the trace gases were observed inside the boundary layer close to the source region with profiles showing decreasing concentrations above the boundary layer. The maximum concentrations (NO_2: $3.5x10^{11}$ (~14.2 ppb), CHOCHO: $6.7x10^{9}$ (~0.3 ppb) and HCHO: $2.6x10^{11}$ molecules cm^{-3} (~10.5 ppb) were observed in the middle of the basin at Brackett airfield. In general, concentrations of these trace gases increased from the coast towards the east, reached the maximum at the middle of the basin and decreased further east. HCHO levels were found to be relatively more uniformly distributed inside the basin compared to NO_2 and CHOCHO. Variations in the boundary layer height within the basin can also be seen in these figures. The boundary layer height gradually increased from ~500 m at the coast (Santa Monica airport) to ~1500 m at Banning to the west.

The CMAQ model results also show most of the trace gases are located inside the boundary layer. CMAQ model results are shown as dotted lines with open circles in the figures. NO_2 was generally found to be slightly overestimated whereas CHOCHO and HCHO are significantly underestimated over much of the air column by the model. There is a good agreement between measured and modeled NO_2 and HCHO above 2 km. Over inland locations, the model underestimates the residual layer concentrations of NO_2, HCHO and CHOCHO between 1-2 km altitudes. Further, CHOCHO levels were significantly lower in the model both inside the boundary layer and in the free troposphere. This could be due to missing CHOCHO formation chemistry in the model.

Figure 3.6.5 and 3.6.6 show vertical profiles at Bakersfield, CA and Page, AZ (at the local airport) on June 15, 2010 and July 19, 2010 respectively. Vertical profile at Page, AZ in the middle of the high desert provides the regional background conditions for these trace gases. The

free troposphere concentration (at ~1.5 km) for NO_2, CHOCHO and HCHO were $1.3x10^9$ (~52 ppt), $6.3x10^8$ (~25 ppt), and $1.1x10^{10}$ (~450 ppt) molecules cm^{-3} respectively.

Air quality in Bakersfield is influenced by urban emissions as well as intense agricultural and oil and gas operations in the surrounding area. Similar to SCAB, the observed concentrations of NO_2, CHOCHO and HCHO in Bakersfield were considerably larger near the surface compared to air aloft. The concentrations for the trace gases inside the boundary layer were found to be 3-5 times smaller compared to SCAB. However, the concentrations in the free troposphere were ~2-3 times larger for NO_2 and HCHO compared to Page, AZ. CHOCHO levels in the free troposphere was similar to the background profile at Page. The agreement between the model results and observations for NO_2 and HCHO near the surface was very good but there was a discrepancy in the boundary layer height. CHOCHO levels were found to be significantly under predicted in Bakersfield as well. Figure 3.6.6 also shows the CHOCHO vertical profile from Knote et al. (2013) (green dashed lines with open triangle). Knote et al. uses WRF-Chem model with emissions updated to reconcile with measurements during CalNex and latest developments in CHOCHO specific chemistry to study SOA formation from CHOCHO. The vertical profile from Knote et al. (2013) is in very good agreement except near the surface and shows that observed CHOCHO can be explained with updated emission and chemistry in atmospheric models.

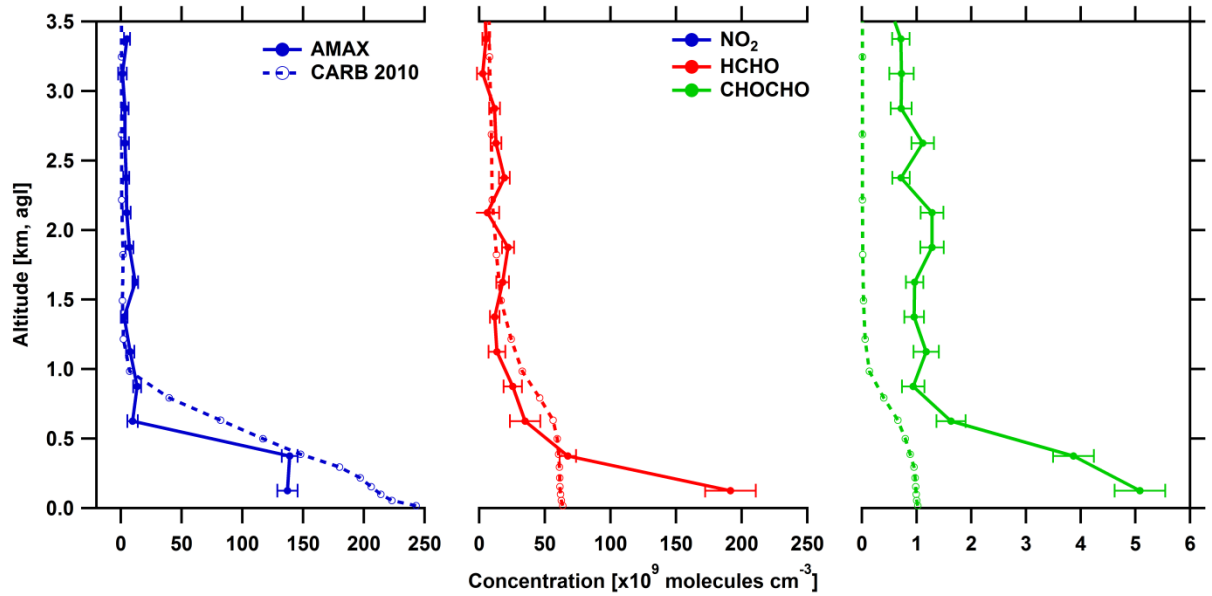

Figure 3.6.1: *Vertical Profiles of NO2 (blue), HCHO (red) and CHOCHO (green) retrieved from CU AMAX-DOAS measurements (solid) and modeled by CMAQ model using CARB 2010 emission inventory (dotted, open circle) on July 16, 2010 at Santa Monica, CA.*

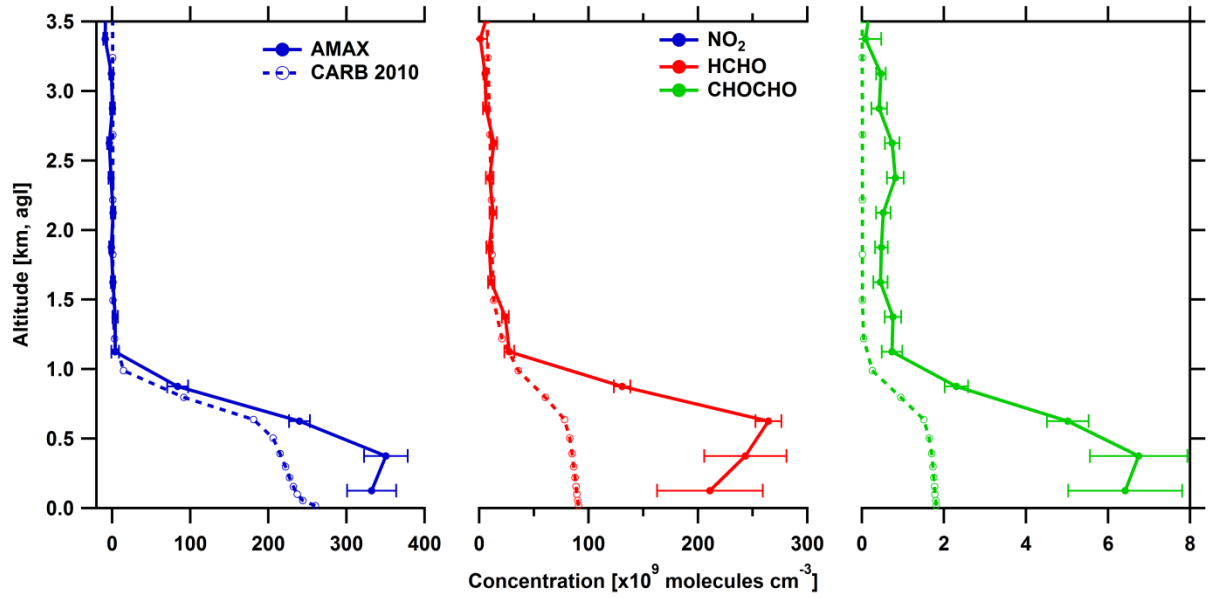

Figure 3.6.2: *Vertical Profiles of NO2 (blue), HCHO (red) and CHOCHO (green) retrieved from CU AMAX-DOAS measurements (solid) and modeled by CMAQ model using CARB 2010 emission inventory (dotted, open circle) on July 16, 2010 at Brackett Field, CA.*

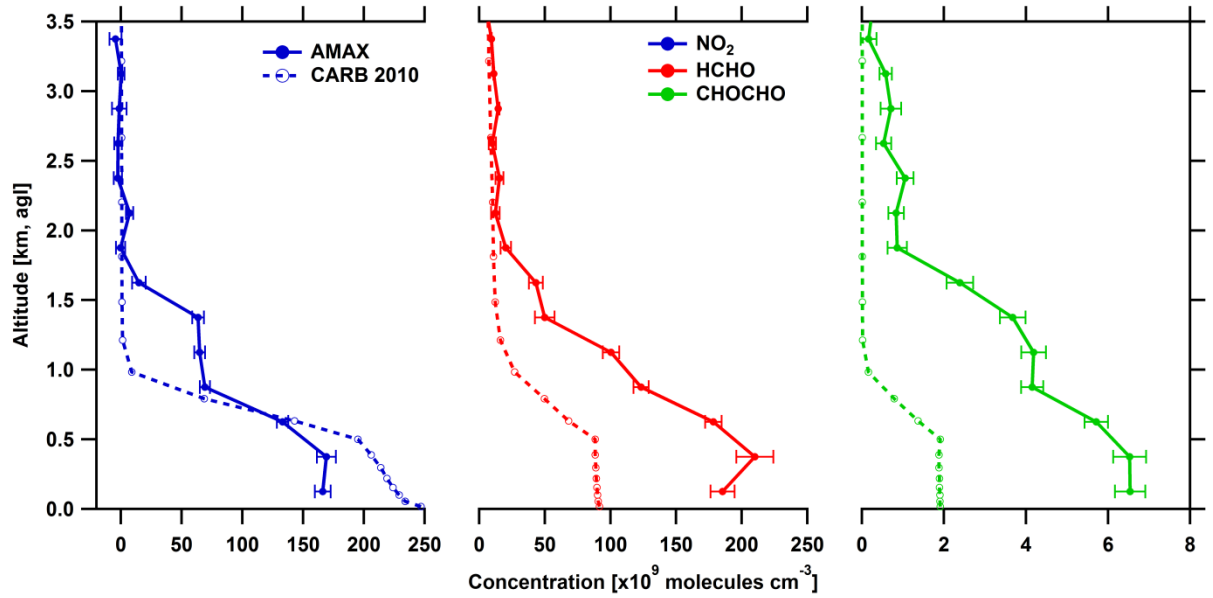

Figure 3.6.3: *Vertical Profiles of NO2 (blue), HCHO (red) and CHOCHO (green) retrieved from CU AMAX-DOAS measurements (solid) and modeled by CMAQ model using CARB 2010 emission inventory (dotted, open circle) on July 16, 2010 at Ontario, CA.*

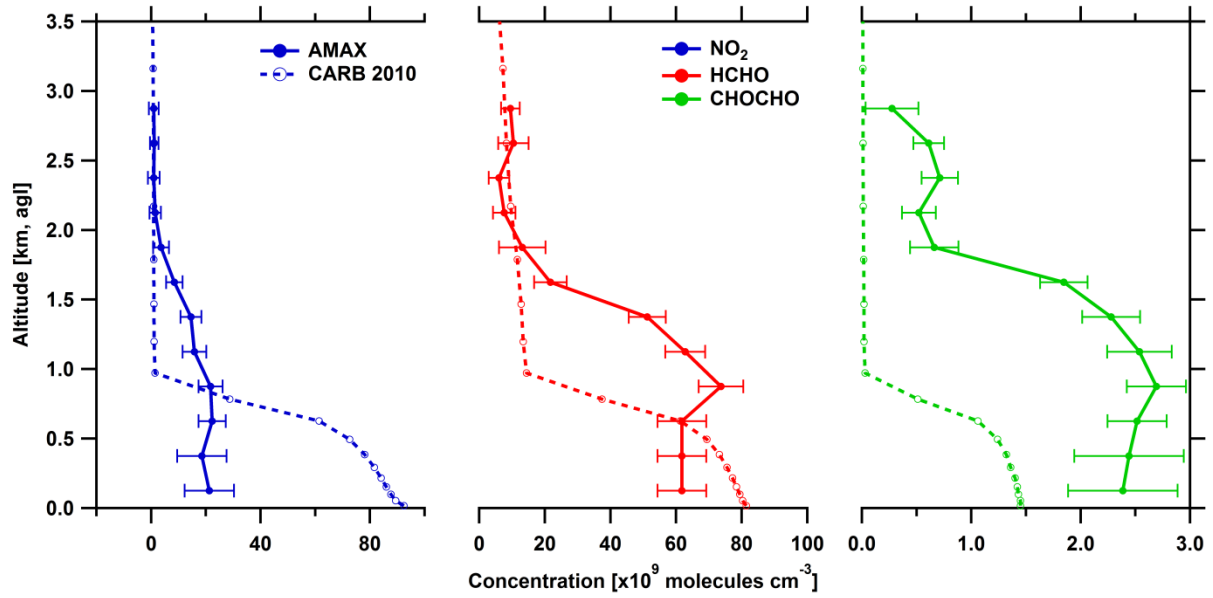

Figure 3.6.4: *Vertical Profiles of NO2 (blue), HCHO (red) and CHOCHO (green) retrieved from CU AMAX-DOAS measurements (solid) and modeled by CMAQ model using CARB 2010 emission inventory (dotted, open circle) on July 16, 2010 at Banning, CA.*

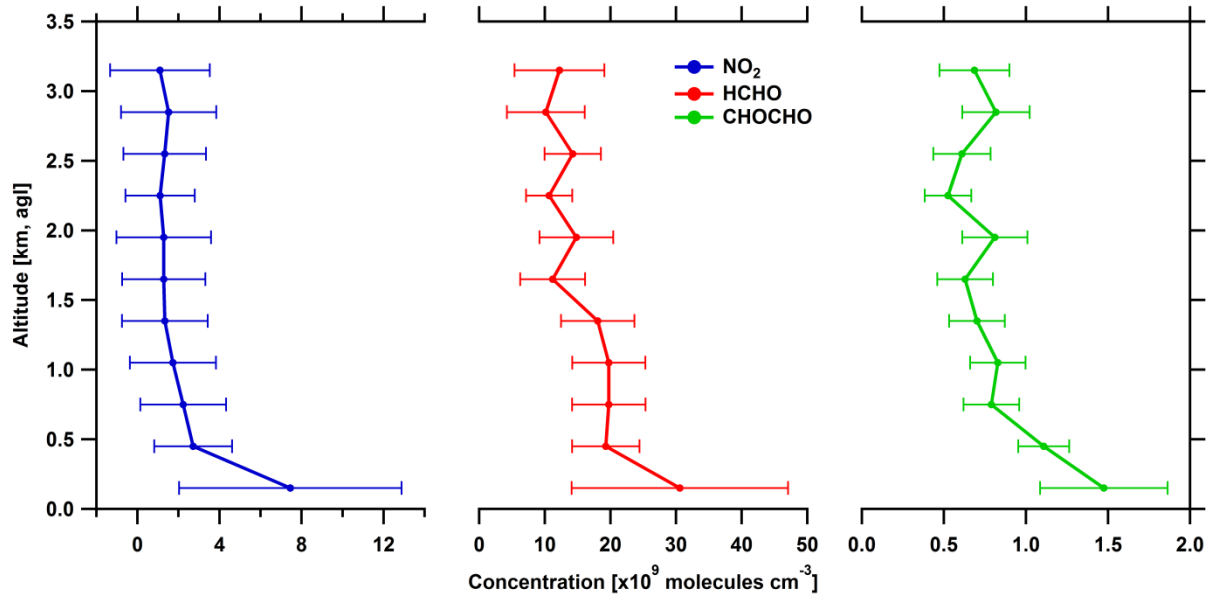

Figure 3.6.5: *Vertical Profiles of NO2 (blue), HCHO (red) and CHOCHO (green) retrieved from CU AMAX-DOAS measurements on July 19, 2010 at Page, AZ.*

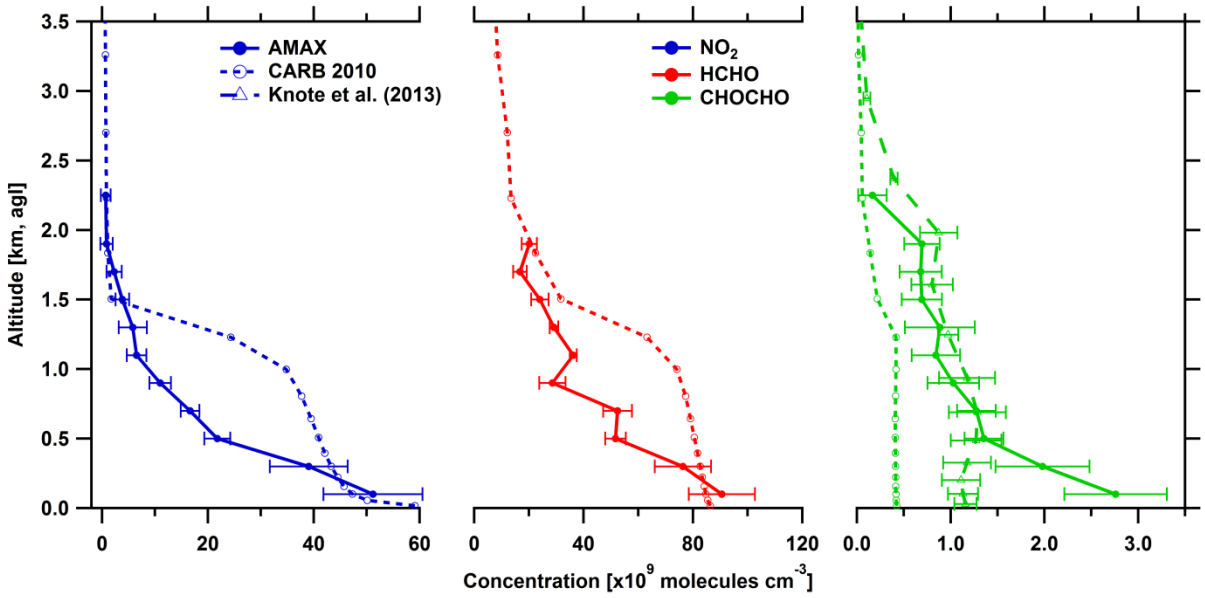

Figure 3.6.6: *Vertical Profiles of NO2 (blue), HCHO (red) and CHOCHO (green) retrieved from CU AMAX-DOAS measurements (solid) and modeled by CMAQ model using CARB 2010 emission inventory (dotted, open circle) on June 15, 2010 at Bakersfield, CA. The green dashed line with open triangle represents CHOCHO profile form Knote et al. (2013).*

3.7 Observation of a reverse weekend O_3 effect in South Coast Air Basin (SCAB) during a very hot weekend in summer 2010.

3.7.1. Introduction

Tropospheric ozone (O_3) has adverse health effects on humans (e.g. as a respiratory irritant causing chest pain, reduced lung function and asthma) and is damaging to vegetation, negatively affecting their growth. It is also a major constituent of photochemical smog. Due to the health and environmental concerns related to O_3, it is recognized as a criteria pollutant by U.S. Environmental Protection Agency and has been regulated by Air Quality Standards. The National Ambient Air Quality Standard (NAAQS) and California Ambient Air Quality Standard (CAAQS) for O_3 are set at 75 ppb and 70 ppb respectively (8 hour maximum). Regulations aimed at reducing O_3 have resulted in decrease in ambient O_3 level in the US over the last few decades. In some areas, however, higher O_3 levels have been observed on the weekends compared to weekday, a phenomenon popularly known as "weekend O_3 effect". We consider the observation of lower O_3 on the weekend compared to weekday as a "reverse weekend O_3 effect".

The occurrence of the "weekend O_3 effect" was first reported in the 1970s in New York City, Washington DC and Los Angeles (Cleveland et al., 1974, Lebron, 1975, Elkus and Wilson, 1977). The weekend ozone effect has been particularly well studied in the Los Angeles area or South Coast Air Basin (SCAB) in California (Blanchard and Tanenbaum, 2003, Chinkin et al., 2003, Fujita et al., 2003, Pollack et al., 2012 and references within). In early 2000s, the California Air Resource Board conducted a major study to better understand the weekend ozone. Reduced emissions of nitrogen oxide (NO_x = NO + NO_2) on weekends are considered to be the dominant cause for the weekend O_3 effect phenomenon (Marr and Harley, 2002a, Marr and Harley, 2002b, Blanchard and Tanenbaum, 2003, Fujita et al., 2003, Yarwood et al., 2003, Yarwood et al., 2008).

On-road motor vehicles are the dominant emissions source of pollutants in the SCAB, contributing > 50% of NO_x, and >25% of reactive organic gases of the total emissions (http://www.arb.ca.gov/ei/emissiondata.htm). Even though heavy duty diesel powered vehicles only represent a very small fraction (<10%) of the total number of on-road vehicles (Chinkin et al., 2003, Ban-Weiss et al., 2008) they are the dominant on-road source of NO_x (Ban-Weiss et al., 2008). Previous studies have shown a large reduction in heavy duty diesel engine vehicles on weekends is responsible for a significant reduction in weekend NO_x emissions (Marr and Harley, 2002a, Chinkin et al., 2003, Harley et al., 2005). In contrast, the light duty, gasoline vehicles which form the majority of the on-road fleet, has similar overall activity on weekday and weekends (Marr and Harley, 2002a, Chinkin et al., 2003, Harley et al., 2005).

Ozone formation is a nonlinear process and is a function of NO_x and volatile organic compounds (VOCs). Hence reductions in the precursors can increase, decrease or leave the O_3 levels unchanged. The photochemical O_3 formation process has been extensively studied (e.g.

Finlayson-Pitts and Pitts Jr, 2000, Seinfeld and Pandis, 2006) and briefly summarized here. The following reactions describe the photochemical O_3 formation in the troposphere.

$$O_3 + NO \rightarrow NO_2 + O_2 \quad \text{(R1)}$$

$$NO_2 + hv \rightarrow NO + O \quad \text{(R2)}$$

$$O + O_2 \rightarrow O_3 \quad \text{(R3)}$$

$$RH + OH + O_2 \rightarrow RO_2 + H_2O \quad \text{(R4)}$$

$$RO_2 + NO + O_2 \rightarrow NO_2 + R'CHO + HO_2 \quad \text{(R5)}$$

$$HO_2 + NO \rightarrow NO_2 + OH \quad \text{(R6)}$$

$$HO_2 + HO_2 \rightarrow H_2O_2 + O_2 \quad \text{(R7)}$$

$$RO_2 + HO_2 \rightarrow ROOH + O_2 \quad \text{(R8)}$$

$$RO_2 + RO_2 \rightarrow \text{product} \quad \text{(R9)}$$

$$OH + NO_2 \rightarrow HNO_3 \quad \text{(R10)}$$

Reactions 1 -3 describe the null NO_x-O_x cycle and does not lead to net O_3 formation. However, when a generic VOC molecule is oxidized by OH radical in the HO_x cycle (Reaction 4-6) to form RO_2, then HO_2 and subsequently regenerate OH, two NO molecules are oxidized to NO_2. The NO_2 molecules then yield O_3 via reaction R3 after undergoing photolysis (R2). These steps bypass the O_3 titration step to form NO_2 (R1) in the NO_x-O_x cycle and the result is a net photochemical O_3 production.

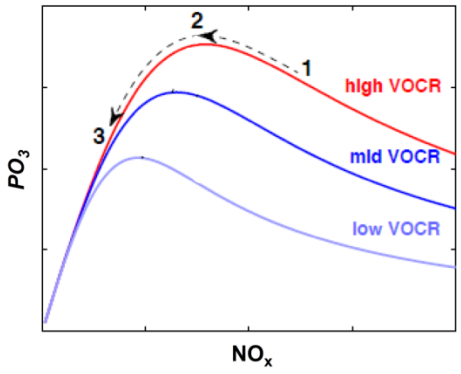

Figure 3.7.1: *The instantaneous O_3 production rate (PO_3) as a function of NO_x for three categories of organic reactivity: high (red), mid (blue) and low (violet). Arrows illustrate change in O_3 production in response to NO_x reductions on weekends. Initial NO_x reduction increases O_3 production at high NO_x levels (1→2). Further NO_x reductions at low NO_x levels decrease O_3 production (2→3). (adopted from Pusede et al., 2012).*

Reactions 7-10 describe the radical chain termination steps which remove the HO_x and NO_x molecules from the O_3 formation cycle. These reactions compete with the Reaction 4-6 for HO_x radicals and depending upon the concentrations of the HO_x and NO_x molecules, either the chain propagating steps or the terminating steps are favored. For example at very high NO_x level, OH reacts with NO_2 to form nitric acid (R10). This reduces the HO_x radical pool and subsequently suppresses O_3 production (NO_x suppressed or VOC limited chemistry). At low NO_x concentrations, NO reacts with HO_2 or RO_2 to increase the OH concentrations. This enhances the rate of oxidation of organic molecules (NO_x limited chemistry). Thus, the ratio of VOC to NO_x plays a critical role in the photochemical O_3 production chemistry. Figure 3.7.1 illustrates the non-linear O_3 formation process as a function of NO_x and VOCs.

Reduced emission of NO_x on weekend results in increased ozone concentrations via two processes: 1) Decreasing the ozone loss by titration with NO (R1) and effectively ensures higher amount of O_3 remain in the atmosphere. 2) Increasing the VOC/NO_x ratio to favor chain propagating steps (R4-6) and enhancing the photochemical O_3 production. This process is illustrated in Figure 3.7.1 by arrow 1→2. Recent results have shown that the photochemical ozone production play a significant role in enhanced O_3 concentrations on the weekend in the Los Angeles Basin (Pollack et al., 2012 and references within). However, if the reduction in NO_x on weekend shifts the photochemical O_3 formation chemistry to a NO_x limited regime, O_3 production on the weekend will decrease resulting in lower O_3 on the weekends. This process is shown by arrow 2→3 in Figure 3.7.1.

Here we report observation of a lower O_3 amount on the weekend compared to the weekday during a very hot day in July 2010. The reduction in NO_x on the weekend was normal. The weekend was marked by a very high ambient temperature (see Fig. 3.7.2a). Our observation is based on measurement aboard the NOAA Twin Otter research aircraft by NOAA TOPAZ lidar and CU AMAX-DOAS instruments. Measurements of O_3 and NO_2 concentrations at California Air Resource Board (CARB) surface monitoring network in SCAB provide supporting evidence to our observation (Fig. 3.7.2b and c). Our observation indicates that the O_3 formation chemistry in SCAB is potentially at its peak on very hot days.

3.7.2 Observations

Our analysis is based on the CU Airborne MAX-DOAS measurements of NO_2 vertical column and NOAA TOPAZ lidar measurements of O_3 profiles and boundary layer height (BLH). We used the BLH estimates and O_3 profiles measured with the TOPAZ lidar to compute O_3 column data integrated over the depth of the BL. Details about the O_3 profile, vertical column and boundary layer height retrieval can be found in Section 3.1 and 3.3. Two research flights with identical flight plans (see Figure 3.7.3) in time and location were flown on Friday, July 16, 2010 and Saturday, July 17, 2010. This weekend was one of the hottest weekends during summer 20 with ambient temperature reaching over C in the basin and the meteorological conditions over the two days were almost identical. Figures 3.7.2a and 3.7.2b show the temperature and wind

speed and direction measured at the Riverside-Rubidoux CARB surface monitoring station. Biogenic VOC emissions such as from forest (Guenther et al., 1993) increase exponentially with temperature. Thus, these two days allows us to study the effect of NO_x reduction on the weekends to photochemical O_3 productions in SCAB when the VOC levels are high.

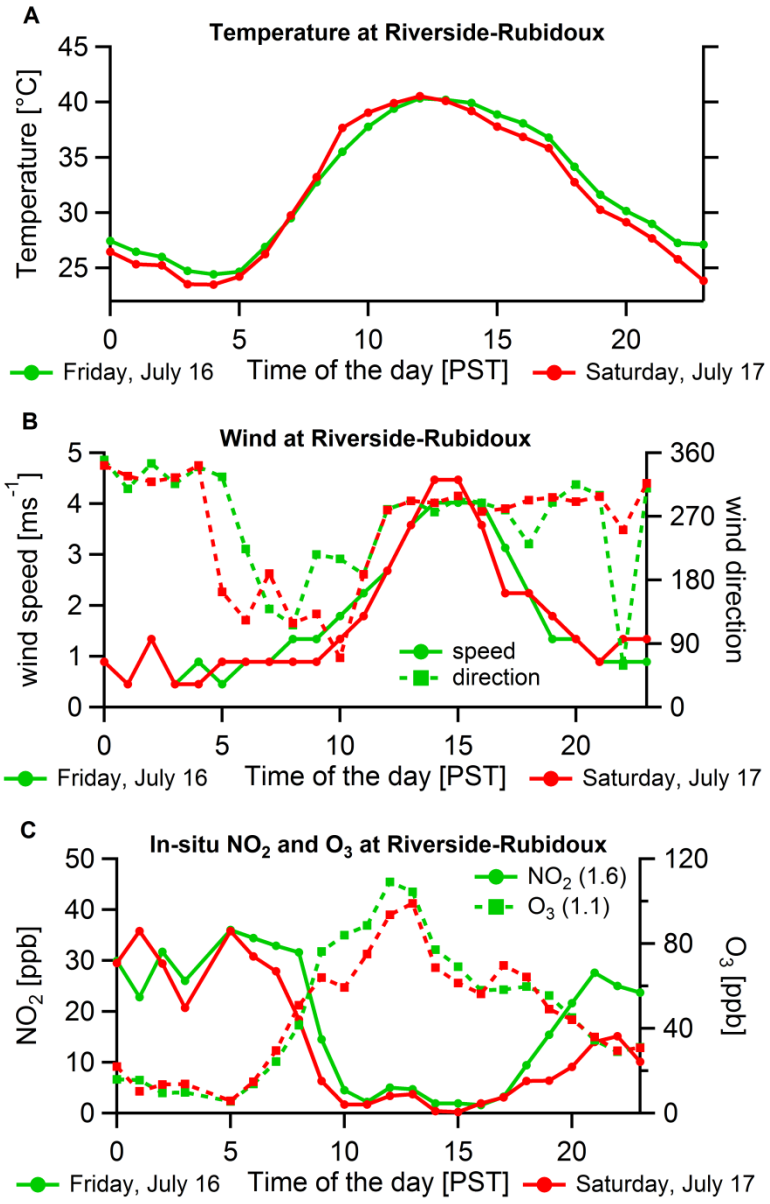

Figure 3.7.2: *Diurnal Cycle of A) temperature, (B) wind speed and direction and (C) NO_2 (solid) and O_3 (dashed) concentrations measured at Riverside-Rubidoux surface monitoring station on July 16 (green) and July 17 (red), 2010. The number in the bracket in panel (C) indicate average weekday to weekend ratio (6:00-18:00 PST).*

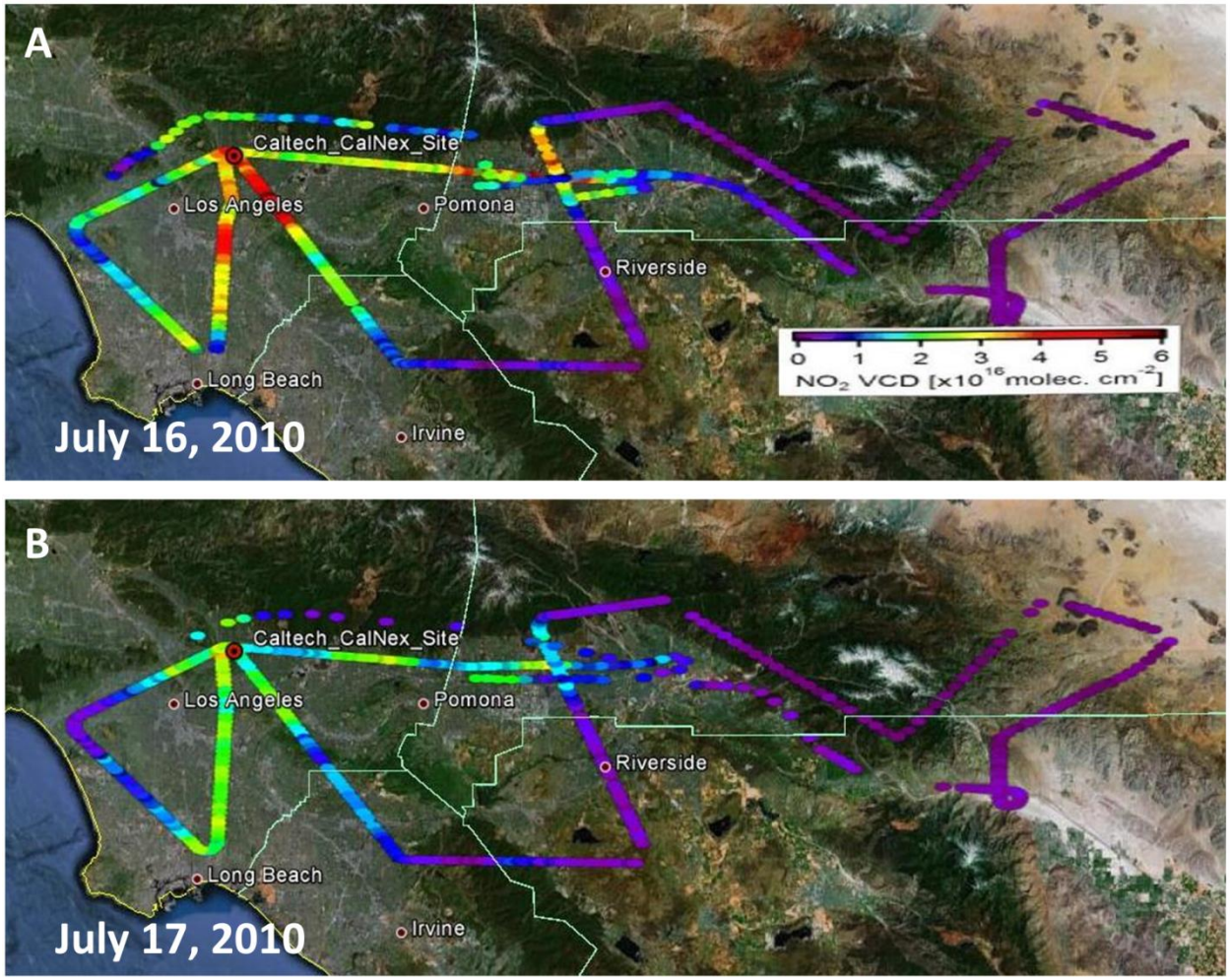

Figure 3.7.3: *Maps of South Coast Air Basin (SCAB) showing NO_2 vertical column densities distribution on (A) July 16, and (B) July 17, 2010.*

Figures 3.7.3a and 3.7.3b show the maps of NO_2 vertical columns distributions in the South Coast Air Basin from the flights on July 16 and 17, 2010 respectively. The corresponding O_3 vertical columns up to the boundary layer height (BLH) distributions maps are shown in Figure 3.7.4a and 3.7.4b. On both days, higher NO_2 amount was observed on the western part of the basin and along the western foothills of San Gabriel Mountains, despite the difference in magnitude. The eastern part of the basin (San Bernardino Mountains and high desert) was found to have very little NO_2. In contrast, higher column amount of O_3 was found in the central and eastern part of the basin along the foothills of San Bernardino Mountains. Taken together the NO_2 and O_3 maps clearly show that O_3 is produced in the downwind of the NO_x source region. NO_2 column amount was lower across the basin on the weekend compared to the weekday. The mean weekday to weekend NO_2 ratio was 1.47±0.07. This ratio is in agreement with the value observed on a different weekend in June (1.45±0.08) and also supported by the measurement at the CalNex ground site in May and June (Pollack et al., 2012). The June weekend was marked by a very different meteorological condition with ambient temperature less than C.%The weekday

to weekend NO_x ratio measured over the past two decades in SCAB measured by various techniques is shown in Figure 3.7.5 and a weekday to weekend ratio >1 is consistently observed (adopted form Pollack et al., 2012). Figure 3.7.6 illustrates the corresponding weekday to weekend ratio for O_3 measured in the SCAB. The red circles represent the NOAA TOPAZ measurement during the two weekends in June and July 2010. A weekday to weekend O_3 ratio < 1 is regularly observed and was also found for the June weekend (0.70±0.03). However, the ratio for the July 17 weekend is markedly different; a ratio > 1 was observed (1.48±0.04). This indicates that the O_3 chemistry on this particular weekend in July 2010 was particularly different compared to the regular weekends.

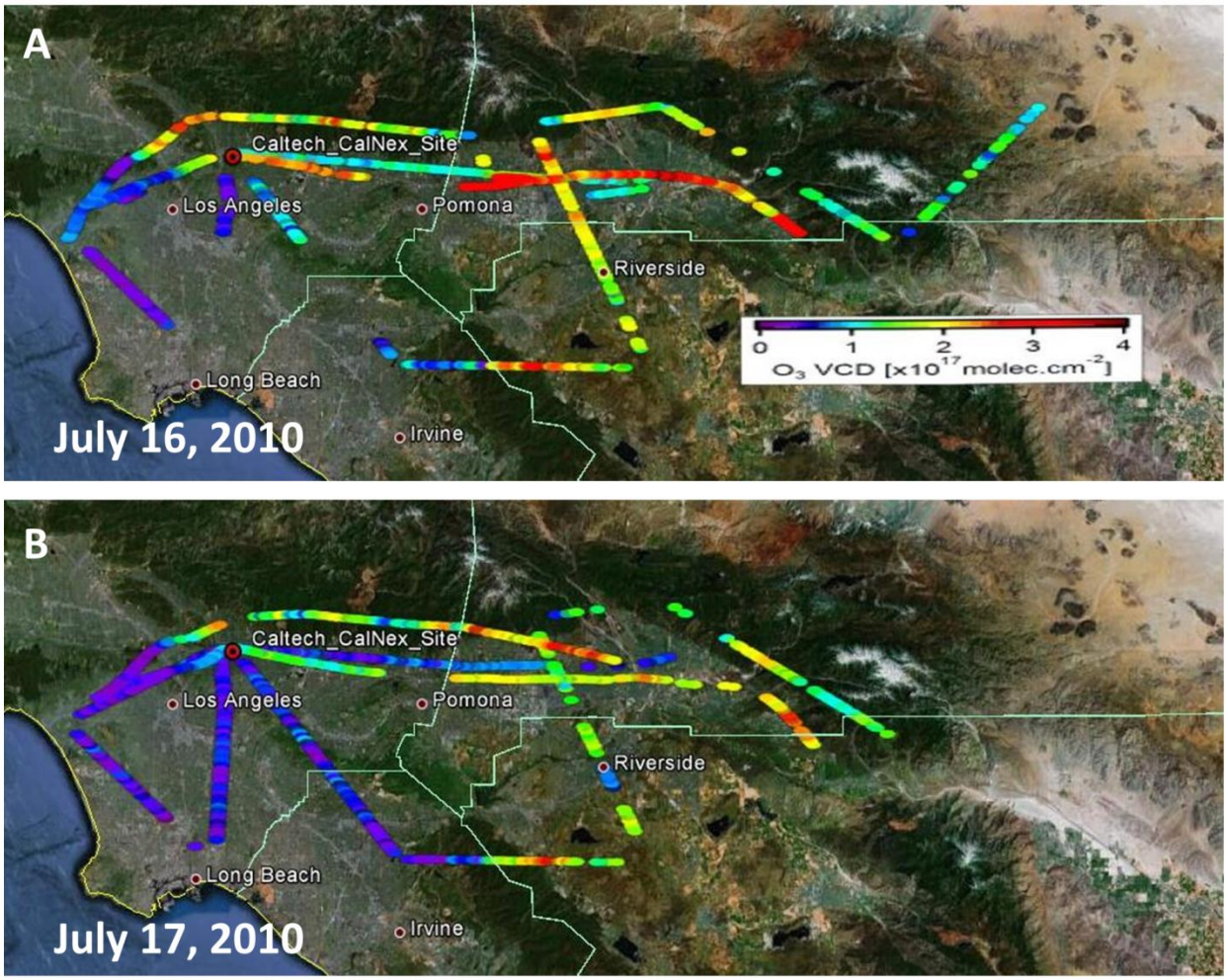

Figure 3.7.4: *Maps of South Coast Air Basin (SCAB) showing O_3 vertical column densities distribution on (A) July 16, and (B) July 17, 2010.*

3.7.3 O_3 Chemistry and trends in SCAB

The NO_x and VOC control regulations aimed at reducing O_3 concentrations in California have resulted in decrease in NO_x, VOCs and consequently O_3 levels in the SCAB for the last few decades. Recent analysis of dataset from 1960 -2010 in SCAB showed that the mixing ratios of

VOCs have decreased at an average annual rate of ~7.5% for the past five decades (Warneke et al., 2012, Pollack et al., 2013). The reduction rate in NO_x levels has been slower at around 2.6% over the same timeframe (Pollack et al., 2013). However, due to new emission control technology and the economic recession, the NO_x levels in Los Angeles have decreased at the rate of ~7% for the last 7 years between 2005 and 2011 (Russell et al., 2012). These decreases in the O_3 precursors have resulted in an average annual decrease in O_3 at the rate of around 2.8% (Pollack et al., 2013).

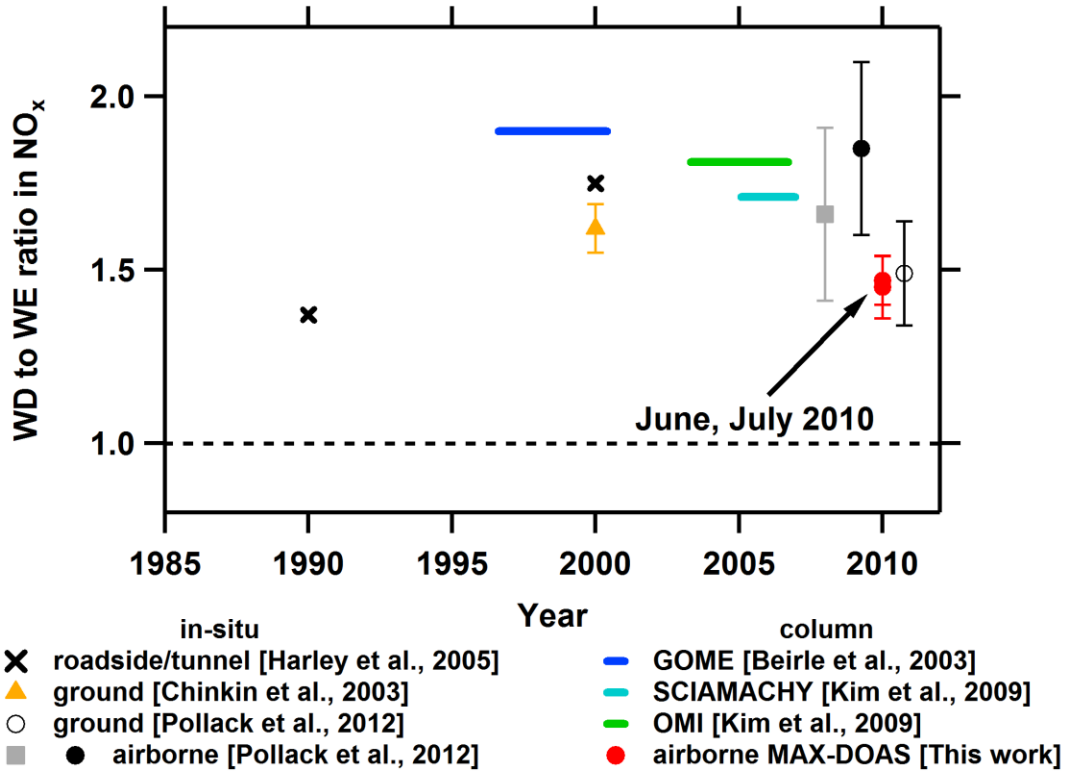

Figure 3.7.5: *Weekday to weekend ratio of NO_x emissions in South Coast Air Basin (SCAB).*

The O_3 formation chemistry in the SCAB is currently in the NO_x suppressed or VOC limited regime (Blanchard and Tanenbaum, 2003). As a consequence, the decrease in NO_x emissions on the weekends have generally resulted in elevated O_3 levels on the weekends. This scenario is indicated by the arrow 1 →2 in Figure 3.7.1. The instantaneous O_3 production rate increases along the VOC reactivity curve on the weekends with large reduction in NO_x emissions but constant VOC levels on the weekends.

The cause for our observation of the lower O_3 amount on the Saturday, July 17 compared to the Friday, July 16 is presently unclear. One plausible possibility are changes in VOC emissions during very hot days. If the O_3 formation chemistry in SCAB, on very hot days, is near the peak of the O_3 production curve shown in Figure 3.7.1 (Point 2), any reduction in NO_x emissions (or shorter NO_x lifetime) under such conditions could result in either no change or decrease in

instantaneous O_3 production rate. This scenario is illustrated by the arrow 2→ 3 in Figure 3.7.1. The lower O_3 on the July 17 weekend is also supported by the measurements at the CARB surface monitoring stations. For example, the monitoring stations at Azusa, Upland, Riverside and San Bernardino in the middle of the basin show either decrease or no change in O_3 concentrations on July 17compared to July 16, 2010 despite the normal weekend reduction in NO_x emissions. The diurnal profile of NO_2 and O_3 mixing ratios measured at the CARB monitoring station in Riverside is shown in Fig. 3.7.2c and shows higher O_3 on Friday (Δ max O_3 = 10.1 ppb). Further analysis of OVOC for these case studies, along with sensitivity studies using atmospheric chemistry models, holds potential to further investigate the causes for the reverse weekend effect in O_3 during hot days from the existing dataset.

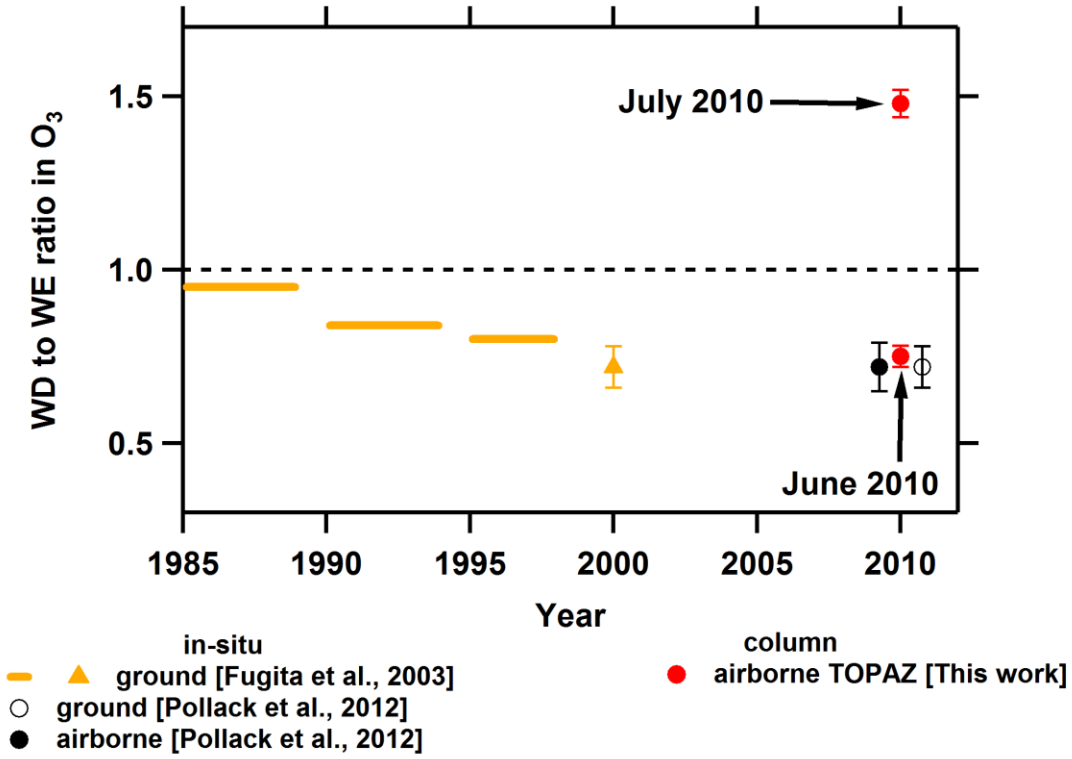

Figure 3.7.6: *Weekday to weekend ratio of O_3 concentrations in South Coast Air Basin (SCAB).*

3.7.4 Policy Implications

New and current NO_x emissions reduction regulations are likely to keep reducing NO_x emissions in the SCAB from the mobile sources in the future. In order to expedite the benefit of the new diesel engine standard (2010), the CARB is requiring all vehicles owners to replace or retrofit older diesel engines to meet the new diesel engine emission standards by 2023 and half of the fleet to meet the new standard by 2014 (http://www.arb.ca.gov/msprog/onrdiesel/documents/TBFinalReg.pdf). As a result of this new regulation, Millstein and Harley (2010) projected a greater than 50% reduction in summer time

NO_x emission in the Los Angeles basin from 2010 to 2015. Further NO_x reduction can also be expected from cars and light duty vehicles with the introduction of the Advanced Clean Cars Program (http://www.arb.ca.gov/msprog/consumer_info/advanced_clean_cars/consumer_acc.htm) which aims to reduce NO_x emission by 75% from the 2014 levels by year 2025.

With the photochemical O_3 production chemistry possibly already at its peak on days with high ambient temperature, these reductions in NO_x will likely reduce O_3 levels in the SCAB in the future. The major benefit of this would be seen during the summer season which is also the ozone season, when the temperature is at its maximum.

3.7.5 Conclusion

We report the observation of a reverse weekend O_3 effect in the South Coast Air Basin in the summer 2010. The usual decrease in NO_x emissions on the weekend was accompanied by reduction in the O_3 levels, in contrast to the weekend O_3 effect where higher O_3 levels are observed on the weekends. Our observation from the aircraft based on column amount of O_3 and NO_2 was also supported by the measurements at the CARB monitoring stations. Our observation of lower O_3 on the weekends indicates that the O_3 production chemistry in SCAB on very hot days, when VOC emissions are at their maximum, is mostly likely at the peak or on the verge of transitioning to the NO_x limited regime. Further decrease in NO_x in the future is likely to increase the frequency of such observations and ultimately result in fewer O_3 non-attainment days in SCAB during the ozone season.

4. Publications and Presentations related to this funding

4.1 Publications:

1. C. Knote, A. Hodzic, J.L. Jimenez, R. Volkamer, J.J. Orlando, S. Baidar, J. Brioude, J. Fast, D.R. Gentner, A.H. Goldstein, P.L. Hayes, W.B. Knighton, H. Oetjen, A. Setyan, H. Stark, R. Thalman, G. Tyndall, R. Washenfelder, E. Waxman, and Q. Zhang. Simulation of Semi-explicit Mechanisms of SOA Formation from Glyoxal in a 3-D Model. 2013, Atmospheric Chemistry and Physics Discussions, 13, 26699-26759. doi:10.5194/acpd-13-26699-2013

2. S. Baidar, R. Volkamer, R. Alvarez, A. Brewer, F. Davies, A. Langford, H. Oetjen, G. Pearson, C. Senff, and R.M. Hardesty. Combining Active and Passive Airborne Remote Sensing to Quantify NO_2 and O_x Production near Bakersfield, CA, 2013. British Journal for Environmental and Climate Change, 3(4), 566-586. doi:10.9734/BJECC/2013/5740

3. H. Oetjen, S. Baidar, N.A. Krotkov, L.N. Lamsal, M. Lechner, and R. Volkamer. Airborne MAX-DOAS Measurements over California: Testing the NASA OMI Tropospheric NO_2 product, 2013, Journal of Geophysical Research - Atmospheres, 118(13), 7400-7413. doi:10.1002/jgrd.50550

4. T.B. Ryerson, A.E. Andrews, W.M. Angevine, T.S. Bates, C.A. Brock, B. Cairns, R.C. Cohen, O.R. Cooper, J.A. de Gouw, F.C. Fehsenfeld, R.A. Ferrare, M.L. Fischer, R.C. Flagan, A.H. Goldstein, J.W. Hair, R.M. Hardesty, C.A. Hostetler, J.L. Jimenez, A.O. Langford, E. McCauley, S.A. McKeen, L.T. Molina, A. Nenes, S.J. Oltmans, D.D. Parrish, J.R. Pederson, R.B. Pierce, K. Prather, P.K. Quinn, J.H. Seinfeld, C. Senff, A. Sorooshian, J. Stutz, J.D. Surratt, M. Trainer, R. Volkamer, E.J. Williams, and S.C. Wofsy. The 2010 California Research at the Nexus of Air Quality and Climate Change (CalNex) field study. 2013, Journal of Geophysical Research - Atmospheres, 118(11), 5830-5866. doi:10.1002/jgrd.50331

5. S. Baidar, H. Oetjen, S. Coburn, B. Dix, I. Ortega, R. Sinreich, and R. Volkamer. The CU Airborne MAX-DOAS Instrument: Vertical Profiling of Aerosol Extinction and Trace Gases. 2013, Atmospheric Measurement Techniques, 6, 719-719-739. doi:10.5194/amt-6-719-2013

6. R. A. Zaveri, W. J. Shaw, D. J. Cziczo, B. Schmid, R. A. Ferrare, M. L. Alexander, M. Alexandrov, R. J. Alvarez, W. P. Arnott, D. B. Atkinson, S. Baidar, R. M. Banta, J. C. Barnard, J. Beranek, L. K. Berg, F. Brechtel, W. A. Brewer, J. F. Cahill, B. Cairns, C. D. Cappa, D. Chand, S. China, J. M. Comstock, M. K. Dubey, R. C. Easter, M. H. Erickson,

J. D. Fast, C. Floerchinger, B. A. Flowers, E. Fortner, J. S. Gaffney, M. K. Gilles, K. Gorkowski, W. I. Gustafson, M. Gyawali, J. Hair, R. M. Hardesty, J. W. Harworth, S. Herndon, N. Hiranuma, C. Hostetler, J. M. Hubbe, J. T. Jayne, H. Jeong, B. T. Jobson, E. I. Kassianov, L. I. Kleinman, C. Kluzek, B. Knighton, K. R. Kolesar, C. Kuang, A. Kubátová, A. O. Langford, A. Laskin, N. Laulainen, R. D. Marchbanks, C. Mazzoleni, F. Mei, R. C. Moffet, D. Nelson, M. D. Obland, H. Oetjen, T. B. Onasch, I. Ortega, M. Ottaviani, M. Pekour, K. A. Prather, J. G. Radney, R. R. Rogers, S. P. Sandberg, A. Sedlacek, C. J. Senff, G. Senum, A. Setyan, J. E. Shilling, M. Shrivastava, C. Song, S. R. Springston, R. Subramanian, K. Suski, J. Tomlinson, R. Volkamer, H. W. Wallace, J. Wang, A. M. Weickmann, D.R. Worsnop, X.-Y. Yu, A. Zelenyuk, and Q. Zhang.Overview of the 2010 Carbonaceous Aerosols and Radiative Effects Study (CARES). 2012, Atmospheric Chemistry and Physics, 12, 7647-7687. doi:10.5194/acp-12-7647-2012

4.2 Conference Presentations:

1. H. Oetjen, S. Baidar, M. Lechner, N.A. Krotkov, L.N. Lamsal, R.J. Alvarez II, S.-W. Kim, C.J. Senff, R. Volkamer. Airborne MAX-DOAS Measurements Over California: Testing the NASA OMI Tropospheric NO_2 Product , (Poster) International DOAS Workshop August 12-14, 2013 Boulder, CO, USA.

2. S. Baidar, H. Oetjen, C. Senff, R. Alvarez, M. Hardesty, A. Langford, S.-W. Kim, M. Trainer, and R. Volkamer. Observation of a Reverse Ozone Weekend Effect in the South Coast Air Basin (SoCAB) During Summer 2010, (Poster) International DOAS Workshop August 12-14, 2013 Boulder, CO, USA.

3. S. Baidar, R. Volkamer, R. Alvarez, A. Brewer, F. Davies, A. Langford, H. Oetjen, G. Person, C. Senff, and M. Hardesty. Combining Active and Passive Airborne Remote Sensing to Quantify NO_2 and O_x Production near Bakersfield, CA, (Poster) International DOAS Workshop August 12-14, 2013 Boulder, CO, USA.

4. H. Oetjen, S. Baidar, M. Lechner, N.A. Krotkov, L.N. Lamsal, R.J. Alvarez II, S.-W. Kim, C.J. Senff, R. Volkamer. Airborne MAX-DOAS Measurements Over California: Testing the NASA OMI Tropospheric NO_2 Product , (Poster) European Geoscience Union General Assembly April 7-12, 2013 Vienna, Austria.

5. S. Baidar, H. Oetjen, C. Senff, R. Alvarez, M. Hardesty, A. Langford, S.-W. Kim, M. Trainer, and R. Volkamer. Observation of a Reverse Ozone Weekend Effect in the South Coast Air Basin (SoCAB) During Summer 2010, (Poster) European Geoscience Union General Assembly April 7-12, 2013 Vienna, Austria.

6. S. Baidar, R. Volkamer, R. Alvarez, A. Brewer, F. Davies, A. Langford, H. Oetjen, G. Person, C. Senff, and M. Hardesty. Combining Active and Passive Airborne Remote Sensing to Quantify NO_2 and O_x Production near Bakersfield, CA, (Oral) European Geoscience Union General Assembly April 7-12, 2013 Vienna, Austria.

7. S. Baidar, H. Oetjen, C. J. Senff, R. J. Alvarez, R. M. Hardesty, A. O. Langford, S. Kim, M. Trainer, R. Volkamer. Observation of a reverse ozone weekend effect in South Coast Air Basin during summer 2010, (Poster) American Geophysical Union Fall Meeting December 3-7, 2012 San Francisco, CA, USA.

8. S. Baidar, H. Oetjen, I. Ortega, C. Cai, A. Kaduwela, S. Kim, R. Volkamer. Vertical profiles and column densities of NO_2 by the CU Airborne MAX-DOAS: comparison with model simulations, (Oral) American Geophysical Union Fall Meeting December 5-9, 2011 San Francisco, CA, USA.

9. H. Oetjen, S. Baidar, L. Lamsal, N. Krotkov, S. Kim, M. van Hoek, P. Veefkind, R. Volkamer. CU Airborne MAX-DOAS measurements: Application for satellite validation, (Oral) American Geophysical Union Fall Meeting December 5-9, 2011 San Francisco, CA, USA.

10. S. Baidar, H. Oetjen, B. Dix, R. Volkamer. Vertical profile retrievals of trace gases and aerosol extinction coefficient from CU AMAX-DOAS measurements, (Poster) 5^{th} International DOAS Workshop July 13-15, 2011 Mainz, Germany.

11. R. Volkamer, S. Baidar, H. Oetjen, I. Ortega, R. Sinreich, S. Kim, C. Cai. Column observations of NOx and OVOC over California during CalNex and CARES, (Oral) CalNex 2010 Data Analysis Workshop Agenda May 16-19, 2011 Sacramento, CA, USA.

12. S. Baidar, H. Oetjen, S. Kim, C. Cai, R. Volkamer. CU Airborne MAX-DOAS measurements over California during CalNex field campaign, (Poster) CalNex 2010 Data Analysis Workshop Agenda May 16-19, 2011 Sacramento, CA, USA.

13. S. Baidar, H. Oetjen, S. Coburn, I. Ortega, B. Dix, R. Sinreich, R. Volkamer. CU Airborne MAX-DOAS measurements over California during CalNex and CARES field campaigns, (Poster) American Geophysical Union Fall Meeting Dec 13-17, 2010 San Francisco, CA, USA.

14. H. Oetjen, S. Baidar, S. Coburn, I. Ortega, B. Dix, R. Sinreich, R. Volkamer. Vertical profile measurement of NO2 by means of the CU airborne MAX-DOAS instrument during CalNex 2010, (Oral) American Geophysical Union Fall Meeting Dec 13-17, 2010 San Francisco, CA, USA.

5. Conclusions

The extensive measurements of NO_2 covering a large spatial area over California, and measurements of HCHO and CHOCHO by CU AMAX-DOAS provide a unique and exciting data set to assess emissions and chemistry of NO_x and VOC in atmospheric chemistry models, and make better models available for air resource management over California.

The telescope pylon of the CU AMAX-DOAS was modified to add vertical profiling capability. A rotatable prism allowed measurements above, below and forward of the plane using the same telescope to characterize the entire atmosphere. NO_2 VCD measurements by the CU AMAX-DOAS were validated by two ground based MAX-DOAS instruments. Agreement between the airborne and ground based instruments was better 10 % for co-incident measurements.

NO_x levels in SCAB and California have been decreasing rapidly over the last decade due to state wide NO_x control policy and economic recession. Our comprehensive mapping of NO_2 is generally consistent with the decrease observed by the satellites measurements between 2005 and 2008. The highest NO_2 vertical columns were found in the western part of the SCAB over downtown Los Angeles and the main thoroughfare connecting eastern and western part of the basin. NO_2 levels decrease by ~80% in the eastern part of the basin and over the high desert. The observed weekly cycle is also consistent with previous studies. A decrease of 20-40% was observed in different parts of SCAB on weekends compared to weekdays. NO_2 column in Sacramento and Bakersfield area were significantly lower compared to SCAB and comparable to background level in SCAB. A strong vertical layering in NO_2 and OVOC is observed that is only partly captured by atmospheric models. Our data provide boundary conditions for atmospheric models, and provide information about pollutant levels aloft.

Comparison of NASA OMI tropospheric NO_2 vertical column with NO_2 vertical column measured by CU AMAX-DOAS showed that NASA OMI NO_2 product (v2.1) delivers high quality data for California during summer season. Fair agreement was found for the temporally and spatially averaged data. The agreement between the two data sets improved with the application of selection criteria such as pixel number in OMI swath, cloud radiance fraction. The removal of large pixels at the edges of the OMI swath was found to be the main driver for improving agreement.

Our NO_2 data was also compared with atmospheric model outputs to evaluate the NO_x emission inventories used in the models. Comparison showed that the older EI (NEI 2005 and CARB 2008) significantly over predicted NO_x in California (factor of 2-3). Model predictions with the latest EI from CARB (CARB 2010) were generally in very good agreement with the observations (within 30% in SCAB and 10% in Sacramento and Bakersfield area).

We demonstrated the potential and feasibility to combine passive and active remote sensing instruments namely the CU AMAX-DOAS, NOAA TOPAZ lidar and NCAS Doppler lidar

aboard a research aircraft to quantify NO_x emission and O_x production from source regions. Our analysis showed large O_3 production over areas with active oil and gas wells near Bakersfield. NO_x emissions from these areas were also higher than what is currently in the emission inventory (CARB 2010). However, NO_x emissions as represented in the CARB 2010 emission inventory agree well with our measurements over Bakersfield city (within 30%).

Our observations showed that the O_3 chemistry in SCAB is possibly at its peak and in the verge of transitioning to NO_x limited regime during very hot days when VOC emissions are at the maximum. Further reduction in NO_x in the future is likely to reduce O_3 levels in SCAB under such scenarios. As high O_3 days mostly occur in summer, SCAB could be finally seeing the benefits of years of NO_x control policy soon.

HCHO and CHOCHO vertical column and profiles from the case studies showed that both these OVOCs are likely ubiquitous over California. Both OVOCs are significantly underestimated by atmospheric models based on CARB 2010 EI, indicating missing VOC sources, or existing shortcomings in the VOC chemistry that are expected to impact oxidative capacity and SOA formation rates. In particular over inland locations, the significant presence of elevated HCHO and CHOCHO between 1-2 km altitudes is not predicted well by several models. The origin of this discrepancy is currently not understood.

Finally, we note that there remain unexplored opportunities to retrieve vertical columns and/or profiles of these OVOCs from the entire CU AMAX-DOAS dataset for comparison with atmospheric models to improve model predictions in California as well as assessment of satellite products for use in regulating air quality over large spatial areas. Our data are measured over spatial scales that bridge between near surface observations and satellites, and facilitate a more direct comparison with atmospheric models.

6. Recommendations for future work

This project has demonstrated a novel and cost effective approach to measure horizontal and vertical distributions of NO_2 and oxygenated hydrocarbons (OVOC) over California. We have brought into existence tools to measure column abundances of carcinogenic formaldehyde, HCHO and mutagenic glyoxal, CHOCHO, an indicator of VOC oxidation and SOA precursor from research aircraft. For two case studies over SCAB we have compared OVOC observations with atmospheric models (Section 3.5 and 3.6), and found that models consistently and significantly underestimate both OVOCs in the boundary layer and in the free troposphere. These missing OVOC sources in atmospheric models above the boundary layer affect the photochemistry inside the boundary layer as air mixes down, and indicate uncertainties about VOC/NOx ratios in the CARB 2010 EI, which translates into uncertain O_3 and secondary aerosol formation. Measurements of HCHO and CHOCHO VCD maps from research aircraft are scarce over California, yet the knowledge about OVOC distributions provide means to track missing VOC sources, evaluate VOC chemistry by constraining the rate of VOC oxidation, assess oxidative capacity in atmospheric models that is a key component to accurately predicting the secondary (inorganic and organic) aerosol source. Only two out of 52 research flights were analyzed for OVOC at the time of completion of this project.

The dataset provides the following opportunities:

1. Extend the divergence flux approach used to calculate NO_x emissions over Bakersfield to OVOC formation rates, and map fluxes over SCAB, Bakersfield, Sacramento, across the US-Mexican border, and over high deserts through the integrated analysis of NOAA TOPAZ O_3 data, CU AMAX-DOAS OVOC and NO_2, and NCAS Doppler lidar winds. Expanding the flux divergence technique towards OVOC could further help determine the sources and spatial distribution of OVOCs (which in part determine oxidative fields) and missing VOC emissions (which would help close the carbon accounting gap and better inform SOA models).
2. Measurements of soil surface temperature from a radiometer aboard the aircraft provide currently unexplored means to further investigate the source of the variable boundary layer height in the San Joaquin valley and Sacramento valley. Irrigation in the Central Valley is expected to cause variations of soil temperature over small spatial scales. The variability of boundary layer height in the Central Valley is currently not understood.
3. Full angle scans by AMAX-DOAS, and the wavelength dependent absorption of NO2 provide means to analyze range resolved NO_2 vertical profiles along the flight track. NO_2 at altitudes above 1 km provides a chemical indicator for recent mixing from the surface, and provides independent means to interrogate boundary layer height variability from a perspective of a short-lived chemical species. It further provides an opportunity to contrast the conditions in the San Joaquin and Sacramento valleys with those in the SCAB.

4. Investigate missing sources for OVOC over SCAB, San Joaquin valley and Sacramento valley that inform about VOC reactivity, O_3 and SOA formation. These three regions are chemically very different, yet continue to face problems of O_3 and PM non-attainment. The existing spectra hold largely unexplored potential to assess the VOC emission inventory, and test VOC oxidation chemistry in the models.
5. Unexplained OVOC in the residual layer can affect the chemistry of O_3 and aerosol formation in the boundary layer upon down-mixing of pollution in the residual layer during morning hours. The available data set has only partially been analyzed and holds unexplored potential to map OVOC in the residual layer more comprehensively by analyzing additional vertical profiles, and investigate the impact of these OVOC on photochemistry.
6. Investigate the sensitivity of O_3 formation to NO_x and VOC concentrations in California. HCHO to NO_x and CHOCHO to NO_x ratios enable us to determine sensitivity of an area to NO_x and VOC control (Duncan et al., 2010). Further, CHOCHO to HCHO ratio provides a useful metric to identify biogenic vs. anthropogenic VOC influences. The comprehensive mapping of these ratios informs decisions about emission controls for NO_x and VOCs.
7. It is now accepted that fine PM pollution is largely formed in the atmosphere as the result of photochemical transformation of gases (secondary aerosol) in addition to direct emissions (primary aerosol). By investigating the OVOC weekend effect, this dataset holds potential to inform control strategies to reduce fine PM that depend on knowledge about oxidative fields, as well as VOC precursors to PM from light-duty and heavy-duty vehicles.
8. Assess quality of satellite retrievals of HCHO and CHOCHO in California over summer months for potential application in air quality monitoring from space. With the planned deployment of geo-stationary satellite instruments like TEMPO in the near future, which will provide hourly measurements of NO_2, HCHO and CHOCHO among others, it would be very advantageous to assess the usefulness of the satellite data for air quality monitoring application.

7. References:

Alvarez II, R. J., Senff, C. J., Langford, A. O., Weickmann, A. M., Law, D. C., Machol, J. L., Merritt, D. A., Marchbanks, R. D., Sandberg, S. P., Brewer, W. A., Hardesty, R. M., and Banta, R. M.: Development and Application of a Compact, Tunable, Solid-State Airborne Ozone Lidar System for Boundary Layer Profiling, J. Atmos. Ocean. Technol., 28, 1258-1272, doi:10.1175/JTECH-D-10-05044.1, 2011.

Anderson, L. G., Lanning, J. A., Barrell, R., Miyagishima, J., Jones, R. H., and Wolfe, P.: Sources and sinks of formaldehyde and acetaldehyde: An analysis of Denver's ambient concentration data, Atmos. Environ., 30, 2113-2123, doi:10.1016/1352-2310(95)00175-1, 1996.

Baidar, S., Oetjen, H., Coburn, S., Dix, B., Ortega, I., Sinreich, R., and Volkamer, R.: The CU Airborne MAX-DOAS instrument: vertical profiling of aerosol extinction and trace gases, Atmos. Meas. Tech., 6, 719-739, doi:10.5194/amt-6-719-2013, 2013.

Ban-Weiss, G. A., McLaughlin, J. P., Harley, R. A., Lunden, M. M., Kirchstetter, T. W., Kean, A. J., Strawa, A. W., Stevenson, E. D., and Kendall, G. R.: Long-term changes in emissions of nitrogen oxides and particulate matter from on-road gasoline and diesel vehicles, Atmos. Environ., 42, 220-232, doi:10.1016/j.atmosenv.2007.09.049, 2008.

Blanchard, C. L. and Tanenbaum, S. J.: Differences between weekday and weekend air pollutant levels in southern California, J. Air Waste Manage. Assoc., 53, 816-828, 2003.

Calvert, J. G., Atkinson, R., Becker, K. H., Kamens, R. M., Seinfeld, J. H., Wallington, T. J. and Yarwood, G.: The Mechanisms of Atmospheric Oxidation of Aromatic Hydrocarbons, Oxford University Press, Oxford, 2002.

Castellanos, J. L., Gomez, S., and Guerra, V.: The triangle method for finding the corner of the L-curve, Applied Numerical Mathematics, 43, 359-373, doi:10.1016/S0168-9274(01)00179-9, 2002.

Chinkin, L. R., Coe, D. L., Funk, T. H., Hafner, H. R., Roberts, P. T., Ryan, P. A., and Lawson, D. R.: Weekday versus weekend activity patterns for ozone precursor emissions in California's South Coast Air Basin, J. Air Waste Manage. Assoc., 53, 829-843, 2003.

Cleveland, W. S., Graedel, T. E., Kleiner, B., and Warner, J. L.: Sunday and Workday Variations in Photochemical Air-Pollutants in New-Jersey and New-York, Science, 186, 1037-1038, doi:10.1126/science.186.4168.1037, 1974.

Davis, K. J., Gamage, N., Hagelberg, C. R., Kiemle, C., Lenschow, D. H., and Sullivan, P. P.: An objective method for deriving atmospheric structure from airborne lidar observations, J. Atmos. Ocean. Technol., 17, 1455-1468, doi:10.1175/1520-0426(2000)017<1455:AOMFDA>2.0.CO;2, 2000.

Deutschmann, T., Beirle, S., Friess, U., Grzegorski, M., Kern, C., Kritten, L., Platt, U., Prados-Roman, C., Pukite, J., Wagner, T., Werner, B., and Pfeilsticker, K.: The Monte Carlo atmospheric radiative transfer model McArtim: Introduction and validation of Jacobians and 3D features, J. Quant. Spectrosc. Radiat. Transfer, 112, 1119-1137, doi:10.1016/j.jqsrt.2010.12.009, 2011.

DiGangi, J. P., Henry, S. B., Kammrath, A., Boyle, E. S., Kaser, L., Schnitzhofer, R., Graus, M., Turnipseed, A., Park, J., Weber, R. J., Hornbrook, R. S., Cantrell, C. A., Maudlin,R.L.,,III, Kim, S., Nakashima, Y., Wolfe, G. M., Kajii, Y., Apel, E. C., Goldstein, A. H., Guenther, A., Karl, T., Hansel, A., and Keutsch, F. N.: Observations of glyoxal and formaldehyde as metrics for the anthropogenic impact on rural photochemistry, Atmospheric Chemistry and Physics, 12, 9529-9543, doi:10.5194/acp-12-9529-2012, 2012.

Duncan, B.N., Yoshida, Y., Olson, J.R., Sillman, S., Martin, R.V., Lamsal, L., Hug, Y., Pickering, K.E., Retscher, R., Allen, D.J., Crawford, J.H., Application of OMI observations to a space-based indicator of NOx and VOC controls on surface ozone formation, Atmospheric Environment, 44, 18, 2213-2223, 2010.

Elkus, B. and Wilson, K. R.: Photochemical Air-Pollution - Weekend Weekday Differences, Atmos. Environ., 11, 509-515, doi:10.1016/0004-6981(77)90067-1, 1977.

Finlayson-Pitts, B. J. and Pitts Jr, J. N.: Chemistry of the Upper and Lower Atmosphere, Academic Press, San Diego, CA, 2000.

Fu, T., Jacob, D. J., Wittrock, F., Burrows, J. P., Vrekoussis, M., and Henze, D. K.: Global budgets of atmospheric glyoxal and methylglyoxal, and implications for formation of secondary organic aerosols, Journal of Geophysical Research-Atmospheres, 113, D15303, doi:10.1029/2007JD009505, 2008.

Fujita, E. M., Stockwell, W. R., Campbell, D. E., Keislar, R. E., and Lawson, D. R.: Evolution of the magnitude and spatial extent of the weekend ozone effect in California's South Coast Air Basin, 1981-2000, J. Air Waste Manage. Assoc., 53, 802-815, 2003.

Garcia, A. R., Volkamer, R., Molina, L. T., Molina, M. J., Samuelson, J., Mellqvist, J., Galle, B., Herndon, S. C., and Kolb, C. E.: Separation of emitted and photochemical formaldehyde in Mexico City using a statistical analysis and a new pair of gas-phase tracers, Atmospheric Chemistry and Physics, 6, 4545-4557, 2006.

Grosjean, D., Grosjean, E., and Gertler, A. W.: On-road emissions of carbonyls from light-duty and heavy-duty vehicles, Environ. Sci. Technol., 35, 45-53, doi:10.1021/es001326a, 2001.

Guenther, A. B., Zimmerman, P. R., Harley, P. C., Monson, R. K., and Fall, R.: Isoprene and Monoterpene Emission Rate Variability - Model Evaluations and Sensitivity Analyses, J. Geophys. Res. Atmos., 98, 12609-12617, doi:10.1029/93JD00527, 1993.

Hansen, P. C.: Analysis of Discrete Ill-Posed Problems by Means of the L-Curve, SIAM Rev, 34, 561-580, doi:10.1137/1034115, 1992.

Harley, R. A., Marr, L. C., Lehner, J. K., and Giddings, S. N.: Changes in motor vehicle emissions on diurnal to decadal time scales and effects on atmospheric composition, Environ. Sci. Technol., 39, 5356-5362, doi:10.1021/es048172+, 2005.

Hayes, P. L., Ortega, A. M., Cubison, M. J., Froyd, K. D., Zhao, Y., Cliff, S. S., Hu, W. W., Toohey, D. W., Flynn, J. H., Lefer, B. L., Grossberg, N., Alvarez, S., Rappenglueck, B., Taylor, J. W., Allan, J. D., Holloway, J. S., Gilman, J. B., Kuster, W. C., De Gouw, J. A., Massoli, P., Zhang, X., Liu, J., Weber, R. J., Corrigan, A. L., Russell, L. M., Isaacman, G., Worton, D. R., Kreisberg, N. M., Goldstein, A. H., Thalman, R., Waxman, E. M., Volkamer, R., Lin, Y. H., Surratt, J. D., Kleindienst, T. E., Offenberg, J. H., Dusanter, S., Griffith, S., Stevens, P. S., Brioude, J., Angevine, W. M., and Jimenez, J. L.: Organic aerosol composition and sources in Pasadena, California, during the 2010 CalNex campaign, Journal of Geophysical Research-Atmospheres, 118, 9233-9257, doi:10.1002/jgrd.50530, 2013.

Kampf, C. J., Waxman, E. M., Slowik, J. G., Dommen, J., Pfaffenberger, L., Praplan, A. P., Prevot, A. S. H., Baltensperger, U., Hoffmann, T., and Volkamer, R.: Effective Henry's Law Partitioning and the Salting Constant of Glyoxal in Aerosols Containing Sulfate, Environ. Sci. Technol., 47, 4236-4244, doi:10.1021/es400083d, 2013.

Kean, A. J., Grosjean, E., Grosjean, D., and Harley, R. A.: On-road measurement of carbonyls in California light-duty vehicle emissions, Environ. Sci. Technol., 35, 4198-4204, doi:10.1021/es010814v, 2001.

Knote, C., Hodzic, A., Jimenez, J. L., Volkamer, R., Orlando, J. J., Baidar, S., Brioude, J., Fast, J., Genter, D. R., Goldstein, A. H., Hayes, P. L., Knigton, W. B., Oetjen, H., Setyan, A., Stark, H., Thalman, R., Tyndall, J., Washenfelder, R. A., Waxman, E., and Zhang, Q.: Simulation of Semi-explicit Mechanisms of SOA Formation from Glyoxal in a 3-D Model, Atmos. Chem. Phys. Discuss., 13, 26699-26759, doi:10.5194/acpd-13-26699-2013, 2013.

Kroll, J. H., Ng, N. L., Murphy, S. M., Varutbangkul, V., Flagan, R. C., and Seinfeld, J. H.: Chamber studies of secondary organic aerosol growth by reactive uptake of simple carbonyl compounds, Journal of Geophysical Research-Atmospheres, 110, D23207, doi:10.1029/2005JD006004, 2005.

Langford, A. O., Senff, C. J., Alvarez,R.J.,,II, Banta, R. M., Hardesty, R. M., Parrish, D. D., and Ryerson, T. B.: Comparison between the TOPAZ Airborne Ozone Lidar and In Situ Measurements during TexAQS 2006, J. Atmos. Ocean. Technol., 28, 1243-1257, doi:10.1175/JTECH-D-10-05043.1, 2011.

Lebron, F.: Comparison of Weekend-Weekday Ozone and Hydrocarbon Concentrations in Baltimore-Washington Metropolitan Area, Atmos. Environ., 9, 861-863, doi:10.1016/0004-6981(75)90046-3, 1975.

Lee, M., Heikes, B. G., Jacob, D. J., Sachse, G., and Anderson, B.: Hydrogen peroxide, organic hydroperoxide, and formaldehyde as primary pollutants from biomass burning, Journal of Geophysical Research-Atmospheres, 102, 1301-1309, doi:10.1029/96JD01709, 1997.

Liggio, J., Li, S. M., and McLaren, R.: Heterogeneous reactions of glyoxal on particulate matter: Identification of acetals and sulfate esters, Environ. Sci. Technol., 39, 1532-1541, doi:10.1021/es048375y, 2005a.

Liggio, J., Li, S. M., and McLaren, R.: Reactive uptake of glyoxal by particulate matter, Journal of Geophysical Research-Atmospheres, 110, D10304, doi:10.1029/2004JD005113, 2005b.

Marr, L. C. and Harley, R. A.: Modeling the effect of weekday-weekend differences in motor vehicle emissions on photochemical air pollution in central California, Environ. Sci. Technol., 36, 4099-4106, doi:10.1021/es020629x, 2002a.

Marr, L. C. and Harley, R. A.: Spectral analysis of weekday-weekend differences in ambient ozone, nitrogen oxide, and non-methane hydrocarbon time series in California, Atmos. Environ., 36, 2327-2335, doi:10.1016/S1352-2310(02)00188-7, 2002b.

Millstein, D. E. and Harley, R. A.: Effects of Retrofitting Emission Control Systems on In-Use Heavy Diesel Vehicles, Environ. Sci. Technol., 44, 5042-5048, doi:10.1021/es1006669, 2010.

Myriokefalitakis, S., Vrekoussis, M., Tsigaridis, K., Wittrock, F., Richter, A., Bruehl, C., Volkamer, R., Burrows, J. P., and Kanakidou, M.: The influence of natural and anthropogenic secondary sources on the glyoxal global distribution, Atmospheric Chemistry and Physics, 8, 4965-4981, 2008.

Oetjen, H., Baidar, S., Krotkov, N. A., Lamsal, L. N., Lechner, M., and Volkamer, R.: Airborne MAX-DOAS measurements over California: Testing the NASA OMI tropospheric NO2 product, J. Geophys. Res. Atmos., 118, 7400-7413, doi:10.1002/jgrd.50550, 2013.

Parrish, D. D., Ryerson, T. B., Mellqvist, J., Johansson, J., Fried, A., Richter, D., Walega, J. G., Washenfelder, R. A., de Gouw, J. A., Peischl, J., Aikin, K. C., McKeen, S. A., Frost, G. J., Fehsenfeld, F. C., and Herndon, S. C.: Primary and secondary sources of formaldehyde in urban atmospheres: Houston Texas region, Atmospheric Chemistry and Physics, 12, 3273-3288, doi:10.5194/acp-12-3273-2012, 2012.

Pearson, G., Davies, F., and Collier, C.: An Analysis of the Performance of the UFAM Pulsed Doppler Lidar for Observing the Boundary Layer, J. Atmos. Ocean. Technol., 26, 240-250, doi:10.1175/2008JTECHA1128.1, 2009.

Platt, U. and Stutz, J.: Differential Optical Absorption Spectroscopy: Principles and Applications, Springer Verlag, Heidelberg, 2008.

Pollack, I. B., Ryerson, T. B., Trainer, M., Neuman, J. A., Roberts, J. M., and Parrish, D. D.: Trends in ozone, its precursors, and related secondary oxidation products in Los Angeles, California: A synthesis of measurements from 1960 to 2010, J. Geophys. Res. Atmos., 118, doi:10.1002/jgrd.50472, 2013.

Pollack, I. B., Ryerson, T. B., Trainer, M., Parrish, D. D., Andrews, A. E., Atlas, E. L., Blake, D. R., Brown, S. S., Commane, R., Daube, B. C., de Gouw, J. A., Dube, W. P., Flynn, J., Frost, G. J., Gilman, J. B., Grossberg, N., Holloway, J. S., Kofler, J., Kort, E. A., Kuster, W. C., Lang, P. M., Lefer, B., Lueb, R. A., Neuman, J. A., Nowak, J. B., Novelli, P. C., Peischl, J., Perring, A. E., Roberts, J. M., Santoni, G., Schwarz, J. P., Spackman, J. R., Wagner, N. L., Warneke, C., Washenfelder, R. A., Wofsy, S. C., and Xiang, B.: Airborne and ground-based observations of a weekend effect in ozone, precursors, and oxidation products in the California South Coast Air Basin, J. Geophys. Res. Atmos., 117, D00V05, doi:10.1029/2011JD016772, 2012.

Rodgers, C. D.: Inverse Methods for Atmospheric Sounding: Theory and Practice, World Scientific, Singapore, 2000.

Russell, A. R., Valin, L. C., and Cohen, R. C.: Trends in OMI NO2 observations over the United States: effects of emission control technology and the economic recession, Atmos. Chem. Phys., 12, 12197-12209, doi:10.5194/acp-12-12197-2012, 2012.

Russell, A. R., Valin, L. C., Bucsela, E. J., Wenig, M. O., and Cohen, R. C.: Space-based Constraints on Spatial and Temporal Patterns of NOx Emissions in California, 2005-2008, Environ. Sci. Technol., 44, 3608-3615, doi:10.1021/es903451j, 2010.

Ryerson, T. B., Andrews, A. E., Angevine, W. M., Bates, T. S., Brock, C. A., Cairns, B., Cohen, R. C., Cooper, O. R., de Gouw, J. A., Fehsenfeld, F. C., Ferrare, R. A., Fischer, M. L., Flagan, R. C., Goldstein, A. H., Hair, J. W., Hardesty, R. M., Hostetler, C. A., Jimenez, J. L., Langford, A. O., McCauley, E., McKeen, S. A., Molina, L. T., Nenes, A., Oltmans, S. J., Parrish, D. D., Pederson, J. R., Pierce, R. B., Prather, K., Quinn, P. K., Seinfeld, J. H., Senff, C. J., Sorooshian, A., Stutz, J., Surratt, J. D., Trainer, M., Volkamer, R., Williams, E. J., and Wofsy, S. C.: The 2010 California Research at the Nexus of Air Quality and Climate Change (CalNex) field study, Journal of Geophysical Research-Atmospheres, 118, 5830-5866, doi:10.1002/jgrd.50331, 2013.

Seinfeld, J. H. and Pandis, S. N.: Atmospheric Chemisty and Physics: from air pollution to climate change, Wiley-Interscience, Hoboken, New Jersey, 2006.

Steck, T.: Methods for determining regularization for atmospheric retrieval problems, Appl. Opt., 41, 1788-1797, doi:10.1364/AO.41.001788, 2002.

Volkamer, R., Coburn, S., Dix, B., and Sinreich, R.: MAX-DOAS observations from ground, ship, and research aircraft: maximizing signal-to-noise to measure 'weak' absorbers, Proc. SPIE, 7462-746203, doi:10.1117/12.826792, 2009.

Volkamer, R., Molina, L. T., Molina, M. J., Shirley, T., and Brune, W. H.: DOAS measurement of glyoxal as an indicator for fast VOC chemistry in urban air, Geophys. Res. Lett., 32, L08806, doi:10.1029/2005GL022616, 2005.

Volkamer, R., Ziemann, P. J., and Molina, M. J.: Secondary Organic Aerosol Formation from Acetylene (C2H2): seed effect on SOA yields due to organic photochemistry in the aerosol aqueous phase, Atmos. Chem. Phys., 9, 1907-1928, doi:10.5194/acp-9-1907-2009, 2009.

Volkamer, R., Martini, F. S., Molina, L. T., Salcedo, D., Jimenez, J. L., and Molina, M. J.: A missing sink for gas-phase glyoxal in Mexico City: Formation of secondary organic aerosol, Geophys. Res. Lett., 34, L19807, doi:10.1029/2007GL030752, 2007.

Vrekoussis, M., Wittrock, F., Richter, A., and Burrows, J. P.: GOME-2 observations of oxygenated VOCs: what can we learn from the ratio glyoxal to formaldehyde on a global scale?, Atmospheric Chemistry and Physics, 10, 10145-10160, doi:10.5194/acp-10-10145-2010, 2010.

Vrekoussis, M., Wittrock, F., Richter, A., and Burrows, J. P.: Temporal and spatial variability of glyoxal as observed from space, Atmospheric Chemistry and Physics, 9, 4485-4504, doi:10.5194/acp-9-4485-2009, 2009.

Warneke, C., de Gouw, J. A., Holloway, J. S., Peischl, J., Ryerson, T. B., Atlas, E., Blake, D., Trainer, M., and Parrish, D. D.: Multiyear trends in volatile organic compounds in Los Angeles, California: Five decades of decreasing emissions, J. Geophys. Res. Atmos., 117, D00V17, doi:10.1029/2012JD017899, 2012.

Washenfelder, R. A., Young, C. J., Brown, S. S., Angevine, W. M., Atlas, E. L., Blake, D. R., Bon, D. M., Cubison, M. J., de Gouw, J. A., Dusanter, S., Flynn, J., Gilman, J. B., Graus, M., Griffith, S., Grossberg, N., Hayes, P. L., Jimenez, J. L., Kuster, W. C., Lefer, B. L., Pollack, I. B., Ryerson, T. B., Stark, H., Stevens, P. S., and Trainer, M. K.: The glyoxal budget and its contribution to organic aerosol for Los Angeles, California, during CalNex 2010, Journal of Geophysical Research-Atmospheres, 116, D00V02, doi:10.1029/2011JD016314, 2011.

Waxman, E. M., Dzepina, K., Ervens, B., Lee-Taylor, J., Aumont, B., Jimenez, J. L., Madronich, S., and Volkamer, R.: Secondary organic aerosol formation from semi- and intermediate-volatility organic compounds and glyoxal: Relevance of O/C as a tracer for aqueous multiphase chemistry, Geophys. Res. Lett., 40, 978-982, doi:10.1002/grl.50203, 2013.

White, A. B., Senff, C. J., and Banta, R. M.: A comparison of mixing depths observed by ground-based wind profilers and an airborne lidar, J. Atmos. Ocean. Technol., 16, 584-590, doi:10.1175/1520-0426(1999)016<0584:ACOMDO>2.0.CO;2, 1999.

Yarwood, G., Stoeckenius, T. E., Heiken, J. G., and Dunker, A. M.: Modeling weekday/weekend Los Angeles region for 1997, J. Air Waste Manage. Assoc., 53, 864-875, 2003.

Yarwood, G., Grant, J., Koo, B., and Dunker, A. M.: Modeling weekday to weekend changes in emissions and ozone in the Los Angeles basin for 1997 and 2010, Atmos. Environ., 42, 3765-3779, doi:10.1016/j.atmosenv.2007.12.074, 2008.

Zaveri, R. A., Shaw, W. J., Cziczo, D. J., Schmid, B., Ferrare, R. A., Alexander, M. L., Alexandrov, M., Alvarez, R. J., Arnott, W. P., Atkinson, D. B., Baidar, S., Banta, R. M., Barnard, J. C., Beranek, J., Berg, L. K., Brechtel, F., Brewer, W. A., Cahill, J. F., Cairns, B., Cappa, C. D., Chand, D., China, S., Comstock, J. M., Dubey, M. K., Easter, R. C., Erickson, M. H., Fast, J. D., Floerchinger, C., Flowers, B. A., Fortner, E., Gaffney, J. S., Gilles, M. K., Gorkowski, K., Gustafson, W. I., Gyawali, M., Hair, J., Hardesty, R. M., Harworth, J. W., Herndon, S., Hiranuma, N., Hostetler, C., Hubbe, J. M., Jayne, J. T., Jeong, H., Jobson, B. T., Kassianov, E. I., Kleinman, L. I., Kluzek, C., Knighton, B., Kolesar, K. R., Kuang, C., Kubatova, A., Langford, A. O., Laskin, A., Laulainen, N., Marchbanks, R. D., Mazzoleni, C., Mei, F., Moffet, R. C., Nelson, D., Obland, M. D., Oetjen, H., Onasch, T. B., Ortega, I., Ottaviani, M., Pekour, M., Prather, K. A., Radney, J. G., Rogers, R. R., Sandberg, S. P., Sedlacek, A., Senff, C. J., Senum, G., Setyan, A., Shilling, J. E., Shrivastava, M., Song, C., Springston, S. R., Subramanian, R., Suski, K., Tomlinson, J., Volkamer, R., Wallace, H. W., Wang, J., Weickmann, A. M., Worsnop, D. R., Yu, X. -., Zelenyuk, A., and Zhang, Q.: Overview of the 2010 Carbonaceous Aerosols and Radiative Effects Study (CARES), Atmospheric Chemistry and Physics, 12, 7647-7687, doi:10.5194/acp-12-7647-2012, 2012.

8. Glossary of Terms, Abbreviations, and Symbols.

AGL	above ground level
AK	averaging kernel
ASL	above sea level
AGU	American Geophysical Union
AMAX-DOAS	airborne multi-axis differential optical absorption spectroscopy
AMF	air mass factor
AOD	aerosol optical depth
AZ	Arizona
BAMF	box air mass factor
BL	boundary layer
BLH	boundary layer height
CA	California
CalNex	California Research at the Nexus of Air Quality and Climate Change
CARB	California Air Resources Board
CARES	Carbonaceous Aerosols and Radiative Effects Study
CHOCHO	glyoxal
CMAQ	Community Multi-Scale Air Quality model
dAMF	differential air mass factor
DOAS	Differential Optical Absorption Spectroscopy
dSCD	differential slant column density
DOF	degrees of freedom
EA	elevation angle
EI	emission inventory
FOV	field of view
FT	free troposphere
FWHM	full width at half maximum
geoAMF	geometric air mass factor
HCHO	formaldehyde
HO_2	hydroperoxy radical
HO_x	$OH + HO_2$
LOS	lines of sight
MAX-DOAS	multi-axis differential optical absorption spectroscopy
NASA	National Aeronautics and Space Administration
NCAS	National Center for Atmospheric Science
NOAA	National Oceanic and Atmospheric Administration
NO	nitric oxide
NO_2	nitrogen dioxide
NO_x	$NO + NO_2$
O_3	ozone

O_x	$O_3 + NO_2$
OH	hydroxyl radical
OMI	Ozone Monitoring Instrument
OVOC	oxygenated volatile organic compound
PM_1	particulate matter less than 1 micron in aerodynamic diameter
$PM_{2.5}$	particulate matter less than 2.5 micron in aerodynamic diameter
PO3	ozone production rate
RF	research flight
RTM	radiative transfer model
SA	surface albedo
SCAB	South Coast Air Basin
SCD	slant column density
SCAB	South Coast Air Basin
SOA	secondary organic aerosol
SSA	single scattering albedo
SZA	solar zenith angle
UV	ultraviolet
VCD	vertical column density
VOC	volatile organic compound
WD	weekday
WE	weekend
WF	weighting function
WRF-Chem	Weather Research and Forecasting Chemistry

Appendix. Other publications that used CU AMAX-DOAS data

1. C. Knote, A. Hodzic, J.L. Jimenez, R. Volkamer, J.J. Orlando, S. Baidar, J. Brioude, J. Fast, D.R. Gentner, A.H. Goldstein, P.L. Hayes, W.B. Knighton, H. Oetjen, A. Setyan, H. Stark, R. Thalman, G. Tyndall, R. Washenfelder, E. Waxman, and Q. Zhang. **Simulation of Semi-explicit Mechanisms of SOA Formation from Glyoxal in a 3-D Model.** 2013, *Atmospheric Chemistry and Physics Discussions*, 13, 26699-26759. doi:10.5194/acpd-13-26699-2013

2. T.B. Ryerson, A.E. Andrews, W.M. Angevine, T.S. Bates, C.A. Brock, B. Cairns, R.C. Cohen, O.R. Cooper, J.A. de Gouw, F.C. Fehsenfeld, R.A. Ferrare, M.L. Fischer, R.C. Flagan, A.H. Goldstein, J.W. Hair, R.M. Hardesty, C.A. Hostetler, J.L. Jimenez, A.O. Langford, E. McCauley, S.A. McKeen, L.T. Molina, A. Nenes, S.J. Oltmans, D.D. Parrish, J.R. Pederson, R.B. Pierce, K. Prather, P.K. Quinn, J.H. Seinfeld, C. Senff, A. Sorooshian, J. Stutz, J.D. Surratt, M. Trainer, R. Volkamer, E.J. Williams, and S.C. Wofsy. **The 2010 California Research at the Nexus of Air Quality and Climate Change (CalNex) field study.** 2013, Journal of Geophysical Research - Atmospheres, 118(11), 5830-5866. doi:10.1002/jgrd.50331

3. R. A. Zaveri, W. J. Shaw, D. J. Cziczo, B. Schmid, R. A. Ferrare, M. L. Alexander, M. Alexandrov, R. J. Alvarez, W. P. Arnott, D. B. Atkinson, S. Baidar, R. M. Banta, J. C. Barnard, J. Beranek, L. K. Berg, F. Brechtel, W. A. Brewer, J. F. Cahill, B. Cairns, C. D. Cappa, D. Chand, S. China, J. M. Comstock, M. K. Dubey, R. C. Easter, M. H. Erickson, J. D. Fast, C. Floerchinger, B. A. Flowers, E. Fortner, J. S. Gaffney, M. K. Gilles, K. Gorkowski, W. I. Gustafson, M. Gyawali, J. Hair, R. M. Hardesty, J. W. Harworth, S. Herndon, N. Hiranuma, C. Hostetler, J. M. Hubbe, J. T. Jayne, H. Jeong, B. T. Jobson, E. I. Kassianov, L. I. Kleinman, C. Kluzek, B. Knighton, K. R. Kolesar, C. Kuang, A. Kubátová, A. O. Langford, A. Laskin, N. Laulainen, R. D. Marchbanks, C. Mazzoleni, F. Mei, R. C. Moffet, D. Nelson, M. D. Obland, H. Oetjen, T. B. Onasch, I. Ortega, M. Ottaviani, M. Pekour, K. A. Prather, J. G. Radney, R. R. Rogers, S. P. Sandberg, A. Sedlacek, C. J. Senff, G. Senum, A. Setyan, J. E. Shilling, M. Shrivastava, C. Song, S. R. Springston, R. Subramanian, K. Suski, J. Tomlinson, R. Volkamer, H. W. Wallace, J. Wang, A. M. Weickmann, D.R. Worsnop, X.-Y. Yu, A. Zelenyuk, and Q. Zhang.**Overview of the 2010 Carbonaceous Aerosols and Radiative Effects Study (CARES)**. 2012, Atmospheric Chemistry and Physics, 12, 7647-7687. doi:10.5194/acp-12-7647-2012